Politecnico di Milano
Department of Structural Engineering
Doctoral School In Structural, Earthquake and Geotechnical Engineering

---

Lifetime Probabilistic Seismic Assessment of Multistory Precast Buildings

Doctoral Dissertation of:
Andrea Titi - 738617

Supervisor:
Prof. Fabio Biondini

The Chair of the Doctoral Program:
Prof. Roberto Paolucci

Year 2012 – Cycle XXIV

Lifetime Probabilistic Seismic Assessment of Multistory Precast Buildings

PhD thesis by Andrea Titi
Supervisor: Prof. Fabio Biondini

February 2012

Doctoral School in Structural, Earthquake and Geotechnical Engineering
Department of Structural Engineering
Politecnico di Milano

Board Committee:

Prof. Roberto Paolucci (Co-ordinator)
Prof. Fabio Biondini
Prof. Gabriella Bolzon
Prof. Claudia Comi
Prof. Alberto Corigliano
Prof. Maria Laura Costantino
Prof. Claudio di Prisco
Prof. Marcodi Prisco
Prof. Roberto Felicetti
Prof. Attilio Frangi
Prof. Pietro Gambarova
Prof. Anna Pandolfi
Prof. Federico Perotti
Prof. Alberto Taliercio
Prof. Pasquale Vena

To my love Federica

Acknowledgements

Behind this work there is no only the hand (and the sweat) of the author, since many persons have contributed to the research. First, a special thank goes to my supervisor, Prof. Fabio Biondini. Without his presence the framework here developed would not been possible; he guided me through the selection of the topic, definition of structures investigated and suggestions on the numerical procedures to apply. Moreover, I cannot forget the detailed review of the manuscript. In other words, during these three years he has taught me a methodology to work in the academic world.

During the PhD, I've had the opportunity to study three months at the University of Ljubljana under the supervision of Prof. Matej Fischinger. First of all, I am grateful to him for the accommodation found; I had a very comfortable room with all the facilities, simplifying a lot my stage in Slovenia. He gave me precious suggestions regarding Performance-based earthquake engineering, in particular with reference to the choice of the limit states. Moreover, I had the rare chance to participate to the Bled workshop, where the most famous researchers in earthquake engineering have explained the recent advances in this awesome field. I have to thank also Prof. Tatjana Isaković, for some suggestions regarding my work and in particular Prof. Matjaz Dolšek, since he had the patience to explain some concepts concerning the probabilistic approach within the PEER methodology and practical advices to perform numerical simulations. Most of the work carried out in this thesis is based on his past researches. My stage in Ljubljana has been very interesting also because the guys I met in the department are very friendly; I want to thank especially Miha for all the suggestions regarding SAFECAST project and practical information on how to spend time visiting Ljubljana and surrounding places. Thanks also to Mirko, Daniel and the other PhD students. HVALA friends.

Thanks to Prof. Giandomenico Toniolo, always kind to give me recommendations for the design stage of the prototype and to Prof. Marco Valente, which offered the opportunity to begin the doctoral study. I want to thank all my friends in the Department of Structural Engineering, in particular Roberto, since he has divided with me "joys and pains" during our studies, Manuel because my favorite "fellow traveler", and Elena, since she is a nice person. Special thanks also to Visar, Federica, Francesco, Yashar (you are a good guy), Bruno, Marco, Giovanna, Anna, Rossella, Fulvio, Juan and all the people in the Department who gave me a

hand. It is a pleasure to work with you in the same place.

My family has played a fundamental role in my growth, so I am grateful to them for all the patience during these years. This thesis depends mostly for their support.

I cannot miss to thank my historical friends, Matteo, Andrea and Matteo; I am proud to have such persons near me, since their help it has always been for me fundamental to go ahead in my studies. Moreover, I cannot forget Alice and Marzia, best "San Giorgio girls"; thanks for your kindness.

Finally, a special thanks goes to my girlfriend, Federica. She has had the patience to follow me throughout all my adventures, giving precious advices, and bearing me every day. Lots of time my behavior has not been good ("sorry Federica, but we cannot see tomorrow because I have to study"), but every day she gives the strength to work and follow my passions. So, only three words are necessary: I LOVE YOU.

To conclude, I want to cite a statement for me very significant, because it encloses in few words the concept of engineering.

> Scientists study the world as it is;
> engineers create the world that never has been.
>
> *Theodore Von Karman*

Abstract

Evaluation of seismic performance of structures during their lifetime is nowadays an emerging issue in the research community. In particular, a key aspect concerns the possibility to include in the seismic assessment the effects of environmental hazards, because current seismic codes and capacity design criteria are time-invariant and do not take into account such problem. Actually, considering the lifetime of a generic structure, the energy dissipating collapse mode may vary over time due to a reduction of both strength and ductility of the sections where plastic hinges are expected to occur during an earthquake. Such an interaction could finally bring to undesired failure mechanisms like weak column-strong beam, unpredicted during the design phase. Regarding environmental hazards, this investigation focuses on the role of a chloride attack, evaluating the loss of mechanical properties of the structural elements.

Among different structures, precast buildings are particularly subjected to the effect of corrosion, because most of their structural members can be directly exposed to the atmosphere. In such conditions, the diffusive attack from external aggressive agents, like sulphates and chlorides, can take place and lead to a deterioration of concrete and steel. Damage induced by corrosion can significantly reduce local strength and ductility, modifying in this way the failure mechanism and the corresponding seismic performance during structural lifetime.

Despite of the extensive research on seismic behavior of precast structures, few studies focused on the lifetime behavior of precast buildings subjected to environmental hazards. In such conditions, the diffusive attack of aggressive agents can lead to a deterioration of mechanical properties of structural members and to a decrease of the overall response. As a consequence, capacity design criteria should be properly calibrated to consider the severity of environmental exposure and the required structural lifetime. In particular, in this investigation the corrosion of reinforcement due to chloride attack is considered, assuming a contamination by chlorides the most significant source of environmental hazard for reinforced concrete structures.

With respect to this problem, in recent years different mitigation strategies emerged, with the purpose to extend the lifetime of reinforced concrete structures or to reduce the potential damage due to strong ground motions. In particular, new advanced materials have been proposed in order to improve the seismic performance of structures and to extend their durability characteristics. Among them, the use of the so called Engineered Cementitious Composite (ECC) in place of normal concrete allows, by an appropriate mix design and adding

a minimum quantity of polimeric fibers (about 2%), the formation of multiple narrow cracking in structural elements. This leads to a localized damage and a more uniform distribution of energy dissipation. Nevertheless, the reduction of the crack width tends to decrease the diffusion process of aggressive agents such as chlorides, with significant benefits in terms of durability.

Finally, considering that all the phenomena involved in this investigation have an inherent variability, the rational approach to take into account their randomness is based on a probabilistic assessment. Moreover, since the nature of the problem is highly non linear, numerical simulations provide the only practical and effective method. In particular, if random variables are included, the numerical process with repeated simulations can be based on Monte Carlo sampling technique, which is particularly effective in treatment of aleatory and epistemic uncertainties. In order to reduce the computational cost involved in the simulation analysis based on plain Monte Carlo method, advanced tools are also needed to have reliable results. A stratified sampling called Latin Hypercube sampling is implemented, since such technique requires a relative small number of simulations to have reliable information on the performance of structural systems.

Based on the considerations above, it is expected a significant influence of environmental hazard on the seismic performance of precast structures during their lifetime, and such influence can be quantified in an effective way using the tools developed in this work. In fact, one of the most relevant contributions of the present investigation is the possibility to show and evaluate how same structures, placing at sites with the same seismic hazard, can have a different seismic reliability depending on the environmental conditions. Such results should lead to improve the current seismic design criteria included in design codes and recommendations to properly take into account the potential coupling among seismic and environmental hazards.

Contents

List of Figures

List of Tables

Chapter 1

Introduction

Evaluation of seismic performance of structures during their lifetime is nowadays an emerging important issue in the scientific community. In particular, a key aspect concerns the possibility to include in the seismic assessment the effects of environmental hazards, because current seismic codes and capacity design criteria are time-invariant and do not take into account such issue. Actually, considering the lifetime of a structure, the energy dissipating collapse mode may vary over time due to a reduction of both strength and ductility of the sections where plastic hinges are expected to occur during an earthquake. Such an interaction could finally bring to undesired failure mechanisms like weak column-strong beam, unpredicted during the design phase. Regarding environmental hazards, this investigation focuses on the role of a chloride attack, evaluating the loss of mechanical properties of the structural elements.

Among different structures, precast buildings are particularly subjected to the effect of corrosion, because most of their structural members can be directly exposed to the atmosphere. In such conditions, the diffusive attack from external aggressive agents, like sulphates and chlorides, can take place and lead to a deterioration of concrete and steel. Damage induced by corrosion can significantly reduce local strength and ductility, modifying, in this way the failure mechanism and the corresponding seismic performance during structural lifetime, Biondini et al. [40]. Several international research projects in the past highlighted important issues on the seismic behavior of precast structures, but none of them focused on the evaluation of the structural performance during lifetime, where seismic hazard can be coupled with the environmental one.

Performance-based earthquake engineering (PBEE) offers an effective methodology to assess the seismic behavior of different kind of structures, regardless their material and configuration. In particular the Pacific Earthquake Engineering Center (PEER) has developed in the last years a comprehensive framework for the PBEE, Porter [198], Moehle and Deierlein [169]. This methodology has successfully implemented in past researches, see e.g. Jalayer [129] and codes, FEMA 356 [84] and FEMA P695 [86]. In particular, through this approach a complete risk analysis on a structure can be done, from hazard of the site to assessment of damage and

monetary losses, including also economical and social issues. Within the present research this methodology, in the following called PEER methodology, will be used for the evaluation of the structural safety, even if the framework developed is more general.

1.1 Research on seismic performance of precast structures

The investigation moves from the general assumption that current seismic codes and capacity design criteria are time-invariant and do not take into account the interaction with environmental hazards. It is however important to predict the lifetime performance of a generic structures, see e.g. Biondini et al. [42], because undesired mechanisms, not considered during design, can appear and modify in a decisive way the structural behavior. To this aim the primary goal of this study is to understand the seismic behavior of multistory RC precast structures during their lifetime. In particular, among different environmental hazards, the diffusive attack induced by chlorides is considered, in order to quantify in a reliable way the structural safety for this kind of buildings.

The present research places oneself in a wider investigation on the seismic performance of precast frames carried out in US (see e.g. the PRESS Programme, Priestley [202]) and in Europe during last decades. Precast concrete structures are quite widespread in Italy and other seismic countries in southern Europe, both for commercial and industrial buildings, where the maximum number of stories is usually limited to two or three or, typically for industrial use, these structures are one-story buildings. Structural members are generally prefabricated, and dry connections with mechanical devices between them are adopted. Beam-to-column joints are usually hinged, so the dissipative zones are located at the base of the columns, where plastic hinges are expected to occur during a strong motion. For these systems, a capacity design based on a collapse mechanism involving the maximum number of stories is required to have a satisfying seismic behavior, Biondini et al. [39].

Considering seismic codes, such as EC8 [74] and NTC 2008 [181], the performance of precast structures under earthquake, assuming a suitable capacity design of connections, can be compared to that of cast-in-place structures in terms of global strength and ductility. This statement is demonstrated on the base of results reached in recent European research studies, namely “ECOLEADER” and “GROWTH”, Biondini and Toniolo [32]. In particular numerical and experimental studies were performed on one story industrial frames, Figure 1.1. First, seismic response of the prototype was investigated in probabilistic terms for lognormally distributed material strengths and under artificial accelerograms, in order to match very well the design response spectrum. A Monte Carlo simulation based on a large sample of incremental nonlinear dynamic analyses up to collapse was therefore carried out for each prototype to compute the statistical parameters of the overstrength, defined as the ratio of the computed value over design value of the seismic capacity. Numerical predictions proved that

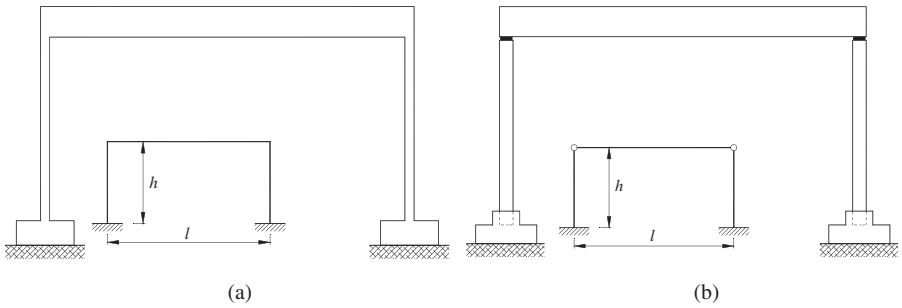

Figure 1.1: Prototypes of one-story frames: (a) monolithic and cast-in-situ; (b) hinged and precast, Biondini and Toniolo [32].

precast structures have the same seismic capacity of the corresponding cast-in-situ structures, and confirmed the adequacy of the values given by the code to the behavior factor of concrete frames ($q = 4.5$).

To support the results, pseudodynamic tests on real buildings have been performed at ELSA (European Laboratory for Seismic Assessment) Laboratory. Figure 1.2 shows a view of the full scale prototypes. The aim of the experimental tests was to compare the seismic capacities of cast-in-situ and precast structures, validating at the same time the analytical model used in the numerical investigations. Different load steps have been scheduled, and the results in terms of force-displacement curves can be seen in Figure 1.3; the direct comparison of the cycles highlights the expected large strength resources of this type of structures against seismic collapse and confirms the overall equivalence of the seismic behavior of precast and cast-in-situ structures. It is worth noting that at the third level for the precast prototype ($a_g = 1.08$), the amplitude of the motion took the jacks to the end of stroke and the test had to be stopped. However, the maximum displacement of 400 mm was reached without any incipient decay of the reaction force and the cover of the critical zones of the columns was still intact. The structural collapse was still far.

The fourth stage of the research has been developed within the "GROWTH" program. Two prototypes consisting of six columns and a mesh of beams and roof elements were designed to investigate the seismic behavior of precast structures with roof elements placed side by side. Figure 1.4 show a views of the prototypes and of the testing plants. The only difference among them was the orientation of the beams and roof elements with respect to the seismic action. Hinged connections were used between roof elements, beams and columns. The control of the pseudodynamic tests was based on two degree of freedoms, associated with the top horizontal displacements of the lateral and of the central frames; the measured top displacements of lateral and central columns during the tests resulted practically coincident, proving that double connections between beams and roof elements gives a rotational restraint in the roof plane which enables the activation of an effective diaphragm action, even if the roof elements are not connected among them. After the pseudodynamic tests, both prototypes have been subjected

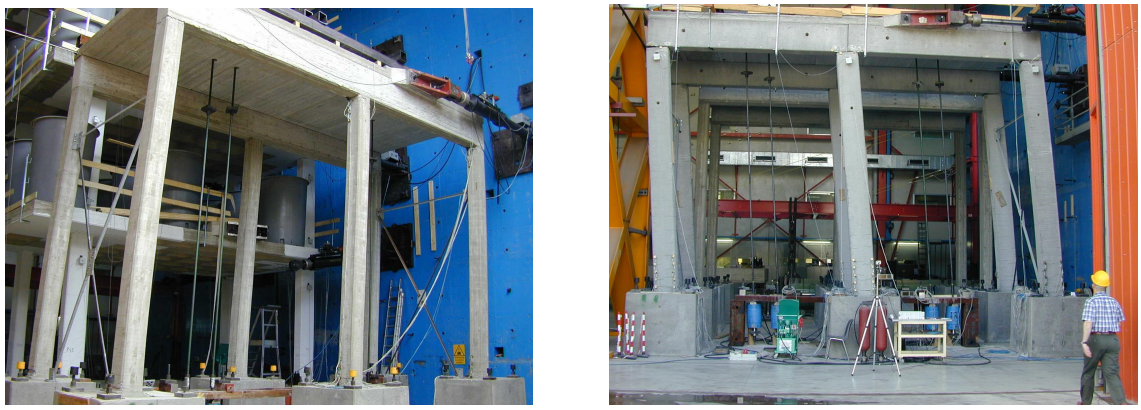

(a) Monolithic and cast-in-situ.

(b) Hinged and precast.

Figure 1.2: View of the structural prototypes, Biondini and Toniolo [31].

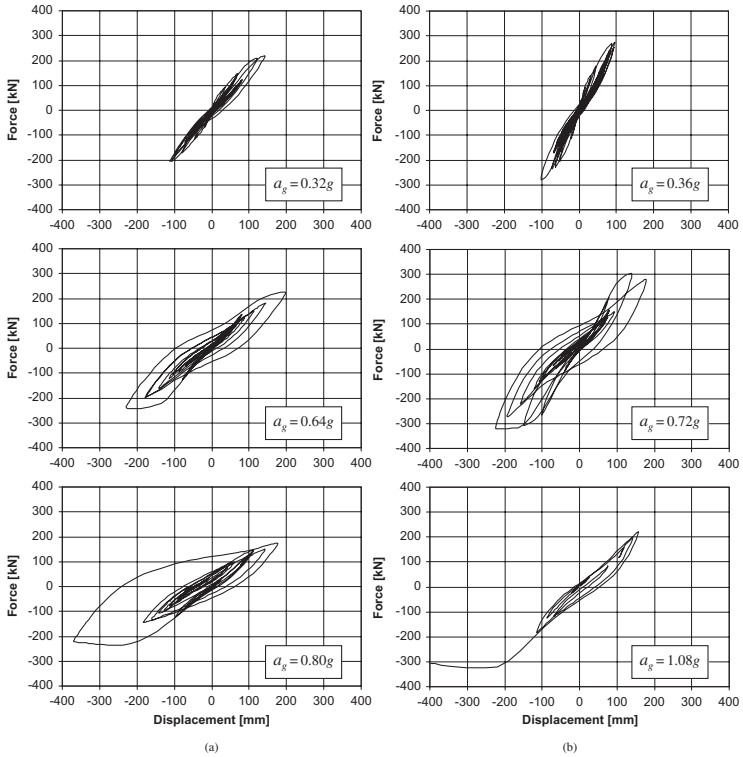

Figure 1.3: Force-displacement diagrams of the pseudodynamic tests: (a) cast-in situ frame; (b) precast frames, Biondini and Toniolo [32].

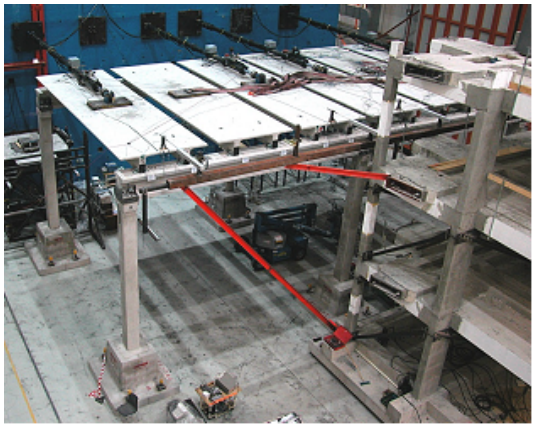

(a) Monolithic and cast-in-situ.

(b) Hinged and precast.

Figure 1.4: View of the structural prototypes with roof elements with axis (a) parallel to the direction of the seismic action (Prototype 1), and (b) orthogonal to the direction of the seismic action (Prototype 2), Biondini et al. [35].

to a cyclic test under imposed displacements up to collapse, Figure 1.5. With a ultimate displacement $d_u \approx 360\,\text{mm}$ and a yielding displacement $d_y \approx 80\,\text{mm}$, a global displacement ductility equal to 4.5 was evaluated, as assumed by the final version of EC8 (EC8 [74]) for the behavior factor of precast frame systems.

The outcomes of the studies carried out under the "ECOLEADER" and "GROWTH" research projects showed the good seismic performance of precast structures under condition that the connections were properly over-dimensioned ("strong connections"). To complete the investigation, their actual behaviour under seismic excitation needs to be addressed. To this aim, the European research program SAFECAST has been recently launched to investigate the seismic performance of connections in precast systems, Biondini et al. [41]. This project involved a campaign of experimental static tests carried out on single specimens, as well as pseudo-dynamic tests on the three-storey full-scale prototype. The aim of this large size experimentation is to provide proper reliable evidences about the seismic behaviour of a common type of precast multi-storey buildings widely used for commercial and industrial purposes. In particular the role of the beam-to-column connections, hinged or moment-resisting, has to be investigated with respect to the inter-story drift control as regulated by the code requirements. This also includes the verification of the accuracy of the ordinary methods of analysis. Therefore, the choice of the prototype has been addressed to a three-story building with a number of spans and bays sufficient to represent the behavior of this type of buildings, the dimensions in plan being the maximum compatible with the capacity of the testing plant of ELSA laboratory, Figure 1.6.

Figure 1.7 shows the image of the prototype, placed against the reaction wall of the laboratory. The horizontal actions are applied symmetrically on the mid axis of the two bays

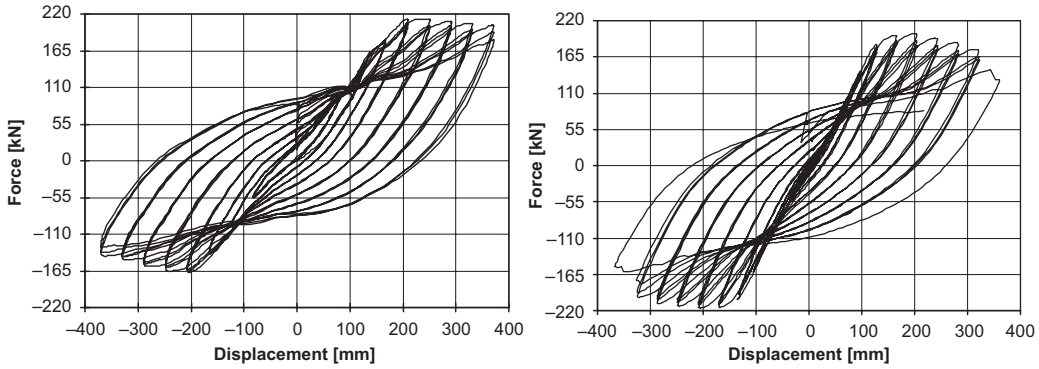

(a) (b)

Figure 1.5: Force-displacement diagrams of the cyclic tests on the structural prototypes with roof elements with axis (a) parallel to the direction of the seismic action (Prototype 1), and (b) orthogonal to the direction of the seismic action (Prototype 2), Biondini and Toniolo [32].

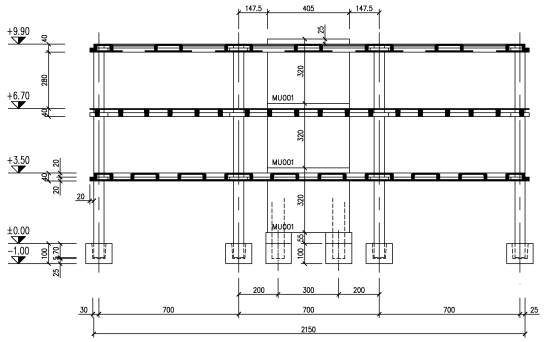

(a) Transversal section.

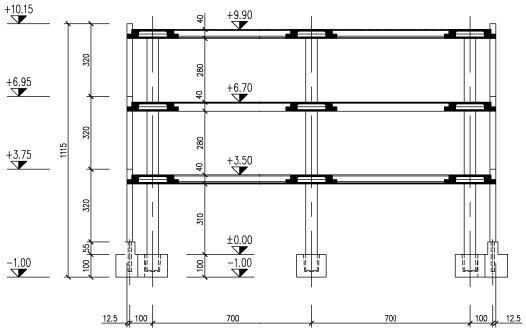

(b) Longitudinal section.

Figure 1.6: View of three-story full-scale prototype for Safecast project, Biondini et al. [41].

(a) Prototype under construction. (b) Prototype completed.

Figure 1.7: Safecast structural prototype tested at ELSA laboratory.

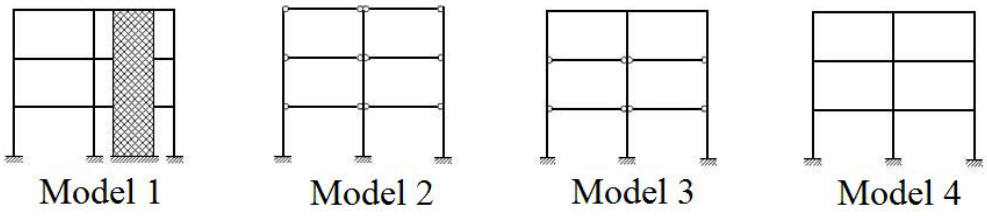

Figure 1.8: Structural schemes of the prototype for SAFECAST project.

in the directions of the beams. Two couples of jacks of 1000 kN of capacity are used at the 2nd and 3rd floor levels and four jacks of 500 kN of capacity are used at the 1st floor level. Steel beams are placed along the two axis to connect all the floor elements and distribute uniformly the applied forces. The loading system works under displacement control with three degrees of freedom and no torsional effects. During the pseudodynamic tests no vertical loads additional to the dead load of the structure are applied. In this way the test situation does not correspond exactly to what considered in the design for the dimensioning of the elements. The prototype during the experimental campaign represents only itself with its mechanical properties. A series of tests has been scheduled, changing subsequently the arrangement of the connection system, in order to study different structural schemes on the same prototype, Figure 1.8. First, a sequence of tests on the dual wall-frame system with the structure connected to the two lateral bracing walls has been performed. Then the bracing walls have been uncoupled and the structure reduced to a pure frame system. A second sequence has been performed on this frame system with all hinged beam-to-column connections. A third sequence has been performed after restraining the top floor joints turned into moment-resisting connections. The final sequence of tests have been performed with the joints of all the floors turned into moment-resisting connections.

Regarding the dual wall-frame system, due to his stiffness, with a computed natural

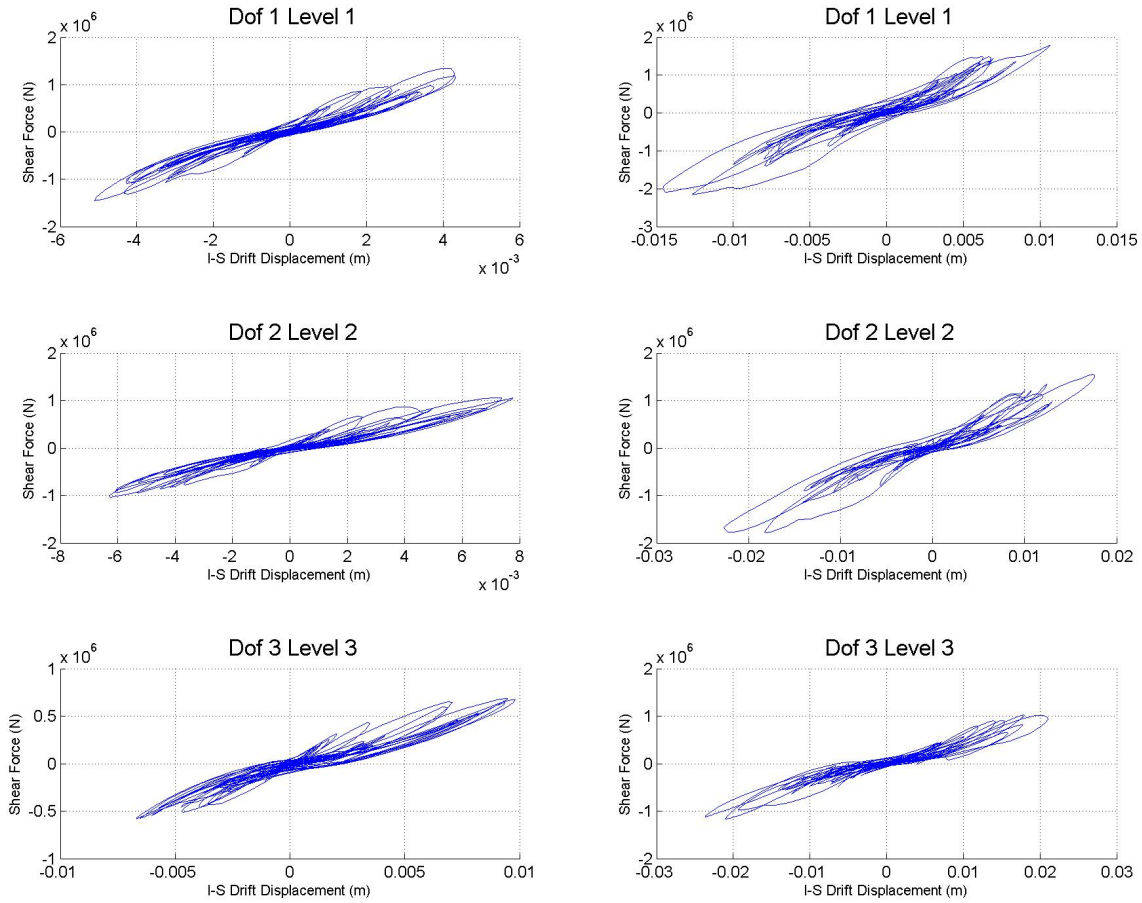

(a) $0.15\,g$. (b) $0.30\,g$.

Figure 1.9: First series of test: force versus inter-story drift cycles, Biondini and Toniolo [33]

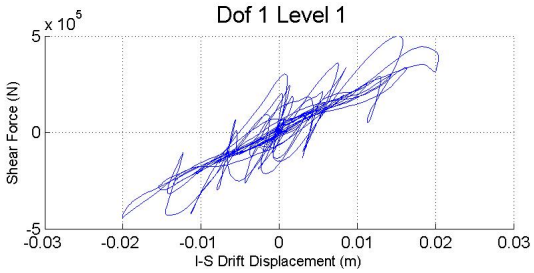

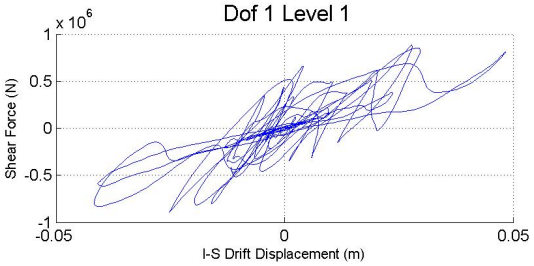

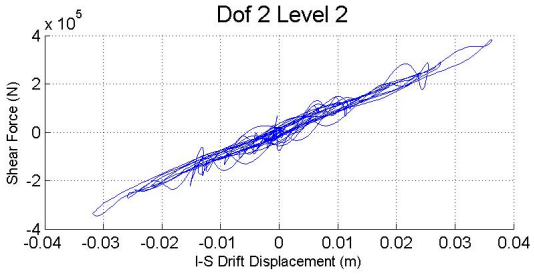

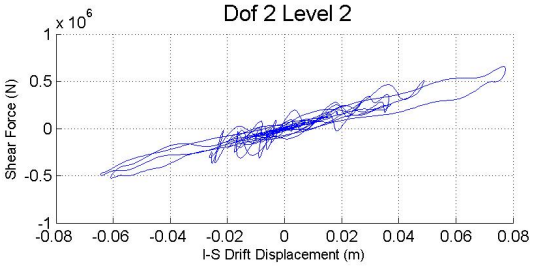

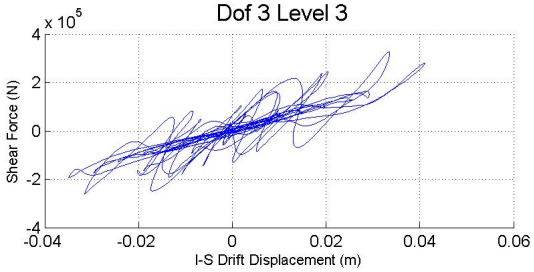

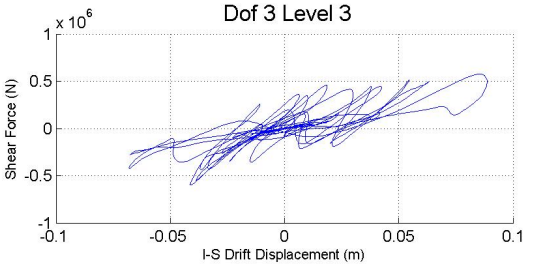

(a) $0.15\,g$. (b) $0.30\,g$.

Figure 1.10: Second series of test: force versus inter-story drift cycles, Biondini and Toniolo [33]

vibration period of 0.27 s, the first vibration mode is the dominant one. At the lower intensity the response remained practically within the elastic range, as shown by the force versus inter-story drift cycles of Figure 1.9a. At the higher intensity the response underwent relevant non linear effects with wider force-drift cycles (see Figure 1.9b). The results are fully significant up to the virtual duration of 12 s at which a local rupture of the joint between the wall and the floor slab at the second floor occurred, leaving the connection with an uneven efficacy. The most important aspect of this first sequence of tests is the diaphragm behavior of the floors for the transmission of the inertia forces to the two bracing walls. The large set of data recorded by the dedicated gauges is under investigation for the deduction of a reliable model to be used in design calculations.

The second sequence of tests was performed on the pure frame system with all hinged beam-to-column connections. The much more flexible arrangement, with a computed natural vibration period of 1.57 s, led to lower inertia forces and higher story drifts. The vibration of the structure is sensibly affected by the higher modes. At the lower intensity the response remained again practically within the elastic range, as shown by the force versus inter-story drift cycles of Figure 1.10a. The maximum inter-story drifts measured at the three levels have been respectively 0.6%, 1.1%, and 1.3% from the lower to the upper floor. These values pointed out the excessive deformability of the hinged frame structure that would require larger sizes of the columns to fulfill the damage limit state imposed by the codes. At the higher intensity the response underwent moderate non linear effects with wider force-drift cycles (see Figure 1.10b). Results for the other two configurations will be provided in few time, when Safecast project will be officially closed.

The results of the SAFECAST project are expected to complete the large research program developed in Europe over the last two decades which provided significant advances in the understanding of the seismic behaviour of precast systems and in the definition of reliable design criteria for this type of structures. Since the purpose of the thesis is the lifetime seismic assessment of multistory precast frames, part of the activity has been devoted to the numerical simulation of the pseudo-dynamic tests, in order to identify the peculiar issues of this kind of structures and to understand the role of connections. In particular, preliminary linear and nonlinear dynamic analyses were performed to set the proper intensity measure for the subsequent experimental tests. The purpose is double: from one side, the comparison between two different methods of analysis allows to highlight the effectiveness of the approximated methodology (dynamic modal analysis) in the estimation of important parameters such as displacements and story forces.

From the other side, the comparison with the experimental results allows to validate the effectiveness of the analytical models used during all the investigation; two different approaches has been implemented (distributed and concentrated plasticity), and the results regarding one of the pseudo-dynamic tests performed can be found in Section 3.4. Because for the

SAFECAST project the seismic behavior of connections is fundamental, in the same section also the results coming from an improved model (where the connections have a nonlinear behavior) are presented. It is however worth nothing to remember that, because this research is still in progress and the data about the behavior of connections are not completely available, the remaining part of the thesis focuses on the seismic assessment of multistory precast frames with strong connections.

1.2 Motivation for study

Despite of different research programs, few studies focus on the lifetime behavior of precast buildings subjected to environmental hazards. In such conditions, the diffusive attack of aggressive agents like sulphates and chlorides can lead to a deterioration of mechanical properties of structural members and to a decrease of the overall response. As a consequence, capacity design criteria should be properly calibrated to consider the severity of environmental exposure and the required structural lifetime. Moreover, the coupling with seismic hazard should be taken into account, integrating the effects of airborne chloride into reliability-based durability design of RC structures, Akiyama et al. [3] and Akiyama et al. [4]. In this investigation the corrosion of reinforcement due to chloride attack is considered, assuming a contamination by chlorides the most significant source of environmental hazard for reinforced concrete structure, Stewart and Rosowsky [229] and Vu and Stewart [242].

With respect to this problem, in recent years different mitigation strategies emerged, with the purpose to extend the lifetime of reinforced concrete structures or to reduce the potential damage due to strong ground motions. The enhancement of the overall behavior can be reached acting on different levels, from global to local. In particular, new advanced materials have been proposed in order to improve the seismic performance of structures and to extend their durability properties. Among them, the use of the so called Engineered Cementitious Composite (ECC), see e.g. Li [146] and Li [147], in place of normal concrete allows, by an appropriate mix design and adding a minimum quantity of polymeric fibers (about 2%), the formation of multiple narrow cracking in structural elements. This leads to a localized damage and a more uniform distribution of energy dissipation. Nevertheless, the reduction of the crack width tends to decrease the diffusion process of aggressive agents such as chlorides, with significant benefits in terms of durability. With a proper tailoring of the micromechanics, this kind of composite material suggests different classes of target applications like collapse resistance under severe mechanical loading and structures requiring durability even when subjected to environmental hazards, Li [147].

Finally, considering that all the phenomena involved in this investigation have an inherent variability, the rational approach to take into account their randomness is based on a probabilistic assessment. Since the nature of the problem is highly non linear, numerical simulations

provide the only practical and effective method. In particular, if random variables are included, numerical process with repeated simulations can be based on Monte Carlo sampling technique, which is particularly effective in treatment of aleatory and epistemic uncertainties. For specialized problems there are also approximated numerical methods for finding solution for a probabilistic application, such as FOSM (Wong [246]). However, Monte Carlo simulation is the principal numerical tool to solve engineering problems involving probability, Ang and Tang [11] and Schueller and Pradlwarter [220]. In particular, in order to reduce the computational cost involved in the simulation analysis based on plain Monte Carlo method, advanced tools are needed to have reliable results. Among them, a stratified sampling called Latin Hypercube sampling is implemented, Iman and Conover [126], Stein [226] and Helton and Davis [113], since such technique requires a relative small number of simulations to have reliable information on the performance of structural systems.

1.3 Objectives and scope

The present study focuses on two main directions. From one side the purpose is to contribute to develop a reliable framework to perform a structural assessment of multistory RC frames subjected to chloride attack during the whole lifetime, in order to understand how environmental hazards can modify the overall seismic performance of this kind of buildings. A set of six low-rise precast frames, from two to four stories, designed according to a capacity criteria is considered (Biondini et al. [39]), changing the size of structural members in order to cover a sufficiently wide range of the structural behavior, from ordinary to less flexible buildings. Nonlinear seismic analyses, both static and dynamic, are performed, within the PEER methodology, during lifetime in order to check the capacity of the structures at different times, considering different limit states, from limited damage up to collapse. In this way it is also possible to verify in a more general way the proposed design criteria for precast structures, not only in terms of required ductility but in the light of a risk analysis. Structural assessment is carried out by using a calibrated element model capable to simulate the flexural response of RC elements up to collapse, see Ibarra et al. [121] and Haselton [112]. Special attention is given in the treatment of uncertainties, in particular those related to structural properties of the members; an advanced Monte Carlo method based on Latin Hypercube Sampling is applied, Dolšek [69], summarizing the results in terms of statistical descriptors.

A rigorous study on diffusion process of aggressive agents in concrete sections is done, implementing a code for the numerical simulation of diffusion mechanism in one-dimensional and bi-dimensional domains, verifying his capability through the comparison with the analytical solution for simple problems, and performing a parametric study in order to check the accuracy of the 1-D description of the problem with respect to the more accurate 2-D approach. Finally, the code is used to simulate the diffusion process of chlorides in the cross-sections of members,

adopted subsequently for the seismic analysis, in order to evaluate during time the reduction of steel bars diameter by introducing a damage index. In this way it is possible to describe the reduction of strength and ductility of the structural elements, with the aim to perform seismic analyses during the lifetime of precast structures.

From the other side a risk mitigation strategy is investigated, working on a local level and improving the characteristics of the material. In particular in the dissipative zones of the structures, where plastic hinges are expected to occur during an earthquake, standard concrete is replaced with another cementitious composite, namely Engineered Cementitious Composite (ECC). The name "Engineered" depends on a proper tailoring of the micromechanics of the material, suitable to match different classes of target applications. In this study ECC is applied in order to improve the overall seismic response of precast structures and their durability during lifetime. On the basis of the element model used to simulate the flexural behavior of concrete members, a moment-rotation law is proposed and subsequently calibrated considering the peculiarity of this composite and the few experimental results available in literature. Nonlinear analyses are then repeated, comparing the overall seismic response during time of both concrete and ECC precast frames.

1.4 Outline

The present dissertation deals with the seismic performance of multistory precast structures subjected to environmental hazards during their lifetime. The first part of the thesis presents an overview of the PEER methodology and related tools to perform a reliable probabilistic seismic assessment of reinforced concrete buildings. Second part introduces the environmental hazard and shows how the problem of chloride diffusion into RC cross-section can be solved numerically using an effective tool. In particular, through the procedures implemented, the lifetime seismic assessment of the structures studied is investigated. Finally, third part describes the potentiality of a mitigation strategy, working on a local level, to improve seismic performance and durability, substituting in the dissipative zones of the structure standard concrete with a cementitious composite, namely Engineered Cementitious Composite (ECC).

In details, **Chapter 2** introduces elements of theory of probability at the base of PEER methodology, and in particular focuses on Monte Carlo simulation for the treatment of uncertainties, Rubinstein and Kroese [214]. The core of the chapter is dedicated to the advanced sampling technique used in the present investigation in order to reduce the computation cost. Latin Hypercube sampling (Iman and Conover [127]) is compared to the plain Monte Carlo simulation, pointing out his effectiveness through the solution of simple problems. Finally, an overview of the probabilistic seismic hazard analysis is presented, introducing all the issues needed to develop hazard and fragility curves or, rather, to describe in a probabilistic way the seismic hazard of a site and the probability, for the structure, of exceeding a particular

damage state in regards to the damage measure adopted.

Chapter 3 shows the results of the probabilistic assessment of seismic performance of multistory RC frame systems using practical tools available within the PEER methodology. The chapter starts introducing the geometrical and mechanical characteristics of the buildings studied, designed according to the EC8 rules, EC8 [74]. Different limit states, defined both on a local and a global level, are introduced, in order to control the performance of the structures, from elastic range up to collapse. An analytical model capable to simulate the flexural behavior of beam and columns members up to collapse is presented, Ibarra et al. [121] and Haselton [112]. Validation of this element regarding precast frames is done, comparing the numerical results with those coming from pseudo-dynamic tests performed within the SAFECAST project. Subsequently, two possible methods for seismic analysis are illustrated. The more accurate incremental dynamic analysis (Vamvatsikos and Cornell [234]) is first described, focusing on different steps of the procedure, in particular the choice of input motion and the representation of uncertainties. Advantages and limitations are shown in the light of the second method used here, that is pushover analysis. The comparison is done because nonlinear static analysis reduces the computational cost and it is easy to implement also for design offices. The probabilistic assessment is based on a LH sampling of the key modeling parameters, evaluating the structural capacity in a statistical way and focusing on the importance of different parameters. Numerical simulations are summarized in terms of fragility curves and hazard scenarios, with a particular emphasis on the role of uncertainties.

Chapter 4 deals with the role of corrosion of rebars as environmental hazard for concrete structures. After a brief introduction on theoretical aspects, the chapter shows the different steps of the evolution of corrosion in the concrete sections and different types (from uniform corrosion to localized pitting corrosion), depending on the source of it. Finally, the consequences of environmental hazard on a local and global level are explained. The deterioration process is therefore simulated through a damage model, and his effectiveness is proved by comparing numerical results with experimental tests performed in the past on beams subjected to different rates of corrosion.

Chapter 5 regards the lifetime seismic prediction of structural capacity for the multistory RC frame structures studied. First of all the modeling of diffusion process of chlorides is deeply investigated, exploiting the capability of a code developed during this dissertation based on a particular type of evolutionary algorithm, known as “cellular automata”, Wolfram [245] and Schiff [219]. Both 1-D and 2-D approaches are considered in order to evaluate the concentration of chloride content within the concrete cross-sections, performing a parametric study to check the accuracy of the 1-D description of the problem with respect to the more accurate 2-D approach. Using then a damage index, the effect of corrosion on steel bars is shown as a reduction of diameter, both for longitudinal and transversal rebars. Finally, considering different times during lifetime of the structures, the mechanical properties of plastic

hinges in the dissipative zones of structural members are updated on the basis of damage process, and nonlinear analyses are repeated in order to evaluate the role of environmental hazard in the overall seismic performance of multistory RC frames.

In **Chapter 6** the capability of a mitigation strategy of seismic risk working on a material level is explored. In, particular this investigation focuses on the use on a special type of cementitious composite, namely Engineered Cementitious Composite (ECC), Li [147]. First of all, the role of micromechanics is considered, showing how it is possible to drive the material to predefined target applications. After that, the properties of ECC are illustrated; the investigation of the compressive, tensile and cyclic behavior, as well as the durability properties, allows to understand the main characteristic of this composite, particularly suitable for the study presented here. Finally, combining the results of experimental tests and the characteristics above explained, a hysteretic law for ECC plastic hinges in terms of moment-rotation relationship is suggested, modifying the equations proposed by Haselton, Haselton [112], for standard concrete element members. The same seismic analyses performed for RC frames are repeated for R/ECC frames during the entire lifetime, in order to compare the results in terms of structural assessment.

To conclude, **Chapter 7** summarizes the results obtained in the present investigation, tracing conclusions as well as limitations and future developments of the work done.

Chapter 2

Probability and earthquake engineering

2.1 Introduction

The chapter presents an overview of some concepts of theory of probability in regards with the PEER methodology. Among different numerical methods, the use of simulation based on Monte Carlo approach is explored, in particular investigating the capability of a stratified sampling technique in order to reduce the computational cost. Last part of the chapter is devoted to the probabilistic seismic hazard analysis (PSHA), introducing the key issues that will be used in the following studies.

2.2 Aleatory and epistemic uncertainties

Considering engineering problems, and in more general terms real world problems, uncertainties are unavoidable. The inherent variability of phenomena and the lack of knowledge of our models does not allow a description of the reality in a deterministic way, so it is crucial to understand the role of statistics and probability. A proper estimation of the main parameters involved in the problem allows to quantify the effects of uncertainties in the design and performance of our systems. In addiction, a probabilistic description of the phenomena is directly connected to a risk analysis, and the role of decision making in the design under uncertainties becomes essential, Ang and Tang [11]. One common way of thinking is to assume in the design the *worst condition*, in order to guarantee in all the situations a huge safety; clearly, without a systematic evaluation of the uncertainties, this kind of approach is a sort of deterministic one and may lead to an over design of structural elements with, consequently, higher costs. A correct approach cannot disregard a proper balance between costs and benefits, assuming probability of exceeding a particular limit state sufficiently low, but at the same time keeping in mind the economic consequences for the design.

In the analysis of complex systems, it is important to distinguish different sources of uncertainty, namely *aleatory uncertainty* and *epistemic uncertainty*. Aleatory uncertainty, as the name suggests, deals with an intrinsic variability of the system studied, while epistemic uncertainty refers to lack of knowledge, Der Kiureghian and Ditlevsen [66]. Sometimes it is difficult to clearly separate this two kinds of uncertainties and, in order to avoid misunderstanding we can think to aleatory uncertainty as randomness, while epistemic one as uncertainty.

Aleatory uncertainty is related to the inherent variability of the phenomena studied, so the outcomes are basically unpredictable. To figure out this kind of randomness, histograms or frequency diagrams can be used; examples can be found in Ang and Tang [11].

Epistemic uncertainty depends on our capability to describe and model real phenomena. Because in every field analytical tools used are idealization and, of consequence, approximated, the results obtained from the analyses are, with a certain degree of error, inaccurate prediction of the reality. This is related to lack of data or knowledge, so in principle it is possible to reduce his variability collecting more data (e.g. by performing more experiments) or giving also judgments. More accuracy in the models translates in a reduction of this variability.

It is important to divide uncertainty into the two categories above mentioned also because the effects are different; aleatory uncertainty leads to the evaluation of a probability, while epistemic uncertainty introduces a variability on the calculated probability. In other words, the first type of uncertainty determines a probability of failure, while second type gives his distribution, Ang and Tang [11].

2.3 Elements of theory of probability

This section presents a general overview of the fundamentals of the theory of probability and the analytical models used to describe it. The aim of the chapter is to illustrate all the tools at the base of the PEER methodology, in the following exploited. As suggested by Ang and Tang [11], "*probability* can be considered a numerical measure of the likelihood of occurrence of an event within an exhaustive set of all possible alternative events." First of all, the space (*possibility space*) within which all the possible events can occur should be identified, like so the event of interest; finally at each event is associated a probability of occurrence. We can also use the concepts of the set theory; in this case, the *possibility space* is the *sample space*, the single possibilities are the *sample points* and an event is a subset of the sample space. Among them, we can identify the following:

- Impossible event, ϕ, so the event without sample points;
- Certain event, S, so the event containing all the sample points;
- Complementary event $\overline{E}$ of an event E, that contains all the points of S that are not in E.

Concerning the terminology, we say that two events are *mutually exclusive* if the occurrence of one exclude the occurrence of the other; in other words the intersection E_1E_2 is the null set ϕ. Two events are *collectively exhaustive* if the union gives the overall sample space, $E_1 \cup E_2 = S$. Like the other branches of mathematics, theory of probability is based on some assumptions, fundamentals axioms where a proof is not required.

Axiom 1. At each event in the space S is associated a probability $P(E) \geq 0$

Axiom 2. The certain event S has a probability $P(S) = 1$

Axiom 3. If two events E_1 and E_2 are mutually exclusive, $P(E_1 \cup E_2) = P(E_1) + P(E_2)$

On the basis of these simple rules all the others can be derived. Among them, particular importance is given to the conditional probability. To understand, we want to evaluate the probability of one event if another one occurs; in mathematical terms, we want to evaluate $P(E_1|E_2)$. In a practical way, we search the occurrence of E_1 in a lower space made by E_2:

$$P(E_1|E_2) = \frac{P(E_1E_2)}{P(E_2)} \tag{2.1}$$

Related to this concept we can introduce the concept of *statistical independence*, so the occurrence of one event is independent from the occurrence of the other.

$$P(E_1|E_2) = P(E_1) \tag{2.2}$$

Exploiting equation 2.1 it is possible to define the *multiplication rule*.

$$P(E_1E_2) = P(E_1|E_2)P(E_2) \tag{2.3}$$

If the events E_1 and E_2 are independent the multiplication rule tells that the joint probability is simply the multiplication of the single probabilities:

$$P(E_1E_2) = P(E_1)P(E_2) \tag{2.4}$$

Clearly these results can be generalized with a set on n events $E_1, E_2, \ldots E_n$. A fundamental theorem at the base of the PEER methodology is the *theorem of total probability*. The idea is that sometimes the probability of an event A cannot be evaluated directly, but depends whether other events E_i occurs or not; the probability of the event A will be the conditional probability of A with respect to the other events E_i, using as weight the probability of occurrence of E_i. The meaning of this theorem is a sort of propagation of the probabilities, from one step to the subsequent, in order to obtain the overall probability of the system; this is in practice the idea at the base of the PEER PBEE methodology.

In mathematical terms, we can consider n events mutually exclusive and collectively exhaustive, $E_1, E_2, \ldots E_n$. Because the definition we can say that $E_1 \cup E_2 \cup \ldots \cup E_n = S$. The

theorem of total probability is derived:

$$\begin{aligned} A &= AS \\ &= A(E_1 \cup E_2 \cup \ldots \cup E_n) \\ &= AE_1 \cup AE_2 \cup \ldots \cup E_n \end{aligned}$$

Because the events E_i are mutually exclusive, $P(A) = P(AE_1) + P(AE_2) + \ldots P(AE_n)$, and using the multiplication rule we have:

$$P(A) \;=\; P(A|E_1)P(E_1) + P(A|E_1)P(E_n) + \ldots + P(A|E_n)P(E_n) \tag{2.5}$$

The second part of this section is devoted to an overview of the analytical models of random phenomena; the details can be found in Ang and Tang [11]. In a probabilistic problem the variables cannot assume just one value, but they have a range of possible ones, each of them with a prescribed probability; they are called *random variables*. Denoting as X a random variable, an event is described such as $X = x$, $X > x$ or $X < x$, where x can assume all the values between two extremes a and b. The probability related to a particular value of the random variable is governed by a prescribed law, namely the *probability distribution*; this rule can be represented by the *cumulative distribution function* (CDF) F_X, defined as:

$$F_X \;=\; P(X \leq x) \tag{2.6}$$

Another possibility of representation is given by the *probability density function* (PDF) that, just considering the continuous case, is defined as:

$$P(a < x \leq b) \;=\; \int_a^b f_X(x)dx \tag{2.7}$$

Equation 2.7 gives the probability that random variable X belongs to the interval $(a, b]$. Following the above definition, the cumulative distribution function can be expressed as:

$$F_X(x) \;=\; P(X \leq x) \;=\; \int_{-\infty}^{x} f_X(\tau)d\tau \tag{2.8}$$

If for $F_X(x)$ the first derivative exist, from equation 2.8 is simply to see that:

$$f_X(x) \;=\; \frac{\partial F_X(x)}{\partial x} \tag{2.9}$$

Figure 2.1 shows an example of a continuous distribution function. Clearly, each function used to represent the probability distribution of a generic random variable must obey to the axioms of the theory of probability. In particular, the function should not assume negative values and the sum of all the probabilities related to the values of the random variable should be equal to 1. In summary:

- $F_X(-\infty) = 0$ and $F_X(+\infty) = 1$;

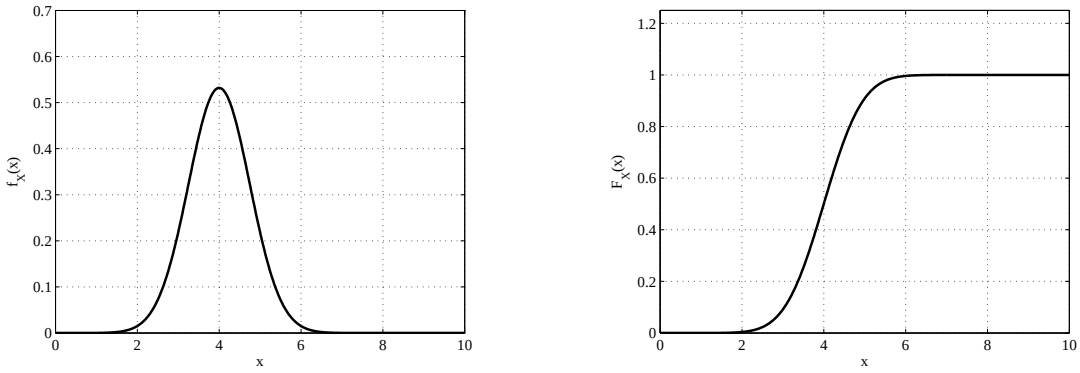

(a) PDF. (b) CDF.

Figure 2.1: Continous distribution function.

- $F_X(x) \geq 0$, and the function is not decreasing with x;
- $F_X(x)$ is continuous on the right of x.

With the knowledge of the form of the distribution function, using CDF or PDF, a random variable is completely described in probabilistic terms; in practice, the exact form is usually missing, so random variables can be described just in an approximated way by using their main descriptors, namely the *moment* of a random variable. The first parameter that everyone have in mind is somehow related to the central values of the range of the random variable; because for each value the probability changes, we can think in terms of a "weighted average", that is the *mean value* $\mu(X)$ or *expected value* $E(X)$:

$$E(X) = \mu(X) = \int_{-\infty}^{+\infty} x f_X(x) dx \tag{2.10}$$

Another parameter of interest is the *median value* x_m, so the value for which the cumulative distribution is the half:

$$F_X(x_m) = 0.5 \tag{2.11}$$

The only knowledge of the central values is not sufficient to have reliable information of the behavior of our random variable; also the dispersion of the values in the range is of interest, in particular with reference to the mean value. The *variance* gives exactly this kind of information, so tells us if the values of the random variables are close to the central value or not; in a mathematical notation we have:

$$Var(X) = \sigma_X^2 = \int_{-\infty}^{+\infty} (x - \mu_X)^2 f_X(x) dx \tag{2.12}$$

Expanding equation 2.12 it is possible to link variance and mean value, in particular $Var(X) = E(X^2) - \mu_X^2$, where $E(X)^2$ is the *mean square value* of the random variable. In order to

represent dispersion with the same unit of the mean value, the square root of the variance is used, introducing the standard deviation σ, defined in equation 2.13. Since the sparsity of the values is described in absolute terms, it is more convenient to refer it to the mean value or, in other words, dispersion is more meaningful if it is measured with regard to the mean value. A nondimensional parameter is therefore introduced (*coefficient of variation*, *c.o.v.*), as indicated in equation 2.14:

$$\sigma_X = \sqrt{Var(X)} \tag{2.13}$$

$$\delta_X = \frac{\sigma_X}{\mu_X} \tag{2.14}$$

Another significant information of a random variable is the degree of asymmetry of his PDF; the measure of this characteristic is the *skewness*, see equation 2.15. If the skewness is zero the PDF has a symmetric shape, otherwise it is asymmetric. In particular skewness higher than zero means that the values on the right of μ_X are more dispersed that those on the left of the central value, vice versa if it is lower than zero. Similarly to the definition of the coefficient of variation, also in this case a more meaningful dimensionless parameter can be defined, namely *coefficient of skewness*, see equation 2.16.

$$E(X-\mu_X)^3 = \int_{-\infty}^{+\infty} (x-\mu_X)^3 f_X(x)dx \tag{2.15}$$

$$\theta_X = \frac{E(X-\mu_X)^3}{\sigma_X^3} \tag{2.16}$$

Finally it is possible to define also the fourth moment of a random variable, namely *kurtosis*, equation 2.17. This parameter measure the "peakedness" of the corresponding PDF, or in other words how the the probability density function is far from a normal distribution. Typically the dimensionless descriptor is the β_2 index of Pearson, defines as indicated in equation 2.18, that is zero for a normal distribution.

$$E(X-\mu_X)^4 = \int_{-\infty}^{+\infty} (x-\mu_X)^4 f_X(x)dx \tag{2.17}$$

$$\beta_2 = \frac{E(X-\mu_X)^4}{\sigma_X^4} \tag{2.18}$$

To conclude the present section, we can extend the same concepts discussed above also for two or more random variables, in particular with reference to the *joint* probability function. Considering two arbitrary random variables X and Y, the probabilities of all possible pairs of values x and y can be represented by the *joint distribution function* $F_{X,Y}$:

$$F_{X,Y}(x,y) = P(X \leq x, Y \leq y) \tag{2.19}$$

Clearly the axioms of the theory of probability still work, in particular $F_{X,Y}(x,y)$ is nonnegative and nondecreasing function of x and y. Moreover:

$$\begin{aligned} F_{X,Y}(-\infty,-\infty) &= 0 & \qquad F_{X,Y}(+\infty,+\infty) &= 1 \\ F_{X,Y}(-\infty,y) &= 0 & \qquad F_{X,Y}(+\infty,y) &= F_Y(y) \\ F_{X,Y}(x,-\infty) &= 0 & \qquad F_{X,Y}(x,+\infty) &= F_X(x) \end{aligned}$$

Joint probability function can be represented also through the *joint* PDF, defined as $f_{X,Y}(x,y) = P(x < X \leq x+dx, y < Y \leq y+dy)$. Then,

$$F_{X,Y}(x,y) = \int_{-\infty}^{x}\int_{-\infty}^{y} f_{X,Y}(u,v)dvdu \tag{2.20}$$

At the opposite, if partial derivatives exist,

$$f_{X,Y}(x,y) = \frac{\partial^2 F_{X,Y}(x,y)}{\partial x \partial y} \tag{2.21}$$

Considering continuous random variables we can define the *conditional* PDF of X given Y,

$$f_{X|Y}(x|y) = \frac{f_{X,Y}(x,y)}{f_Y(y)} \tag{2.22}$$

For the conditional PDF of Y given X equation 2.22 still works, just swapping the indices. Using then the theorem of total probability, see equation 2.5, the *marginal* PDFs can be obtained:

$$f_X(x) = \int_{-\infty}^{+\infty} f_{X|Y}(x|y)f_Y(y)dy = \int_{-\infty}^{+\infty} f_{X,Y}(x,y)dy \tag{2.23}$$

$$f_Y(y) = \int_{-\infty}^{+\infty} f_{Y|X}(y|x)f_X(x)dx = \int_{-\infty}^{+\infty} f_{X,Y}(x,y)dx \tag{2.24}$$

Finally we are interested in finding some relationship between two random variables X and Y; the joint second moment is:

$$E(XY) = \int_{-\infty}^{+\infty} xyf_{X,Y}(x,y)dxdy \tag{2.25}$$

If random variables are statistical independent, second moment is simply the multiplication of the singular expected value, $E(XY) = E(X)E(Y)$. *Covariance* is defined as the joint second central moment:

$$Cov(X,Y) = E[(X-\mu_X)(Y-\mu_Y)] = E(XY) - E(X)E(Y) \tag{2.26}$$

If random variables are statistical independent covariance is zero. This descriptor gives information on the relationship between X and Y; $Cov(X,Y)$ *large and positive* means that the values of both random variables are large or small with respect to their central values,

while a covariance *large and negative* means that if the values of one random variable are big those of the other are small, or vice versa, always with respect to the central value. Finally a covariance near zero means that there is no *linear* relationship between X and Y, or the relationship is nonlinear. As just seen above, it is better to refer to a dimensionless parameter; in this case we can define the *coefficient of correlation*:

$$\rho = \frac{Cov(X,Y)}{\sigma_X \sigma_Y} \tag{2.27}$$

The coefficient of correlation ranges from -1 to 1, and it measures the strength of the linear relationship between two random variables.

This short overview has the purpose to introduce the main factors within the theory of probability that are at the base of the PEER methodology; more details can be found in each statistical and probability book, e.g. Ang and Tang [11] and Ross [213].

2.4 Monte Carlo simulations

The solution of real engineering problems usually cannot find through an analytical approach due to the complexity of the systems studied. In many fields the only practical way is to exploit numerical methods, in particular when random variables are involved in the analysis process. During lifetime a generic structure can be subjected to a variety of loads, so the system ranges from different *states*, from limited damage up to complete failure. Structural reliability analysis has the aim to define these possible *limit states*, assigning for each of them a probability of exceedance. In literature there are different numerical methods that allows to define such probabilities, and a general overview can be found in Pinto [195] and Lupoi et al. [157]. Using a mathematical formulation, it is possible to define a *limit state function* $L(\boldsymbol{x})$, where $\mathbf{x}$ is the vector containing all the parameters involved in the analysis, that assumes the following values, Lupoi et al. [157]:

$$L(\boldsymbol{x}) := \begin{cases} > 0 \text{ if the limit state is not exceeded} \\ = 0 \text{ if the limit state is reached} \\ < 0 \text{ if the limit state is exceeded} \end{cases} \tag{2.28}$$

Clearly we are interested in all the conditions in which $L < 0$, so the probability of failure can be seen as $P_f = Pr(L < 0)$; introducing the joint probability of failure $f_{\boldsymbol{x}}$ and a *failure domain* $\mathscr{F}$, the probability of failure can be expressed as indicated:

$$P_f = Pr(\boldsymbol{x} \in \mathscr{F}) = \int_{\mathscr{F}} f_{\boldsymbol{x}} d\boldsymbol{x} \tag{2.29}$$

The core of each numerical method used in structural reliability analysis is the resolution of the integral in equation 2.29. Even if in literature approximated methods such as FORM

and SORM can be applied for particual problems, see e.g. Wong [246] and Der Kiureghian [65], Monte Carlo simulation is widely recognized as the more reliable and effective approach to solve problems involving random variables.

Using a Monte Carlo simulation, it is useful to introduce an index $I_f(\boldsymbol{x})$, which can assume only discrete values depending on whether the random variables are or not in the failure domain,

$$I_f(\boldsymbol{x}) := \begin{cases} 1 \text{ if } \boldsymbol{x} \in \mathscr{F} \\ 0 \text{ if } \boldsymbol{x} \notin \mathscr{F} \end{cases} \tag{2.30}$$

With the above definition the integral in equation 2.29 can be seen as:

$$P_f = \int I_f(\boldsymbol{x}) f_{\boldsymbol{x}} d\boldsymbol{x} = E[I_f(\boldsymbol{x})] \tag{2.31}$$

In other words Monte Carlo simulation relies with the evaluation of an expected value. The first step is the choice of the number of simulations to perform or, in other words, the size of the random variables; for each of them, random numbers should be generated, according to their prescribed probability functions. A review of different approaches to generate random numbers, both for discrete and continuous variables, is done in Rubinstein and Kroese [214] and Ross [213]. In this way the estimate of the probability of failure it is simply a counting of the number of times that our parameters fall in the failure domain, $I_f(\boldsymbol{x_i}) = 1$.

$$\widehat{P}_f = \frac{1}{N_{sim}} \sum_{i}^{N_{sim}} I_f(\boldsymbol{x_i}) = \frac{N_f}{N_{sim}} \tag{2.32}$$

We can see that the estimate of the mean value is unbiased:

$$E[\widehat{P}_f] = E\Big[\frac{1}{N_{sim}} \sum_{i}^{N_{sim}} I_f(\boldsymbol{x_i})\Big] = \frac{1}{N_{sim}} \sum_{i}^{N_{sim}} E[I_f(\boldsymbol{x_i})] = \frac{1}{N_{sim}} N_{sim} P_f = P_f \tag{2.33}$$

Regarding the variance we can write:

$$\begin{aligned} Var(\widehat{P}_f) &= E\Big[\big(\frac{\sum_i^{N_{sim}} I_f(\boldsymbol{x_i})}{N_{sim}} - P_f\big)^2\Big] \\ &= E\Big[\frac{\big[\sum_i^{N_{sim}} I_f(\boldsymbol{x_i}) - P_f\big]^2}{N_{sim}^2}\Big] \\ &= \frac{1}{N_{sim}^2}\Big(E\big[\sum_i^{Nsym} I_f^2(\boldsymbol{x_i})\big] + E\big[\sum_i^{N_{sim}} P_f^2\big] - E\big[\sum_i^{N_{sim}} 2 I_f(\boldsymbol{x_i}) P_f\big]\Big) \\ &= \frac{1}{N_{sim}^2}\Big(\sum_i^{Nsym} E[I_f^2(\boldsymbol{x_i})] + \sum_i^{Nsym} E[P_f^2] - 2P_f E[I_f^2(\boldsymbol{x_i})]\Big) \\ &= \frac{1}{N_{sim}^2}\Big(N_{sim} P_f + N_{sim} P_f^2 - 2N_{sim} P_f^2\Big) \\ &= \frac{1}{N_{sim}}[P_f(1 - P_f)] \end{aligned} \tag{2.34}$$

Looking at the coefficient of variation the effectiveness of this method can be clearly understood:

$$c.o.v. = \frac{\sqrt{Var(\widehat{P}_f)}}{E[\widehat{P}_f]} = \frac{\sqrt{P_f(1-P_f)/N_{sim}}}{P_f} = \sqrt{\frac{1-P_f}{N_{sim}P_f}} \tag{2.35}$$

It is evident from equation 2.35 that the reduction of dispersion strongly depends on the number of simulations N_{sim}; for example, if we want to halve the variability, the number of simulations should be increased by a factor of 4. Because in structural analysis the probabilities of failure involved are very low, depending on the limit state considered, the number of simulations required to obtain reliable results should be very high. In conclusion, a standard Monte Carlo approach becomes not feasible due to the computational cost, also because the single structural analysis, in particular in seismic field, could require lot of computation time due to the nonlinearity of the system. To overcome this issue, in the last decades great effort was done in the development of "advanced" Monte Carlo approach to reduce the number of simulations required to obtain reliable results. Next section shows a general overview of these methods, while the subsequent one focuses on the methodology used in the present investigation.

2.4.1 Variance reduction techniques

Looking at equation 2.34, an improvement of a plain Monte Carlo approach can be reached with a reduction of the variance; in this way reliable results can be obtained with a small number of simulations or, in other words, with a small number of systems analyzed. In literature many variance reduction techniques have been proposed, and in the following an overview is presented.

Antithetic variables

Using simulation, suppose that we are interested in the estimation of $\theta = E[X]$ (in our case $\theta = P_f$ and $X = I_f$). Assuming then that two random variables X_1 and X_2 has the same distribution and the same mean value θ it is possible to write:

$$Var\left(\frac{X_1 + X_2}{2}\right) = \frac{1}{4}[Var(X_1) + Var(X_2) + 2Cov(X_1, X_2)] \tag{2.36}$$

Looking at the equation, a reduction of variance could be reached if the two random variables are negative correlated ($Cov < 0$). How X_1 and X_2 can be established in order to give a negative correlation? Suppose that X_1 is a function of m random numbers such as $X_1 = g(U_1, U_2, \ldots, U_m)$, where U_i are independent random numbers, uniformly distributed on the interval $[0, 1]$. The same definition can be also applied to $1 - U$. Consequently, $X_2 = g(1 - U_1, 1 - U_2, \ldots, 1 - U_m)$ has the same distribution of X_1. Finally, because U and

$1-U$ are negative correlated, the expectation is that also X_1 and X_2 has the same property; this is true if the function g is monotone. After the generation of uniformly distributed random numbers U_i to compute X_1, there is no need to generate other independent random numbers to compute X_2, but the idea is to compute it using the set $1-U_i$. In this way the variance is reduced, at least for monotonic function, and the other advantage is that just one generation, instead of 2, of random numbers must be computed. Details can be found in Ross [213].

Control variates

As in the previous section, we are interested in the estimate $\theta = E[X]$, where X is an output of our simulation. Let assume that also Y is an output of the simulation for which the mean value is known, $E[Y] = \mu_Y$. Because equation 2.33, for an arbitrary constant k also the quantity $X + k(Y - \mu_Y)$ is an unbiased estimator of θ. The corresponding variance is:

$$Var\left(X + k(Y - \mu_Y)\right) = Var(X + kY) = Var(X) + k^2 Var(Y) + 2kCov(X, Y) \tag{2.37}$$

Putting the derivative of $Var(X + k(Y - \mu_Y))$ with respect to k equal to zero, the optimal value k^* that minimize the variance is obtained:

$$k^* = -\frac{Cov(X, Y)}{Var(Y)}$$

that, substituted in equation 2.37, gives:

$$Var\left(X + k^*(Y - \mu_Y)\right) = Var(X + k^*Y) = Var\left(X - \frac{Cov(X, Y)}{Var(Y)}Y\right) = Var(X) - \frac{[Cov(X, Y)]^2}{Var(Y)} \tag{2.38}$$

Quantity Y is called *control variate* for the estimator X. For example, if X and Y are positive correlated (k^* is negative) a big value of Y correspond to a big value of X (with respect to the mean value). Equation 2.38 in this case tells that a better estimation of X is obtained reducing his value. A compact and meaningful notation for equation 2.38 is achieved dividing both terms for $Var(X)$, so:

$$\frac{Var\left(X + k^*(Y - \mu_Y)\right)}{Var(X)} = 1 - \rho^2_{X,Y} \tag{2.39}$$

where $\rho_{X,Y}$ is the coefficient of correlation.

Importance sampling

Importance sampling is one of the most used approach in reliability analyses, Melchers [164] and Glynn and Iglehart [102]. The idea is to drive samples of random parameters $\boldsymbol{X} = (X_1, X_2, \ldots, X_n)$ from a distribution function $f(\boldsymbol{x})$ that belongs to the domain of

interest, in our case the failure domain $\mathscr{F}$. Suppose again that we are interested in the estimation of:

$$\theta = E[h(\boldsymbol{X})] = \int h(\boldsymbol{x}) f(\boldsymbol{x}) dx \tag{2.40}$$

but for some reasons a direct approach, namely a direct estimation of $h(\boldsymbol{X})$, is not possible. Equation 2.40 can be rewritten with the above notation:

$$\theta = \int \frac{h(\boldsymbol{x}) f(\boldsymbol{x})}{g(\boldsymbol{x})} g(\boldsymbol{x}) dx = E_g \left[\frac{h(\boldsymbol{X}) f(\boldsymbol{X})}{g(\boldsymbol{X})} \right] \tag{2.41}$$

Repeating simulations N_{sim} times, the estimator of θ has the form:

$$\widehat{\theta} = \frac{1}{N_{sim}} \sum_{i}^{N_{sim}} \frac{h(\boldsymbol{x}_i) f(\boldsymbol{x}_i)}{g(\boldsymbol{x}_i)} \tag{2.42}$$

while the variance $Var(\widehat{\theta})$, considering that the expected value of the value is an unbiased estimation of θ, is:

$$Var(\widehat{\theta}) = E\left[\frac{1}{N_{sim}} \frac{\sum_i^{N_{sim}} h(\boldsymbol{x}_i) f(\boldsymbol{x}_i)}{g(\boldsymbol{x}_i)} - \theta \right] = E\left[\frac{\sum_i^{N_{sim}} (h(\boldsymbol{x}_i) f(\boldsymbol{x}_i)/g(\boldsymbol{x}_i))^2}{N_{sim}^2} \right] \tag{2.43}$$

Second equality comes from equation 2.34. With a proper choice of the function $g(\boldsymbol{x})$ the variance of the estimator can drop to zero; in particular, in equation 2.43 $Var(\widehat{\theta})$ comes to zero if:

$$g(\boldsymbol{x}) = g_{opt}(\boldsymbol{x}) = \frac{h(\boldsymbol{x}) f(\boldsymbol{x})}{\theta} \tag{2.44}$$

where in the present investigation θ is the probability of failure P_f and $h(\boldsymbol{x}) = I_f(\boldsymbol{x})$. In practice, optimal point cannot be computed because it requires *a priori* knowledge of the probability of failure. Strategies to search proper important density functions $g(\boldsymbol{x})$ can be found in Ross [213].

Subset simulation

In the last decade a new methodology, specifically developed to structural reliability problems concerning dynamic contest, with particular emphasis to seismic risk analysis, Au and Beck [15], Au and Beck [16] and Au et al. [17], emerged. The basic idea in order to overcome the high computational cost required for a plain Monte Carlo simulation is to express the probability of failure P_f by a subsequent multiplication of larger conditional probabilities. Given the failure domain $\mathscr{F}$, suppose to consider a decreasing nested sequence of failure regions, $\mathscr{F}_1 \supset \mathscr{F}_2 \supset \ldots \mathscr{F}_m = \mathscr{F}$; the generic region can be expressed as $\mathscr{F} = \bigcap_i^k \mathscr{F}_i, k = 1, \ldots m$. Exploiting the definition of conditional probability, we have:

$$P_f = P(\mathscr{F}_m) = P(\mathscr{F}_1) \prod_{i}^{m-1} P(\mathscr{F}_{i+1}|P(\mathscr{F}_i)) \tag{2.45}$$

In other words subset simulation allows to split the overall problem, so the evaluation of the total probability of failure, into the subsequent solution of m small problems, where a direct Monte Carlo approach (MCS) can be effectively applied. In particular, the evaluation of the first probability $P(\mathscr{F}_1)$ occurs with a plain MCS, while it was found that the application of the Markov Chains method, Rubinstein and Kroese [214] and Ross [213], is an effective tool for the evaluation of the conditional probabilities, which gives the samples for $\widehat{P}_{i+1}$ using the samples generated in the previous step for the evaluation of $\widehat{P}_i$. All the details of the procedure, as well as the use of the *Metropolis-Hastings* (Metropolis et al. [167]) algorithm on the base of the Markov Chain, can be found in Au and Beck [15].

Among different techniques available in literature in order to reduce the computational cost of plain Monte Carlo simulation, the present investigation focuses on a particular version of a stratified sampling, namely Latin Hypercube Sampling, considering the effective version proposed by Vorechovskı and Novák [240]. Details are presented in the next section.

2.4.2 Latin Hypercube Sampling

One of the major drawbacks of plain MonteCarlo simulation technique is the computational cost, especially for time consuming problems or when small probability of failure are needed. In particular, as explained in Ang and Tang [11], the sample size N_{sim} of the random variables is proportional to the inverse of the theoretical probability. Since in earthquake engineering the usual probabilities of failure are very small (10^{-5}, 10^{-6}), this means that a reasonable number of samples is around to some hundreds of thousands. Considering different methods for the seismic analysis of structures (Chopra [55], Datta [64]), it is common accepted that nonlinear dynamic analysis is the most refined one; clearly, the effort to solve thousands of nonlinear analyses, also for very simple systems, should require a lot of time.

To overcome this important issue in the last decades different simulation techniques were developed. For a review of this methods see Ross [213], Rubinstein and Kroese [214], Schueller and Pradlwarter [220]. In this investigation the set of structural models is determined through the application of the Latin Hypercube Sampling (Helton and Davis [113], Iman and Conover [127], Stein [226], Vořechovskỳ and Novák [241]). Latin Hypercube Sampling, abbreviated in the following as LHS, is an advanced MonteCarlo technique that uses the stratification of the theoretical probability functions of the random variables X_i in order to reduce the size of sample data. Usually two steps are required in order to build the sampling matrix: in the first one, samples from each marginal distribution are carefully chosen in order to represent their probability density functions (PDF). Finally, the sample matrix is re-arranged in order to match within a certain tolerance the target correlation matrix. In the following the two

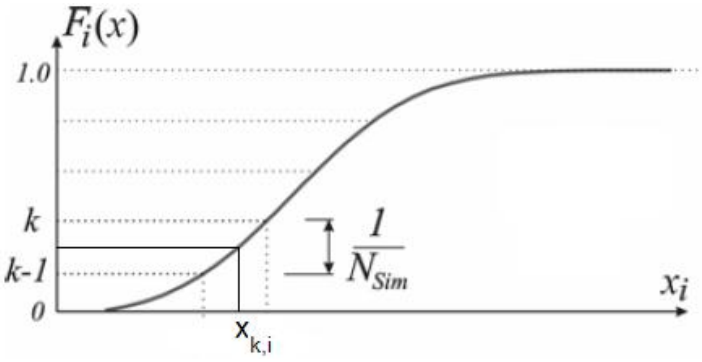

Figure 2.2: Illustration of the sampling of random variable X_i.

steps will be described in detail.

As mentioned before, the first step is the generation of samples from each marginal distribution. The usual strategy is to divide the cumulative distribution function (CDF) into N_{sim} equally spaced intervals, and then choosing one sample from each of them. One possibility is to consider the sample in the middle of the k-th strata, Figure 2.2. Applying the inverse transformation of the CDF, each sample is defined as:

$$x_{k,i} = F_i^{-1}(p_{k,i}) = F_i^{-1}\left(\frac{k-0.5}{N_{sim}}\right) \tag{2.46}$$

where $x_{k,i}$ is the k-th sample of the i-th random variable X_i and F^{-1} is the inverse of the corresponding CDF. Through this "stratification" all the range of variation of the generic random variable is explored. The same procedure is applied for the N_{var} random variables. To build the sampling matrix the N_{sim} values of the first variable are randomly paired without replacement with the N_{sim} samples of the second random variables. These pairs are then randomly paired with the N_{sim} values of the third variable X_3, and this process continues until all the random variables are paired without replacement, Helton and Davis [113]. The sample matrix so obtained is called Latin Hypercube, $\boldsymbol{X} = [\boldsymbol{X_1}, \boldsymbol{X_1}, ..., \boldsymbol{X_{Nvar}}]$.

To visualize the procedure, the generation of a LHS is illustrated with reference to two uniform random variables X_1 and X_2, with lower and upper bound respectively equal to [1;1.5] and [0;1]. The CDFs of the random variables are subdivided into 10 strata, Figure 2.3, and one value is selected from each of the interval. Finally the generation of LHS is completed by randomly pairing without replacement the resulting values for X_1 and X_2, Helton and Davis [113]. Because the pairing is completely random there are different LHSs admissible, as it can be seen in Figure 2.4

Before to explain the procedure to impose a prescribed correlation it is possible to visualize through a simple example, where the analytical solution is known, how LHS sampling is significantly more effective than random sampling, i.e. also with a small sample size the result in terms of mean and standard deviation estimate is very close to the real value. In particular a lognormal variable X with mean $\mu = 27.4$ and a standard deviation $\sigma = 4$ is

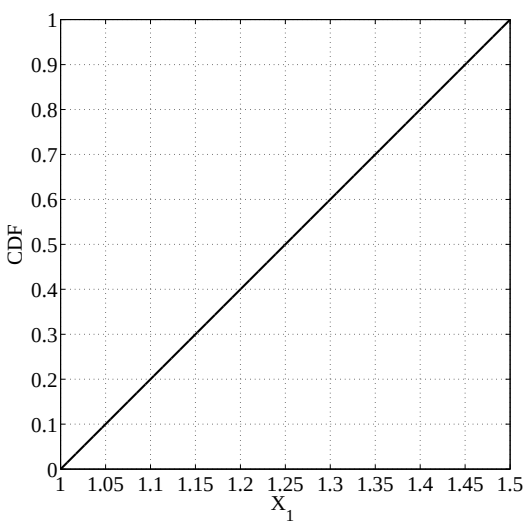

(a) CDF for variable X_1.

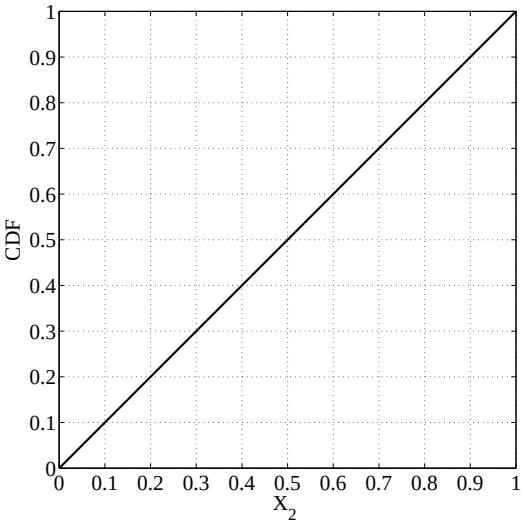

(b) CDF for variable X_2.

Figure 2.3: Subdivision of the CDFs into 10 equal probability strata.

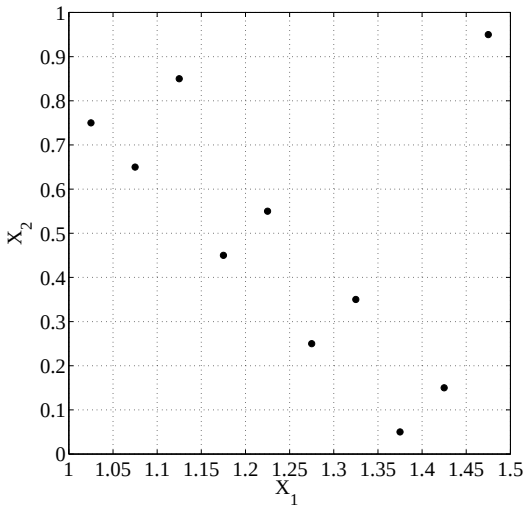

(a) LHS. First pairing between X_1 and X_2.

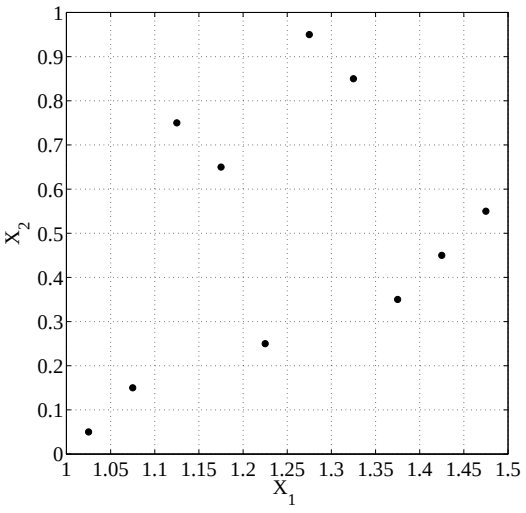

(b) LHS. Second pairing between X_1 and X_2.

Figure 2.4: Examples of LHS for the random variables X_1 and X_2 with 10 samples.

chosen. Random and LH sampling are set considering different sample sizes N_{sim}, from 10 to 50000. Figures 2.5a and 2.5b show, for each sample size, the error between the analytical solution and the sampling scheme. Also for a very small sample size the error related to LHS is significant lower than that predicted by the simple random sampling, both in the estimate of mean value and standard deviation. Tables 2.1 and 2.2 summarize the percentage error on statistical values (mean, standard deviation, percentile at 5% and 95%) for the two sampling techniques. Another important issue, clearly shows in Figure 2.5, is the monotonic behavior of this methodology in the estimate of actual values when sample size increases.

The second step concerns the application of the prescribed correlation between random variables, because during the sampling procedure an undesired correlation is introduced, especially if the number of samples N_{sim} is small, Vořechovskỳ and Novák [241]. In the following two procedures will be described in order to apply the predefined correlation between the variables (e.g. 0 if uncorrelated). In particular two parameters can be used to measure the degree of correlation between random variables, namely the *Pearson correlation coefficient* and the *Spearman correlation coefficient* (Ang and Tang [11]). The first one is defined by:

$$r_{x_i,x_j} = \frac{\sum_{k=1}^{N_{sim}}(x_{ki}-\overline{x}_i)(x_{kj}-\overline{x}_j)}{\left[\sum_{k=1}^{N_{sim}}(x_{ki}-\overline{x}_i)^2\right]^{1/2}\left[\sum_{k=1}^{N_{sim}}(x_{kj}-\overline{x}_j)^2\right]^{1/2}} \tag{2.47}$$

where

$$\overline{x}_i = \sum_{k=1}^{N_{sim}}(x_{ki}/N_{sim}) \qquad \overline{x}_j = \sum_{k=1}^{N_{sim}}(x_{kj}/N_{sim})$$

Pearson correlation coefficient takes value between -1 and 1 and gives a measure of the strength of the linear relationship between two random variables. A value equal to ± 1 stands for a perfect linear relationship, while 0 means no relationship or a nonlinear trend between them.

Spearman correlation coefficient has an analogous definition, but using in this case the rank of the data. The rank represents the position of a generic sample when all the data of that random variables are sorted in ascending order; for example the smallest value has rank 1, the second rank 2 and so on, where the biggest value has a rank equal to the number of samples, N_{sim}. *Spearman correlation coefficient* is defined as following:

$$R_{x_i,x_j} = \frac{\sum_{k=1}^{N_{sim}}[R(x_{ki})-\overline{R}(x_i)][R(x_{kj})-\overline{R}(x_j)]}{\left[\sum_{k=1}^{N_{sim}}\Big(R(x_{ki})-\overline{R}(x_i)\Big)^2\right]^{1/2}\left[\sum_{k=1}^{N_{sim}}\Big(R(x_{kj})-\overline{R}(x_j)\Big)^2\right]^{1/2}} \tag{2.48}$$

where $R(x_{ki})$ and $R(x_{kj})$ denote the rank-transformed value of x_{ki} and x_{kj} while $\overline{R}(x_i)$ and $\overline{R}(x_j)$ are defined as $(N_{sim}+1)/2$. As explained before for the *Pearson correlation coefficient* also the *Spearman correlation coefficient* takes values between -1 and 1, but in this case the meaning is a little bit different, because it assesses the strength of the monotonic relationship between two variables. In other words, it gives a prediction of how a value of a random

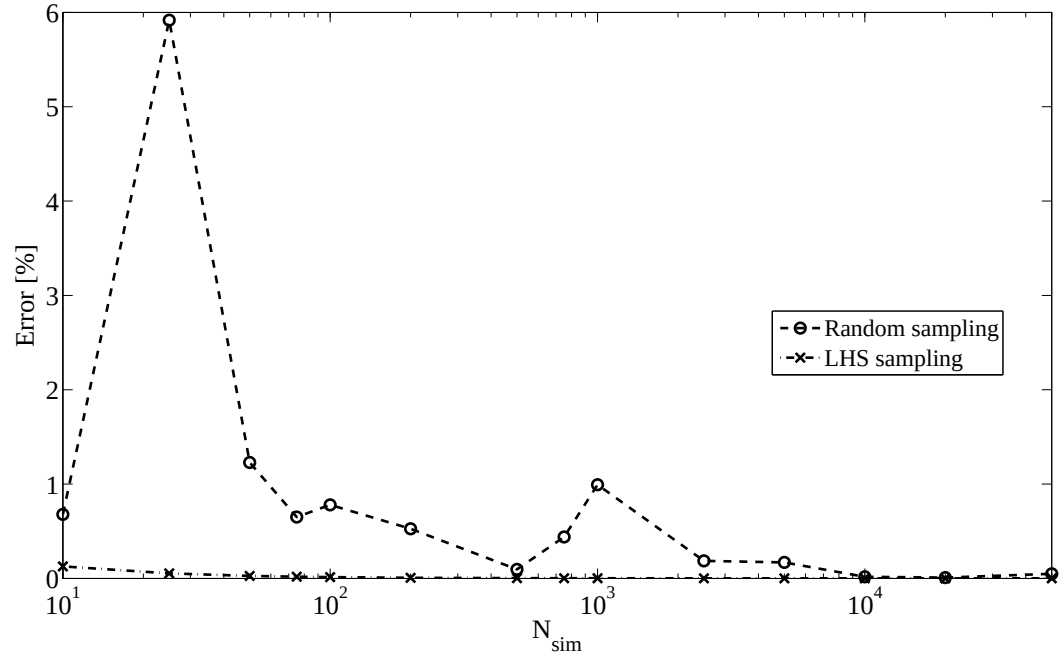

(a) Error on mean value.

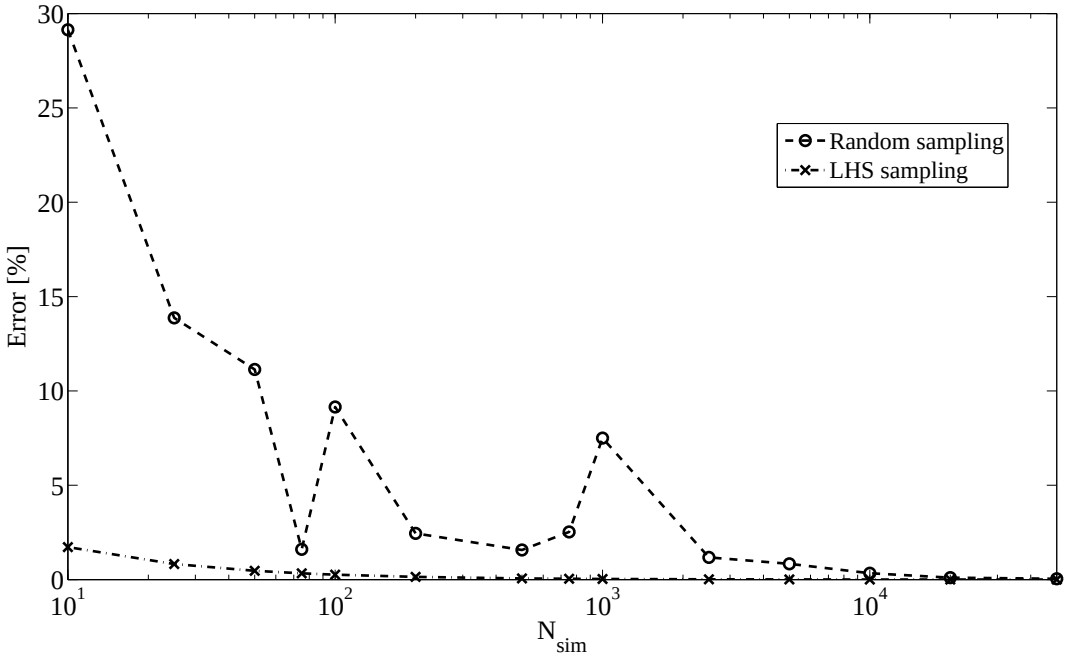

(b) Error on standard deviation.

Figure 2.5: Examples of LHS for the random variables X_1 and X_2 with 10 samples.

Table 2.1: Estimate of the error on statistical parameters for random sampling

N_{sim}	$\Delta\mu$[%]	$\Delta\sigma$[%]	$\Delta x_{5\%}$[%]	$\Delta x_{95\%}$[%]
10	0.678	29.141	11.398	4.081
25	5.918	13.874	2.596	11.520
50	1.229	11.135	0.013	2.927
100	0.779	9.151	0.988	0.633
200	0.523	2.451	1.053	1.974
500	0.095	1.568	0.773	1.469
1000	0.994	7.498	0.118	2.814
5000	0.170	0.837	1.051	0.828
10000	0.017	0.335	0.338	0.162
50000	0.049	0.041	0.063	0.065

Table 2.2: Estimate of the error on statistical parameters for LH sampling

N_{sim}	$\Delta\mu$[%]	$\Delta\sigma$[%]	$\Delta x_{5\%}$[%]	$\Delta x_{95\%}$[%]
10	0.128	1.720	0.00	0.00
25	0.053	0.823	0.454	0.555
50	0.027	0.464	0.00	0.00
100	0.014	0.259	0.026	0.031
200	0.007	0.143	0.006	0.008
500	0.003	0.064	0.001	0.001
1000	0.001	0.035	0.0003	0.0003
5000	0.0003	0.008	0.00	0.00
10000	0.0001	0.004	0.00	0.00
50000	0.000	0.001	0.00	0.00

variable should be small or large depending on how small or large is another variable. In this investigation the procedure to induce a predefined correlation between the variables of the LHS will refer to the *Spearman correlation coefficient*.

The first procedure was introduced in the work of Iman and Conover (Iman and Conover [127]); it has some advisable properties:

1. Distribution free. It can be applied to all statistical distributions;
2. Simplicity. There are no unusual mathematical techniques to apply;
3. General. It can be applied to any sampling scheme;
4. Marginal distributions of each random variables are preserved.

Here the methodology will be explained, with reference to the work of Iman and Conover [127] and Helton and Davis [113]. Let start to assume that at the end of LHS a matrix $\boldsymbol{X}$, with N_{sim} rows and N_{var} columns, is generated:

$$\boldsymbol{X} = \begin{bmatrix} x_{11} & x_{12} & \dots & x_{1N_{var}} \\ x_{21} & x_{22} & \dots & x_{2N_{var}} \\ \vdots & \vdots & & \vdots \\ x_{N_{sim}1} & x_{N_{sim}2} & \dots & x_{N_{sim}N_{var}} \end{bmatrix}$$

where N_{sim} is the number of samples for each random variable and N_{var} is the number of random variables. The idea is to rearrange the single columns of X in order to match within a certain tolerance the desired correlation matrix, in the following denotes as $\boldsymbol{C}$, that have the same size $N_{sim} \times N_{var}$:

$$\boldsymbol{C} = \begin{bmatrix} c_{11} & c_{12} & \dots & c_{1N_{var}} \\ c_{21} & c_{22} & \dots & c_{2N_{var}} \\ \vdots & \vdots & & \vdots \\ c_{N_{sim}1} & c_{N_{sim}2} & \dots & c_{N_{sim}N_{var}} \end{bmatrix}$$

where the generic value c_{ij} is the rank correlation coefficient between random variables $\boldsymbol{X_i}$ and $\boldsymbol{X_j}$. Since it is no possible to find directly a transformation matrix which results in the target correlation matrix, Iman and Conover [127], scores are used for which the desired matrix $\boldsymbol{C}$ and the rank correlation matrix of $\boldsymbol{X}$ are close one to each other. For this reaason, a new matrix with size $N_{sim} \times N_{var}$ is defined:

$$\boldsymbol{S} = \begin{bmatrix} s_{11} & s_{12} & \dots & s_{1N_{var}} \\ s_{21} & s_{22} & \dots & s_{2N_{var}} \\ \vdots & \vdots & & \vdots \\ s_{N_{sim}1} & s_{N_{sim}2} & \dots & s_{N_{sim}N_{var}} \end{bmatrix}$$

Each column of $\boldsymbol{S}$ contains a random permutation of the N_{sim} van der Waerden scores $\Phi^{-1}[i/(N_{sim}+1)]$ (Conover [59]), where Φ^{-1} is the inverse of the standard normal distribution. A Cholesky factorization (Quarteroni et al. [204]) of $\boldsymbol{C}$ is used in order to rearrange each columns of $\boldsymbol{S}$. Here it is assumed that $\boldsymbol{C}$ is symmetric and positive-definite, so:

$$\boldsymbol{C} = \boldsymbol{P}\boldsymbol{P}^T$$

where $\boldsymbol{P}$ is a lower triangular matrix. Using matrix algebra, if the correlation matrix of $\boldsymbol{S}$ is the identity matrix $\boldsymbol{I}$, then $\boldsymbol{S}^* = \boldsymbol{S}\boldsymbol{P}^T$ is the correlation matrix of $\boldsymbol{C}$. Once that $\boldsymbol{S}^*$ is built, the final matrix $\boldsymbol{X}^*$ is obtained rearranging each column of $\boldsymbol{X}$ considering the same rank order coming from $\boldsymbol{S}^*$. Two conditions should be verified to complete the process, Helton and Davis [113]:

1. The correlation matrix of $\boldsymbol{S}$ should be close enough to the identity matrix;
2. The correlation matrix of $\boldsymbol{S}^*$ should be approximately equal to the rank correlation matrix of $\boldsymbol{S}^*$.

Let start to examine the first condition. Denoting by $\boldsymbol{E}$ the correlation matrix of $\boldsymbol{S}$, usually it is not exactly the identity matrix, but using again a Cholesky factorization it is possible to obtain it. In particular:

$$\boldsymbol{E} = \boldsymbol{Q}\boldsymbol{Q}^T$$

where $\boldsymbol{Q}$ is a lower triangular matrix. This can be done because the properties of $\boldsymbol{E}$ (it is symmetric and positive-definite). Finally $\boldsymbol{S}^*$ is defined as:

$$\boldsymbol{S}^* = \boldsymbol{S}(\boldsymbol{Q}^{-\mathbf{1}})^T\boldsymbol{P}^T$$

In this way $\boldsymbol{S}^*$ has $\boldsymbol{C}$ as its correlation matrix. About the second condition, hypothesis is satisfied using an appropriate way to define matrix $\boldsymbol{S}$; in Iman and Conover [127] it is explained that the use of the van der Waerden scores is a effective approach in order to build matrix $\boldsymbol{S}$. Finally, the procedure is completed if the rank correlation matrix related to $\boldsymbol{S}^*$ is close enough to the target matrix. Figure 2.6 shows the effects of imposing rank correlations equal to $0.00, 0.25, 0.50, 0.75, 0.9, 0.99$ on a couple of random variable X_1 and X_2. X_1 is a standard normal variate, while X_2 is a uniform variate with lower and upper bound equal to ± 4.

To test the effective of LHS, with or without imposing a correlation, with respect to the simple random sampling, two simple functions are evaluated in a probabilistic term. The first one is the monotonic function f_1:

$$f_1(X,Y) = X + Y + XY + X^2 + Y^2 + X \cdot \min\Big[\exp(3Y), 10\Big] \tag{2.49}$$

where X and Y are two uniform random variables with lower and upper bound equal respectively to [1;1.5] and [0;1]. The sampling scheme is performed setting $N_{sim} = 10, 25, 100$, repeating the

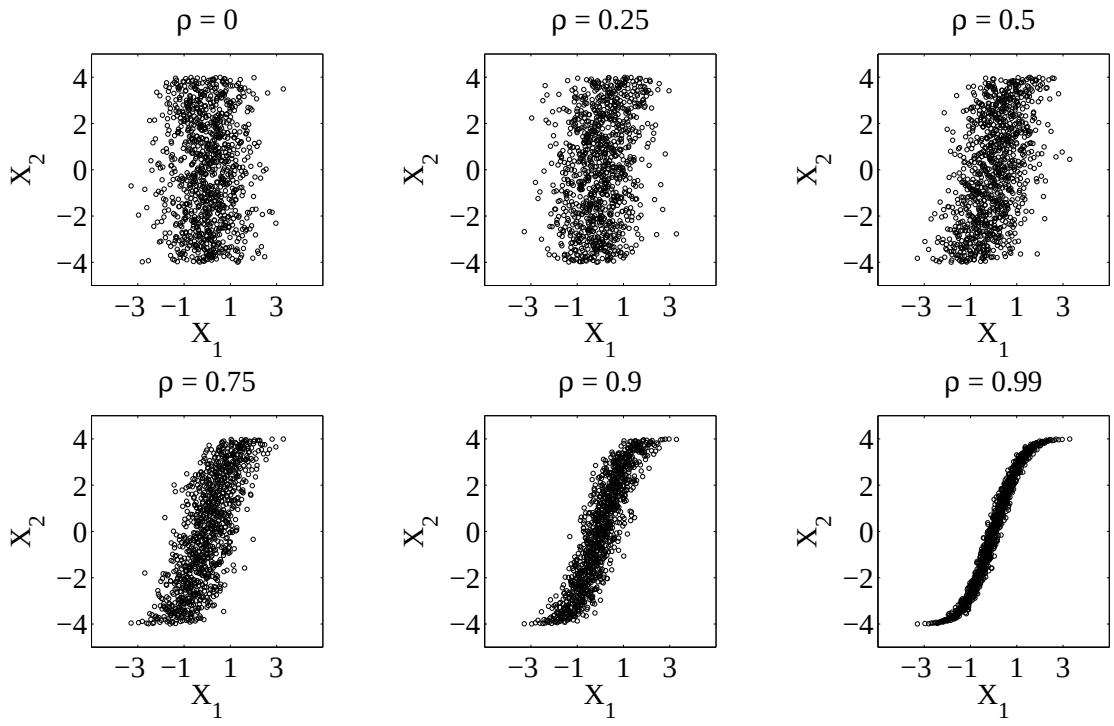

Figure 2.6: Example of imposing a rank correlation between a standard normal variate X_1 and a uniform one X_2.

simulation 10 times for each size in order to test also the stability of the sampling technique. In Figure 2.7 the CDF of the function f_1 is showed for different values of sampling size. In all cases LHS gives better results than simple random sampling. In particular, considering that the random variables are uncorrelated, little bit better results are obtain when the impose correlation is applied. The LHS gives also more stable results considering repetitions of the same simulation with a certain sampling size. This is clear considering Figure 2.8; each picture shows the mean value and the upper and lower confidence interval with a tolerance of 5%. As it can be seen, in case of LHS with imposed correlation the dispersion of the results is very low, also considering 10 samples.

The second test refers to the non monotonic function f_2:

$$f_2(X,Y) = X + Y + XY + X^2 + Y^2 + Xg(Y) \tag{2.50}$$

where $h(Y) = (Y - 11/43)^{-1} + (Y - 22/43)^{-1} + (Y - 33/43)^{-1}$ and $g(Y)$ is defined as:

$$g(Y) := \begin{cases} h(Y), & \text{if } |h(Y)| < 10 \\ 10, & \text{if } h(Y) \geq 10 \\ -10, & \text{if } h(Y) \leq -10 \end{cases}$$

Also in this case X and Y are two uniform random variables with lower and upper bound equal respectively to [1;1.5] and [0;1]. The sampling scheme is performed setting $N_{sim} = 10, 25, 100,$

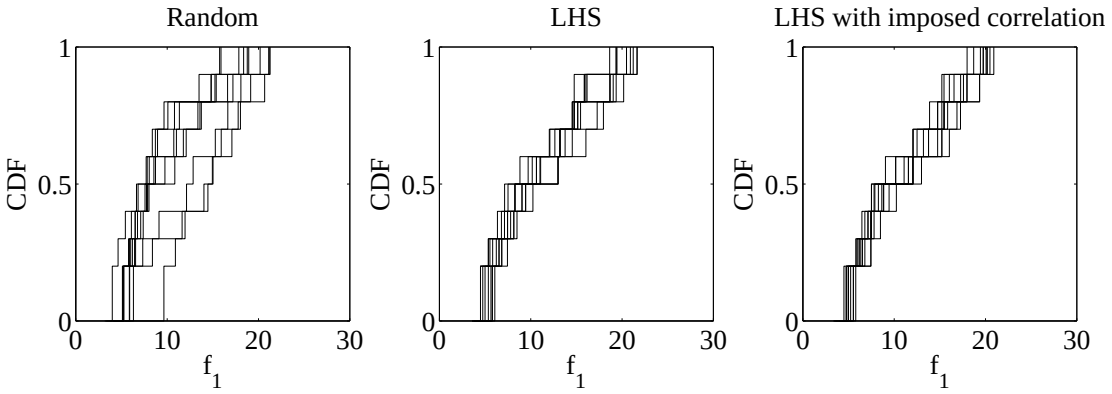

(a) $N_{sim} = 10$.

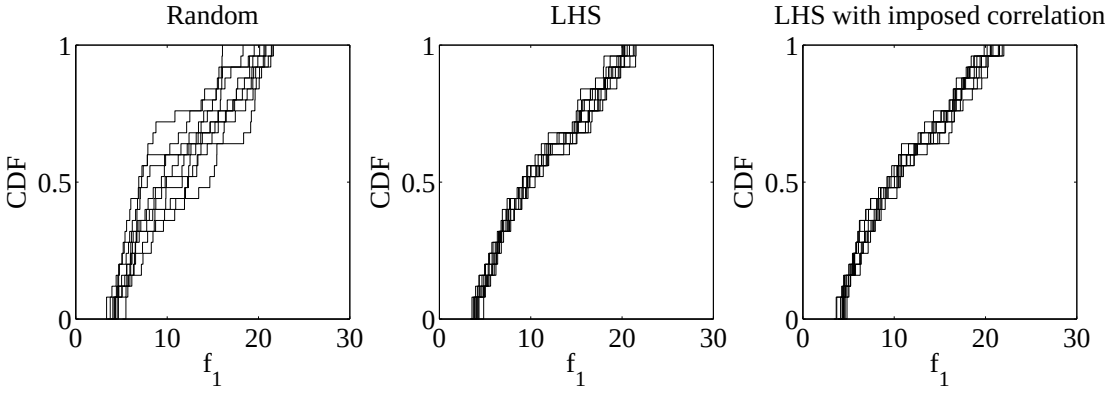

(b) $N_{sim} = 25$.

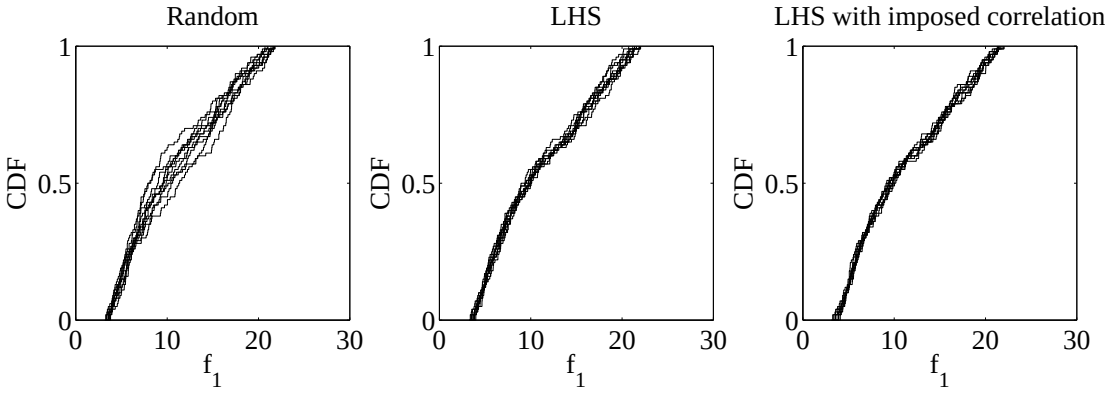

(c) $N_{sim} = 100$.

Figure 2.7: Evaluation of function f_1 varying the sample size N_{sim} for different sampling techniques.

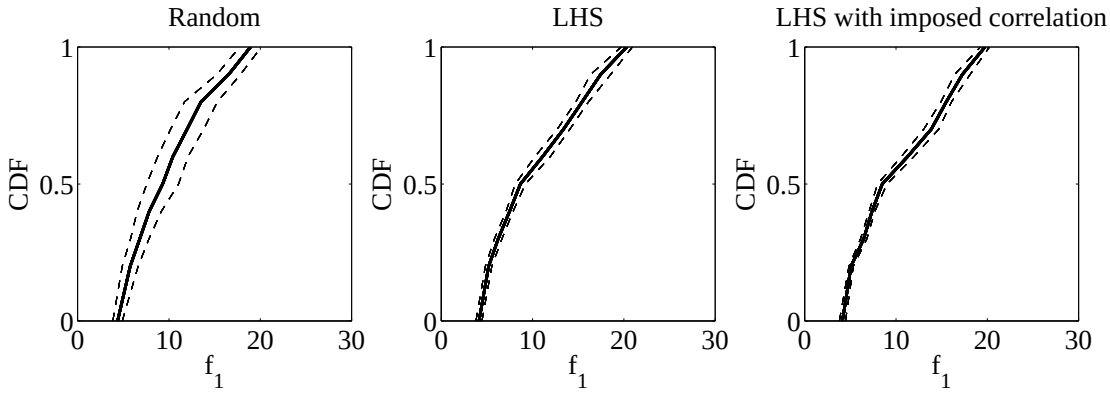

(a) $N_{sim} = 10$.

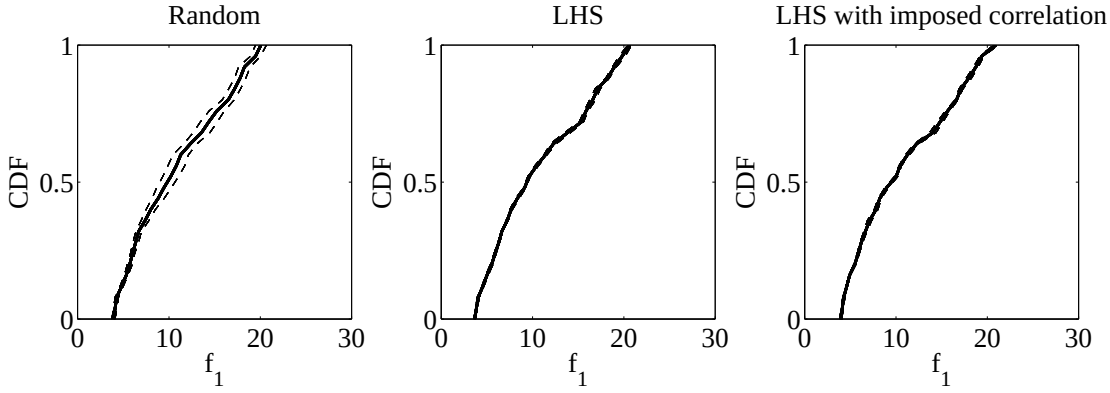

(b) $N_{sim} = 25$.

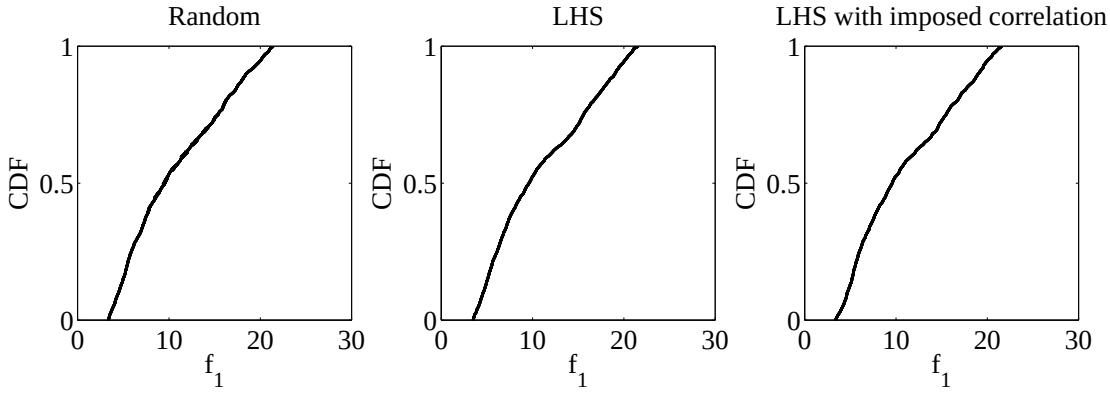

(c) $N_{sim} = 100$.

Figure 2.8: Evaluation of confidence interval for function f_1 varying the sample size N_{sim} for different sampling techniques.

considering again 10 repetitions for each sampling scheme to test the stability of the technique. In Figure 2.9 the CDF of the function f_2 is showed for different values of sampling size. In all cases LHS gives better results than simple random sampling, and the difference is more significant than the previous case. Random variables are set to be uncorrelated, so better results are obtain when the impose correlation is applied. The LHS gives also more stable results considering repetitions of the same simulation with a certain sampling size. This is clear considering Figure 2.10; as for the monotonic function each picture shows the mean value and the upper and lower confidence interval with a tolerance of 5%. As it can be seen, in case of LHS with imposed correlation the dispersion of the results is very low, also considering 10 samples.

Although in some application this method to impose correlation is effective, there are also some drawbacks. In particular the scheme has more difficulties when simulating correlated variables, because the procedure can be performed only once and there is no way to improve the results, Vořechovskỳ and Novák [241]. To achieve a positive definite correlation matrix the number of samples should be higher than the number of random variables, so this procedure is not robust enough in case of MonteCarlo simulations with a huge number of variables and a limited number of samples, Vořechovskỳ and Novák [241].

To overcome this problem different methods, see e.g. Huntington and Lyrintzis [119], has been proposed. In particular, the problem to impose a prescribed correlation matrix can be seen as an optimization problem, where the goal is to match within a certain tolerance the target matrix or, in the same terms, to minimize the difference between the actual matrix and the target one. In mathematical language, the idea is to minimize the difference between the correlation matrix associated with the LHS, $\boldsymbol{S}$ and the target matrix $\boldsymbol{K}$. The "difference" can be measured by using a norm of the maximum difference between correlation coefficients:

$$E_{max} = \max_{1 \le i < j \le N_{var}} |S_{i,j} - K_{i,j}| \tag{2.51}$$

or using an overall norm, normalized to the total number of random variables, that takes into account the differences between all correlation coefficients, Vořechovskỳ and Novák [241]:

$$E_{tot} = \frac{2}{N_{var}(N_{var}-1)} \sqrt{\sum_{i=1}^{N_{var}-1} \sum_{j=i+1}^{N_{var}} (S_{i,j} - K_{i,j})^2} \tag{2.52}$$

Since the optimization process is related to the ordering in the sampling scheme, the problem usually has some local minima, and within them the aim is to search the global minimum; in order to have chance to escape from a local minimum a stochastic optimization process able to explore all the region of interest is implemented. Objective function E can be minimized applying two steps, namely "mutation" and "selection".

Mutation. In this first stage one variable (one column of the sampling matrix $\boldsymbol{X}$) is randomly selected and two randomly ranks of that vector are chosen and exchanged. After this

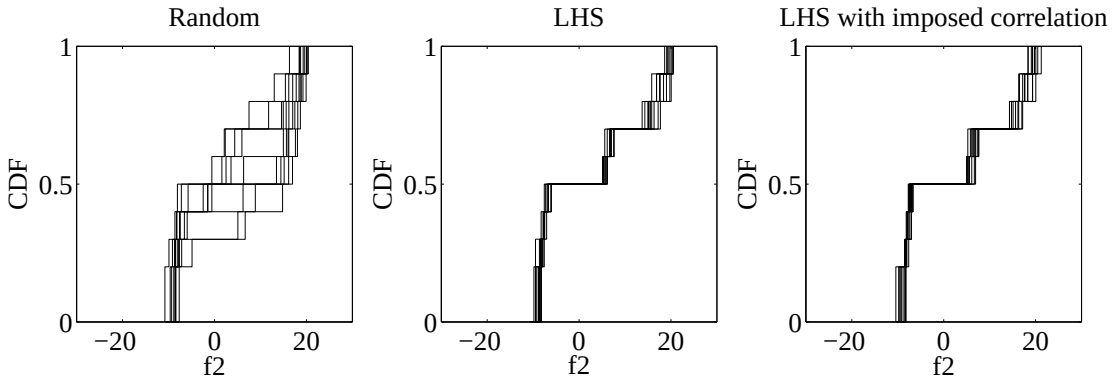

(a) $N_{sim} = 10$.

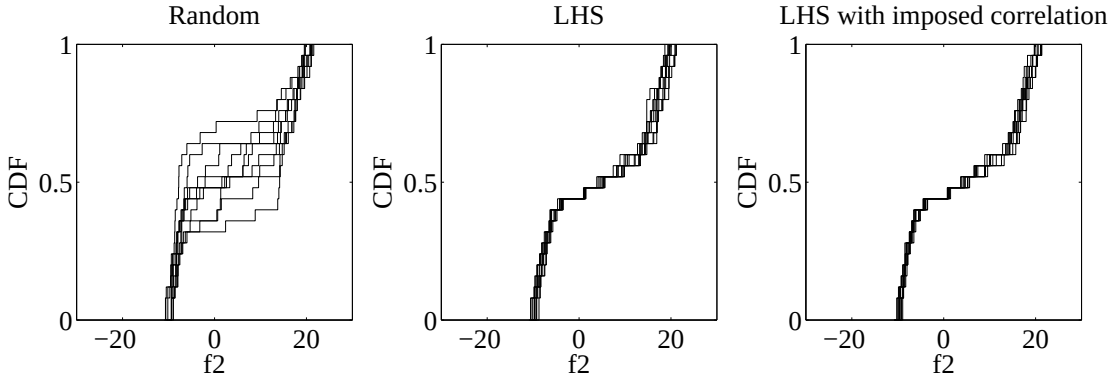

(b) $N_{sim} = 25$.

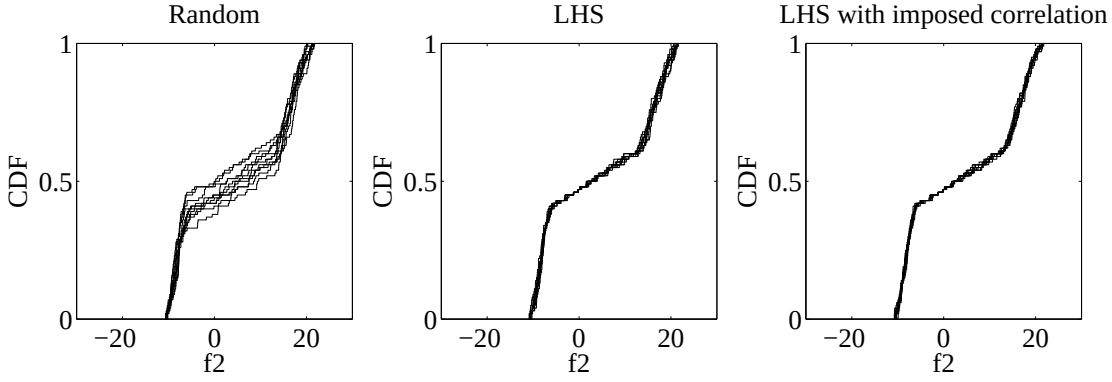

(c) $N_{sim} = 100$.

Figure 2.9: Evaluation of function f_2 varying the sample size N_{sim} for different sampling techniques.

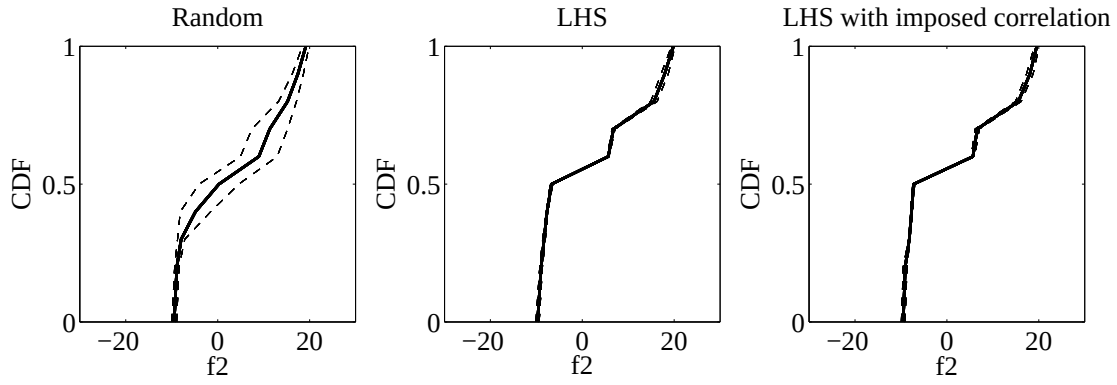

(a) $N_{sim} = 10$.

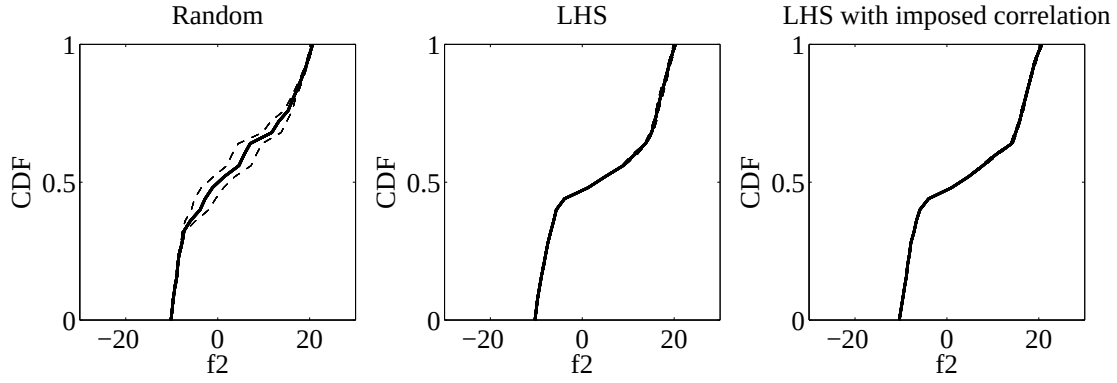

(b) $N_{sim} = 25$.

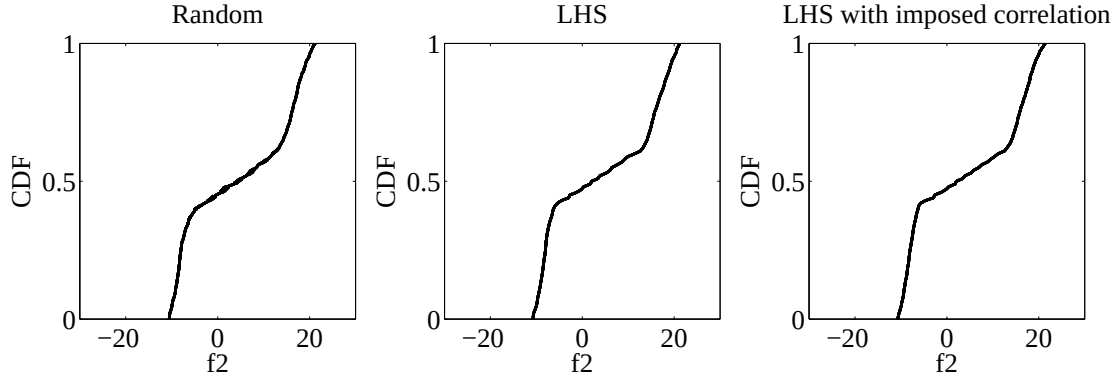

(c) $N_{sim} = 100$.

Figure 2.10: Evaluation of confidence interval for function f_2 varying the sample size N_{sim} for different sampling techniques.

the newly correlated matrix ("offspring") is evaluated and compared with the previous one ("parent").

Selection. In this step the algorithm chooses the best norm, and the related sampling matrix will survive for the next generation. The process is iterative in order to reduce step by step the objective function until a certain tolerance is reached.

Considering this simple scheme it was observed that in many cases the algorithm fails into a local minimum, because the only possibility to improve the process is the acceptance of the "offspring". One possibility to refine the selection stage is the implementation of a Simulated Annealing (SA) approach, see Kirkpatrick et al. [134]. Originally this method was developed in order to numerically simulated the heat treatment of a metal, where the material changes his crystal structure to improve the properties. This technique is based on the Boltzmann probability distribution:

$$P_r(E) \approx \exp\left(\frac{-\Delta E}{k_b \cdot T}\right) \tag{2.53}$$

where ΔE is the difference of the norms before and after the random change, T is the temperature and $k_b = 1.381 \times 10^{23}\,\mathrm{JK}^{-1}$ is the constant of Boltzmann. The probability represents the condition of a system in thermal equilibrium at a temperature T, where the energy is distributed in a probabilistic way among all the states ΔE. Also at low temperature there is small chance that the system is locally in a high energy state; subsequently there is a small probability that the system moves from a local energy minimum to a better one. In other words, there is a small probability to escape from a local minimum in order to search a global one, Vořechovskỳ and Novák [241]. At this point, there are two possibilities to improve the optimization technique:

1. New arrangement of sample matrix $\boldsymbol{X}$ is automatically accepted if the norm E decrease;
2. If the new arrangement does not decrease the norm E the "offspring" is however accepted with a certain probability given by P_r.

In particular new arrangement is accepted if:

$$Z = \exp(-\Delta E/T) - R > 0$$

where R is a random uniformly distributed variable between 0 and 1. T is the temperature, and the name comes from the application in metallurgy. In this case the initial temperature represents the maximum norm E, i.e. the norm evaluated in which all the coefficients of the correlation matrix S are ± 1, depending if $K_{i,j}$ is positive or negative. To simulate the real process of annealing, the temperature should be decrease after a predefined number of mutations; in this study, from a stage to the following one, the temperature decreases with a ratio equal to 0.95, similar to the value used elsewhere, Kirkpatrick et al. [134]. The overall

Table 2.3: Statistical parameters of the normal variates used in the comparison test between sampling techniques.

N_{var}	μ	σ
1	1.0	0.5
2	2.5	2.0
3	−4	5.0
4	10	2
5	7	0.5
6	3	1.0
7	9	0.2
8	−6	0.4

process stops when a small temperature is reached (e.g. 10^{-5}), and the number of mutations depends on the size of problem. If the number of random variables N_{var} is around 10 and the number of samples is less than 100, a reasonable number is 1000, Dolšek [69]. In this investigation the maximum number of mutations is set to 1000.

The capability of LHS with Simulated Annealing (LHS-SA) is compared with the other methods described in this section (random, LHS, LHS with "Iman and Conover" correlation (LHS-IC)) considering a random function where the analytical solution is known. In particular the function g is defined as the sum of 8 uncorrelated normal variables:

$$g = \sum_{i=1}^{N_{var}} X_i, \qquad N_{var} = 1, 2 \ldots, 8 \tag{2.54}$$

where mean values and standard deviation of each variate are listed in Table 2.3. As explained in Ang and Tang [11] the sum of normal random variables is also a normal random variable with mean and standard deviation respectively equal to:

$$\mu = \sum_{i=1}^{N_{var}} \mu_i, \qquad \sigma = \sqrt{\sum_{i=1}^{N_{var}} \sigma_i^2} \tag{2.55}$$

Figure 2.11a shows the estimate of the mean value between random, LHS and LHS-IC, while Figure 2.11b refers to the results of LHS-SA. Last sampling technique is separated from the other because in the first case the sample size goes from 10 to 500000, while in the second from 10 to 50, in order to highlight the capability of this method. Figure 2.12 shows the estimate of the standard deviation while in Figure 2.13 is shown the estimate, in percentage, of the norm of the difference between the correlation matrix and the prescribed one, see equation 2.52.

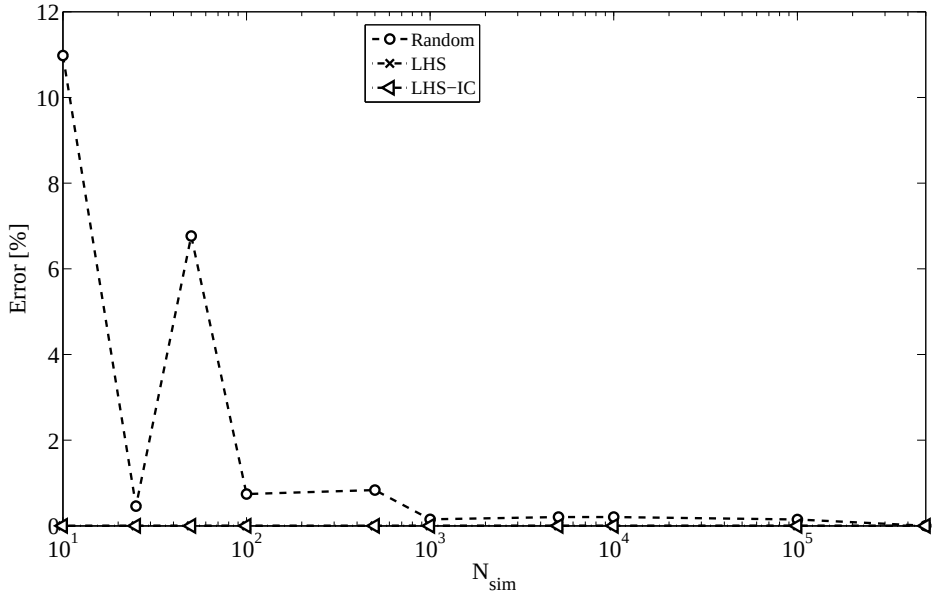

(a) Random, LHS and LHS-IC.

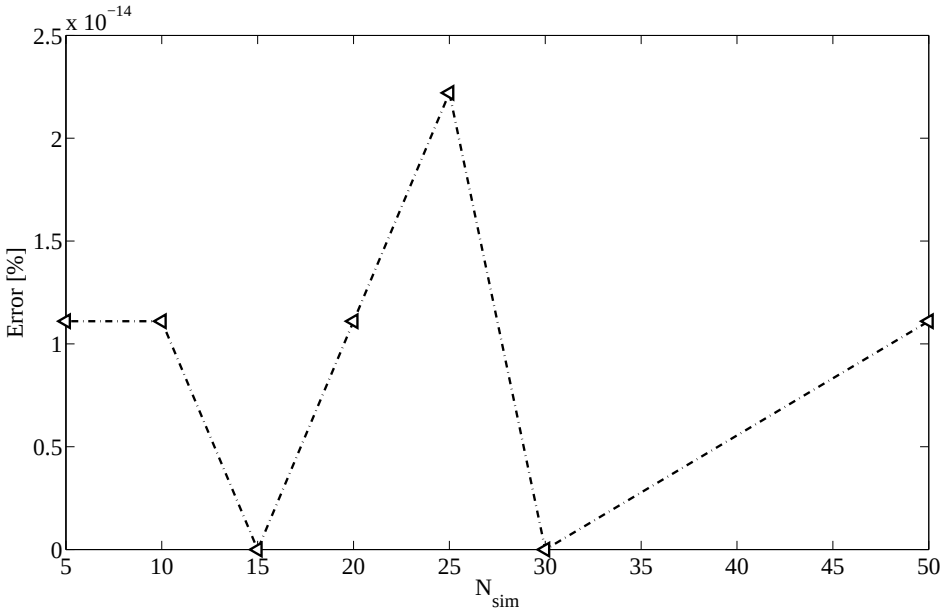

(b) LHS-SA.

Figure 2.11: Error on the estimate of the mean value considering different sampling techniques.

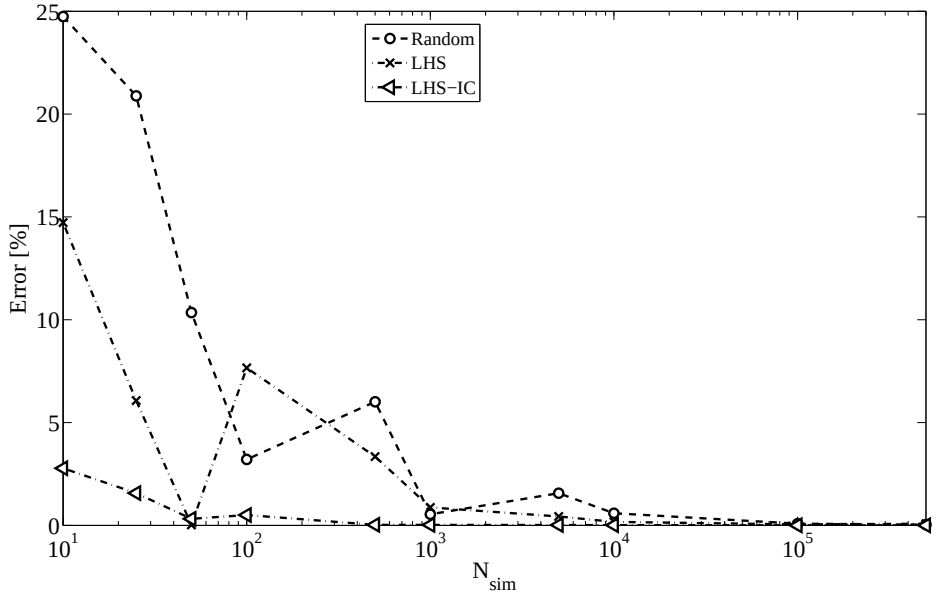

(a) Random, LHS and LHS-IC.

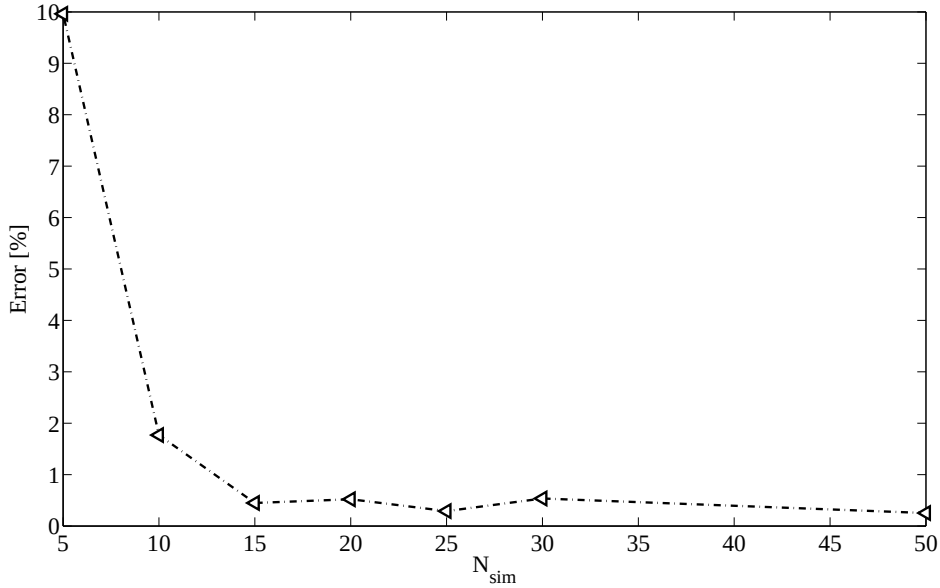

(b) LHS-SA.

Figure 2.12: Error on the estimate of the standard deviation considering different sampling techniques.

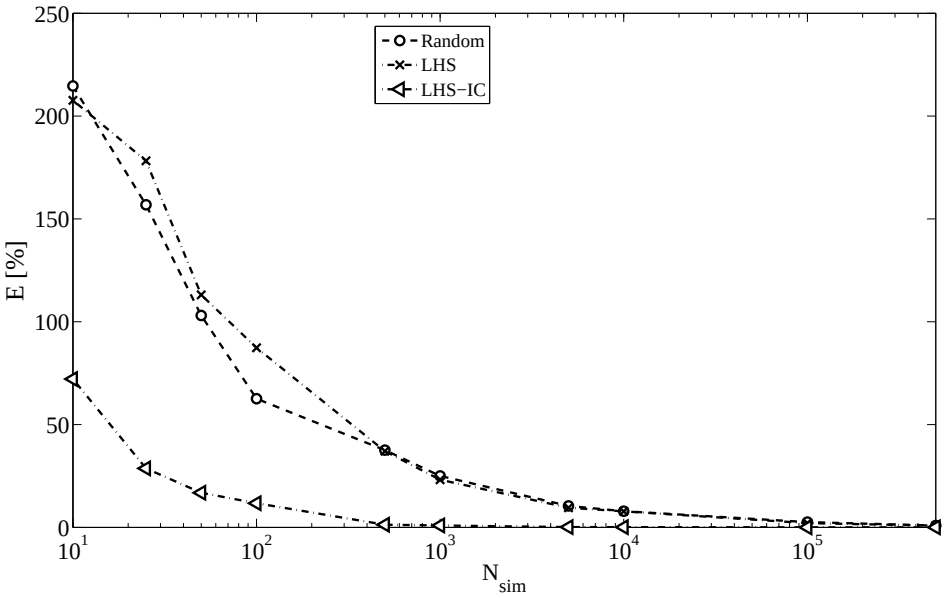

(a) Random, LHS and LHS-IC.

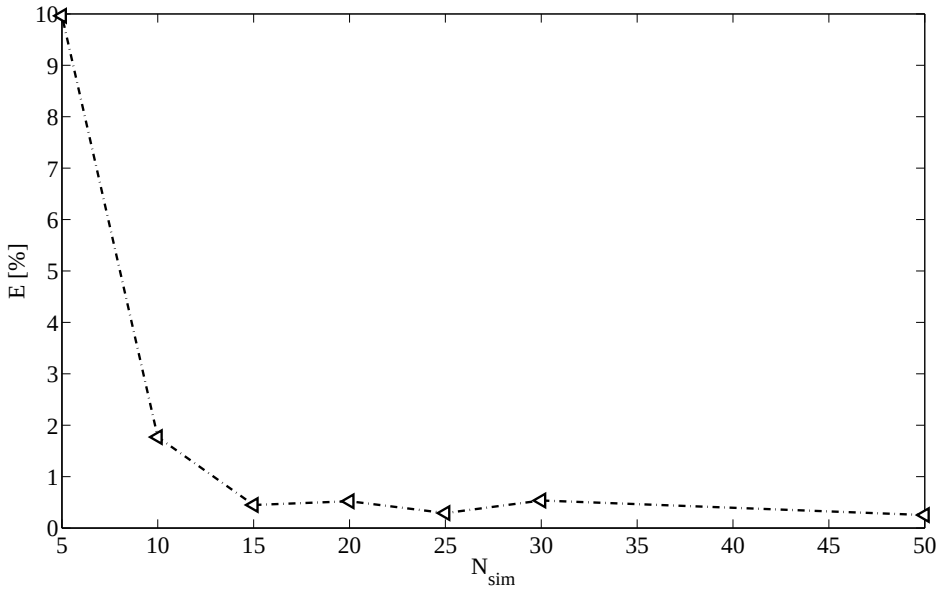

(b) LHS-SA.

Figure 2.13: Norm of the difference between correlation matrix and prescribed one considering different sampling techniques.

Table 2.4: Error on the estimate of statistical parameters considering random sampling, LHS and LHS-IC.

N_{sim}	**Random**			**LHS**			**LHS-IC**		
	$\Delta\mu$ [%]	$\Delta\sigma$ [%]	E [%]	$\Delta\mu \cdot 10^{-12}$ [%]	$\Delta\sigma$ [%]	E [%]	$\Delta\mu \cdot 10^{-12}$ [%]	$\Delta\sigma$ [%]	E [%]
10	10.98	24.74	5.42	0.00	14.73	5.24	0.01	2.78	1.82
25	0.46	20.89	3.96	0.01	6.07	4.50	0.01	1.57	0.72
50	6.77	10.35	2.60	0.04	0.02	2.86	0.01	0.32	0.43
100	0.74	3.21	1.58	0.01	7.66	2.21	0.07	0.50	0.30
500	0.84	6.01	0.95	0.00	3.35	0.94	0.02	0.03	0.03
1000	0.15	0.54	0.63	0.04	0.88	0.59	0.04	0.02	0.02
5000	0.21	1.57	0.26	0.33	0.43	0.24	0.18	0.02	0.00
10000	0.21	0.59	0.20	0.16	0.17	0.20	0.47	0.01	0.00
100000	0.15	0.08	0.06	0.08	0.05	0.05	0.79	0.00	0.00
500000	0.00	0.04	0.02	0.46	0.08	0.02	0.31	0.00	0.00

Table 2.5: Error on the estimate of statistical parameters considering LHS-SA.

N_{sim}	**LHS-SA**		
	$\Delta\mu \cdot 10^{-13}$ [%]	$\Delta\sigma$ [%]	E [%]
5	0.11	9.96	7.22
10	0.11	1.77	0.54
15	0.00	0.45	0.23
20	0.11	0.52	0.1
25	0.22	0.29	0.05
30	0.00	0.54	0.05
50	0.11	0.25	0.05

Some considerations can be done looking at the results listed in Tables 2.4 and 2.5. First of all, the estimate of mean value performed with LHS gives always very good results, regardless of the sample size. About the estimation of standard deviation, both LHS techniques with imposed correlation give better results with respect to random sampling or simple LHS; also in this case the sample size is not so important, but the only requirement is that the sample size should be higher than the number of variable. Finally, considering the evaluation of the norm of the difference between correlation matrix, see equation 2.52, Latin Hypercube Sampling associated with Simulated Annealing is superior with respect to the sampling with method given by Iman and Conover (Iman and Conover [127]). For example, if we consider the last columns of Tables 2.4 and 2.5, the same norm is reached with a number of samples approximately $5 \div 10$ times smaller for LHS-SA.

In conclusion, comparing random sampling and LHS-SA, the latter technique is significantly better than the former, in particular in the estimate of standard deviation; the same error is reached using a sample size hundred of times smaller, saving computational cost. In the light of all these considerations, structural models used in the following for all the seismic analyses will be establish on the base of Latin Hypercube Sampling with Simulated Annealing.

2.5 Probabilistic seismic hazard analysis

Probabilistic seismic hazard analysis (PSHA) is one of the step involved in the evaluation of the seismic risk for a particular site; sometimes the terms *risk* and *hazard* are used to describe the same issue, however there are some differences. *Risk* has a more general meaning, because involves also social and economical aspects, and his definition is the probability that social or economic consequences of earthquakes will equal or exceed specified values at a site, during a specified exposure time. *Hazard* concerns the physical phenomena induce damages or negative effects on human activities. Equation 2.56 can be used as a reference for the definition of seismic risk:

$$\text{SEISMIC RISK} = \text{SEISMIC HAZARD x VULNERABILITY x LOSS} \tag{2.56}$$

where "vulnerability" stands for probability of exceedance of a particular limit state due to a predefined seismic intensity and "loss" represents the economic/social damages; symbol "x" represents a convolution between the three parameters. Among different approaches available in literature, PEER has developed in the last years a reliable framework for performance bases assessment, Porter [198] and Moehle and Deierlein [169]. Within the present investigation, the PEER methodology is applied in order to assess the seismic performance of RC multistory frame structures subjected to environmental hazard, with emphasis on the vulnerability, without considering the loss analysis. A meaningful picture of the steps involved in the PEER PBEE approach is shown in Figure 2.14. In the figure $p[A|B]$ represents the conditional

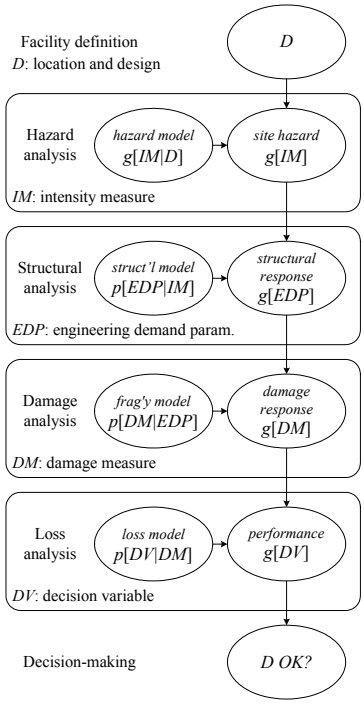

Figure 2.14: Scheme of the PEER PBEE methodology (after Porter [198]).

probability of A given B, while $g[A|B]$ means the occurrence frequency of A given B or, in other word, the slope of the curve (in this case the hazard curve). From a mathematical point of view, equation 2.56 is translated as expressed in equation 2.57:

$$g(DV|D) = \int\int\int P(DV|DM,D)P(DM|EDP,D)P(EDP|IM,D)g(IM|D)dIMdEDPdDM \qquad (2.57)$$

where vulnerability combines structural and fragility analysis. This section deals with the hazard analysis, while the next one is devoted to the development of fragility curves. In the following chapter different methods to perform a seismic analysis are explored.

There are two different approaches to perform a seismic hazard analysis, deterministic (DSHA) and probabilistic (PSHA). A review of the two approaches can be found in Krinitzsky [140], Romeo and Prestininzi [211] and Bommer [43]. Within the deterministic approach, seismic hazard is computed with reference to a single earthquake that occurs at a fixed distance to the site and with a prescribed ground motion probability level, while in the probabilistic scheme seismic hazard is computed considering all possible earthquakes from all possible sources and probability of occurrences. Both methods use attenuation laws to estimate ground motion parameters, but the main difference is that in PSHA time is explicit while in DSHA not. Considering the variabilities normally affect an engineering problem, in this investigation the probabilistic approach is used, based on the fundamental work of Cornell, Cornell [62]; the disadvantage is that with this method the concept of "design earthquake" is lost.

In PSHA it is possible to identify three different steps, namely *occurrence laws*, *attenuation*

laws and *distribution of occurrences in time*. Next sections deal with the above issues.

2.5.1 Recurrence laws

A recurrence law gives the *average rate* at which an earthquake of some size will be exceeded. The first attempt to introduce a relationship between the magnitude of the earthquakes and their occurrence has been done by Gutemberg, Gutenberg and Richter [109]. The recurrence law has the form:

$$\log(\lambda_M) = A - bM \tag{2.58}$$

where λ_M is the *mean annual rate* of an earthquake exceeding magnitude M, namely the number of earthquakes with a magnitude higher than M divided by the time of interest. A and B are constants depending by the seismicity of the region, in particular A is the *activity parameter*, that is the number of events with magnitude higher than 0, while B refers to the likelihood of large and small earthquakes of the region. For example, a decrease in the value of B, or in other words a decrease in the slope of the curve in equation 2.58, means an increase in the likelihood of larger earthquakes, Sen [223].

It is more useful to express equation 2.58 into the exponential form:

$$\lambda_M = 10^{A-bM} = \exp(\alpha - \beta M) \tag{2.59}$$

From an engineering point of view, a magnitude lower that a minimum value M_{min} is not of interest in terms of potential consequences on the structure studied. Equation 2.59 can be used to evaluate the cumulative distribution function $F(M)$ for the magnitude of earthquakes higher then a minimum threshold value; using the definition of conditional probability, equation 2.1, the following expression is obtained:

$$\begin{aligned} F_M(m) &= P(M \leq m | M > M_{min}) \\ &= P(M_{min} < M \leq m) \\ &= \frac{\lambda_{M_{min}} - \lambda_M}{\lambda_{M_{min}}} \\ &= 1 - \exp\left(-\beta(M - M_{min})\right) \end{aligned} \tag{2.60}$$

If derivative exists, also the PDF for the magnitude of earthquakes higher then M_{min} is defined:

$$f_M(m) = \frac{\partial F_M}{\partial M} = \beta \exp\left(-\beta(M - M_{min})\right) \tag{2.61}$$

Equation 2.61 theoretically predicts magnitudes without an upper limit, that is no feasible in practice. An attempt has been done in order to introduce an upper bounds, Kramer [137]; CDF and PDF are therefore expressed in equation 2.62 and 2.63.

$$F_M = \frac{1 - \exp\left[-\beta(M - M_{min})\right]}{1 - \exp\left[-\beta(M_{max} - M_{min})\right]} \tag{2.62}$$

$$f_M = \frac{\beta \exp\left[-\beta(M - M_{min})\right]}{1 - \exp\left[-\beta(M_{max} - M_{min})\right]} \tag{2.63}$$

Gutenberg-Richter recurrence law is not the only model to describe the distribution of earthquake magnitudes; for example another model is the so called *Characteristic earthquake*, see e.g. Schwartz and Coppersmith [221]. However, available worldwide seismic data does not support other models being adopted, Sen [223]. PEER methodology is then based on Gutenberg-Richter recurrence law.

2.5.2 Ground motion models

Second step refers to estimate of ground motion parameters. To this aim, attenuation relationships or, better ground motion models, are used. These equations give the probability distribution of ground motion intensity IM (e.g. the peak ground acceleration PGA or the spectral acceleration for a particular period) depending on the main descriptors of a ground motion (magnitude, distance, fault mechanisms, etc., see Stewart et al. [228]) with the corresponding variability. A review of different intensity measure used to describe a ground motion can be found in Riddell [208] and Elnashai et al. [77]. Typically, the equations are calibrated through a regression analysis of data collected among different observations, and the generic function is the following:

$$\ln(IM) = \mu(M, R, \boldsymbol{\theta}) + \sigma(M, R, \boldsymbol{\theta}) \cdot \varepsilon \tag{2.64}$$

where $\ln(IM)$ is a random variable with his main statistical descriptors mean value μ and standard deviation σ. M and R are magnitude and distance while $\boldsymbol{\theta}$ collects other parameters involved in the process. ε is a standard normal variable that represents variability on $\ln(IM)$. Attempt has been done by different researchers all over the world in order to elaborate ground motion models for different sites; to this purpose, attenuation relationships for Europe, US and Japan have been developed. Reader can refers to Elnashai et al. [77]. A significant improvement was done recently with the introduction of the "NGA" (Next generation attenuation models) by Power, Power et al. [201], that has a wide applicability; in particular, in Campbell and Bozorgnia [50] the applicability of these models to Europe is investigated. Moreover, following the developments of structural codes toward a performance based approach, namely representing capacity and demand due to a ground motion through displacements, attenuation relationships involving displacement response spectra are emerging, Cauzzi and Faccioli [52].

Combining all the above information, ground motion models allow to compute the probability of exceedance of a particular intensity measure $\overline{IM}$, given a magnitude and a distance. In analytical form, exploiting the total probability theorem, it is possible to write:

$$P(IM > \overline{IM}) = \int_{m_{min}}^{m_{max}} \int_{0}^{r_{max}} P(IM > \overline{IM}|m,r) f_M f_R dm dr \tag{2.65}$$

where $P(IM > \overline{IM}|m,r)$ comes from the attenuation relationship, f_M comes from Gutenberg-Richter law, see equation 2.61, while f_R is the PDF of the distance and depends on the type of geometrical source (point, line, etc ...). In equation 2.65 the joint probability between magnitude and distance is simply the multiplication of the marginal probability because the hypothesis of independence. Introducing the information on the occurrence of an earthquake in the site of interest, equation 2.65 is rewritten as explained below, Bazzurro and Cornell [22]:

$$\lambda(IM > \overline{IM}) = \lambda(M > m_{min}) \int_{m_{min}}^{m_{max}} \int_{0}^{r_{max}} P(IM > \overline{IM}|m,r) f_M f_R dm dr \tag{2.66}$$

where $\lambda(M > min)$ is the rate of occurrence of an earthquake with magnitude higher than the lower bound. Equation 2.66 can be also generalized if multiple sources are present:

$$\lambda(IM > \overline{IM}) = \sum_{i}^{Nr_{sources}} \lambda(M_i > m_{min}) \int_{m_{min}}^{m_{max}} \int_{0}^{r_{max}} P(IM > \overline{IM}|m,r) f_M f_R dm dr \tag{2.67}$$

2.5.3 Distribution of occurrences in time

If the rate of exceedance is computed for different levels of the intensity measure, the hazard curve is obtained, which is the primary results of a PSHA. An example can be visualize in Figure 2.15.

Integral depicted in equation 2.66 in practice cannot be solved through analytical formula, so numerical methods are applied. Because the parameters involved are random variables, Monte Carlo simulation is an effective tool for the development of hazard curve, Ebel and Kafka [72] and Musson et al. [175]. Examples on his application can be found in Sen [223]. Last step concerns the introduction of a temporal model, in order to compute the probability that a predefined ground motion level is exceeded within a time interval, typically 50 years. When PSHA first appears, Cornell [62], Poisson process was selected; for his validity, some assumption should be made:

1. Stationarity. If the mean annual rate of frequency is λ, in a small time interval Δt the probability of occurrence is $\lambda \Delta t$, for any time t considered;

2. Non-multiplicity. The probability of occurrence of two or more events in a short interval Δt is negligible with compared to $\lambda \Delta t$;

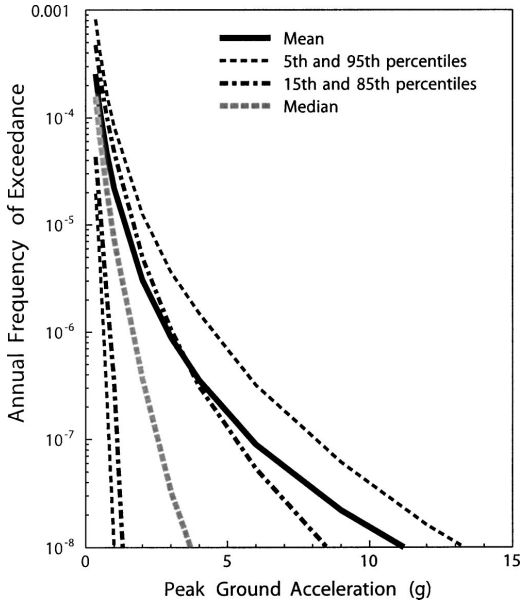

Figure 2.15: Seismic hazard curves from the Yucca Mountain project (Stepp et al. [227], Abrahamson and Bommer [1]).

3. Independence. The occurrence of an event in a given time interval is statistically independent of that in any other nonoverlapping interval.

The validity of the assumptions above cited is argued, in particular for point 2 and 3. Point 2 is denied due to the presence of foreshocks and aftershocks during an earthquake, while point 3 is is in contradiction with the *Elastic Rebound theory*. In spite of these issues, time arrivals of future events are modeled through a Poisson process because successful applications in past years and especially because it is the simplest model capturing the basic characteristic of the problem. The violation of the hypothesis can be also partially overcome considering that the sum of non Poisson process is a Poisson process, Ang and Tang [11]. If the average number of earthquakes in a time interval is ξ, the probability that the number of occurrence N is equal to a predefined value n is:

$$P(N = n) = \exp(-\xi)\frac{\xi^n}{n!} \tag{2.68}$$

Introducing the *mean rate of occurrence* λ in a time interval t, equation 2.68 can be rewritten as:

$$P(N = n) = \exp(-\lambda t)\frac{(\lambda t)^n}{n!} \tag{2.69}$$

Denoting as T the length of time of interest, the probability that 0 events occur in that period is:

$$P(N = 0) = \exp(-\lambda T)\frac{(\lambda T)^0}{0!} = \exp(-\lambda T) \tag{2.70}$$

Table 2.6: Probability of exceedance and return period for a time interval of 50 years.

$P[\%]$	λ	$T_R[years]$
63	0.0199	50
10	0.0021	475
5	0.0010	975
2	0.0004	2475

Conversely, the probability that *at least* one event will occur is:

$$P = 1 - 0 \text{ events occur} = 1 - \exp(-\lambda T) \tag{2.71}$$

Equation 2.71 is more significant if expressed in a logarithmic format, in order to highlight the rate of occurrence λ (or the *return period* T_R, that is the inverse):

$$\ln(P) = \ln(1 - \exp(-\lambda T)) \Rightarrow \exp(-\lambda T) = \ln(1 - P) \Rightarrow \lambda = -\frac{\ln(1 - P)}{T} \tag{2.72}$$

Assuming a time interval T (usually equal to 50 years) and a range of probability P_i the probability of exceedance can be computed, as indicated in Table 2.6.

Selecting an intensity measure, at each value is associated the seismic hazard of a site expressed in terms of the above probability of exceedance or, equivalently, in terms of return period. About Italy, great effort has been done in order to develop such curves, considering intensity measure refers to acceleration, Montaldo et al. [170] and displacement, Faccioli and Villani [79]. The main reference is the INGV (Istituto Nazionale di Geofisica e Vulcanologia), see website http://esse1.mi.ingv.it/; an example of such curves, with reference to PGA, is shown in Figure 2.16. Details can be found in Meletti and Montaldo [166].

2.6 Development of fragility curves

Regardless the specific seismic hazard of a site, the vulnerability of a structure can be evaluated through the so called *fragility function* or *fragility curve*, which expresses the probability of exceeding a particular limit state given a predefined value of intensity measure. Usually the performance states are in the nonlinear range of behavior, so it is necessary to perform a set of nonlinear analyses in order to extrapolate statistics on the results. Fragility function is the probability that a suitable damage state DM (e.g. the maximum interstory drift) is higher that a threshold value $\widehat{DM}$ when the intensity measure assumed IM is equal to a particular value $\widehat{IM}$, see equation 2.73:

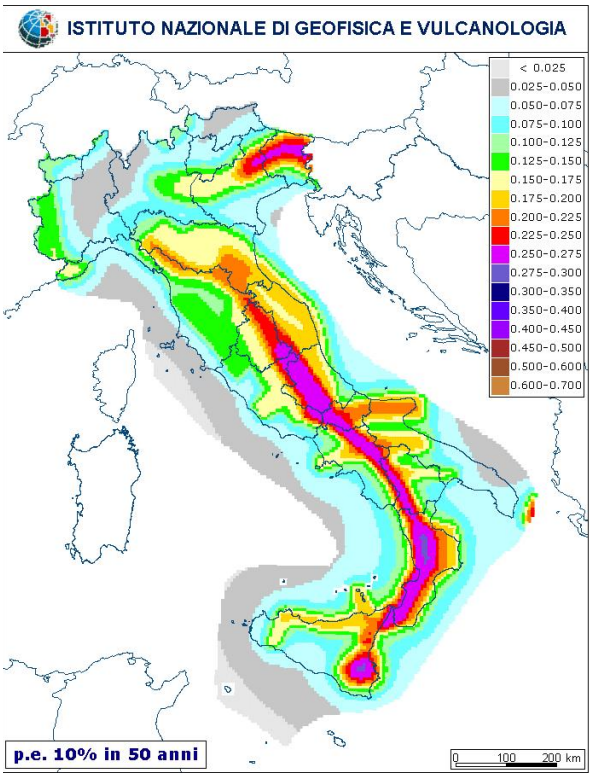

(a) $\lambda = 10\%$.

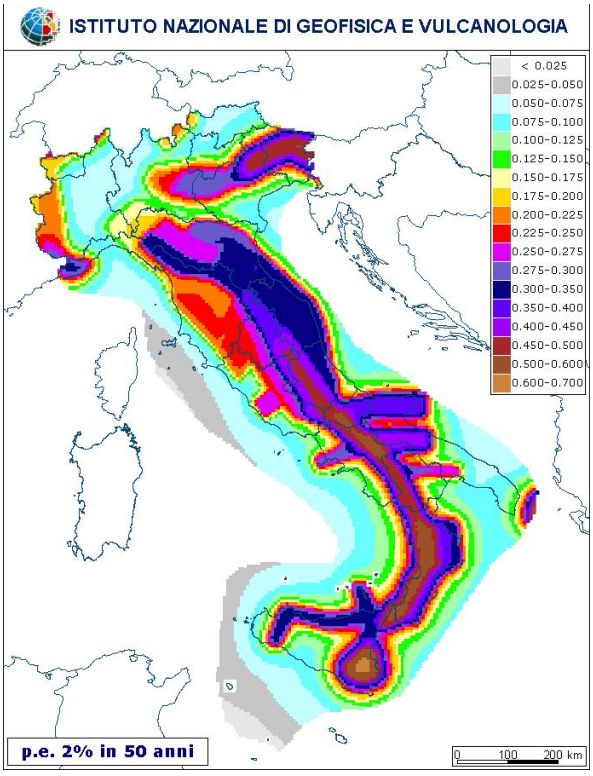

(b) $\lambda = 2\%$.

Figure 2.16: Probabilities of exceedance of PGA for Italy with reference to a period of 50 years, Meletti and Montaldo [166].

$$F_{DM}(IM) = P[DM \geq \widehat{DM} | IM = \widehat{IM}] \tag{2.73}$$

Fragility curve is obtained integrating on all the values of the intensity measure, equation 2.74

$$P_f(IM) = \int_0^{+\infty} f_D(DM|IM) F_C(DM) dDM \tag{2.74}$$

where $f_D(DM|IM)$ is a proper probabilistic model regarding demand (usually assumed as a lognormal distribution, Jalayer [129]) and $F_C(DM)$ is the cumulative distribution function of the capacity. It is important to highlight that the fragility function depends not only from the characteristic of the structure but also from the ground motion, and the influence of his different features typically depends on the choice of the intensity measure, Pinto [196].

Different methodologies exist in order to compute fragility functions; a set of procedures from different kind of data can be found in Porter et al. [197]. Another important issue regards the possibility to highlight in a suitable way the effect of uncertainties coming from record to record variability (a set ground motion records) and modeling. For the second case, a simulation method based on Monte Carlo approach, eventually coupled with strategies to reduce the computational cost, see e.g. Liel et al. [155], seems the better option to perform nonlinear analyses. Finally, combining hazard curve of the site of interest and fragility function, the probability of exceeding a particular performance level within a time period can be computed. This is one of the main outcome of the PEER PBEE methodology.

2.7 Conclusions

This chapter highlights the importance of a probabilistic approach in seismic engineering. First of all, a review of the main concepts in the theory of probability is presented, in order to illustrate all the mathematical tools that are applied in this investigation. Regarding numerical methods that are used nowadays to solve engineering problems, particular emphasis is given to Monte Carlo approach, which is particularly effective when random variables are involved in the process. Because the unfeasible computational cost associated with a plain simulation, a review of different strategies able to reduce the variance, so the number of simulations required, is illustrated and, among them, the use of a particular stratified sampling, namely Latin Hypercube sampling, is adopted. Through simple problems where the analytical solution exists, the effectiveness of this technique is highlighted, constituting the base to sample the random variables introduced subsequently for the seismic assessment of the systems studied.

Second part of the chapter is devoted to probabilistic seismic hazard analysis, and the main steps required to develop hazard curve are reviewed. Finally, the procedure to develop fragility curves is shown, in order to highlight how the vulnerability of a structure, with regards to a predefined ground motion level, can be expressed in a reliable way. Combining all these concepts, namely hazard curve and fragility, the probability of exceeding a particular limit

state over a period of time can be evaluated; this is the main concept at the base on the Performance based Earthquake Engineering.

Chapter 3

Probabilistic assessment of seismic performance

3.1 Introduction

This chapter deals with the assessment of seismic performance of multistory RC precast frame systems within the PEER methodology, with particular emphasis on the probabilistic approach. The choice of the best sampling for the random variables that will be used in the investigation is based on the Latin Hypercube sampling, Iman and Conover [127] and Helton and Davis [113]. First of all, the archetypes of the structures studied are presented, highlighting their main characteristics. Section 3.3 is devoted to the choice of a suitable hysteretic law able to predict the flexural collapse of reinforced concrete structural members, introducing the analytical model and the equations for the calibration of the principal parameters. Next two sections review the two methods used in this study to perform nonlinear seismic analyses, namely incremental dynamic analysis (IDA) and pushover. The respective key issues are addressed, underlining their advantages and drawbacks.

Subsequently, random variables involved in the analysis are selected, using LHS in order to create the set of structures to perform the probabilistic assessment; particular importance is given to the choice of the proper number of samples able to predict in a reliable way the structural capacity of RC precast systems. To this purpose a sequence of two steps is considered; first of all, the potential "candidate" N_{sim} is evaluated with reference to the comparison between the theoretical correlation matrix and the matrix obtained at the end of the sampling procedure. Second step requires to perform nonlinear analyses, each of them with a different number N_{sim}, comparing the results until the differences are small; final choice is done considering a *Kolmogorov-Smirnov* test for the goodness of fit, Ang and Tang [11].

Finally, the results of the IDA and pushover analyses are shown, comparing the outcomes in terms of structural capacity. Selecting then different sites in Italy and considering their respective hazard curves, the probabilities of failure for a set of limit states, from limited

damage up to collapse, are computed, in order to evaluate the mean annual frequency of exceedance of limit states chosen.

3.2 Archetypes of multistory precast frame systems

Over the last years the assessment of seismic performance of precast structures was deeply investigated. Intensive studies, coupling experimental tests and probabilistic numerical analyses, showed that also for precast buildings with hinged beams the same design criteria for cast-in-situ structures can be applied, with the only requirement to avoid brittle failure of connections, Biondini and Toniolo [32]. In literature different solutions have been proposed in order to guarantee ductility to connections, see e.g. "PRESS" program (Pampanin et al. [186], Pampanin [185]), where the effectiveness of unbonded post-tensioned tendons is studied. Recently, a European project namely "SAFECAST", involving universities and companies, is focusing on the performance of innovative mechanical connections in precast buildings structures under seismic conditions, Biondini et al. [41]. With appropriate dimensioning of members and connections, hinged precast structures are able to to provide good seismic performance as monolithic cast-in-place structures, Biondini et al. [39]. Because at the present time Eurocode 8, EC8 [74], does not cover the seismic design of this type of structures, capacity design are required; to this aim the same approach applied for monolithic cast-in-situ frames is considered, Biondini et al. [38].

Here it is presented only a sinthesys of the procedure adopted for the design of precast structures; for all the details readers can refer to Biondini et al. [39]. Considering a behavior controlled by the fundamental mode, a linear distribution of floor forces is applied to the structure; with a proper capacity design criteria, Paulay and Priestley [192], a global collapse mechanism is achieved; because the flexibility of the systems studied, a behavior factor q equal to the displacement ductility μ is chosen, following the well known "equal displacement" rule, see e.g. Chopra [55] and Elnashai et al. [77]. With these characteristics, a linear static analysis is then performed in order to design the critical cross-sections at the base of the columns and the connections between columns and beams. Due the hypothesis at the base of the procedure, a parametric analysis is carried out, changing the key parameters (e.g. stiffness of the members, number of stories, ...). Performing subsequently a modal analysis and a pushover one, the influence of higher modes and the displacement capacity of the structures is clearly highlighted, in order to understand the range of applicability of such procedure. In the following, the design parameters coming from such analyses are introduced.

Structures are designed assuming a story weights, equal for each floor, of 1200 kN, story heights equal to 4 m, a design peak ground acceleration $a_g = 0.35g$ and a behavior factor $q = 4$. For all the columns the same cross-section is considered, using concrete $C40/50$ and a steel $B450C$. The minimum amount of longitudinal reinforcement prescribed by code is adopted,

Table 3.1: Design parameters for the multistory buildings.

	2 story frame			3 story frame		4 story frame
T_1[s]	2.50	1.00	0.75	2.50	1.50	2.50
F[kN]	34	70	140	50	106	67
M_{sd}[kN m]	224	699	933	470	986	806
b[cm]	45	70	80	60	80	80
A_s	8Φ18	16Φ20	20Φ20	16Φ18	20Φ20	20Φ20

EC8 [74], because it is higher than that required by design; so $\rho_s = \rho_{min} = 0.01$. A set of six structural systems is investigated, changing both the number of stories and the size of the cross-section. Table 3.1 presents all the design parameters involved in the analysis, where F is the total column base shear, M_{sd} is the bending moment at the base of the column at the first story, b is the cross-section size and A_s is the longitudinal reinforcement. For each number of story, in order to decrease the value of the fundamental period, the size of the cross-section should be increased; however no other dimensions are studied because outside the range of practical interest.

About longitudinal reinforcement, prescriptions given by Eurocode 8 for high-ductility class are followed, EC8 [74]. In particular the diameter of the hoops and the spacing follow the requirements illustrated in equation 3.1:

$$\begin{aligned} d_{bw} &\geq 0.4 d_{bL,max} \cdot \sqrt{f_{ydL}/f_{ydw}} \\ s &= \min(b_o/3, 125, 6 d_{dbL}) \end{aligned} \tag{3.1}$$

where d_{bL_max} is the maximum longitudinal diameter, f_{ydL} and f_{ydw} are the yielding strength of the longitudinal and transversal reinforcement, respectively, and b_o is the minimum dimension of the concrete core. Considering the data listed in Table 3.1, the diameter of the hoops $d_{bw} = 8$ mm and the spacing is 10 cm. Regarding durability requirements, a class designation XD (corrosion induced by chlorides), EC2 [73], the net cover of concrete is assumed equal to 35 mm. Figure 3.1 shows the four different column cross-sections adopted in the investigation, while in Figure 3.2 the archetypes of the structures are introduced.

3.3 Choice of a suitable hysteretic law to predict collapse behavior

In the perspective of the Performance-based Earthquake Engineering, Ghobarah [97], one of the main challenge is the assessment of the seismic performance of different kind of structures

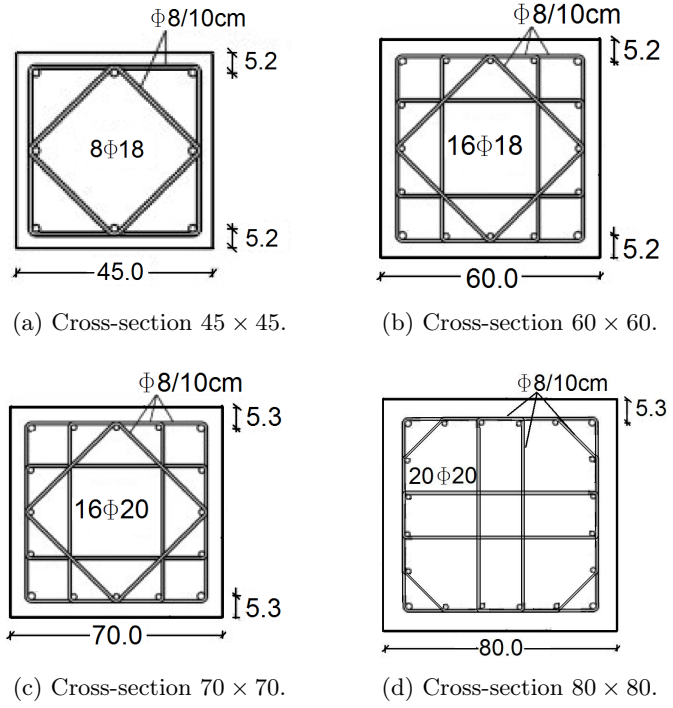

(a) Cross-section 45 × 45. (b) Cross-section 60 × 60.

(c) Cross-section 70 × 70. (d) Cross-section 80 × 80.

Figure 3.1: Layout of the cross-sections used in the investigation. Measure in cm.

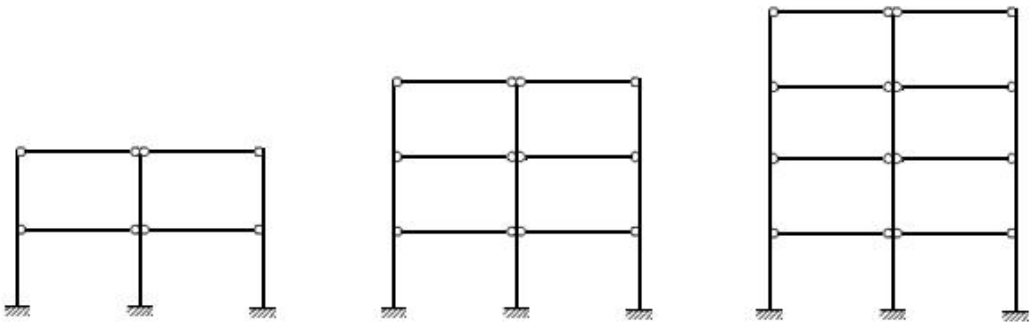

Figure 3.2: Archetypes of multistorey precast buildings.

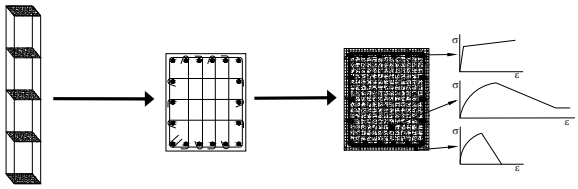

Figure 3.3: Distributed plasticity model for a RC member, Liel et al. [154].

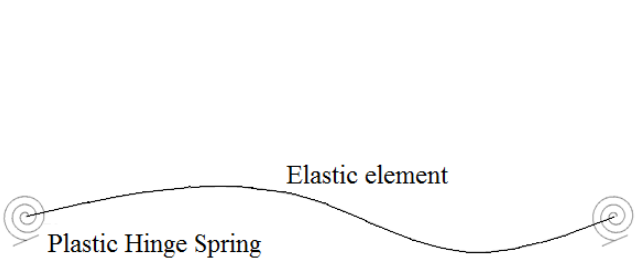

(a) Concentrated plasticity model.

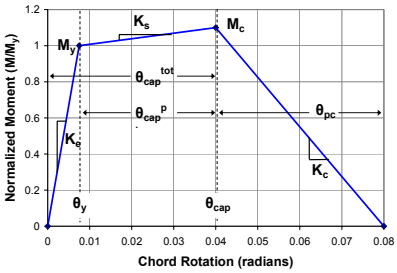

(b) Moment-rotation relationship of the nonlinear springs.

Figure 3.4: Lumped plasticity model for a RC member.

during their entire range of behavior, from limited damage if subjected to minor earthquakes up to near collapse when major ones are involved. Such an information can be evaluated in a reliable way if appropriate tools are considered; among them, a proper modeling of the nonlinear behavior of structural members is one the key factor. In practice there are two options to take into account the nonlinear behavior of elements, namely distributed and lumped plasticity models. In a distributed plasticity model the nonlinear behavior is spread along the entire length of the element, and the generic section is usually discretized into fibers; at each fiber is associated the constitutive law of the corresponding material, e.g. for a RC cross section the stress-strain models for concrete and steel are applied, see Figure 3.3, eventually taking into account the confinement effect due to the hoops.

On the other side lumped plasticity model are simpler and computationally less expensive because plasticity is concentrated within a predefined length of the member, namely the "plastic hinge"; if the length has a finite length, nonlinearity can be represented by an hysteretic law such as moment-curvature relationship, while if the length is zero, nonlinearity is lumped into a nonlinear spring, using e.g. a moment-rotation relationship, Figure 3.4. Between the two ends, the element has elastic properties, eventually modified to take into account the effect of cracking and bond slip. A review of different hysteretic models suitable for modeling the nonlinear behavior of concrete members can be found in Otani [183].

Apparently, a fiber discretization of the sections, spreading the nonlinear behavior along the entire length of the members, seems a better choice for nonlinear seismic analysis of structures. In fact, the choice of one modeling rather than the other depends on the purpose of

the investigation; in particular, if collapse is required, a lumped plasticity modeling is a better option for simulating strength and stiffness degradation, Liel et al. [154]. Considering a RC frames where the behavior is flexurally-dominated, collapse depends on the strain-softening behavior of beam-column members due to a combination of concrete crushing, yielding of bars coupled with their buckling. Research is pushing hard in order to develop fiber models capable to include such phenomena; for example, in Monti and Nuti [171], the behavior of reinforcing bars including buckling is experimentally studied through monotonic and cyclic tests, and an analytical model is proposed.

In Spacone et al. [224] a fiber beam-column model with a formulation flexibility-based is presented; since within this modeling the equilibrium is always respected, also the highly nonlinear behavior of concrete members can be properly considered, without reducing the size of the finite elements. In a companion paper, see Spacone et al. [225], some applications are presented. In Biondini [27] a 3-D finite beam element for seismic analysis of concrete structures is developed, including also a description of damage in terms of damage indices at multiple levels, from local to global behavior.

In spite of these important advances, fiber models nowadays are not fully calibrated and validated to capture strain softening associated with buckling and fracture of the longitudinal steel reinforcing bars; if buckling is the main issue to induce a flexural strength softening, distributed models cannot be used directly to estimate collapse, Liel et al. [154]. On the opposite, if the user is interested in tracking the crack path and the estimate of yielding, fiber models become the better option. Although lumped plasticity models loose in accuracy for the evaluation of the linear and mild nonlinear behavior of concrete members, the presence of a decreasing branch in the moment-rotation backbone, Figure 3.4b, allows to consider in a reliable way the softening behavior and, of consequence, the estimation of collapse.

Due to the above considerations, a lumped plasticity model will be used in the present study; in the following, a review of the main characteristics of the hysteretic law adopted is shown. In particular, the plastic hinges at the ends of the structural members are based on the nonlinear spring developed by Ibarra (see Ibarra et al. [121]) and subsequently implemented in *OpenSees*, Mazzoni et al. [163], by Altoontash, Altoontash [7]. However other formulations can be used, and a critical review can be found in Fischinger et al. [93]. The choice depends on the capability to take into account multiple modes of deterioration that induce the collapse of RC frames; in particular, four modes are considered, namely *basic strength deterioration*, *post-capping deterioration*, *unloading stiffness deterioration* and *accelerated reloading stiffness deterioration*. For collapse estimate, post-capping behavior is the key factor.

The nonlinear spring has a trilinear backbone curve, Figure 3.5, associated with the above hysteretic laws to simulate progressive damage; for all the modes an energy index is used to describe the cyclic deterioration. This parameter, β, depends on two factors: one is λ, the normalized energy dissipation capacity, and one is c, the exponent term that measures the

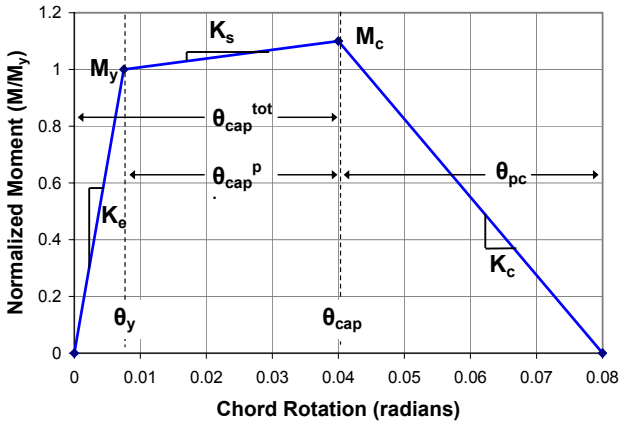

Figure 3.5: Moment-rotation backbone curve for Ibarra model, Haselton [112].

rate, namely the velocity, at which the deterioration occurs. In details:

$$\beta_i = \left(\frac{E_i}{E_t - \sum_{j=1}^{i} E_j} \right)^c \tag{3.2}$$

where β_i is the cyclic deterioration in excursion i, E_i is the hysteretic energy dissipated in excursion i, $\sum E_j$ is the hysteretic energy dissipated in all previous excursions through loading in both positive and negative directions and E_t is the reference hysteretic energy dissipation capacity, $E_t = \lambda F_y \delta_y$, see Ibarra et al. [121].

This kind of approach is quite different with respect to cumulative damage models. In the latter case a "counter", usually called *damage index*, is used to evaluate the level of damage (e.g. a value equal to 1 refers to a complete failure) but typically does not incorporate the evidence that a cumulative damage induces a deterioration of strength and stiffness of the structural members, accelerating the collapse. It is however possible to make a comparison between the procedure proposed in Ibarra et al. [121] and the damage models including two contributions, e.g. the well known Park-Ang index, Park and Ang [190]. In the former damage includes a cyclic deterioration controlled by the energy dissipation and a deterioration due to the softening branch of the backbone curve, Figure 3.5. In the latter, damage index is a linear combination between a strain parameter and an energy one, equation 3.3.

$$DM = \frac{\delta_M}{\delta_U} + \frac{\hat{\beta}}{F_y \delta_U} \int dE \tag{3.3}$$

where DM is a damage index, δ_M is the maximum displacement under earthquake, δ_U is the maximum displacement under a monotonic load, and $\hat{\beta}$ is a structural performance parameter. In practice, the parameters δ_U and $\hat{\beta}$ of this cumulative damage model are analogous to the capping point δ_C and dissipation capacity λ of the deterioration model proposed by Ibarra.

Backbone curve and cyclic behavior depend on seven parameters, namely M_y, K_e, M_c/M_y, $\theta_{cap,pl}$, θ_{pc}, λ and c, as indicated in Figure 3.5. The model allows also to include a residual

strength; for steel members a value higher than zero is recommended, Lignos [156], while for RC members the parameter is typically close to zero. Other details, especially for non-ductile members, can be found in Krawinkler and Lignos [138]. Finally, recommendations concerning the modeling of the nonlinear behavior of structural members can be found also in the FEMA P695 report, FEMA P695 [86].

The parameters listed above have been calibrated considering 255 experimental tests on RC columns; a regression analysis has been subsequently performed in order to develop empirical equations used as input for the modeling of the nonlinear springs. A comprehensive and deep investigation about this procedure can be found in Haselton [112]. In particular the data come from the study on rectangular columns included in the PEER Structural Performance Database (Berry et al. [24]), where the performance of members with ductile and non-ductile detailing have been examined; among this large set of data, 220 columns failed in a flexural mode, while the remaining in a flexural-shear mode, due to lack of seismic detailing. All the parameters investigated cover the practical range of values, including axial load ratio, strength of the concrete, longitudinal and transversal steel ratio.

To calibrate element model parameters, columns have been studied as cantilever columns through OpenSees platform (Mazzoni et al. [163]), dividing each element into three parts: two nonlinear rotational springs at both ends and an elastic element in between, Figure 3.4a. The object of the calibration procedure was the definition of the parameters of the nonlinear springs. Main attention has been given to a proper calibration of the capping point and post-capping strength deterioration, because these factors have a strong impact in the evaluation of collapse capacity, Liel [153]. In particular, as clearly indicated in Figure 3.6, two different types of deterioration can be identified, namely *in-cycle strength degradation* and *cyclic strength degradation*. The former induces a decrease in the strength within the same cycle or, in other words, the element has a negative stiffness; the latter is related to a decrease in the strength considering two subsequent cycles of deformation, but the stiffness is always positive. It is extremely important to keep separated these two sources of deterioration in order to avoid mistakes in the modeling; e.g. in Figure 3.6a it is shown the correct procedure, where both modes of deterioration are included, while in Figure 3.6b the wrong modeling appears, since only the in-cycle deterioration is activated in order to simulate the behavior of the cantilever column. Such an approach has a deep consequence in the estimation of collapse capacity; in Haselton [112] it is shown how probability of collapse for SDOF systems subjected to earthquakes changes if the sources of deterioration are not properly taken into account.

The result of the calibration procedure is a set of empirical equations to estimate the main parameters involved in the definition of the properties of the nonlinear spring used in the modeling. In Haselton [112] these equations have been compared with the results of previous research, e.g. Panagiotakos and Fardis [187], in order to highlight advantages and limitations of such procedure. In the following a review of the equations developed is presented; for each of

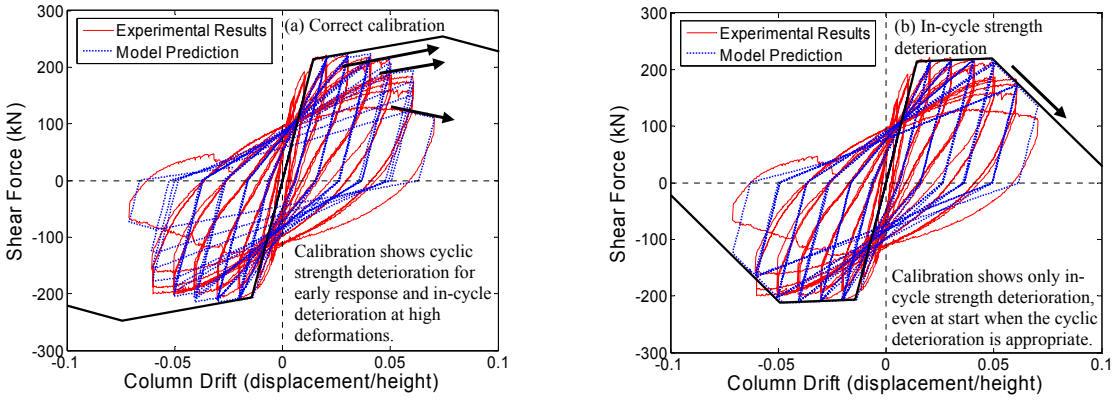

(a) Correct calibration.

(b) Wrong calibration.

Figure 3.6: Illustration of two types of calibration for a cantilever column (after Haselton [112].)

them not only the central value is given (the outcome of the equation) but also the dispersion. This factor is very important for the probabilistic approach that it will be illustrated in the next sections.

Effective stiffness

Due to the effect of cracking, the stiffness of RC members depend on the load applied. Equation 3.4 gives an estimate of the secant stiffness to yield, depending on the axial load ratio ν and the shear span ratio L_s:

$$\frac{EI_y}{EI_g} = -0.07 + 0.59\left[\frac{P}{A_g f_c}\right] + 0.07\left[\frac{L_s}{H}\right] \qquad 0.2 \leq \frac{EI_y}{EI_g} \leq 0.6 \tag{3.4}$$

where $\nu = P/(A_g f_c)$, I_g is the inertia of the gross section and H is the length of the member. About dispersion of the results, considering a lognormal distribution, the logarithm of standard deviation $\sigma_{LN} = 0.28$. The expression takes into account not only the flexural behavior but also an additional flexibility due to shear and bond-slip. The lower and upper limits depend on the experimental data, since for the lower bound few cases with low axial load have been found, while for the upper one the scatter tends to increase increasing the axial load. The estimation of the initial stiffness of the member is not a trivial issue, and a lot of research has been done in this field. In FEMA 356 (FEMA 356 [84]) approximated procedures are allowed, in particular using $0.5EI_g$ if the axial load ratio is lower than 0.3 and $0.7EI_g$ if $\nu > 0.3$. Other recommendations can be found in Priestley et al. [203], where it is explained that one of the fundamental problem of the *force-based design* is the choice of the appropriate stiffness for the element members.

Moment at yielding

Moment at yielding M_y is evaluated through a moment-curvature analysis of the section, in order to include the confinement effect due to the transversal steel; within the core of the sections, see Figure 3.1, the equations of Mander (Mander et al. [158]) are used in order to include an increase in strength and ductility. Another possibility is to compute the flexural strength considering the procedure proposed by Panagiotakos and Fardis, Panagiotakos and Fardis [187].

Capping rotation capacity

Plastic rotation θ_{cap} is estimated as indicated in equation 3.5; the uncertainty on the results has a logarithmic standard deviation $\sigma_{LN} = 0.45$. This parameter is affected mainly by the axial load ratio $\nu = P/(A_g f_c)$ and by the transversal steel ratio ρ_{sh}; other parameters of interest are the strength of concrete f_c and the longitudinal steel ratio ρ. In equation 3.5 a_{sl} is an index equal to 1 or 0 depending if reinforcing bar slip is included in the rotation capacity or not; because slip usually occurs $a_{sl} = 1$.

$$\theta_{cap} = 0.12(1 + 0.4a_{sl}) \cdot 0.2^{\nu} \cdot (0.02 + 40\rho_{sh})^{0.52} \cdot 0.56^{0.01 f_c} \cdot 2.37^{10\rho} \tag{3.5}$$

It is important to highlight that equation 3.5 has been calibrated just considering columns with a symmetric layout of reinforcement; in principle such equation cannot be applied to beams, due to their unsymmetric arrangement. If the element is loaded in such that the side with more steel is in tension the rotation capacity is smaller since, due to equilibrium, the concrete is subjected to larger compressive stresses and strains, Haselton [112]. In order to overcome this limitation, the same coefficient computed by Fardis and coworkers (Fardis and Biskinis [83]) analyzing columns with generic reinforcement arrangement is used, equation 3.6. In the present investigation only columns have a nonlinear behavior, so apparently this coefficient is not necessary (columns are symmetric); however, due to the unsymmetric diffusion of chlorides on the cross-sections, reinforcement layers in the columns have different rates of corrosion. In this way, during time, backbone curve of the nonlinear spring tend to have an unsymmetric behavior. The expression for Fardis' coefficient is:

$$\text{Coeff}_{\text{Fardis}} = \left[\frac{\max\left(0.01, \frac{\rho' f_y}{f_c}\right)}{\max\left(0.01, \frac{\rho f_y}{f_c}\right)} \right]^{0.175} \tag{3.6}$$

where ρ and ρ' are the longitudinal steel ratios in the tension and compression side respectively.

Post capping rotation capacity

This parameter plays an important role in the prediction of the collapse capacity; the proposal equation is:

$$\theta_{pc} = (0.076)(0.031)^{\nu}(0.02 + 40\rho_{sh})^{1.02} \leq 0.1 \tag{3.7}$$

where ν is the axial load ratio, ρ_{sh} is the transversal steel ratio and the logarithm of the standard deviation $\sigma_{LN} = 0.72$. The upper bound comes from the lack of reliable data for elements with shallow post-capping slopes, Haselton [112] and Liel [153]; according to the authors the value should be conservative considering cross-sections well confined.

Post-yield hardening stiffness

Hardening slope is described in terms of ratio between capping and yielding moment, M_c/M_y; axial load and concrete strength are the most significant parameters, and the outcome of the regression analysis is equation 3.8:

$$M_c/M_y = (1.25)(0.89)^{\nu}(0.91)^{0.01 f_c} \tag{3.8}$$

where the dispersion of the data is described by $\sigma_{LN} = 0.10$. Considering a typical range for f_c and ν, the ratio predicted by equation 3.8 comes from 1.11 to 1.22; in order to simplify the problem, a constant value equal to 1.13 is recommended.

Cyclic energy dissipation capacity

This factor is related to the deterioration of strength and stiffness of the spring during nonlinear analysis. In particular, with reference to the Ibarra model, Ibarra et al. [121], four modes of cyclic deterioration are considered, namely basic strength deterioration, post-cap strength deterioration, unloading stiffness deterioration and accelerated reloading stiffness deterioration. Theoretically for each of them a dissipation energy capacity λ and an exponent term c used to describe the rate of deterioration is assigned. To simplify the estimate, for each mode the same factor λ is applied, and a value $c = 1$ is used (there is the hypothesis that all modes have the same rate of deterioration). The predicted equation for energy dissipation capacity is shown in 3.9:

$$\lambda = (127.2)(0.19)^{\nu}(0.24)^{s/d}(0.595)^{V_p/V_n}(4.25)^{\rho_{\mathrm{sh,eff}}} \tag{3.9}$$

where s/d is the ratio of stirrup spacing to column depth, $\rho_{\mathrm{sh,eff}}$ is the effective transversal steel ratio and V_p/V_n is the ratio of shear at flexural yielding to shear strength. Last term is evaluated according to equation 3.10, Kramar [135]:

$$
\begin{aligned}
V_p &= M_y/L_s \\
V_n &= V_c + V_s \\
V_c &= 0.0166\sqrt{f_c}hd \\
V_s &= A_{sh}zf_y/s
\end{aligned}
\tag{3.10}
$$

With the predicted equations listed above the nonlinear springs applied at the ends of the structural members in the frames investigated can be calibrated, in order to perform nonlinear simulations exploiting two different seismic analysis methods, highlighting pro and contra of the two approaches.

3.4 Validation of the model used

The analytical model of the nonlinear spring illustrated in the previous section is very effective in the prediction of collapse behavior of RC frames, Goulet et al. [105]; anyway, all the applications described in literature regard frame systems with moment-resisting connections and not precast buildings, where the joints between columns and beams are typically modeled as hinged connections ("strong connections"). SAFECAST project gave the opportunity to test the Ibarra model also for this kind of structures. In particular, as anticipated in Chapter 1, the prototype experimentally studied allows different structural schemes, from shear wall system to emulative frame. One of the task of the research is therefore the numerical simulation of pseudo-dynamic tests in order to understand the seismic behavior of different kind of connections and the overall performance of the prototype. Here, results regarding frame with hinged connections (Model 2 in Figure 1.8) are shown.

Because experimental program at the ELSA Laboratory involved different pseudo-dynamic tests (one or two for each structural scheme), it has been decided to bound the intensity measure in order to avoid extended damage at the beginning of the champaign, so to study in a deep way the performance of all the schemes. Only for the last frame, Model 4 in Figure 1.8, also a cyclic test up to collapse has been performed. For sake of brevity, the results on Model 2, considering a PGA equal to $0.15g$, are illustrated. After a preliminary phase selection, nonlinear dynamic analyses has been carried out with reference to the Tolmezzo accelerogram, modified in order to match the Eurocode 8 spectrum for soil class B, EC8 [74]. Figure 3.7 shows the input motion (scaled up to $1g$) and the corresponding response spectrum.

Both a distributed plasticity model (see Figure 3.3) and a concentrated plasticity one (Figure 3.4) have been implemented for the numerical simulation. Because the low seismic intensity reached in the pseudo-dynamic test, it is expected that fiber model allows a better estimation of the response, Liel et al. [154]; if structural members do not go deeply in the nonlinear range, a model where plasticity is spread for the entire length is capable to capture

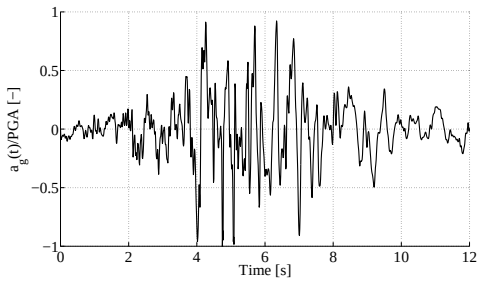

(a) Modified Tolmezzo accelerogram.

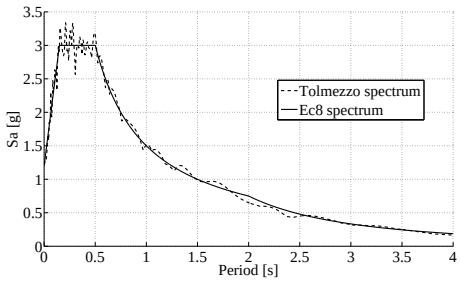

(b) Response spectrum compared with EC8 spectrum for soil class B.

Figure 3.7: Ground motion input used in SAFECAST project.

basic deterioration of the concrete due to his higher refinement. Although the use of nonlinear spring at the end of the elements gives results with a lower accuracy, the intent of this validation is to show that also this approach allows to catch the main characteristics of the response. With such validation, it possible to extend the use of the Ibarra model for the archetypes of the precast frames studied in the present investigation.

Figure 3.8 shows the response of Model 2 (hinged connections) to an input motion with a PGA equal to $0.15g$ in terms of story displacements. As explained before, distributed plasticity model predicts in a better way the seismic behavior; however, also the concentrated plasticity model catches the important features of the response. As it can be seen, the phase (at least until 10 seconds) is correct, as well as the peak displacements. For both modeling, at the end of the ground motion there is a delay in the response between numerical simulation and experimental test, probably for the activation of the nonlinear behavior of the connections, here represented simply with perfect hinges.

To overcome this problem, the model has been improved including nonlinear springs between columns and beams, as indicated in Figure 3.9a. In particular the hysteretic material included in OpenSees library (Mazzoni et al. [163]) has been applied on the basis of the available data on the connections. Figure 3.10 highlights the different accuracy in the prediction of story displacements for fiber model without or with the nonlinear modeling for the connections, when the frame is subjected to an earthquake with $PGA = 0.3g$.

The research on the seismic performance of connections in precast frames is not completed yet, and further investigations are needed to clarify the actual behavior of beam-to-column hinged joints. However, these results illustrate the effectiveness and accuracy of the numerical modeling. In the following, the lifetime behavior will be studied based on the models above described.

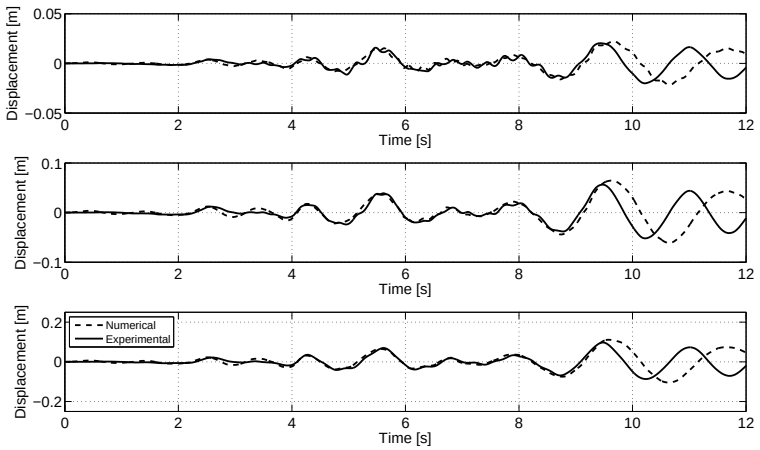

(a) Distributed plasticity model.

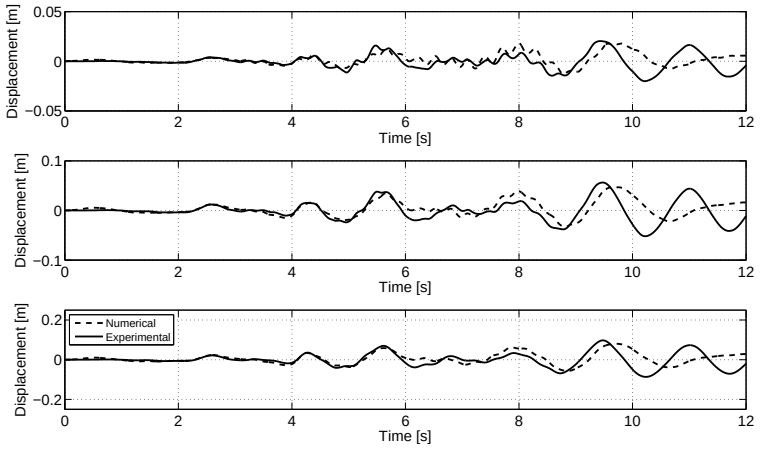

(b) Concentrated plasticity model.

Figure 3.8: Prediction of story displacements for Model 2, $PGA = 0.15g$.

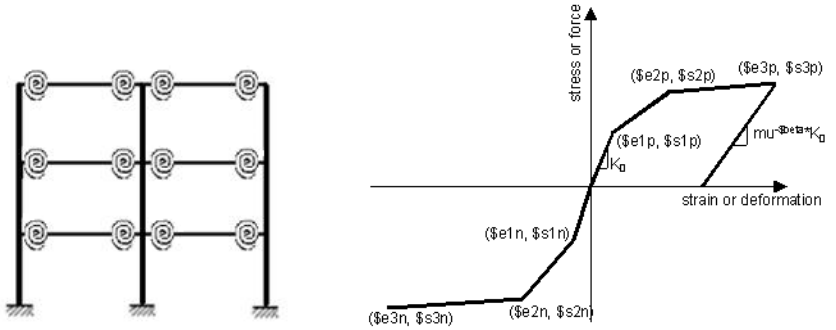

(a) Model 2 with nonlinear springs for the modeling of the connections.

(b) Hysteretic law adopted, Mazzoni et al. [163].

Figure 3.9: Modeling of nonlinear behavior for connections.

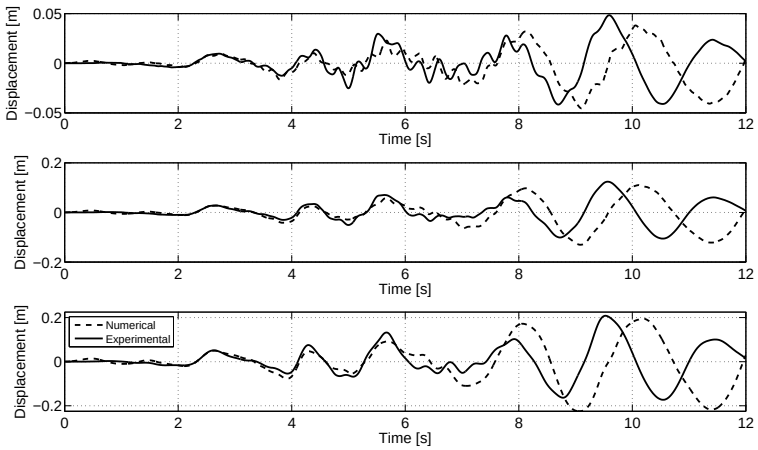

(a) Fiber model, perfect hinges.

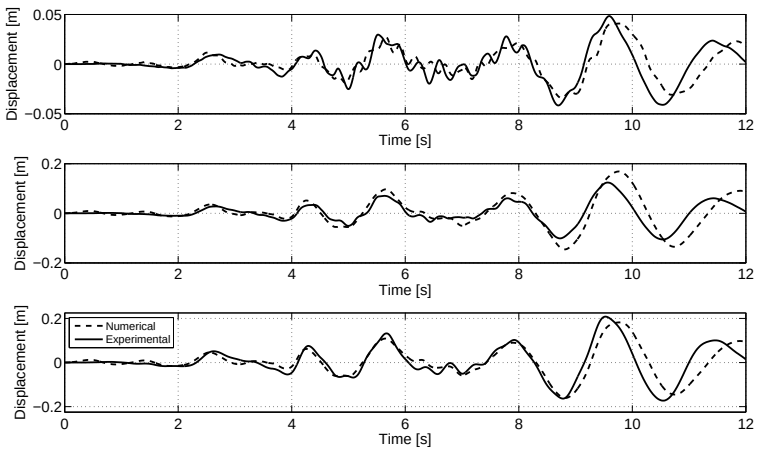

(b) Fiber model, hysteretic law for the connections.

Figure 3.10: Prediction of story displacements for Model 2, $PGA = 0.3g$.

3.5 Numerical simulation via Incremental Dynamic Analysis

Among different methods to assess the seismic performance of different structural systems, nonlinear dynamic analysis is recognized the most reliable one, even if computational costly, Clough and Penzien [58], Chopra [55], Elnashai et al. [77] and Datta [64]. Typically, one set of accelerograms (natural or artificial) is selected, the dynamic analyses run and for each of them the performance of the structure is investigated considering some key factors (e.g. the top displacement, hysteresis loops at the base on the columns, etc ...). Depending on the intensity level of the record chosen, the system can have an elastic behavior or going deeply in the nonlinear range; from the other side, the use of a nonlinear static analysis gives, in a static way, a complete picture of the performance of the structure, from limited damage up to collapse. The idea on the base of the incremental dynamic analysis, Vamvatsikos [232], Vamvatsikos and Cornell [234], and Vamvatsikos and Cornell [236] is to multiple dynamic analyses on the same structure, scaling each time the intensity, in order to cover the full behavior. Some codes, e.g. FEMA P695 [86], recommend this method for the assessment of the global collapse capacity of the structures; due to the growth of computer computational power, this procedure is become widely available. Moreover, first applications using a parallel processing are emerging in literature, Vamvatsikos [233]. It is also worth noting that this approach is well-suited with the performance-based earthquake engineering, Vamvatsikos and Cornell [235], since all the limit states of interest can be easily evaluated.

Before performing an incremental dynamic analysis, two quantities must be selected, namely the intensity measure (IM) and the damage measure (DM). Intensity measure is a non-negative parameter used to scale up the records, while a damage measure is a non-negative parameter able to characterize the seismic response of the structure; another problem concerns the implementation of the algorithm to perform IDA, which should be reliable and effective. To this purpose, next sections review these important issues, while details can be found in Vamvatsikos [232]. The outcome of the procedure is the IDA curve, which is a plot of a state variable (DM) recorded in an IDA study versus one or more IMs that characterize the applied scaled accelerogram, Vamvatsikos and Cornell [234]. Finally, because one single IDA curve cannot represent in a suitable way the complete behavior of structure, from elastic range up to collapse, a suite of accelerograms must be used, in order to explore the variability of the performance and to develop statistics on the response. As an example, Figure 3.11 shows a collection of 30 IDA curves.

3.5.1 Selection of ground motion input and choice of intensity measure

Different metrics are used in order to represent seismic intensity, considering scalar quantities or vector values. Typically PGA is exploited due to his simplicity; however this quantity is connected only with the ground motion characteristics and not with the response of the

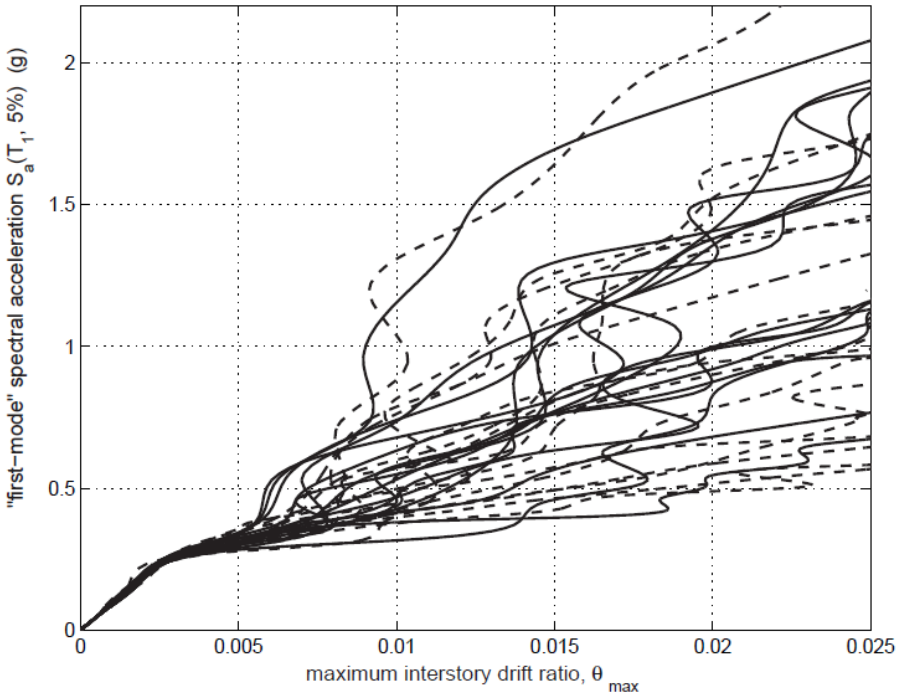

Figure 3.11: Example of IDA study for 30 records, Vamvatsikos [232].

structure, so it does not contain information on the system studied. To overcome this problem, researchers in last years have proposed the use of the pseudo-spectral acceleration evaluated at the fundamental period ($S_a(T_1)$), see e.g. Zareian and Krawinkler [249] and Liel et al. [155]. This choice typically performs better than the use of PGA, but it required that the fundamental period, namely the first, is the most important period resulting from a modal analysis; if higher modes play a key role in the overall behavior of the structure (e.g. for tall buildings with long periods), maybe this choice is not the proper one.

Other researchers have also proposed vector quantities to represent intensity measure, namely $[S_a(T_1), \varepsilon]$, where ε is a measure of the difference between $S_a(T_1)$ and the median of spectral acceleration predicted by the attenuation law with reference to T_1. In practice ε is an indicator of the spectral shape; details can be found in Baker and Cornell [18] and Baker and Cornell [19]. Moreover, it has been shown that the practice of scaling up ground motions without consideration of ε is likely to result in overestimation of the demand on the structure. A comparison of the adequacy of alternative ground motion intensity measures for the estimation of structural responses can be found in Giovenale et al. [98], while in Appendix A a list of different ground motion indices proposed in the last decades is shown.

Regardless the intensity measure, in any case the recommendation is to choose a sufficient and efficient one, Pinto [196], that means low variability; low variability of the candidate implies that the median response of the structural analysis can be estimated more efficiently. Among the pool of intensity measure available, usually the PGA or the spectral acceleration

at the fundamental period ($S_a(T_1)$) are used, and the last one tend to have a small dispersion. However, peak ground acceleration is selected as the IM candidate in present investigation in order to simplify the problem, because the spectral acceleration $S_a(T_1)$ is not a trivial IM since the period of the structure differs from model to model due to introduction of modeling uncertainties required for the probabilistic approach, Dolšek [69]. Moreover, there are other two issues regarding the final choice of the IM value. One it is the nature of the ground motion adopted, since using of artificial accelerograms also PGA has a low dispersion. The second is the type of structures investigated (precast systems with medium to long periods); in this case the choice of the spectral acceleration at the fundamental period could not be so appropriated.

Another big challenge in order to perform nonlinear dynamic analyses is the selection of the ground motion input, Iervolino and Cornell [122]; in literature there are essentially three approaches, and the main characteristics of each of them are reviewed in the following. It is also important to remember that seismic codes such as Eurocode 8 (EC8 [74]) and Italian code (NTC 2008 [181]) assume spectral compatibility to the elastic design spectrum as the main criterion. However, due to the availability of strong motion recordings, the use of natural accelerograms is become popular in the last years, Elnashai et al. [77]. On-line databases can be exploited to select an appropriate suite of records, depending on the site of interest; examples are the European Strong Motion Database (http://www.isesd.hi.is/ESD_Local/frameset.htm) and the PEER NGA Database (http://peer.berkeley.edu/products/strong_ground_motion_db.html). Clearly they provide a realistic seismic input to the structure, but typically the main drawback is the low compatibility of their response spectrum with that prescribed by the code so, in order to get reliable information, a large set of accelerograms should be selected.

To overcome this problem, in last years great effort has been done in order to develop a robust strategy for the selection of a set of natural records complying the EC8 spectra, Iervolino et al. [123]. The result of this research has been REXEL (Iervolino et al. [125]), a computer program that provides a suitable set of accelerograms compatible with a code spectrum, given as input the characteristics of the site of interest (e.g. class type of the soil, a range of magnitude and distance, etc ...). Regarding ground motion input selection, other recommendations can be found in FEMA document (FEMA P695 [86]); in particular it is suggested that the standard deviation of the natural logarithm of the spectra should be around 0.5 for short periods and 0.6 for long periods. Even if in this study artificial earthquakes are used, as explained later, preliminary considerations has been done also with reference to natural records; in particular, using REXEL, a set of 20 ground motion inputs from European Strong Motion Database has been selected, Ambraseys et al. [8], with reference to a soil class B. Figure 3.12 shows their response spectrum and standard deviation of the natural logarithm. As we can appreciated in Figure 3.12a, the variability of the accelerograms is high, but the mean spectrum match very well the prescribed one.

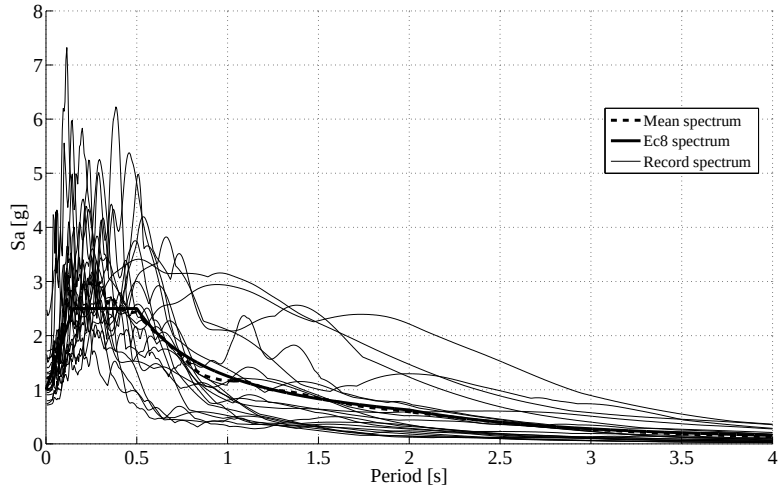

(a) Elastic spectrum of recorded earthquakes, mean value and EC8 spectrum for soil claa B.

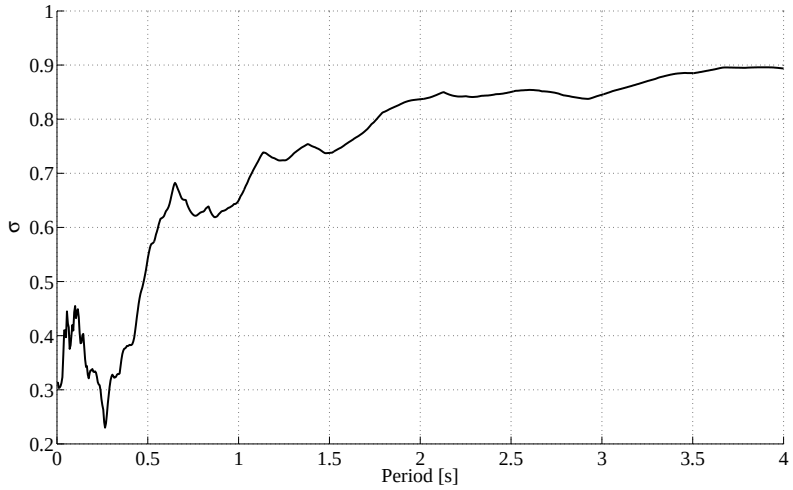

(b) Standard deviation of the logarithm of the spectra.

Figure 3.12: Response spectra and their dispersion for recorded accelerograms.

Another possibility available in literature is to couple the selection of recorded earthquakes with a *wavelet transform* that modifies the signal and provides a good match with the prescribed response spectrum, Gurley and Kareem [108], Mukherjee and Gupta [174] and Hancock et al. [111].

On the other side, artificial accelerograms can be employed; generation is based on random vibration theory, Bendat and Piersol [23], modifying iteratively the Fourier amplitude spectrum of each accelerogram generated in order to match the prescribed spectrum. The most widely used approach is to develop a stationary signal with a constant power spectral density (*white noise signal*), subsequently enveloped in a trapezoidal shape to simulate the non-stationary characteristics of ground motion. Adapting iteratively the amplitudes of the corresponding Fourier spectrum, a very good match with the code spectrum can be reach, also for the single signal; the procedure is described in Clough and Penzien [58], and the well-known computer program SIMQKE (Gasparini and Vanmarcke [95]) works in this way. Using this methodology the signals have a frequency content higher than that of realistic earthquake and are unrelated to the physics of earthquake stress wave generation and propagation, Elnashai et al. [77]; the consequence is usually an unrealistic demand on the systems studied, with a cyclic response overestimation.

An improvement can be reached considering non-stationary signals, that are based on physical parameters of an earthquake (e.g. magnitude and distance) but typically are not compatible with a prescribed spectrum. Following the work of Sabetta and Pugliese (Sabetta and Pugliese [215]), where attenuation laws of response spectra have been developed using Italian strong motion data in order to simulate artificial earthquakes as a function of magnitude, distance and site geology, in Mucciarelli et al. [173] a computer program named BELFAGOR has been developed. It consists of two steps: in the first one, a synthetic accelerogram is generated, for which time length, amplitude and distribution of phases depend on magnitude and distance of the event considered. Finally, an iterative procedure adjusts the amplitudes of the spectrum in order to match the prescribed one. According to the authors the signal obtained is more realistic than a pure artificial earthquake, and the frequency content is close to that of a natural earthquake. In Pousse et al. [200] an improvement of the Sabetta and Pugliese model is presented, adopting a stochastic procedure able to model also the ground-motion natural variability.

A comparison on the use of different types of ground motion input can be found in Iervolino et al. [124], where nonlinear dynamic analyses have been performed on SDOF systems with both non-degrading and degrading behavior, highlighting the peculiarity of each choice; in particular, as just mentioned before, if the cyclic response is considered, artificial record classes show a significant overestimation of the demand.

For the present investigation SIMQKE program (Gasparini and Vanmarcke [95]) has been used to generate a set of 25 earthquakes that match very well the Eurocode 8 spectrum for soil

class B, Figure 3.13a; in particular, following the recommendations in seismic codes (EC8 [74] and NTC 2008 [181]), each ground motion has a length at least equal to 25 s and a stationary interval $\Delta t \geq 10$ s. In order to increase the variability, three classes are considered, namely:

1. 10 earthquakes with a total length of 25 s and a stationarity interval of 10 s;
2. 10 earthquakes with a total length of 30 s and a stationarity interval of 12 s;
3. 5 earthquakes with a total length of 40 s and a stationarity interval of 15 s.

Since each accelerogram matches very well the code spectrum due to the generation procedure, the variability is not so high, as can be seen in Figure 3.13b, where the logarithm of the standard deviation of the spectra is shown. The values are lower than the limit recommeded by FEMA P695, FEMA P695 [86]. It is clear that such procedure to develop artificial accelograms is completely detached from the physical parameters of a ground motion, leading to a higher loading on the structure with respect to realistic input motion but, as explained in Kramar et al. [136], "... applied loading is more critical than the actual loading at a given site; hence, the final results should be conservative.". Moreover, artificial earthquakes have been successfully employed in another research of the seismic performance of precast structures, Biondini and Toniolo [32].

3.5.2 Choice of the damage parameter

Second important issue when an incremental dynamic analysis is performed is the choice of a suitable damage measure DM that can be easily evaluated and allows to give reliable information on the performance of the system studied. In literature there are different proposals, considering both local and global parameters; possible choices are e.g. maximum base shear, maximum top displacement, cumulative hysteretic energy, Park-Ang index (Park and Ang [190]), maximum floor acceleration, maximum interstory drift. None of the parameters listed above is the best solution; if the focus is on the potential damage of non-structural elements, peak floor accelerations are the natural choice, while for potential damage of structural elements, the displacement approach seems better than the force one, Priestley et al. [203]. To this aim, maximum interstory drift becomes a good choice, where the interstory drift θ is defined as the ratio between interstory displacement and interstory height, $\theta = \Delta x / \Delta h$; in this way also local collapse mechanism can be recognized ("weak story"). This approach is reflected also in the definition of the limit states; in past years seismic code such as FEMA 356 (FEMA 356 [84]) gave recommended values of maximum interstory drifts depending on the limit state considered, from limited damage up to near collapse, and on the type of structural system, e.g. concrete or steel frame, wall building and so on.

Recently, new perspective are emerging, with the intention to define limit states at a local level (for example reaching of yielding or capping point) and then translate them to a global

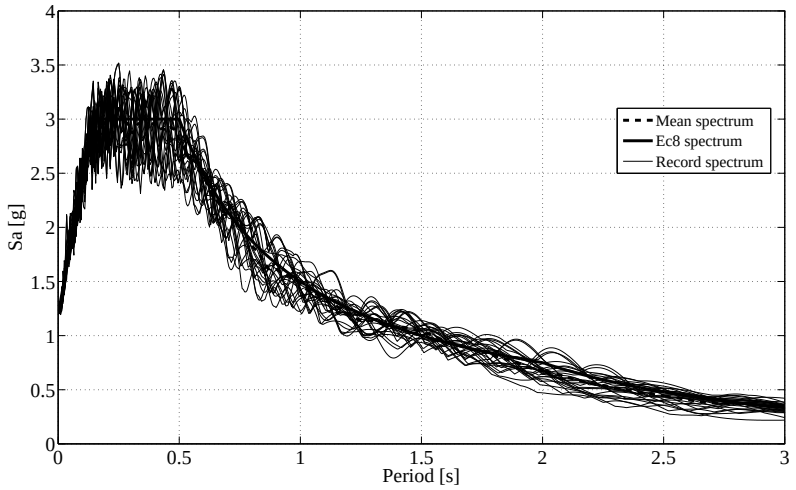

(a) Elastic spectrum of artifical earthquakes, mean value and EC8 spectrum for soil class B.

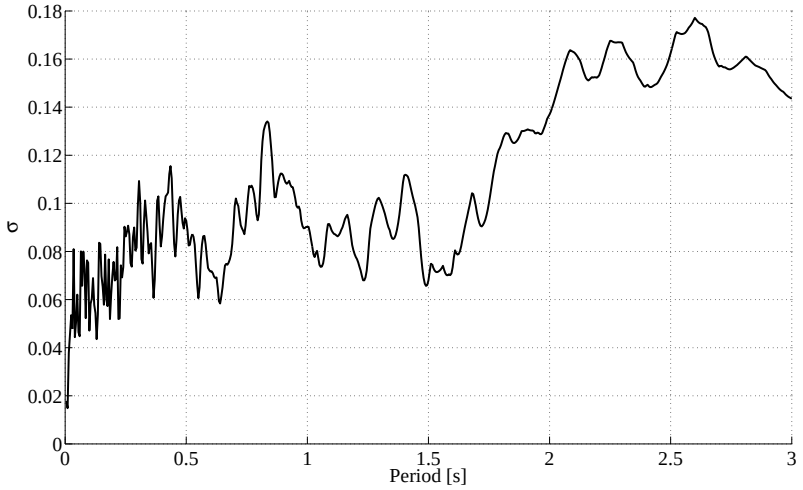

(b) Standard deviation of the logarithm of the spectra.

Figure 3.13: Response spectra and their dispersion for artificial accelerograms.

level, Dolšek [70]. The advantage of this methodology is to identify in a reliable way the conditions at which damage effectively occurs; using the old approach, values suggested could be accurate enough for a particular category of structures but not for others; for example, threshold values given by FEMA 356 for concrete frames may be too low for precast frames, because usually this kind of system is more flexible than the emulative one. In the present investigation both methods are implemented; the first one is used only in a preliminary phase, with the purpose to select the proper sample size for the probabilistic approach. The second one will be used for the risk analysis.

3.5.3 Practical tools for IDA

To conclude this brief review on incremental dynamic analysis, the procedure on how to interpolate IDA curves and the algorithm implemented are summarized. Due to high computational cost required, it is not feasible to perform tens of nonlinear dynamic analyses for each earthquake; usually 10 to 20 runs are employed, so the IDA curve is based on this reduced number of points. A proper post-processing of the results allow to enrich the curve without performing other analysis, in order to extrapolate the IM and DM values for the entire range of performance, from elastic behavior up to collapse. Discrete points can be interpolated using a piecewise linear approximation or a spline interpolation; the latter one provide the better results, Vamvatsikos and Cornell [236]. There are two possible options: extrapolate values of IM given DMs, or extrapolate values of DM given IMs; looking at the outcome of IDA, see Figure 3.11, each curve can have alternatively hardening and softening branches until collapse is reached (flatline of the curve). To this aim, for a given IM only one value of DM is returned; viceversa the relationship between DM and IM is not monotonic, so for a sigle DM can correspond more IM values. Due to these considerations, the IM approach is followed; an example of the fitting of an IDA curve can be seen in Figure 3.14.

Despite to the simplicity of the idea at the base of an IDA investigation, his implementation is not so straightforward; in particular, as indicated in Vamvatsikos and Cornell [234], two issues should be preserved, namely *demand* and *capacity resolution*. First one means that the gap between two adjacent IM values should not be higher than a certain tolerance, in order to spread the data almost equally for the entire range. Second one means that a concentration of points is necessary around collapse point in order to bracket it properly. To this reasons a simple *stepping algorithm* is not a good choice; exploiting this procedure a predefined step value for IM is chosen, and the accelerogram is subsequently scaled up until collapse is reached. Clearly the method is not optimized because a certain IM step value could be effective for some earthquake and not for others, that is some IDA curves could be rich enough and others not.

A better choice is to introduce a searching technique, in order to balance the distribution of runs for each record; in particular a *hunt & fill* algorithm is implemented. After a first

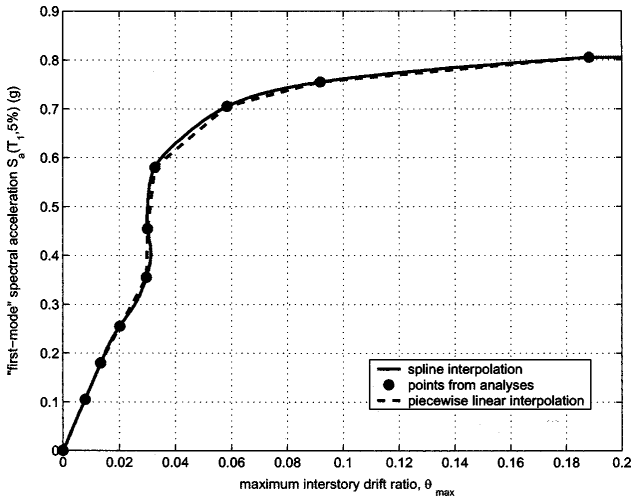

Figure 3.14: Interpolation of an IDA curve, Vamvatsikos and Cornell [236].

elastic analysis, using a very low intensity, the IM is scaled up in order to reach in few runs the collapse point. Subsequently, a bisection method is applied, in order to bracket the collapse, within a certain tolerance, selecting an IM value between the highest non-collapsing point and the lowest one. Finally, the fill phase fits the curve, in order to have gap between all the non-collapse points below a certain tolerance. For example, in the present study a 2% of tolerance for the bracket phase and a maximum gap between adjacent IM values equal to $0.10g$ are chosen. Readers interested can find other details in Vamvatsikos and Cornell [234], Vamvatsikos and Cornell [236] and Buratti [46]; the entire procedure is illustrated from Figures 3.15 to 3.17.

Finally, care is required in the use of solution schemes, because systems are deeply pushed into the nonlinear range up to global failure. Here collapse is seen as loss of dynamic equilibrium, so the system is not able to sustain vertical loads, and the IDA curve reaches a flatline; because algorithm can encounter in non-convergence solutions, different procedures are employed (e.g. Newton-Raphson with line search, Modified Newton scheme, Broyden method), eventually reducing the convergence tolerance. A description of these methods can be found in Zienkiewicz and Taylor [251], while in Liel et al. [154] their use in IDA is illustrated.

3.6 Numerical simulation via Pushover Analysis

In the previous section the steps required to perform an incremental dynamic analysis have been illustrated. It is well-recognized that a nonlinear time history analysis is the best approach to assess the seismic performance of a generic structure, Chopra [55], however, as explained before, careful is needed in order to have reliable results. In particular the choice of the input motion is the main issue, and the implementation of IDA is not so straightforward for the practitioners. Due to above considerations, in last years the use of nonlinear static procedures

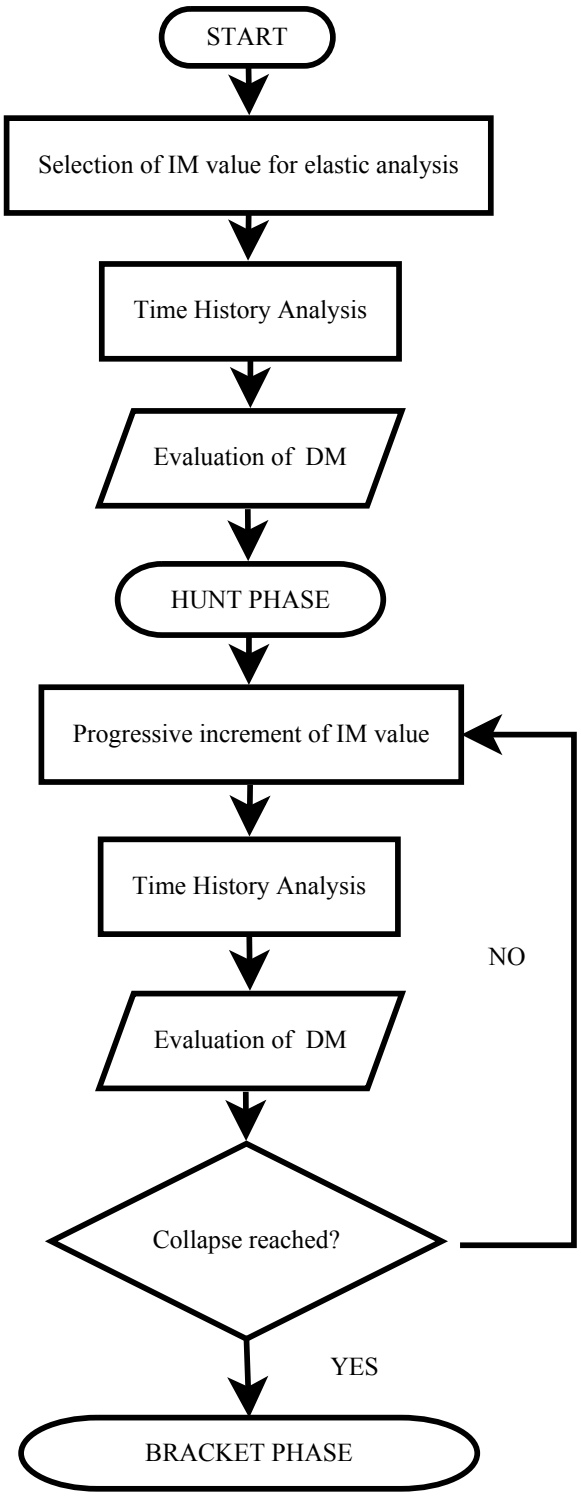

Figure 3.15: Flow chart for performing IDA (1 of 3).

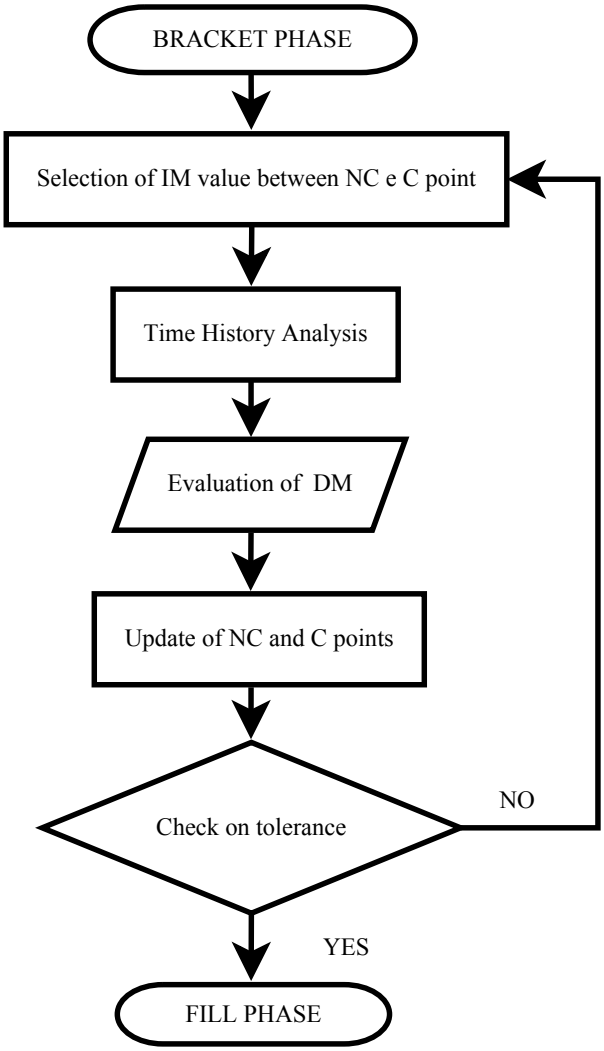

Figure 3.16: Flow chart for performing IDA (2 of 3).

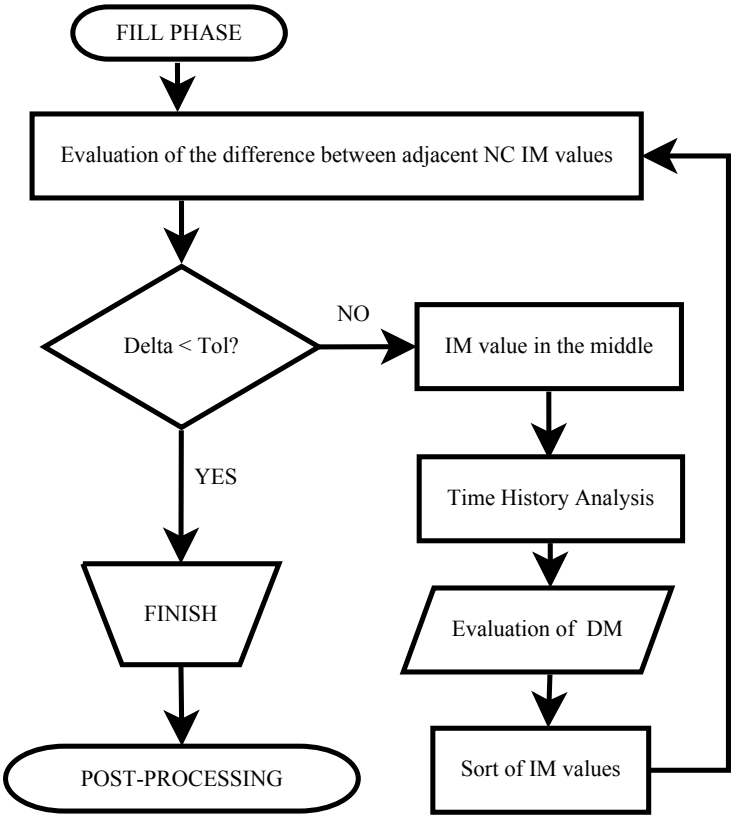

Figure 3.17: Flow chart for performing IDA (3 of 3).

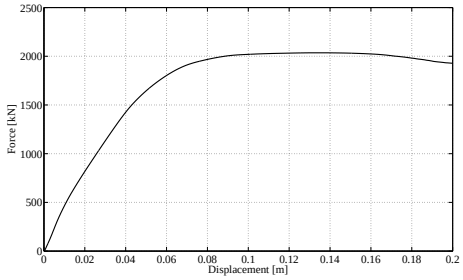

Figure 3.18: Example of a pushover curve for a multistory building.

is emerging; a review of different approaches available can be found in FEMA 440 [85]. The common idea is to "push" the structure with a particular load pattern, in order to cover the complete range of behavior, from elastic up to severe damage. Because the analysis is static the computational cost is lower, however careful is needed in the modeling of the nonlinear behavior of structural members and in the shape of load pattern applied.

In particular, second point represents the main issue involved in such method, and different proposals are available in literature. Usually an invariant force pattern is applied to the structure, for which there is the hypothesis that inertia forces remain constant throughout the ground motion; as indicated in Krawinkler and Seneviratna [139] this is true if the structure is mainly controlled by the fundamental mode and has one single yielding mechanism. If different failure modes are expected or higher modes play an important role, at least two load patterns should be used, e.g. a uniformly distributed one and an inverted triangular one, proportional to the first modal shape. A comparison between pushover and dynamic analysis can be found also in Mwafy and Elnashai [176], where it is suggested that the use of pushover analysis can be appropriate in particular for low rise and short period frame structures, and meaningful information can be extrapolated taking care of modeling and choice of the load pattern.

The outcome of a pushover analysis is the so called *pushover curve* or *capacity curve*, which is a plot of the total base shear at the base of the system depending on the top displacement, Figure 3.18; this format is particularly meaningful since allows to visualize the global "yielding point" of the structure, corresponding to the point where the slope has a sudden drop, and the global ductility, which it can be defined as the ratio between the ultimate displacement and the yielding one. Usually ultimate displacement is estimated as the displacement refers to a 20% drop of base shear with respect to the maximum value. Finally, pushover curve can be seen as the hysteretic backbone curve of an equivalent SDOF system, which represents approximately the global behavior of the original MDOF system.

As indicated above, the main limitation of a standard pushover analysis is the inability to take into account the effect of higher modes and variation of load pattern due to the stiffness deterioration of structural members when subjected to an earthquake. To this purpose, in past years attempts have been done in order to improve the methodology. Considering the influence

of higher modes, Chopra and Goel (Chopra and Goel [56]) proposed a modal pushover analysis (MPA); the idea is to push the structure with different load patterns coming from modal analysis, transform each pushover curve in a SDOF system, compute the target displacement for each of them, finally evaluating the target displacement of the original MDOF system by using a modal combination analysis, such as SRSS. In his original format the method allowed only the estimate of displacement parameters for regular buildings, but subsequently improvements have been made to include also the estimation of member forces (Goel and Chopra [103]), application for irregular buildings (Chopra and Goel [57]) and other structures like bridges (Paraskeva et al. [188]). Since the method is based on a decoupling of modal properties also in the inelastic range, reliable results can be found if the structure does not go deeply in the nonlinear range of behavior. Moreover, each load pattern is assumed constant during the analysis.

To overcome this problem, adaptive pushover has been introduced, Bracci et al. [44]; the idea is to change the pattern of forces applied to the structure during the analysis, in order to consider the effect of damage on the distribution of stiffnesses of structural members. A description of the procedure can be found in Elnashai et al. [77]. Despite to the conceptual superiority, there is no an unanimous consensus on his effectiveness, particularly in what concerns the estimation of deformation patterns of buildings, Antoniou and Pinho [12].

3.6.1 Reduction to SDOF system through N2 method

Following the PEER methodology ([129], [169]) the structural capacity depends on the formulation adopted. In particular, the EDP-based formulation expresses the capacity in terms of a suitable engineering demand parameter, while the IM-based one requires the structural capacity expressed in term of the intensity measure adopted. In this work the IM formulation is used, and the peak ground acceleration is chosen as the intensity measure. Since the investigation is performed using pushover analyses, there is the need to translate the information coming from it in a format suitable for the PEER methodology, relating top displacement (for different limit states) to peak ground acceleration. This is done using the N2 method (Fajfar and Gašperšič [82], Fajfar [80] and Fajfar [81]). The elastic response spectrum used matches the requirement of EC8 (EC8 [74]) for soil class B ($S = 1.2, T_C = 0.5\,\mathrm{s}$).

The procedure requires the definition of the equivalent single degree of freedom (SDOF) system, which is defined through a linearization of the pushover curve for the MDOF system, Figure 3.19.

The key parameters of such an approximation are the yielding displacement D_y and the yielding strength F_y. The properties of the SDOF system are determined by dividing the corresponding properties of the MDOF system by the transformation factor Γ:

$$\Gamma = \frac{m_{SDOF}}{\sum m_i \phi_i^2}; \qquad m_{SDOF} = \sum m_i \phi_i$$

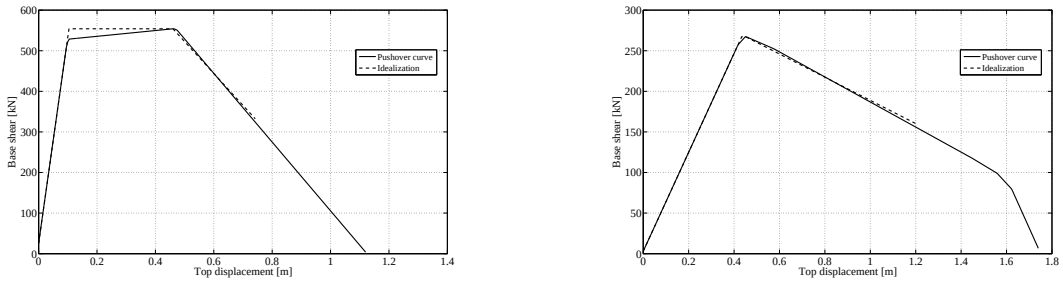

(a) 2 story building, section 80 × 80.

(b) 4 story building, section 80 × 80.

Figure 3.19: Example of idealization of pushover curve for multistory buildings investigated.

where ϕ_y is the modal shape vector of the predominant translational mode, normalized by the roof component. The yielding point of the equivalent SDOF system is simply obtained as $d_y^* = D_y/\Gamma$ and $f_y^* = F_y/\Gamma$. Subsequently the period of the equivalent system is:

$$T_{SDOF}^* = 2\pi \cdot \sqrt{\frac{m_{SDOF} \cdot d_y^*}{f_y^*}}$$

In all cases studied the period of the SDOF system exceeds the corner period T_C, so the equal displacement rule can be applied. For each limit state the corresponding mean spectral acceleration is evaluated in the following way:

$$S_{a,ls} = d_{ls}^* \cdot \left(\frac{2\pi}{T_{SDOF}}\right)^2$$

where $d_{ls}^* = D_{ls}/\Gamma$. Finally, the capacity of the system in terms of peak ground acceleration for each limit state is:

$$a_{g,ls} = \frac{S_{a,ls}}{S \cdot \eta \cdot 2.5} \frac{T_{SDOF}}{T_C}$$

where S is the soil factor ($= 1.2$) and η is the parameter related to the viscous damping ($= 1$ for 5% of damping).

The procedure is repeated for all the structures investigated, each of them analyzed during the whole lifetime, as subsequently explained, in order to consider the effect of environmental hazard on the overall seismic performance. Once the capacity in terms of PGA is obtained, fragility curves can be established, as well as the evaluation of frequency of exceeding a particular limit state using the PEER methodology, Dolšek and Fajfar [71]. Because two seismic methods are used, it is also meaningful to compare the estimated capacity in order to give suggestions on the applicability of approximated methods like pushover analysis.

Last section of the chapter is devoted to the presentation of the results of the risk analysis for the multistory precast structures investigated at time 0, before the introduction of the environmental hazard, in order to establish the initial capacity of the systems and to understand

subsequently the effect of corrosion on seismic performance. Before that, next section illustrates how the uncertainties in the modeling are taken into account, exploiting LHS explained in Section 2.4.2.

3.7 Incorporating modeling uncertainties

In order to deeply investigate the seismic performance of the precast systems, uncertainties should be included in the analysis (Schueller and Pradlwarter [220], Zareian and Krawinkler [249]). Uncertainties in ground motion are taken into account considering a pool of records, each scaled up to collapse (here seen as a dynamic collapse, so the structure is not able to sustain gravity loads). Uncertainties related to the modeling (Dolšek [70], Liel et al. [155]) are introduced via random variables of important parameters, each with a predefined probability distribution. In particular 9 random variables are selected, namely:

1: Mass (equal for each story) m;

2: Compressive strength of the concrete f_{cm};

3: Yield strength of the steel f_{ym};

4: Damping ξ;

5: Initial stiffness of the nonlinear springs $EI_{\text{eff}}/EI_{\text{gross}}$;

6: Ratio between maximum moment and moment at yield M_{cap}/M_y;

7: Rotation at maximum moment Θ_{cap};

8: Rotation in the post-capping branch Θ_{pc};

9: Energy dissipation capacity λ;

Table 3.2 depicts the probability distributions used. In this investigation is assumed that random variables are uncorrelated, Dolšek [69].

Because the computational cost required in plain MonteCarlo simulations, an advanced method is selected in order to reduce the effort. A promising approach is represented by the Latin Hypercube Sampling (Helton and Davis [113], Stein [226]). The description of the procedure is illustrated in Section 2.4.2; here the procedure adopted in order to choose the appropriate sample size, so the number of different models, is described. In particular two issues need to be addressed, one related to the statistical properties of the sampling matrix and one related to the results of the structural analysis. The former requires that the size of the sampling should be enough to ensure that the correlation matrix resulting from the

Table 3.2: Characterization of random variables used in the investigation

Parameter	Mean or median	COV	Distribution	Reference
m[kN]	1200	0.1	Normal	Ellingwood [76]
f_{cm}[MPa]	48	0.2	Normal	Melchers [165]
f_{ym}[MPa]	450	0.05	Lognormal	Melchers [165]
ξ	0.03	0.4	Normal	Porter et al. [199]
$EI_{\text{eff}}/EI_{\text{gross}}$	1	0.28	Lognormal	Haselton [112]
M_{cap}/M_y	1	0.1	Lognormal	Haselton [112]
Θ_{cap}	1	0.45	Lognormal	Haselton [112]
Θ_{pc}	1	0.72	Lognormal	Haselton [112]
λ	1	0.49	Lognormal	Haselton [112]

Table 3.3: Evolution of the norm E and maximum difference $S_{i,j} - K_{i,j}$ for different sample sizes.

N_{sim}	10	15	20	30	50
E	0.0057	0.0021	0.0010	0.0005	0.0005
E_{max}	0.0871	0.0277	0.0128	0.0078	0.0075

sampling procedure is close to the prescribed one (Iman and Conover [127]). This can be seen through the evaluation of the norm:

$$E = \frac{2}{N_{var}(N_{var}-1)} \sqrt{\sum_{i=1}^{N_{var}-1} \sum_{j=i+1}^{N_{var}} (S_{i,j} - K_{i,j}^2)}$$

where $S_{i,j}$ and $K_{i,j}$ are respectively the generated and the prescribed correlation coefficients between random variables X_i and X_j. Because the norm can be seen as an objective function, different numerical methods can be used in order to minimize it. An effective method is represented by the Simulated Annealing procedure (Dolšek [69], Vořechovskỳ and Novák [241]). Table 3.3 shows the evolution of the norm E and the maximum difference between the generated and the prescribed correlation coefficients $S_{i,j}$ and $K_{i,j}$ with reference to different sample sizes N_{sim}; due to the optimization process, the correlation among variables is close to zero, as theoretically prescribed. In particular a sample size equal to 30 seems acceptable from a statistical point of view.

The second consideration is related to the influence of the sample size on the results coming from the structural analysis. Usually the appropriate number should be selected in order to obtain "stable" results even changing the number of sampling. In this case, since data can be summarized into fragility curves, a test of goodness of fit could be effective; in particular,

considering that the probability distribution of IM related to a particular limit state has typically a lognormal distribution (Jalayer [129]), the cdf coming from numerical simulations can be compared with the theoretical one using a *Kolmogorov-Smirnov* test (Ang and Tang [11]).

Considering the results of past researches, it has found that the number of sampling should be at least double with respect to the number of random variables (Dolšek [69]). In order to verify the effect of the number of samples on the structural response and to choose the proper value different analyses are realized, changing each time the number of models. In particular IDA analyses are performed considering 10, 15, 20, 30 and 50 different models, and for each of them two accelerograms are used. Here only the results for the 2 story building with cross-section 45×45 are presented and discussed, but the same conclusions attain also for the other structural systems.

Within the pool of 25 earthquakes, two are chosen in order to have the highest difference in terms of spectral acceleration around the first mode vibration period. The indication of a proper value N_{sim} coming from the structural response is combined with the minimum sampling requirement to match within a certain tolerance the prescribed correlation matrix in order to define the final size of the random variables.

For each simulation and for each earthquake 3 parameters are monitored, such as PGA at collapse (PGA_C), maximum interstory drift at collapse (Drift) and top displacement at collapse (Disp); also the dispersion β is evaluated, here seen as the standard deviation of the natural logarithm, Dolšek [69]. Finally, the difference between the quantities determined on the basis of the selected N_{sim} and the quantities determined by assuming $N_{sim} = 50$ is presented. The estimation of the above parameters, for the two different accelerograms, are reported in Table 3.4 and Table 3.5. No significant differences can be seen changing the size of the sampling. To better understand the role of the number of sampling, in Figure 3.20 and Figure 3.21 the same parameters are plotted considering the ratio between the quantity determined on the basis of the selected N_{sim} and the quantity determined by assuming $N_{sim} = 50$. In particular on the left, from top to bottom, are shown the trend of PGA, maximum interstory drift and top displacement, while on the right the corresponding dispersions are plotted. The dispersion seems to have a higher uncertainty.

Finally a Kolmogorov-Smirnov test is performed comparing the cumulative distribution function coming from the data with the lognormal distribution that is used in the PEER PBEE methodology. The maximum difference D_n between the two cumulative distribution functions is presented in Table 3.6 together with the critical value D_n^{α}, considering a significance level $\alpha = 5\%$. In all the cases the test is satisfied. Figures from 3.22 to 3.26 show the comparison between the cdf coming from simulation and the theoretical cdf for the different limit states, here defined in terms of maximum interstory drift, as recommended in FEMA 356, FEMA 356 [84]:

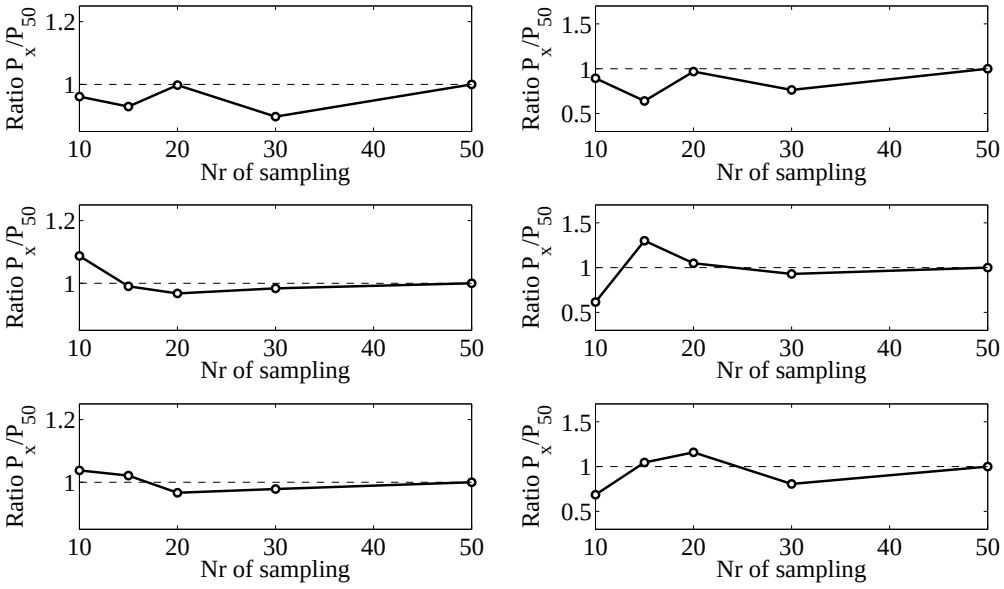

Figure 3.20: Effect of size sampling on different parameters for earthquake 1

DL: Damage Limitation. Maximum interstory drift 1%;

LS: Life Safety. Maximum interstory drift 2%;

CP: Collapse Prevention. Maximum interstory drift 4%;

DI: Dynamic Instability. Flatline.

In the present investigation, combining the information coming from statistical properties on the correlation matrix and results of structural analyses, a sample size equal to 30 sampling seems a reasonable choice.

3.8 Results of numerical simulations

In the following the main outcomes from nonlinear dynamic and static analyses are presented, with reference to the structures at the beginning of their life, $t = 0$. One important issue regards the definition of limit states, because they can be referred to the overall behavior or to the local one. In particular, two different approaches are presented. In the first one, widely used because his simplicity, limit states refer to different values of maximum interstory drift, depending on the structural system (e.g. concrete or steel frames, shear wall buildings, ect ...). This approach has been used in the previous section in order to define a proper value for the sample size performing IDA analyses, exploiting the recommended values give in FEMA 356, FEMA 356 [84]; the main drawback of such procedure is that the values are "only"

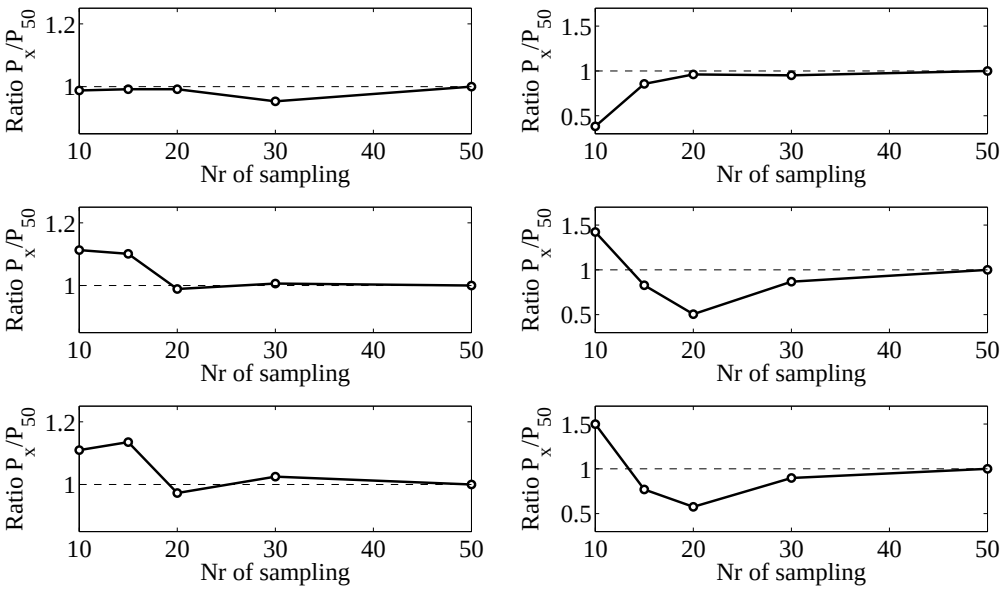

Figure 3.21: Effect of size sampling on different parameters for earthquake 2

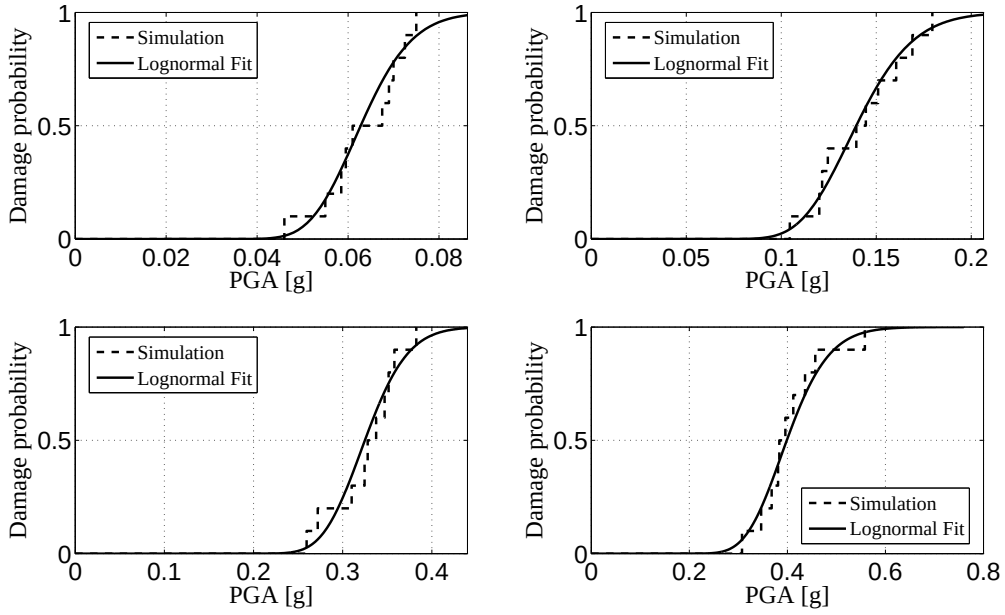

Figure 3.22: Comparison between cdf coming from simulation and lognormal cdf for sampling size equal to 10

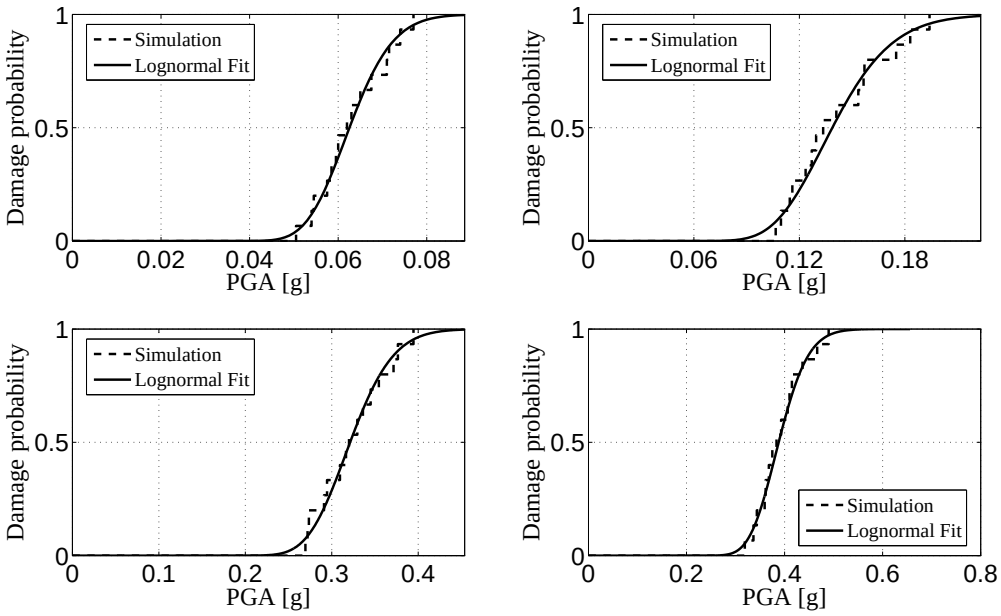

Figure 3.23: Comparison between cdf coming from simulation and lognormal cdf for sampling size equal to 15

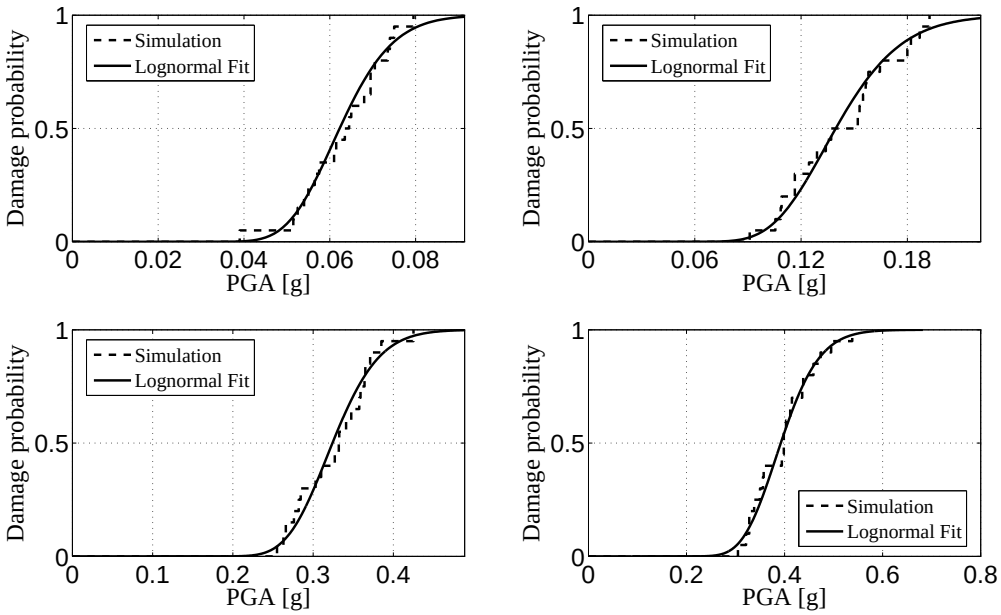

Figure 3.24: Comparison between cdf coming from simulation and lognormal cdf for sampling size equal to 20

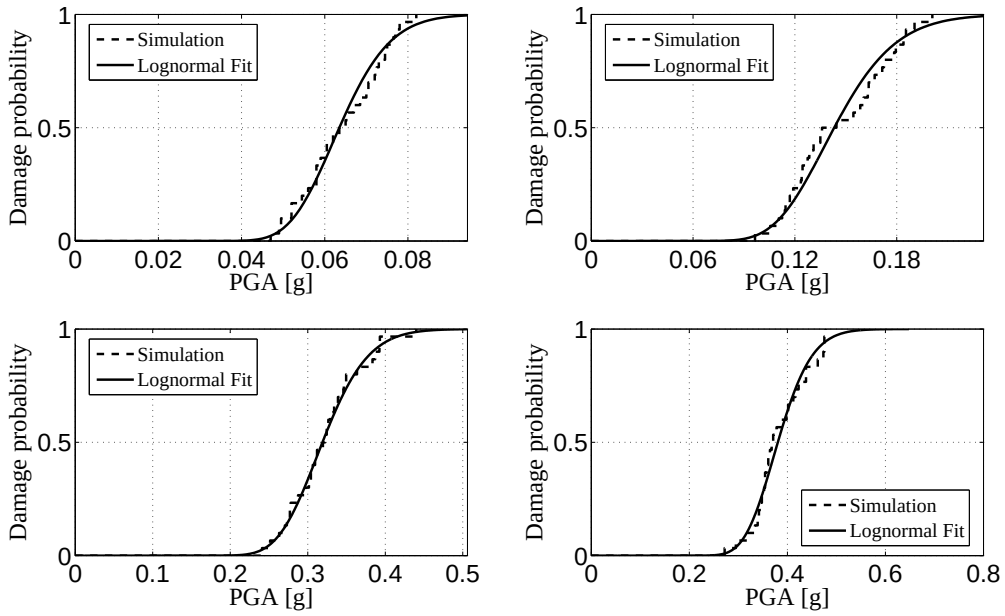

Figure 3.25: Comparison between cdf coming from simulation and lognormal cdf for sampling size equal to 30

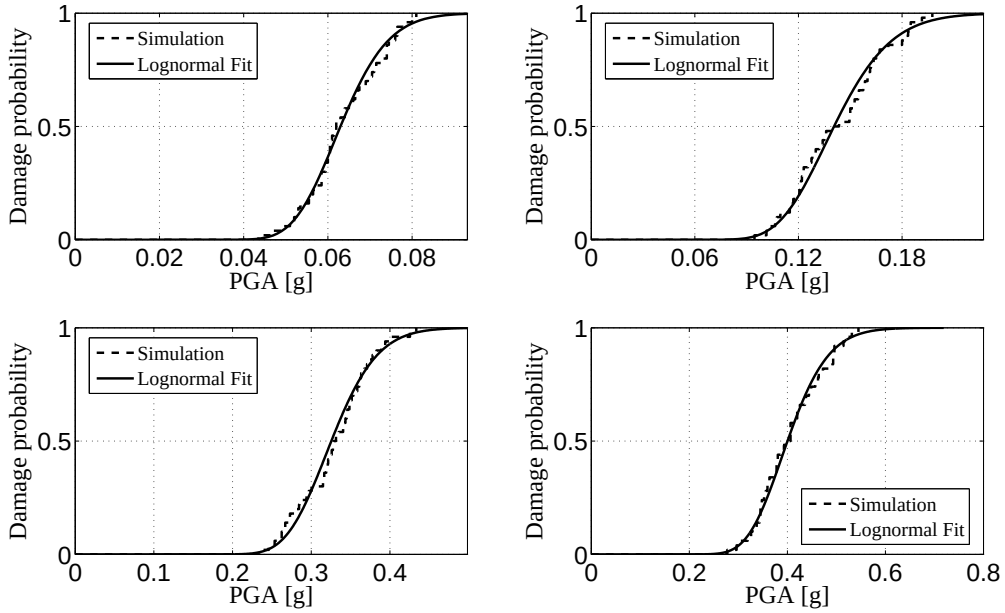

Figure 3.26: Comparison between cdf coming from simulation and lognormal cdf for sampling size equal to 50

Table 3.4: Monitoring of different parameters at collapse for earthquake 1

N_{sim}	$PGA_C[g]$	$\Delta[g]$	β_{PGA}	Δ	Drift [%]	Δ[%]	β_{Drift}	Δ	Disp [m]	$\Delta[m]$	β_{Disp}	Δ
10	0.445	0.007	0.217	0.006	7.92	0.438	0.206	−0.013	0.453	0.017	0.206	−0.040
15	0.407	−0.031	0.148	−0.0635	7.47	−0.019	0.247	0.028	0.446	0.009	0.259	0.0125
20	0.437	0.0005	0.202	−0.010	7.30	−0.019	0.236	0.017	0.422	−0.015	0.266	0.0194
30	0.393	0.045	0.187	−0.025	7.42	−0.067	0.197	−0.022	0.427	−0.009	0.193	−0.054
50	0.438		0.212		7.49		0.219		0.437		0.247	

Table 3.5: Monitoring of different parameters at collapse for earthquake 2

N_{sim}	$PGA_C[g]$	$\Delta[g]$	β_{PGA}	Δ	Drift [%]	Δ[%]	β_{Drift}	Δ	Disp [m]	$\Delta[m]$	β_{Disp}	Δ
10	0.359	−0.004	0.114	0.008	9.38	0.952	0.347	0.101	0.576	0.057	0.446	0.176
15	0.360	−0.003	0.094	−0.011	9.28	0.851	0.238	−0.008	0.589	0.070	0.264	−0.006
20	0.360	−0.003	0.116	−0.010	8.33	−0.093	0.176	−0.070	0.505	−0.014	0.188	−0.082
30	0.346	0.017	0.093	−0.013	8.48	0.052	0.321	0.075	0.532	0.013	0.403	0.133
50	0.363		0.106		8.42		0.246		0.519		0.270	

Table 3.6: Maximum difference between simulated and prescribed cdf and critical value for a 5% significance level for different size sampling

N_{sim}	D_n^α	D_n			
		DL	LS	CP	DI
10	0.41	0.105	0.210	0.161	0.195
15	0.34	0.097	0.095	0.182	0.119
20	0.27	0.122	0.142	0.170	0.128
30	0.24	0.074	0.161	0.073	0.096
50	0.19	0.073	0.124	0.071	0.096

suggested values, reasonable for the structural systems presented, but may be not appropriate for a specific case. In order to verify their applicability for multistory precast frame structures, typically more flexible than cast-in-situ systems, a second approach is introduced considering the local behavior of the plastic hinges.

As also indicated in Dolšek [70], at the element level limit states are defined as follows:

- DL (Damage Limitation): The reinforcement of structural element starts to yield;
- LS (Life Safety): The rotation of the plastic hinge corresponds to the rotation at the capping point, see Figure 3.5;
- NC (Near Collapse:) The rotation of the plastic hinge corresponds to the ultimate rotation (20% reduction with respect to the maximum moment)

At a global level, DL limit state is reached if all the columns at a generic story are in the DL limit state, while LS and NC limit states are reached if one column reaches the capping moment or the ultimate rotation, respectively. However, if the base shear is lower than 80% of the maximum base shear coming from a pushover analysis, NC limit state falls in the softening branch of the pushover curve and corresponds to a 20% reduction with respect to the maximum base shear, while LS limit state is equal to the 75% of the NC top displacement, Dolšek [70]. When performing IDA analyses, also complete failure can be estimated, here referring to a dynamic instability (DI); because structural systems cannot sustain vertical loads, IDA curve reaches a flatline.

The two methodologies are then compared, performing IDA analyses and pushover ones, also to give suggested values for the maximum interstory drifts. It is worth nothing to remind that NC limit states defined above is related to a ductile collapse mechanism, due to a modern design philosophy (e.g. EC8 EC8 [74]), where brittle failures are not admissible. Usually

this kind of mechanism is related to the shear strength, so in the present investigation also a comparison between shear capacity and shear demand on structural elements is done, in order to check the effectiveness of the design procedure adopted, Biondini et al. [39]. Total shear capacity depends on three contributions, Isaković et al. [128], namely:

- V_c: shear strength of an element without shear reinforcement;
- V_N: influence of the compressive stresses to the increase in shear strength;
- V_w: contribution of shear reinforcement.

Following the recommendations of Eurocode 8 (EC8 [74]), shear capacity V_R is evaluated as indicated in equation 3.11:

$$\begin{aligned} V_R &= [V_N + V_c + V_w] \\ &= \frac{h-x}{2L_v} \min(N; 0.55 A_c f_c) + \\ &+ \left(1 - 0.05 \min(5; \mu_\Delta^{pl})\right) \left[0.16 \max(0.5; 100\rho_{tot}) \left(1 - 0.16 \min(5; \frac{L_v}{h})\right)\right] \sqrt{f_c} A_c + \\ &+ \left(1 - 0.05 \min(5; \mu_\Delta^{pl})\right) V_w^b \end{aligned} \tag{3.11}$$

where h is the depth of the cross section, x is the neutral axis depth, L_v is the shear span (equal to the height of the columns), μ_Δ^{pl} is the plastic part of the rotational ductility, ρ_{tot} is the longitudinal steel ratio and V_w^b depends on transversal steel reinforcement:

$$V_w^b = \rho_w \cdot b_w \cdot z \cdot f_{yw} \tag{3.12}$$

where ρ_w is the transversal steel ratio, b_w is the width of cross-section web, z is the internal level arm and f_{yw} is the yielding strength of transversal reinforcement.

In order to compare shear capacity and demand the story shear capacity to demand ratio (DCR) is used; a value equal or higher than 1 points out the achievement of a brittle collapse failure. It is important to foresee that the structures investigated are not sensitive to a brittle collapse (DCR values are always lower than 1); however, because corrosion can affects in a severe way the transversal steel strength, also a potential brittle limit state is estimated. In particular a DCR value equal to 0.5 is selected, Celarec et al. [53].

3.8.1 IDA and pushover curves for RC frames

Results of IDA analyses and pushover ones will be presented in this section, with the purpose to assess the capacity of the systems studied for different limit states at the beginning of their lifetime. Because the inclusion of modeling uncertainties, IDA analysis allows to separate in a clear way the effect of the sources of variability, in the following named as “record to record

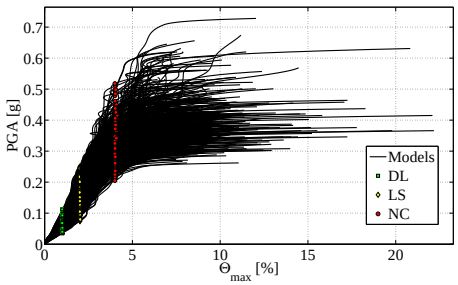

(a) Extended IDA, 2 story building with cross-section 45×45.

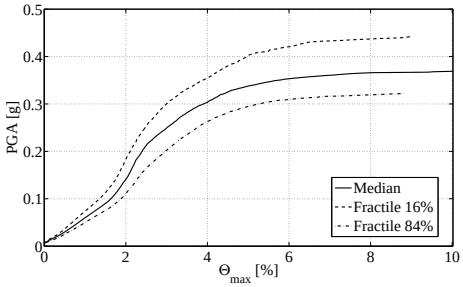

(b) IDA summary, 2 story building with cross-section 45×45.

Figure 3.27: Extended IDA curves and their fractiles at time $t = 0$.

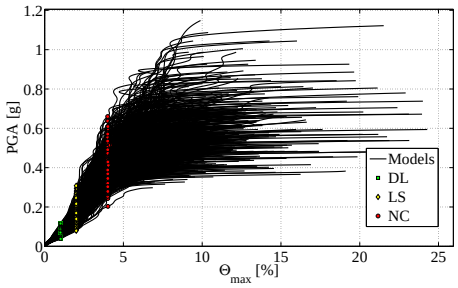

(a) Extended IDA, 3 story building with cross-section 60×60.

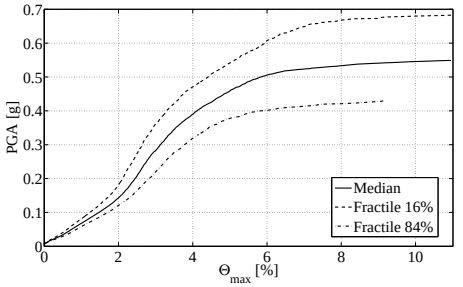

(b) IDA summary, 3 story building with cross-section 60×60.

Figure 3.28: Extended IDA curves and their fractiles at time $t = 0$.

variability (R)" and "modeling uncertainties (U)"; if both are simultaneously considered, we refer to it as "RU". Due to the probabilistic approach adopted, IDA curves can be summarized into fractiles; in particular median (50%), 16% and 84% values are selected, Vamvatsikos and Cornell [234], in order to cover a wide range in the seismic behavior and to understand the dispersion in the results. For example, Figures 3.27 and 3.28, as an example, show extended IDA curves for all the earthquakes and all the random variables together with summarized IDA for 2 story and 3 story building with columns cross-section 45×45 and 60×60, respectively.

Even if the nominal period for the structures is the same (2.5 s) the capacity of the 3 story building is slightly higher. Table 3.7 summarizes the structural capacity in terms of peak ground acceleration for all the systems studied. As can be seen, an increase in cross-section size, taking constant the number of stories, improves the capacity, due to the increase in strength and ductility. At the same, considering the same cross-section, structural capacity tends to decrease considering a higher number of stories.

Because the inclusion of modeling uncertainties, IDA method allows also to understand the importance of random variables involved in the process with reference to the engineering demand parameter (EDP) introduced, here equal to the maximum interstory drift θ, Dolšek

Table 3.7: Median capacity in terms of PGA from IDA analysis at different limit states for all the structures investigated

Frame	DL [g]	LS [g]	NC [g]
2 Story 45 × 45	0.060	0.141	0.3040
2 Story 70 × 70	0.108	0.332	0.748
2 Story 80 × 80	0.134	0.451	0.832
3 Story 60 × 60	0.068	0.144	0.390
3 Story 80 × 80	0.085	0.215	0.699
4 Story 80 × 80	0.079	0.168	0.497

[69]. There is no a unique approach to highlight such importance however, due to the use of LHS to sample random variables, an effective way concerns the introduction of Spearman rank-order correlation coefficient ρ that, for the generic ith variable, is defined as (Vořechovskỳ and Novák [241]):

$$\rho_i = 1 - \frac{6\sum_{j=1}^{N_{sim}} \left(r(x_{j,i}) - r(EDP_j)\right)^2}{N_{sim}\left(N_{sim}^2 - 1\right)} \tag{3.13}$$

where $x_{j,i}$ is the jth outcome of the random variable X_i, N_{sim} is the number of simulations and r represents the rank of the jth sample value of random variable or response variable. The coefficient ranges from -1 to 1; a value close to 1 means that the corresponding random variable has a positive effect on the response parameter chosen, viceversa if ρ is close to -1. A value near zero means that a particular random variable has not remarkable effects on EDP. Figure 3.29 shows the Spearman rank coefficients for all the structures investigated, considering the collapse limit state (DI). In particular each bar refers to a particular earthquake, while the horizontal line is the median value. The sensitivity of each random variable to the seismic response is quite different if we consider the frames with the higher vibration periods, Figures 3.29a, 3.29c and 3.29e and the other systems, Figures 3.29b, 3.29d and 3.29f. This can be understood if we remember that for the first ones the design method applied is not appropriate due to the low behavior factor computed, Biondini et al. [38]. In particular, for these cases the positive correlation between ultimate rotation and seismic capacity is not so clear.

On the opposite, for 2 story buildings with column cross-section 70 × 70 and 80 × 80 and 3 story building with column cross-section 80 × 80 the sensitivity of the parameters is clearly pointed out. Mass and initial stiffness have a negative correlation with respect to the response, while damping, ultimate rotation and energy dissipation capacity are positive correlated as expected.

The same structures are investigated also via pushover analysis, because this methodology

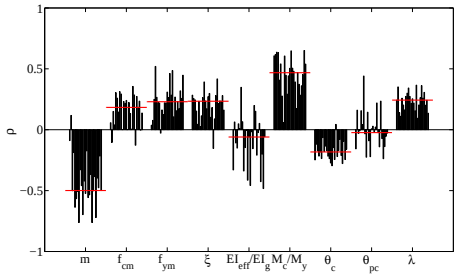

(a) 2 story building with cross-section 45×45.

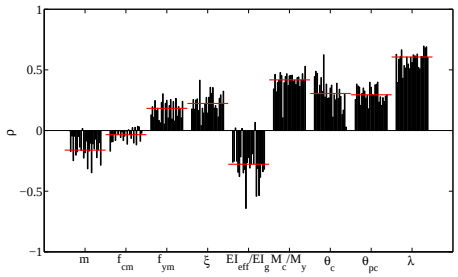

(b) 2 story building with cross-section 70×70.

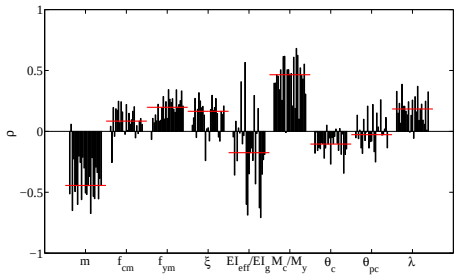

(c) 3 story building with cross-section 60×60.

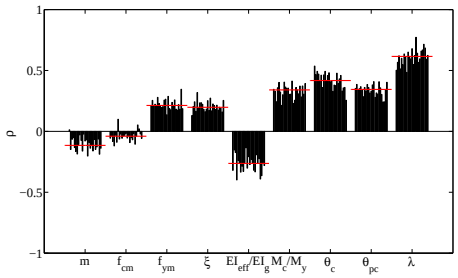

(d) 2 story building with cross-section 80×80.

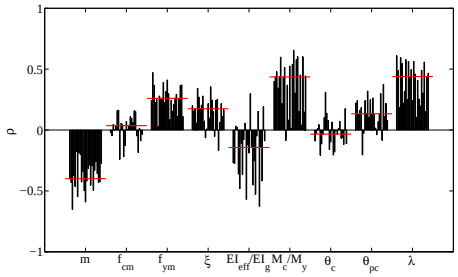

(e) 4 story building with cross-section 80×80.

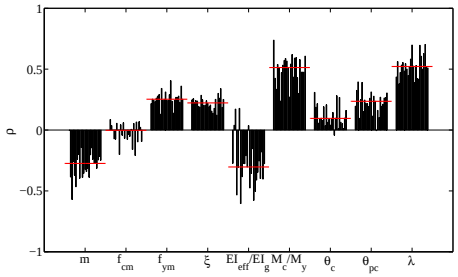

(f) 3 story building with cross-section 80×80.

Figure 3.29: Spearman rank correlation coefficients for all the structures investigated at time $t = 0$. Dynamic Instability limit state.

has a lower computational cost, despite to the accuracy. In this case limit states are defined in a different way, first exploring the local behavior of the plastic hinges, and subsequently defining them on the global level as explained before. Such procedure is more correct from an analytical point of view, and allows to verify if the maximum interstory drifts given by the codes can be effective also for precast systems. The same random variables are adopted, so for each frame 30 structural models are selected. Figure 3.30 represents the capacity curves of the buildings in terms of top displacement versus base shear, where limit states are indicated with different dots. Due to the high value of story masses (nominal value equal to 1200 kN) P-delta effects are significant, and the hardening branch can be seen only for buildings with large column cross-section.

In many cases NC limit state is governed by the drop of base shear, because it occurs earlier with respect to the reaching of ultimate rotation in the plastic hinges. It is also important to highlight that such limit state refers to a ductile mechanism, since shear strength is always higher than shear demand, as can be seen in Figure 3.31 where DCR are plotted for each precast systems.

Table 3.8 shows the median values of base shear for the set of structures analyzed; due to the significant influence of P-delta effects, in almost each case the hardening branch is not present, so the softening part starts immediately after the achievement of the capping points. Hardening behavior appears if the structure is sufficiently stiff, e.g. for 2 story buildings with cross section 80×80, as also evident from Figure 3.30d. Table 3.9 shows the median top displacements for different limit states; one important emerging issue is the influence of the cross-section size with respect to the displacement reached. For example, taking constant the number of stories, an increase in the size of columns tends to decrease the displacement corresponding to the DL limit state, but at the same time tends to increase the displacements related to LS and NC limit state. Because DL limit state corresponds in practice to the last point of the elastic point, an increase in stiffness, due to the increase of cross-section size, reduces the range of elastic behavior but at the same, because a simultaneous increase in ductility, the plastic resources (related to LS and NC limit state) are enhanced.

Looking at Table 3.10 some considerations emerge. In particular, an increase in cross-section size taking constant the number of stories, improves the capacity, due to the increase in strength and ductility. At the same time, considering the same cross-section, structural capacity in terms of DL limit state is also improved increasing the number of stories, while LS and NC limit states are related to a lower intensity, due to a wider spreading of plastic resources within the structure.

Finally, it is possible to compare the PGA capacity (with reference to 5^{th} percentile) for DL, LS and NC limit states carried out by performing IDA and pushover analyses, illustrated in Figure 3.32. In this case two different considerations can be done; for frames where the proposal capacity design is not appropriate the differences in terms of structural capacity

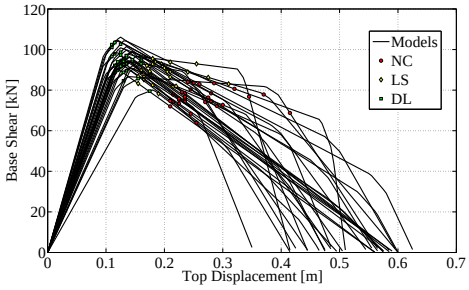

(a) 2 story 45×45.

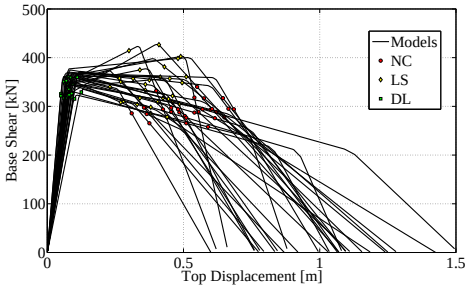

(b) 2 story 70×70.

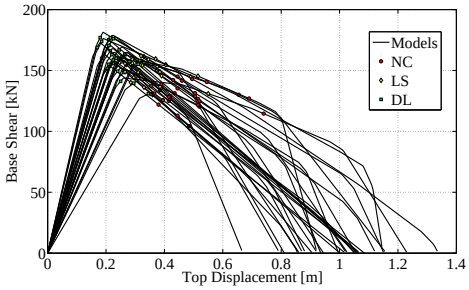

(c) 3 story 60×60.

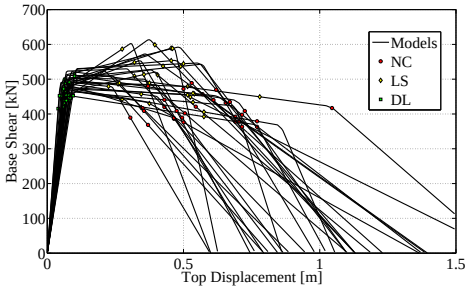

(d) 2 story 80×80.

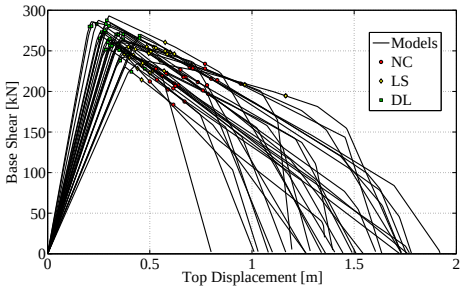

(e) 4 story 80×80.

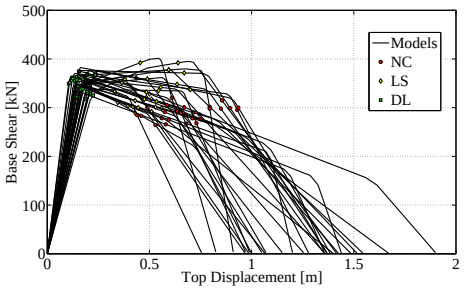

(f) 3 story 80×80.

Figure 3.30: Capacity curves for buildings studied at time $t = 0$.

Table 3.8: Median base shear from pushover analysis at different limit states for all the structures investigated

Frame	**DL** [kN]	**LS** [kN]	**NC** [kN]
2 Story 45×45	95.25	88.82	75.87
2 Story 70×70	353.96	342.60	291.06
2 Story 80×80	480.73	485.26	408.75
3 Story 60×60	161.77	149.14	129.48
3 Story 80×80	357.30	332.39	290.54
4 Story 80×80	265.58	243.34	213.05

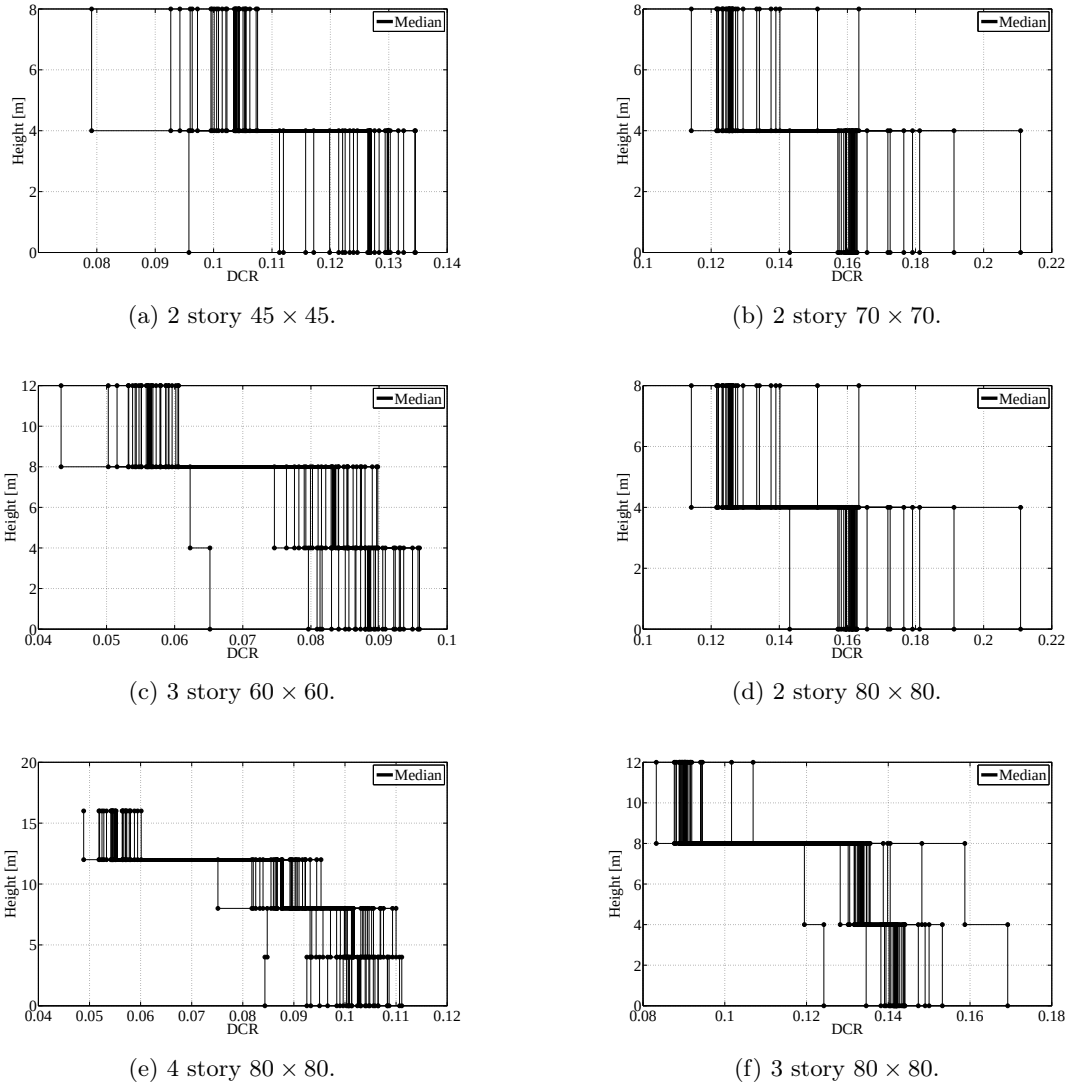

(a) 2 story 45 × 45.

(b) 2 story 70 × 70.

(c) 3 story 60 × 60.

(d) 2 story 80 × 80.

(e) 4 story 80 × 80.

(f) 3 story 80 × 80.

Figure 3.31: Demand over capacity ratio for buildings studied at time $t = 0$.

Table 3.9: Median top displacement from pushover analysis at different limit states for all the structures investigated

Frame	**DL** [m]	**LS** [m]	**NC** [m]
2 Story 45 × 45	0.130	0.180	0.240
2 Story 70 × 70	0.078	0.390	0.520
2 Story 80 × 80	0.068	0.399	0.533
3 Story 60 × 60	0.230	0.330	0.440
3 Story 80 × 80	0.165	0.493	0.658
4 Story 80 × 80	0.313	0.501	0.663

Table 3.10: Median capacity in terms of PGA from pushover analysis at different limit states for all the structures investigated

Frame	DL [g]	LS [g]	NC [g]
2 Story 45 × 45	0.107	0.147	0.196
2 Story 70 × 70	0.160	0.737	0.988
2 Story 80 × 80	0.173	0.987	1.320
3 Story 60 × 60	0.149	0.202	0.271
3 Story 80 × 80	0.187	0.522	0.701
4 Story 80 × 80	0.205	0.293	0.387

prediction between the two methods are considerable, Figures 3.32a, 3.32c and 3.32e. Moreover, for such configurations, the effect og higher modes tend to be quite important, so pushover method with a distribution of story forces corresponding to the first mode has some drawbacks. On the other side, for buildings with a nominal vibration period lower than 2.5 s the results are close one to each other, except for Life Safety limit state. This could mean that the recommended value equal to 2% for maximum interstory drift is not well suitable for precast systems, and a higher threshold can be used. Moreover, also the suggested maximum interstory drift for DL limit state could be increase a little bit. Such considerations prove, within a Performance-based approach, that multistory precast systems have a capacity comparable to that of cast-in-situ frames, as expected.

3.8.2 Collapse fragility curves

One of the main outcome of the analyses in the PEER methodology is the development of fragility curves. These function represent the probability of exceedance of a particular limit state given a certain engineering demand parameter (EDP), here described by intensity of the ground motion in terms of PGA. The procedure is the following: for each limit state, the corresponding PGA value is stored in the database by performing a nonlinear analysis. Subsequently, all the results are sorted in an ascending order, and a stepwise cumulative distribution function is plot. Usually the results can be represented by a lognormal distribution, see e.g. Jalayer [129], so it is possible to compare the outcomes of the MonteCarlo simulation with the analytical cdf, which is evaluated on the base of the mean value and the standard deviation of the parameter of interest, e.g. the PGA related to a particular limit state.

An important advantage in the use of extended IDA is the possibility to develop fragility curves only for record to record variability, modeling uncertainties or both. The statistical description of the results is based on the estimate of the median value and the corresponding

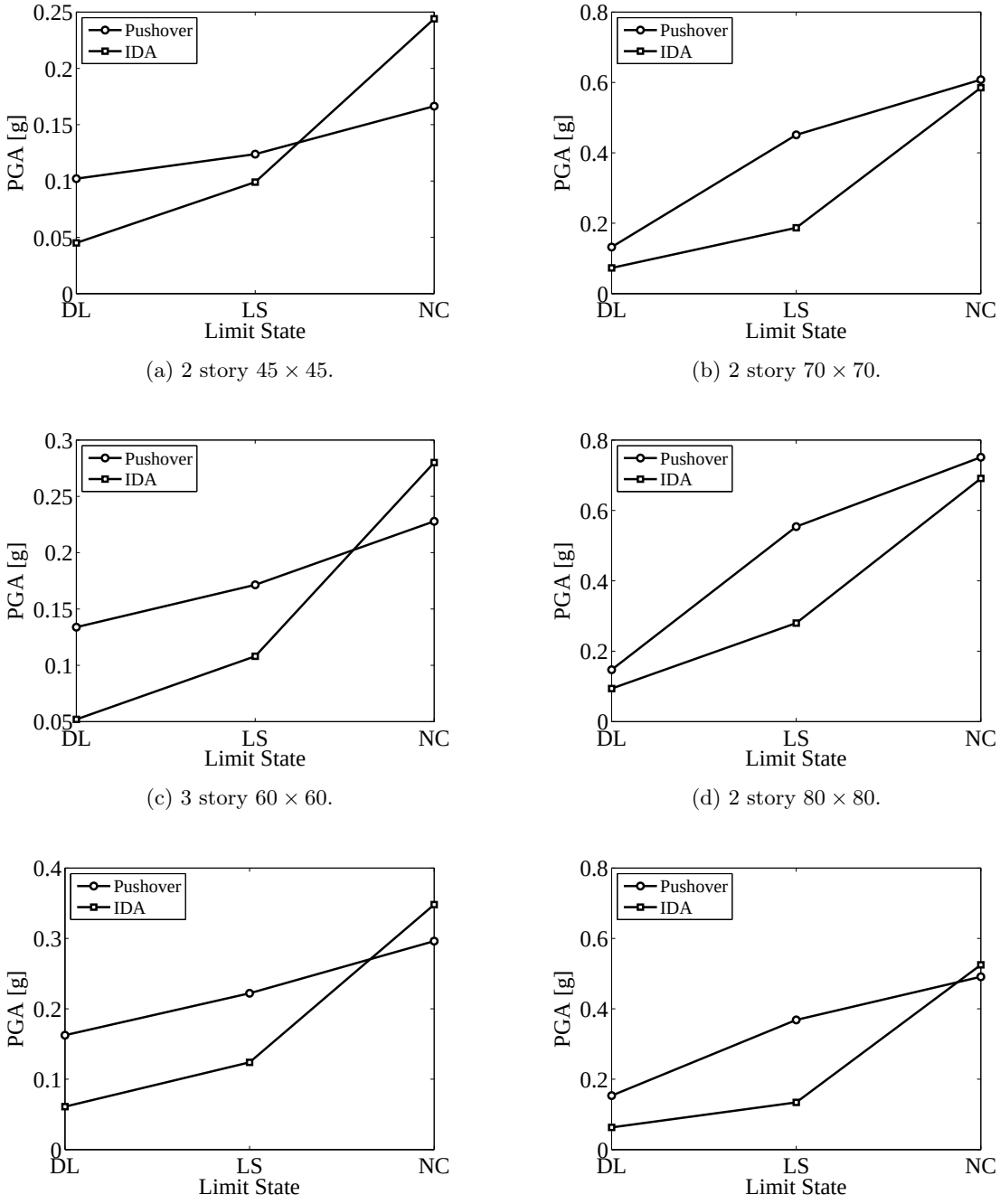

(a) 2 story 45×45.

(b) 2 story 70×70.

(c) 3 story 60×60.

(d) 2 story 80×80.

(e) 4 story 80×80.

(f) 3 story 80×80.

Figure 3.32: Comparison between capacity in terms of PGA ($5th$ percentile)for buildings studied at time $t = 0$.

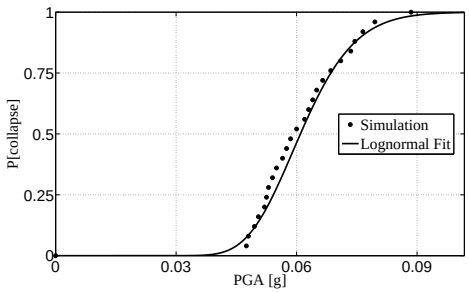

(a) Damage Limitation limit state.

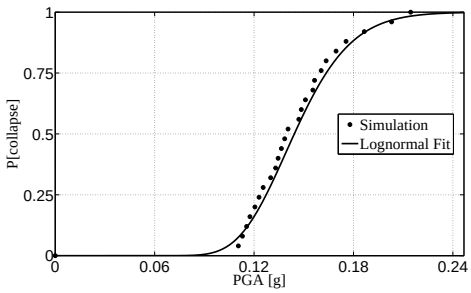

(b) Life Safety limit state.

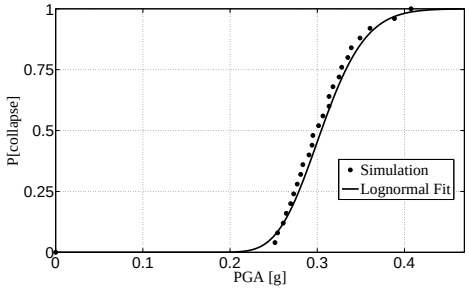

(c) Near Collapse limit state.

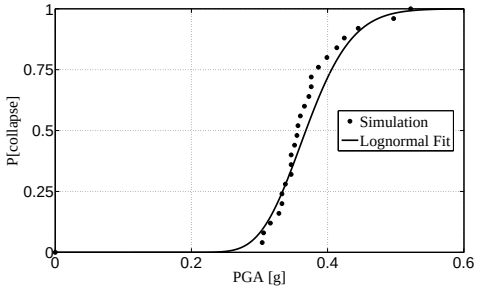

(d) Dynamic Instability limit state.

Figure 3.33: Fragility curves for record to record variability from IDA analysis for 2 story building with column cross-section 45×45.

dispersion, here defined as the standard deviation of the natural logarithm, which is calculated as the average value of the $\beta_{16} = \log(y_{50}/y_{16})$ and $\beta_{84} = \log(y_{84}/y_{50})$, where y_{16}, y_{50} and y_{84} represent the 16, 50 and 84% fractile in terms of the EDP chosen, Dolšek [69]. Figure 3.33 presents the fragility curves considering only record to record variability for 2 story building with column cross-section 45×45; as it can be seen the results of Monte Carlo simulation (dots) match very well the analytical cdf curve, which represent a lognormal distribution of probability of exceedance.

When both the two sources of uncertainties are considered, fragility curves have the shape illustrated in Figures 3.34 and 3.35. Here, including modeling variability, fragility functions tend to flat, so there is an increase in the dispersion. This happens also when the effects of different types of uncertainties are combined using the so called "mean estimate approach"; within this method, both record to record variability and modeling uncertainties are described through lognormal random variables, independent one to each other. The resulting distribution is also lognormal, where the median is unchanged and the logarithmic variance is the sum of the two.

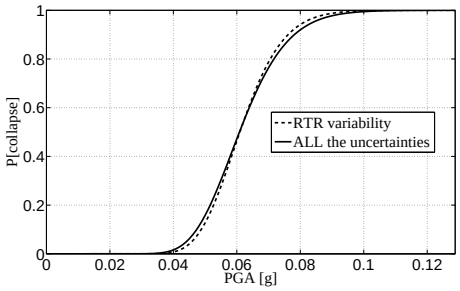

(a) Damage Limitation limit state.

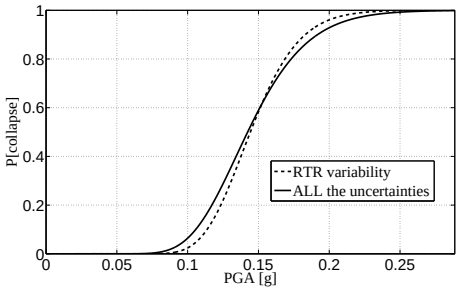

(b) Life Safety limit state.

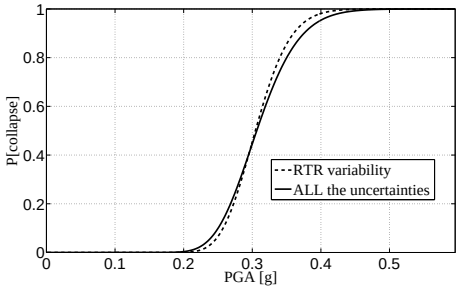

(c) Near Collapse limit state.

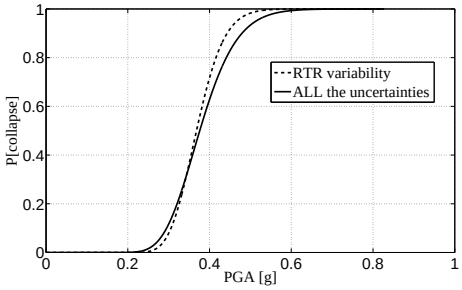

(d) Dynamic Instability limit state.

Figure 3.34: Fragility curves including all the uncertainties from IDA analysis for 2 story building with column cross-section 45×45.

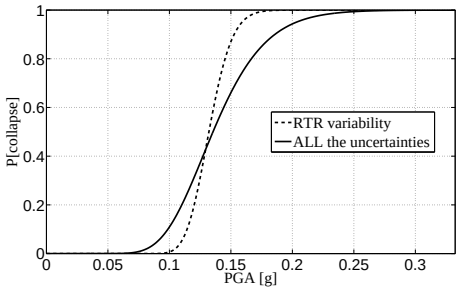

(a) Damage Limitation limit state.

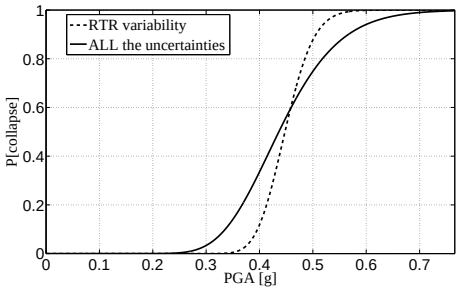

(b) Life Safety limit state.

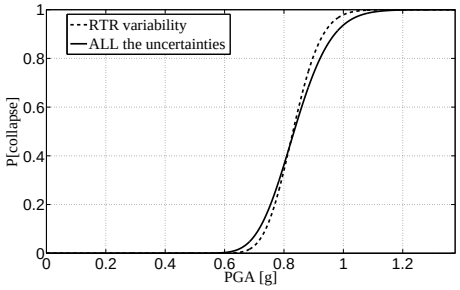

(c) Near Collapse limit state.

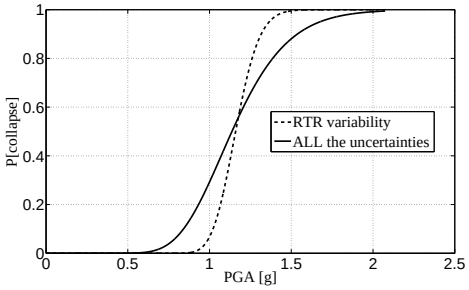

(d) Dynamic Instability limit state.

Figure 3.35: Fragility curves including all the from IDA analysis for 2 story building with column cross-section 80×80.

3.8.3 Hazard scenario and seismic risk

In order to perform a seismic risk analysis, the information coming from the structural analysis (namely the fragility functions for different limit states, see e.g. Lupoi et al. [157]) should be combined with the hazard scenario. The final result states the annual probability of exceedance of a particular limit state (MAF=mean annual frequency of exceedance), expressed here as:

$$\lambda_{LS} = \int_0^\infty P_r(D > C|IM) \cdot dH_S(x)dx \tag{3.14}$$

where the first term ($P_r(D > C|IM)$) is the probability that the demand exceeds the capacity given a particular EDP (for example the ground motion intensity), namely the fragility function, while the second term is the slope of the hazard curve. The hazard curve shows the annual probability of exceedance of a certain value of the intensity measure IM chosen, here referred to the PGA, for a particular site. These data can be computed in different way: for Italy the information comes from the National Institute of Geophysical and Vulcanology (http://esse1.mi.ingv.it/). Four different sites are selected, ranging from low to high seismic intensity. In particular the sites are:

1: Milano (as reference);

2: Gemona del Friuli;

3: S.Benedetto del Tronto;

4: Messina.

Figure 3.36 shows the hazard curves for each site, considering 9 values of probability, from 81% of probability of exceedance in 50 years to 2%, Meletti and Montaldo [166]. As it can be seen, the site of Milano has a very low level of seismicity, while Gemona and Messina has the higher value. The data are referred to the median value together with the 16^{th} and the 84^{th} percentile. To compute MAF values, the integral represented in equation 3.14 can be solved by a numeric scheme or, under certain assumptions, in an analytical way; the second approach follows the SAC-FEMA methodology, Jalayer [129], and the assumptions are reported below:

1: The collapse capacity S_C has a lognormal distribution;

2: Hazard function H_S has a lognormal distribution with a dispersion $\sigma_{ln(H_s)}$ and its median approximated by a power-law expression with parameters k and k_0;

3: The global variance coming from numerical analyses can be expressed as the sum of the variance due to ground motion (RTR) and variance due to uncertainties in modeling (U).

$$\sigma^2_{\ln S_{C(tot)}} = \sigma^2_{\ln S_{C(RTR)}} + \sigma^2_{\ln S_{C(U)}} \tag{3.15}$$

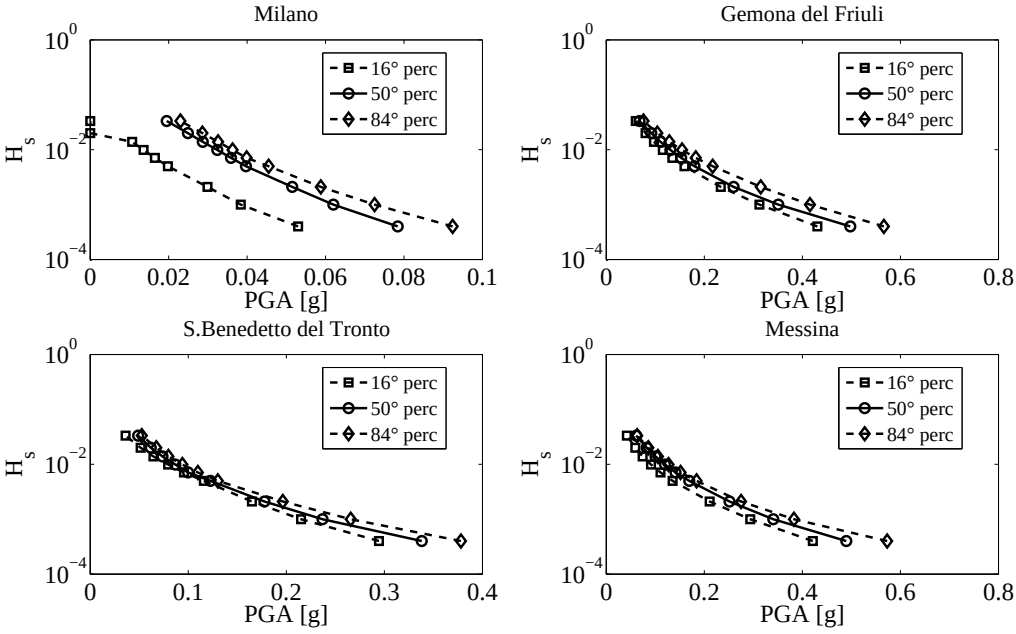

Figure 3.36: Hazard curves for the selected sites.

With these assumptions, the mean annual frequency of exceedance of a particular limit state can be expressed in the following closed-form relation:

$$\lambda_{LS} = \tilde{H}_S(IM_{S_C}) \cdot \exp\left(\frac{1}{2}\sigma^2_{\ln H_S}\right) \cdot \exp\left[\frac{1}{2}k^2 \cdot \left(\sigma^2_{\ln S_{C(RTR)}} + \sigma^2_{\ln S_{C(U)}}\right)\right] \tag{3.16}$$

In equation 3.16 the median value of the hazard curve has a power-law expression:

$$H_S(IM) = k_0 \cdot IM^{-k} \tag{3.17}$$

where the parameters k_0 and k are estimated through a nonlinear regression analysis, see Ang and Tang [11]. The outcomes of such procedure can be seen in Figure 3.37 for the different sites analyzed. Because the estimation of λ_{LS} (equation 3.16) requires also to include a dispersion for hazard curve, a value $\sigma^2_{\ln H_S} = 0.5$ is chosen, Kramar et al. [136]. In Figures 3.38a and 3.38b such value is applied in order to obtain the 16^{th} and the 84^{th} percentile curves for the sites of S.Benedetto and Messina; the choice seems appropriate because the computed curves suite very well the seismological data.

Performing IDA analyses it is easy to evaluate MAF values by a numerical integration and through the analytical formulation, in order to compare such results; in particular for each site the probability of exceedance related to different limit states (DL, LS, NC and DI) is computed, and finally a regression analysis is performed in order to cover the entire range of behavior. Figure 3.39 shows the comparison between the structural performance curves coming from the two approaches illustrated above for 2 story building with column cross-section 45×45. As can be seen the analytical formulation gives higher values, so the probability of exceedance

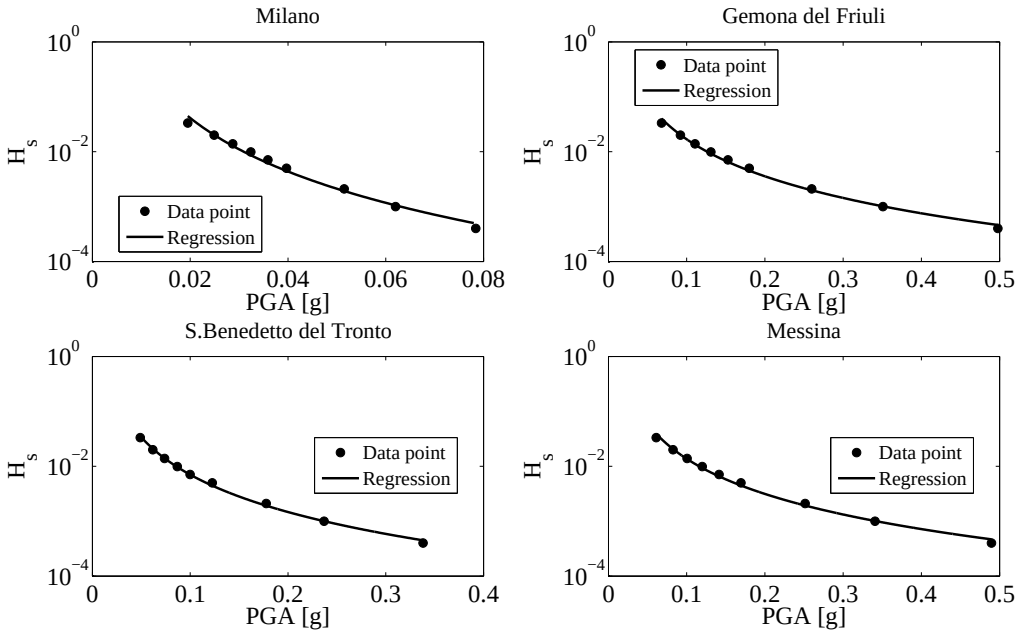

Figure 3.37: Results of the regression analysis on the hazard curve.

tends to be overestimated if the approximated methodology is applied, in order to lead the practitioners on the safety side.

The comparison between IDA and pushover analysis can be also made with respect to the estimate of MAF values, exploiting the analytical formulation, since performing pushover analyses only the modeling variability is computed, record to record variability is added a posteriori, following recommended values given in literature. In particular the dispersion β is set equal to 0.2, 0.3 and 0.4, for DL, LS and NC limit states respectively, FEMA P695 [86] and Celarec et al. [53]. Clearly, the differences in terms of structural capacity illustrated above are reflected also in this case. However, because the evaluation of MAF is strongly influenced by the slope of hazard curve, the most significant deviations are found around Damage Limitation limit state, where the slope is higher, as indicated in Figures 3.40 and 3.41.

Finally, evaluation of seismic risk is carried out with reference to two different parameters, Kramar et al. [136]:

1: The 5^{th} percentile PGA capacity;

2: The probability of collapse over a period of 50 years;

The first parameter can be seen as a characteristic value (PGA_k), and it is compared with the design PGA for different sites and different limit states according to the Italian Standard Code (NTC 2008 [181]). The second parameter is computed according with the Probabilistic Seismic Hazard Analysis (Cornell [62], Sen [223]), considering a Poisson process; in this case

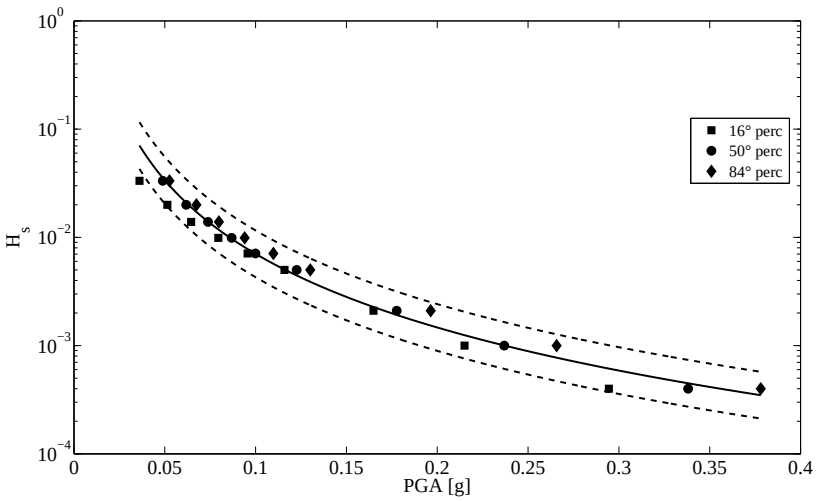

(a) S.Benedetto.

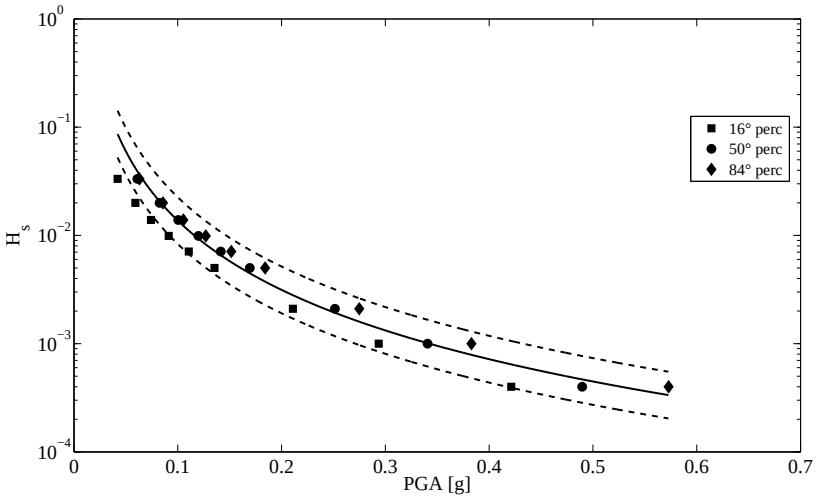

(b) Messina

Figure 3.38: Median and percentile hazard curves.

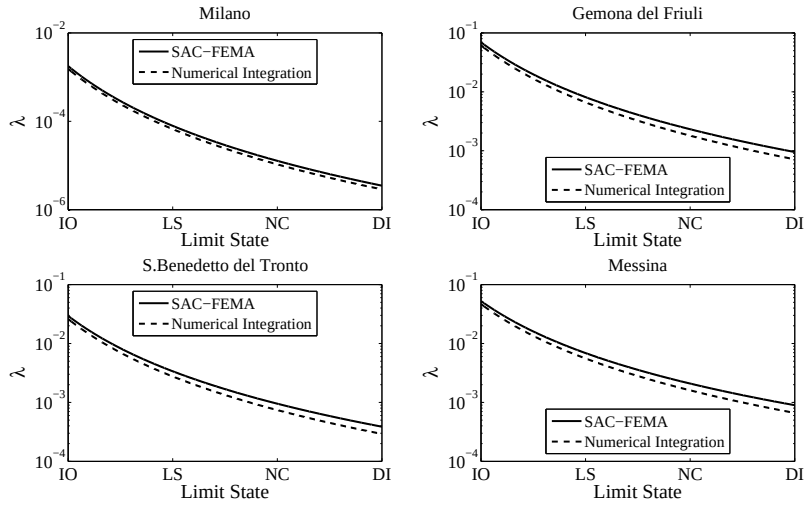

Figure 3.39: MAF values for 2 story building with column cross-section 45×45.

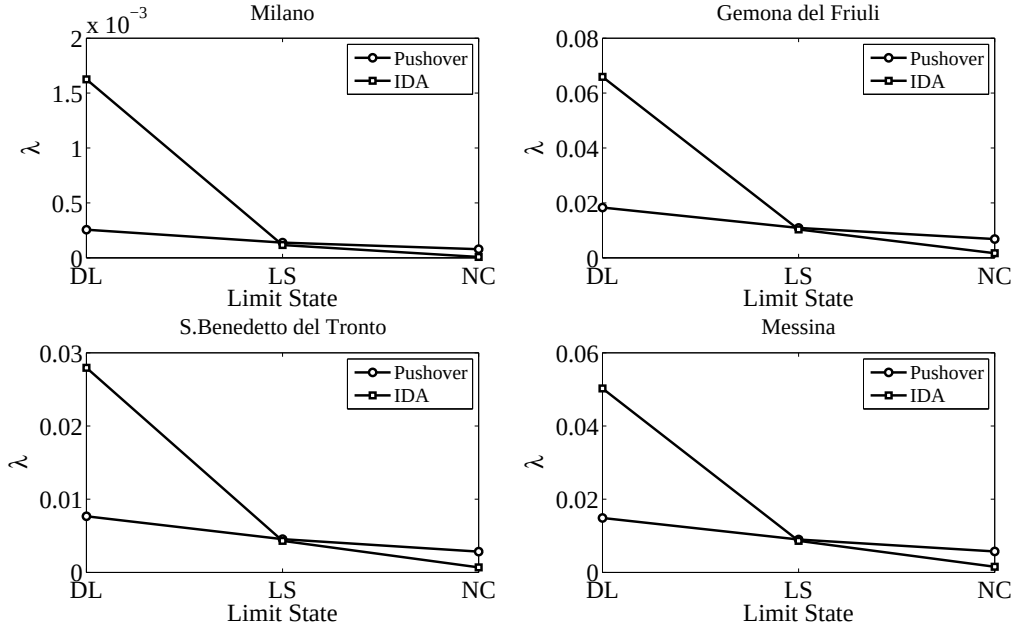

Figure 3.40: Comparison of MAF estimation for 2 story building with column cross-section 45×45.

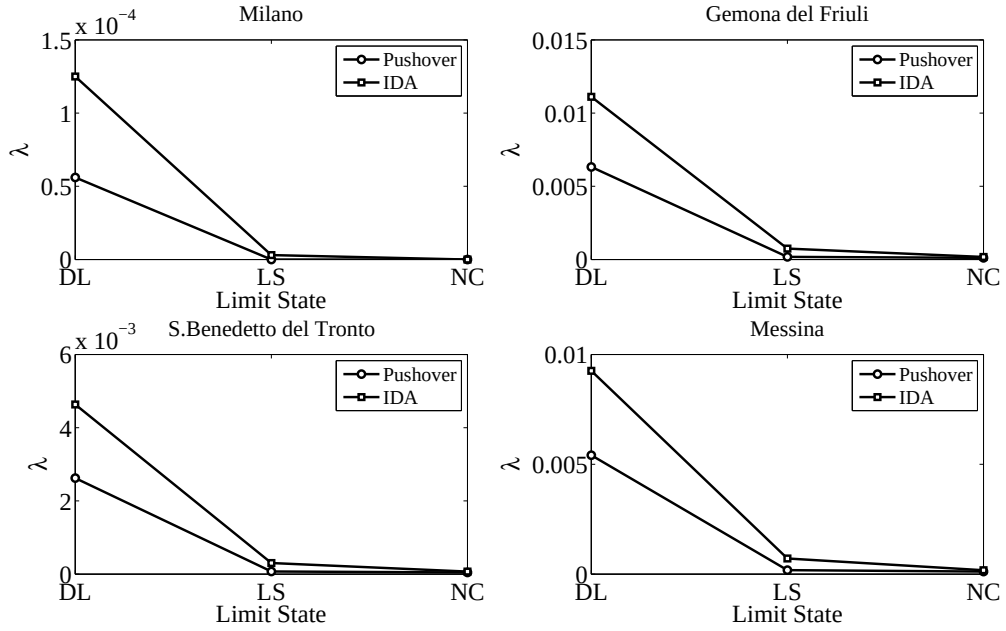

Figure 3.41: Comparison of MAF estimation for 2 story building with column cross-section 80×80.

the probability of exceedance during a time period V_r is expressed as:

$$P_{r,LS} = 1 - \exp(-\lambda_{LS} \cdot V_r)$$

where V_r is the time period (50 years) and λ_{LS} is the instantaneous value of MAF. This probability is compared with that related to a particular limit state and, according to Italian Code, the following values are taken into account:

DL: Damage limitation limit state. $P_r = 63\%$ in 50 years.;

LS: Life safety limit state. $P_r = 10\%$ in 50 years.;

NC: Collapse prevention limit state. $P_r = 5\%$ in 50 years.;

In case of IDA analysis also the state of collapse (loss of dynamic equilibrium) is considered, assuming a probability $P_r = 2\%$ in 50 years, or a return period equal to 2475 years.

Concerning the design PGA, in the new Italian code (see NTC 2008 [181]) the national country is subdivided into grids, and for each node three parameters are given, namely:

a_g**:** Maximum horizontal acceleration;

F_0**:** Maximum amplification factor for horizontal response spectrum;

T_C^***:** Period within the response spectrum where the constant velocity branch begins;

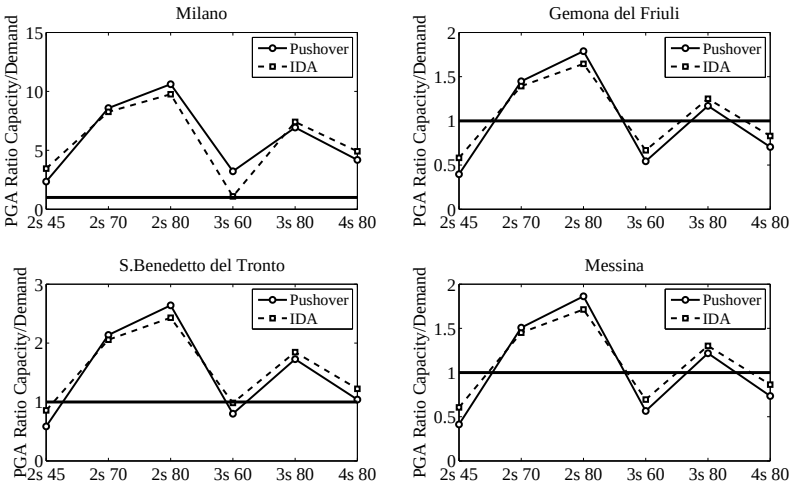

Figure 3.42: Ratio between capacity and demand PGA for NC limit state.

For each site the parameters listed above are selected considering limit states chosen, so with the chosen return period. Finally the PGA at design is computed as:

$$PGA_d = S_s \cdot a_g \tag{3.18}$$

where S_s is the soil factor, determined in the following way (for soil class B):

$$S_s := \begin{cases} 1.4 - 0.4F_o \cdot a_g, & \text{if } 1 \leq S_s \leq 1.2 \\ 1, & \text{if } S_s < 1 \\ 1.2, & \text{if } S_s > 1.2 \end{cases} \tag{3.19}$$

Figure 3.42 shows the ratio between the 5% percentile of the PGA carried out by nonlinear analyses and PGA at design considering NC limit state; a value higher than 1 means that the system studied has a capacity higher than the demand, so it is on the safety side. It is worth nothing that the structural systems where the proposed capacity design criteria is not appropriate are those where the ratio is lower than 1. Another issue, as just expressed above, is that pushover and IDA analysis predict values close one to each other, so the recommended value of 4% as maximum interstory drift is suitable also for precast systems.

To conclude, Figure 3.43 presents the ratio between capacity and demand in terms of probability of exceedance of NC limit state in 50 years. Here the difference are higher, because to compute MAF with pushover analysis an arbitrary dispersion was introduced to simulate record to record variability. Also in this case the ratio is lower than 1 for frames where the design method proposed in Biondini et al. [39] is not applicable.

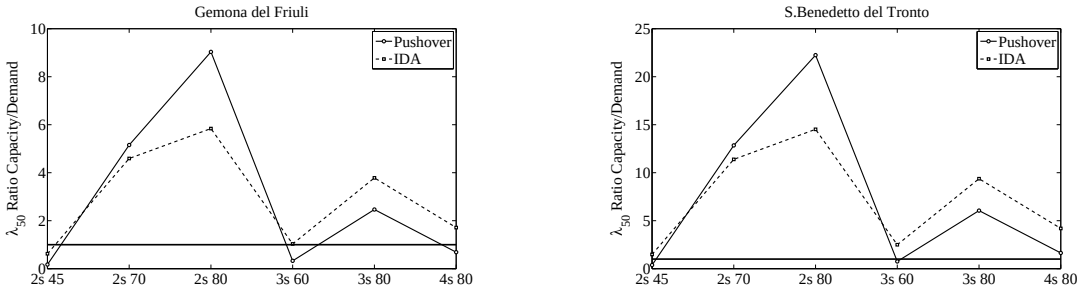

(a) Gemona.

(b) S.Benedetto

Figure 3.43: Ratio between capacity and demand probability of exceedance of NC limit state.

3.9 Conclusions

In this chapter the seismic performance of multistory precast frames at the beginning of their lifetime is assessed within the PEER methodology. First, the archetypes of the systems studied are presented, following a capacity design; the number of stories and the size of the columns change in order to cover the range of practical interest for these type of structures, underlining in which conditions the design method proposed in Biondini et al. [39] is reliable or not. Subsequently, the analytical model specifically developed in order to simulate collapse of RC frames is illustrated; since in past years the Ibarra model has been used for the seismic assessment of cast-in-situ frames, a preliminary validation is done considering the results of the experimental tests carried out at the ELSA Laboratory for the SAFECAST projects. The good match between numerical simulation and the outcome of one of the pseudo-dynamic test allows to extend this model for the simulation of collapse capacity of the archetypes investigated.

Two different approaches are then presented, in particular IDA analysis and pushover one; the main features of both methods are highlighted, with emphasis on advantages and drawbacks. Exploiting the advanced MonteCarlo procedure described in Chapter 2, 9 random variables are selected, each of them with the proper distribution, in order to include in the seismic assessment the modeling uncertainties. One of the most valuable issue is the selection of different limit states, just considering the overall behavior, as suggested by codes such as FEMA 356 [84], or investigating the local behavior of plastic hinges; the first choice is related to IDA analysis, while the second refers to pushover ones.

Finally, results of numerical simulation are presented for the two different methodologies; the effect of modeling variability is clearly depicted through the development of fragility curves; subsequently, considering different sites in Italy, the corresponding hazard curves are evaluated in order to compute the vulnerability for the systems investigated. For different limit states MAF are computed, and the seismic risk is then carried out considering two different parameters, namely the PGA capacity and the probability of collapse during the lifetime, here

set to 50 years. The comparison of the results between the two types of analysis clearly shows that for precast system the recommended values in terms of maximum interstory drift usually used for cast-in-situ regarding DL and LS limit states can be increased, due to higher flexibility of such systems. A maximum interstory drift equal to 4% for NC limit state is on the contrary a suitable threshold also for precast systems, because pushover and IDA analysis gives similar results considering different parameters such as PGA capacity or MAF for a particular limit state.

Since in the following all these analyses will be repeated for different times, considering the environmental hazard, pushover method is adopted, in order to reduce the computational cost within a probabilistic approach.

Chapter 4

Damage processes in concrete structures exposed to corrosion

4.1 Introduction

Environmental hazard plays a fundamental role in the lifetime performance of a generic structure. Typically in a structural analysis only the mechanical properties of the materials adopted are considered but, if the effects of aggressive agents are not properly taken into account, the capacity of the system investigated could be greatly overestimated. In particular, the present investigation focuses on how the seismic performance of RC frames can be affected by environmental hazard, because nowadays structural codes are based on time-invariant design criteria, but the combined effect of earthquake loading and aggressive agents can lead to undesired collapse mechanisms, with a consequent drop of structural capacity.

Among different damage processes on reinforced concrete structures, the corrosion of reinforcement bars is the main factor. At the beginning of their lifetime bars are protected by a passive film, but the diffusion of carbon dioxide (carbonation) or chlorides can lead to the initiation and propagation of such phenomenon. In the first case the pH drops near neutral conditions, so the passive film cannot developed and bars are subjected to a uniform corrosion; in the second one, chlorides destroy the protective film, starting a localized corrosion (pitting).

First, the electrochemical issues will be briefly revisited, considering both carbonation and chloride attack. Next section is devoted to the modeling of corrosion, with particular emphasis on chloride induced corrosion, being the subject of the present investigation. Subsequently, the effect of corrosion on reinforcement bars and concrete is illustrated, in order to highlight how the mechanical properties of the materials can be jeopardized during their lifetime. Finally, the consequences on the overall behavior are briefly summarized.

4.2 Theoretical aspects of the corrosion

At the beginning of the lifetime, the environment of concrete is highly alkaline (pH>12.5) due to the products of the hydration of concrete; within such conditions bars are protected for the presence of a passive film. However, during time the diffusion of aggressive agents tend to decrease the alkalinity of the environment or to destroy locally the film, leading to a drop in the mechanical performance of the materials.

4.2.1 Electrochemical issues

The phenomenon of corrosion in a metal is an electrochemical process that involves the following steps:

- Anodic reaction of metal oxidation, which develops the corrosion products and releases electrons in the crystal grating of the metal;
- Cathodic reaction where the oxygen is reduced and the electrons produced in the anodic reaction are spent;
- Electrons flow in the crystal grating, in which a current is generated within the metal;
- Generation of a current in the surrounding environment, with a migration of the ions in the liquid solution in contact with the metal.

Considering iron, the anodic reaction is:

$$\mathrm{Fe} \longrightarrow \mathrm{Fe}^{2+} + 2\,\mathrm{e} \tag{4.1}$$

while the corresponding cathodic reaction is the reduction of the oxygen;

$$\mathrm{O_2} + 2\,\mathrm{H_2O} + 4\,\mathrm{e} \longrightarrow 4\,\mathrm{OH}^- \tag{4.2}$$

Exploiting the Faraday's first law, the loss of mass can be expressed as:

$$|\Delta m| = \left|\frac{M}{z \cdot F}\right| q \tag{4.3}$$

where M is the molar mass of the metal [g/mol], z is the number of ions produced in the anodic reaction, q is the electric charge [C] and F is the Faraday's constant (96487 C). Dividing both terms in equation 4.3 by the area of the metal and time of interest, the velocity of mass lost is obtained:

$$v_m = \frac{1}{At}\,|\Delta m| = \frac{1}{At}\left|\frac{M}{z \cdot F}\right| q \tag{4.4}$$

Usually this parameter is expressed in [g/(m^{2}year)]; finally, the corrosion penetration v_p [µm/year] is obtained dividing the velocity of mass lost by the corresponding specific weight.

Because the exchange of electrons between anode and cathode, the corrosion current density i_{corr} is a measure of the velocity of corrosion; the process can be activated only if the potential at equilibrium of the anodic reaction is lower than that of the cathodic one, so $E_{eq,an} < E_{eq,cat}$. The potential corrosion E_{corr} and the velocity of corrosion i_{corr} can be evaluated looking at the Evan's diagrams.

The main product of the corrosion is the so called "red rust"; combining equations 4.1 and 4.2, in the presence of water and oxygen, it is possible to obtain:

$$2\,Fe(OH)_3 \longrightarrow 2\,H_2O + (Fe_2O_3)H_2O \tag{4.5}$$

where $(Fe_2O_3)H_2O$ is the red rust. Since the volume of the products of the corrosion is three to four times larger than the original volume of steel, the formation of the rust induces high internal stresses, so the concrete near the reinforcement tends to crack and eventually the spalling of the cover can occur. In any case, since all the reactions involved in the process need water and oxygen, if one of the two is not available in the environment corrosion cannot initiated.

4.2.2 Carbonatation

The environment within concrete is highly alkaline due to the hydration phenomena that occur; however, carbon dioxide (CO_2) presents in the atmosphere tends to react with the alkaline components and calcium idroxide ($Ca(OH)_2$). In this way the pH decreases, until the condition of passivation cannot be sustain. Although the carbonation reaction involves intermediate steps, in synthesis can be written as:

$$CO_2 + Ca(OH)_2 \longrightarrow CaCO_3 + H_2O \tag{4.6}$$

Such phenomenon does not induce a direct damage to the concrete, but has important consequences on the reinforcement steel; pH drops to values lower than 11.5 (threshold for conditions of passive without the presence of chlorides), so corrosion can start. Carbonation begins of the external surface of the concrete and then it propagates in depth. From an analytical point of view, penetration can be represented as stated in equation 4.7:

$$x = K \cdot t^{1/n} \tag{4.7}$$

where x is the penetration depth and t is time; n is a coefficient equal to 2 for porous concretes, while it is a little bit higher for compact ones. Finally, K is the carbonation coefficient, measured in [mm/year$^{1/2}$], and it is related to the velocity of the carbonation. This coefficient depends both from environmental conditions and characteristics of the concrete. It is possible to understand the depth of the carbonation on a generic structure spraying a solution of

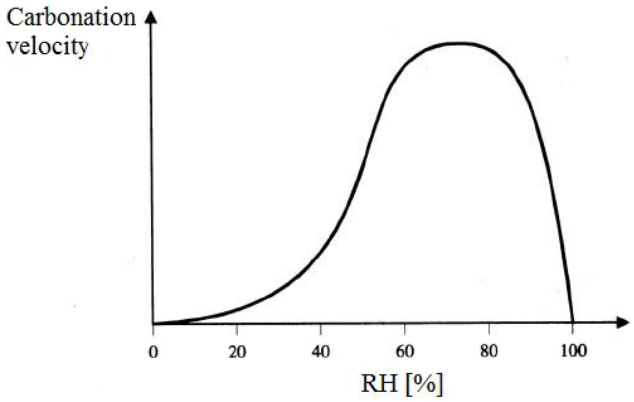

Figure 4.1: Influence of relative humidity on the velocity of carbonation, Pedeferri and Bertolini [194].

phenolphthalein on a concrete surface; the zones with a pink color are not carbonated yet, so the constant K in equation 4.7 can be estimated.

The main parameter to evaluate the propagation of the carbonation is the relative humidity of the concrete (RH); clearly the transport of carbon dioxide is easier if the porous are filled with air respect to water, so for saturated concrete propagation cannot occur. From the other side, chemical reaction needs water to start, so for a content of water lower than 40% the velocity is negligible. The waste conditions are reached if RH ranges from 50% to 80%, Figure 4.1.

It is extremely important to consider, in practice applications, the microclimate, because different zones of the structure can be subjected to different conditions of humidity and temperature. For example, the penetration of carbonation is always higher in the zones protected from the rain; key factors are the time in which a structure is wet and the frequency of wet/dry cycles. Typically, the coefficient of carbonation K ranges from 2 to 15 $\mathrm{mm/year^{1/2}}$]; exploiting equation 4.7, only for $K < 2.8$ it is possible to obtain a carbonation depth lower than 20 mm after 50 years, Figure 4.2.

Once the front line of carbonation reaches the reinforcement and the conditions for passivity disappear, corrosion can start in presence of oxygen and water. This process is mainly governed by the resistivity of the concrete, which is strictly related to the water content; for structures exposed to the atmosphere, oxygen is always available, so corrosion depends practically by the relative humidity of the concrete. In particular, a higher water content reduces the resistivity, so corrosion velocity increase. For good quality concrete, corrosion velocity is negligible for RH values lower than 80%; in this case, corrosion can be considered only during "wet time", namely the time when $RH > 80\%$. If concrete is saturated, corrosion can reach maximum velocity near 100-200 µm/year, Figure 4.3; however, in usual condition carbonation is related to a corrosion velocity ranges from 5-10 µm/year.

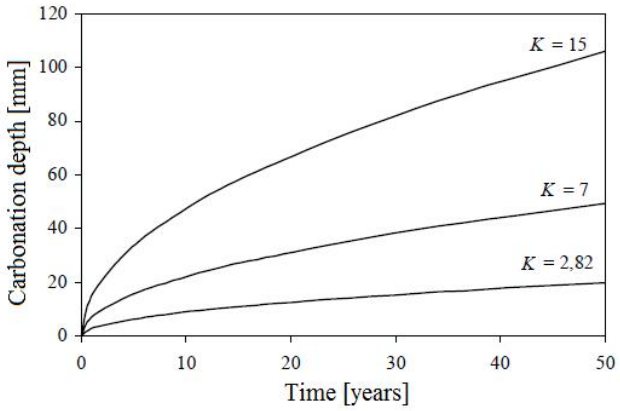

Figure 4.2: Influence of coefficient K on the carbonation depth, Pedeferri [193].

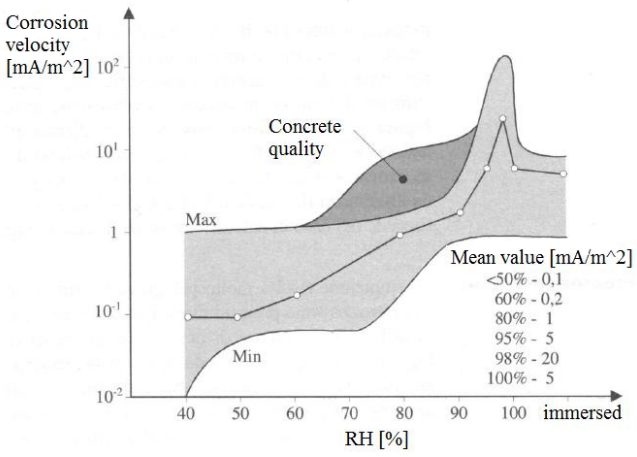

Figure 4.3: Influence of RH on carbonation corrosion velocity, Pedeferri [193].

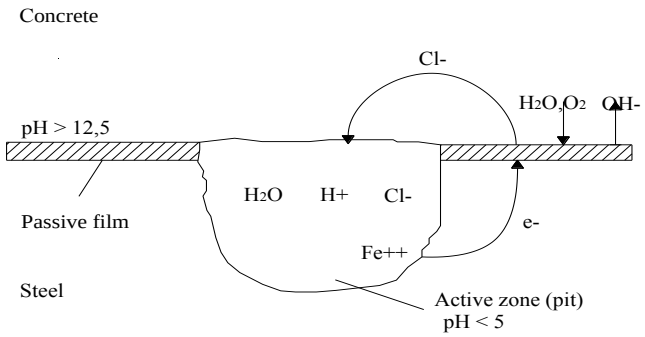

Figure 4.4: Pitting mechanism, Bertolini et al. [26].

4.2.3 Chloride attack

Corrosion induced by chlorides is different with respect to carbonation. In this case, the passive film around reinforcement bars is locally broken due to the presence of chlorides that penetrate in the concrete from outside, e.g. considering structure in a marine environment or roads where de-icing salts are used during winter. Chlorides can also be present in buildings for particular industrial applications. Corrosion starts when the chloride content near reinforcement reaches a critical threshold, that depends on the electrical potential of the bars; since this parameter is governed by the availability of oxygen, critical threshold is particularly low for structure exposed to atmosphere, while is higher for structures under water. Considering the local rupture of the film, corrosion follows the pitting mechanism; electric current from anodic zone to cathodic one induces a migration of chlorides toward the former one, with a significant decrease of pH. On the contrary, cathodic zone increase the alkaline conditions, enhancing the passive film, Figure 4.4.

It is important to remember that only the free chlorides in solution can attack the passive film, Razaqpur and Isgor [206]; however, for simplicity, critical threshold is given in terms of total chloride content, usually expressed in terms of percentile with respect to the mass of cement in the concrete. Critical threshold depends on the characteristics of the concrete and exposure conditions. In a Portland concrete, without carbonation, corrosion risk is not significant for values lower than 0.4%, while is high is the content exceeds 1%, Pedeferri [193]. In structures under water, typically corrosion cannot occur due to the absence of oxygen in the concrete porous.

During time, the concentration of chlorides within concrete increases until the critical threshold is reached; the corresponding time is called *initiation time*. The main parameters are the concentration of chlorides on the surface and the characteristics of the concrete that govern the transport of the aggressive agent. Such phenomenon is generally complex, potentially involving different mechanisms like permeation, diffusion and absorbing. Depending on the conditions, transport of chloride may be driven by one or a combination of these three mechanisms. Permeation occurs in the presence of a pressure gradient, and it is very important

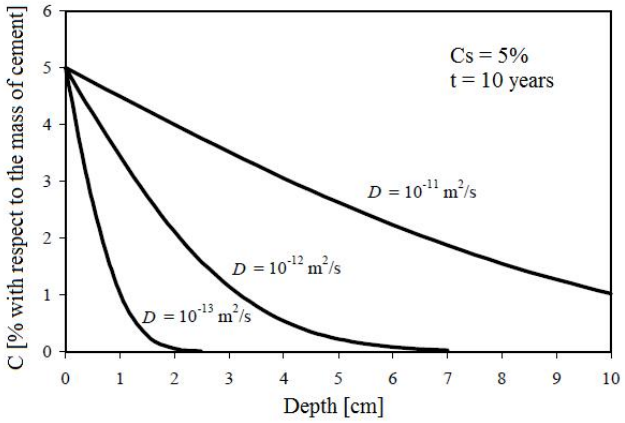

Figure 4.5: Chlorides diffusion profiles after 10 years, with a surface concentration $C_s = 5\%$, for different values of D (Pedeferri [193]).

for concrete structures under water such as offshore structures. Absorption is related to a capillary pore suction, and it is the predominant transport process when the unsaturated concrete is exposed to chloride solution.

Diffusion is the most commonly studied transport process of chloride ions. This mechanism depends by a concentration gradient created between the concrete element surface and the pore solution. Fick's law is applied in order to study the penetration of chlorides within concrete members; although pure diffusion occurs only for saturated concrete, the solution of equation 4.9 gives in any case acceptable results, confirmed by experimental tests on real structures. The uni-directional nonstationary flow, as stated before, is expressed by the second Fick's law, Stewart and Rosowsky [229]:

$$\frac{\partial C}{\partial t} = D_e \frac{\partial^2 C}{\partial x^2} \tag{4.8}$$

where C is the concentration of the aggressive agent and D_e is the effective diffusion coefficient, depending on the material. Assuming that the concentration on the surface is constant, as well as D_e, if at time 0 the material does not contain chlorides, the solution of equation 4.8 is:

$$C(x,t) = C_s \cdot [1 - \text{erf}\left(\frac{x}{2\sqrt{D_e t}}\right)] \tag{4.9}$$

where C_s is the concentration on the surface, and erf is the error function. This solution is also used to estimate the diffusion coefficient, comparing the profiles obtained by equation 4.9 with those coming from experimental tests. It ranges from 10^{-13} to $10 \times 10^{-10}\,\text{m}^2/\text{s}$ depending on the characteristics of the concrete; in Figure 4.5 different chlorides diffusion profiles are shown, depending on the diffusion coefficient adopted.

Once the chloride content reaches the critical threshold around reinforcement bars, corrosion occurs, and the velocity can increase from $50 - 60\,\mu\text{m/year}$ up to $1\,\text{mm/year}$ if the relative humidity grows from 70% to 90% and the chloride content increase from 1% to 3%. In

a relatively limited time the area of reinforcement bars can drop to unacceptable values, determining a premature failure of the structural element.

Next sections are devoted to the modeling of the corrosion phenomenon, with reference to chloride induced corrosion, analyzing the effects on the materials (steel and concrete), and on a global level.

4.3 Modeling of the corrosion phenomenon

Corrosion is a complex phenomenon, involving different mechanisms and depending on many parameters. In literature different studies can be found, in order to understand the fundamental factors. Both experimental tests and numerical simulations has been carried out, with the purpose to investigate the effects on a local and a global level, and also to develop analytical models. Among different aggressive agents, the presence of chlorides plays the fundamental role, Vu and Stewart [242], so this section is dedicated to the study of chlorides induced corrosion. Regardless the type of corrosion, it is generally assumed that the evolution of damage in a generic structure follows the Tuutti formulation, Tuutti [230]: when the conditions for the onset of corrosion are reached, damage can propagate within concrete members, with a reduction of the cross-section of reinforcement bars and the develop of cracks, follow by the spalling of concrete cover and finally to the failure of structural member, Figure 4.6. Such approach gives only qualitative information on the evolution of damage, so the single factors need to be properly considered and studied; in any case some considerations can be done immediately. For example, as clearly indicated in Figure 4.6, it is not correct to break off the lifetime of a structure at the time where the corrosion starts, but it is essential to understand how different effects depicted in the figure can affect the capacity of the member and, of consequence, the capacity of the structural system.

4.3.1 Initiation phase

Initiation time is the time that elapses between the construction of the structure and the develop to favorable conditions for the beginning of the corrosion; with reference to chlorides induced corrosion, it means until when the concentration of the aggressive agents around reinforcement bars reaches the critical threshold. Using a concrete of good quality and a proper cover, initiation time can significantly increase, Figure 4.7.

As indicated before, the transport of chlorides in concrete is a complex phenomenon, involving different mechanisms; experimental tests carried out in the past have however demonstrated that the hypothesis of a diffusion mechanism is acceptable, using an effective diffusion coefficient D_e. As indicated above, the simplest model is the Fick's first law, which assumes a linear relationship between the mass flow and the concentration gradient. The combination of the Fick's model with the mass conservation principle leads to the Fick's second

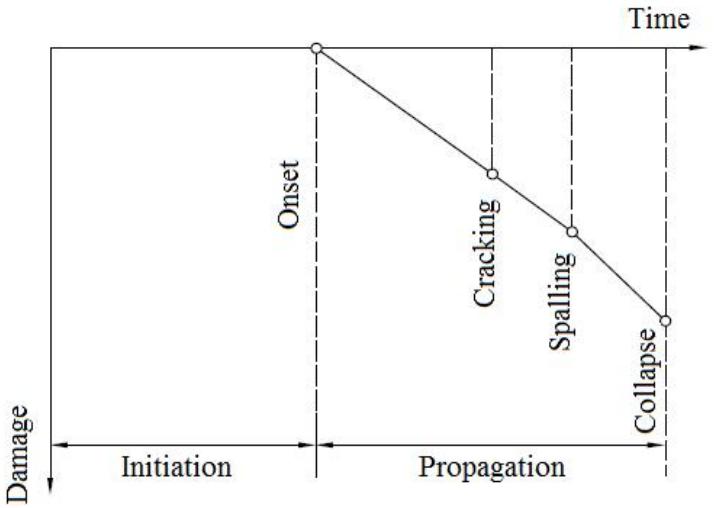

Figure 4.6: Damage evolution due to corrosion, Gjørv [99].

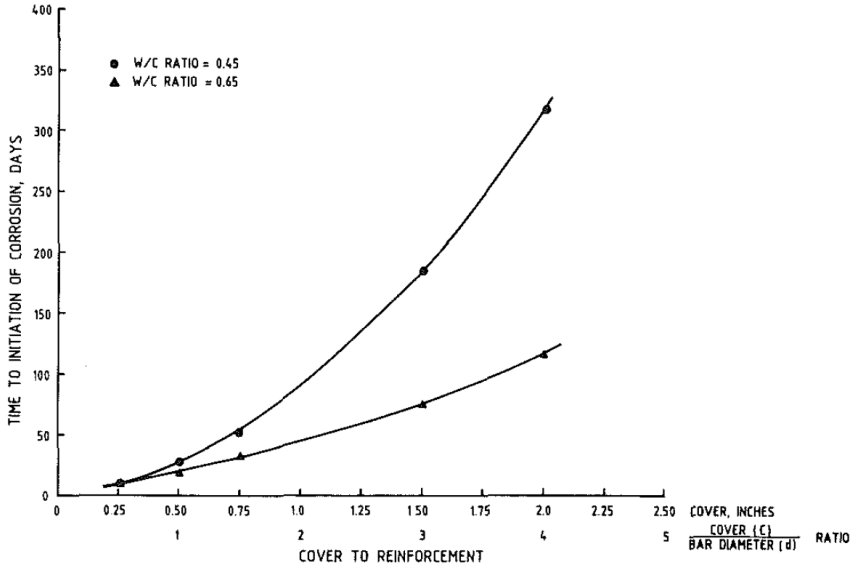

Figure 4.7: Influence of cover and concrete quality on corrosion initiation time, Rasheeduzzafar and Al-Gahtani [205].

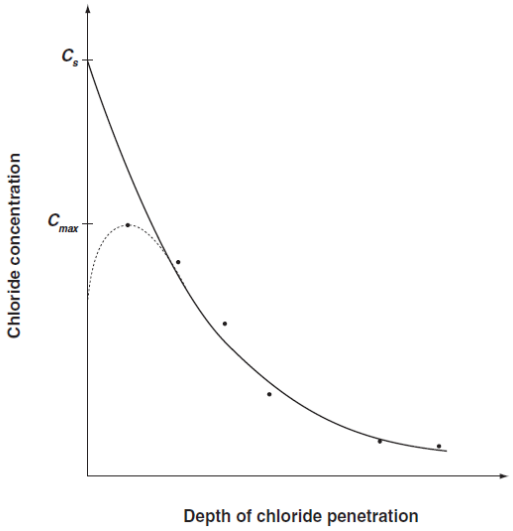

Figure 4.8: Definition of surface chloride concentration through a regression analysis of experimental data, Gjørv [99].

law; assuming an isotropic media, the problem is described by the following second-order partial differential equation, Glicksman [101]:

$$-\nabla \cdot (-D_e \nabla C) = \frac{\partial C}{\partial t} \tag{4.10}$$

where $C = C(\boldsymbol{x}, t)$ is the mass concentration of the component at point $\boldsymbol{x} = (x, y, z)$ and time t, and $\nabla C = \boldsymbol{grad} C$. Typically the problem of the penetration of chlorides into concrete cross-sections is studied in a uni-dimensional form, so the solution of equation 4.10 is expressed as:

$$C(x,t) = C_s \cdot \left[1 - \mathrm{erf}\left(\frac{x}{2\sqrt{D_e t}}\right)\right] \tag{4.11}$$

The concentration of chlorides on the surface C_s and the diffusion coefficient D_e can be obtained by a regression analysis on the results of experimental tests, as shown in Figure 4.8. The transport occurs only in the presence of water; if the concrete has a low relative humidity, there is no diffusion of chloride ions.

4.3.2 Onset of corrosion

When the passive film around reinforcement bars is locally broken, corrosion starts. This happens when the chloride content within the concrete reaches a threshold value, namely critical concentration C_{crit}. In literature there is no a common definition of critical concentration: from a scientific point of view, it is defined as the chloride content sufficient to locally brake the passive film, while from a practice vision it can be also defined as the concentration related to a visible damage on the structure. It is worth nothing to remember that only free chlorides

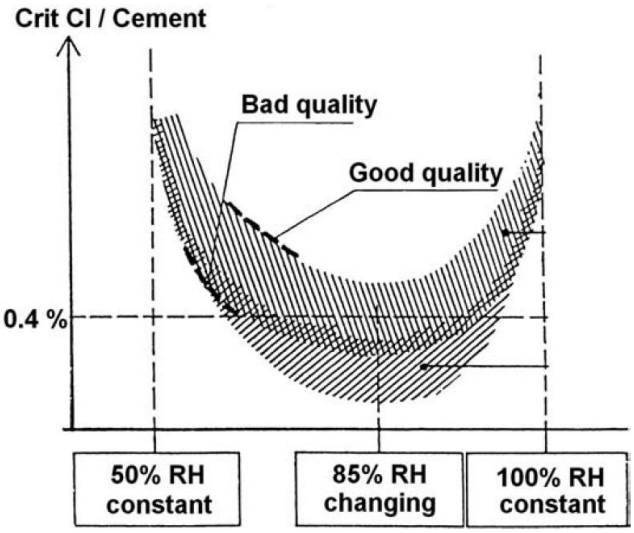

Figure 4.9: Relationship between critical concentration, exposure conditions and quality of the concrete, Gjørv [99].

are involved in the corrosion process, Razaqpur and Isgor [206], even if C_{crit} is expressed, for simplicity, in terms of total chloride content with respect to the mass of cement, or sometimes as the ratio between Cl^- and OH^-, that depends on the pH value.

In literature, suggested values for chloride corrosion on structures exposed to atmosphere ranges from 0.1% to 2%; Figure 4.9 shows the relationship between critical concentration, exposure conditions and quality of the concrete. As indicated, in order to perform durability analyses, a value equal to 0.4% is suggested. Because the problem investigated involves different parameters, each associated with uncertainties, a probabilistic approach should be adopted. Recommendations can be found in Model Code, fib 2006 [87], where the critical concentration is modeled as a random variable with a beta distribution, with lower and upper bound equal respectively to 0.2% and 2%, and mean value equal to 0.6%.

Once the critical concentration is known, equation 4.9 can be used to estimate the initiation time:

$$t_{init} = \frac{x^2}{4D_e}\left[\text{erf}^{-1}\left(1 - \frac{C_s}{C_{crit}}\right)\right]^{-2} \tag{4.12}$$

where x is the concrete cover, C_s is the surface concentration and C_{crit} is the critical content. In Enright and Frangopol [78] a probabilistic approach is carried out in order to evaluate the initiation time; in particular, for each of the parameters indicated in equation 4.12 is associated a probabilistic distribution, and a Monte Carlo analysis is performed. Some results are indicated in Figure 4.10.

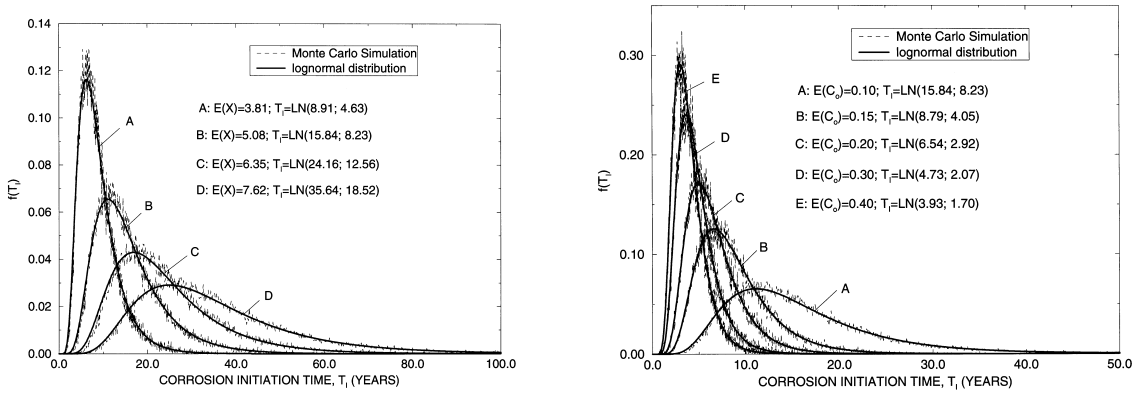

(a) Influence of cover depth.

(b) Influence of surface concentration.

Figure 4.10: Probabilistic estimation of corrosion initiation time, Enright and Frangopol [78].

4.3.3 Rate of corrosion

Next step concerns the evaluation of the corrosion velocity V_{corr} [µm/year], that can be expressed in terms of corrosion current intensity i_{corr} [mA/m^2] through the Faraday's law:

$$V_{corr} = 1.16 \cdot i_{corr} \tag{4.13}$$

There are different techniques to measure the corrosion current; one of the most used is the linear polarization technique (LPT), that enables the estimation of the polarization resistance and from that the corrosion rate. In particular if the metal/electrolyte interface is perturbed by a weak current, the potential E has a little variation dE, or in other words the metal is polarized. The ratio dE/i is the polarization resistance R_p, that is inversely proportional to the corrosion velocity:

$$i_{corr} = \frac{B}{R_p} \tag{4.14}$$

where B is the potential applied (usually equal to 26 mV for corroding and 52 mV for non-corroding steel) and R_p is the potential resistance (Ω^{-1} m^{-2}). Equation 4.14 gives a mean value, but the actual current in correspondence of the pit can be significantly higher, so the corrosion velocity obtained can underestimate the real penetration. Other details, as well as the description of other techniques, can be found in Razaqpur and Isgor [206].

One of the main parameters that affects the corrosion velocity is the resistivity of the concrete $\rho[\Omega\,\mathrm{m}]$, Andrade and Alonso [10] and Morris et al. [172]. Resistivity depends essentially on the water content in the pores of the concrete, as clearly indicated in Figure 4.11. Usually the relationship between resistivity and corrosion velocity can be approximated by a linear function, as indicated in Gulikers [107]; Figure 4.12 shows an example of it.

Corrosion velocity can be also expressed with reference to the ratio between the concentration of CH^- and OH^-, see Figure 4.13.

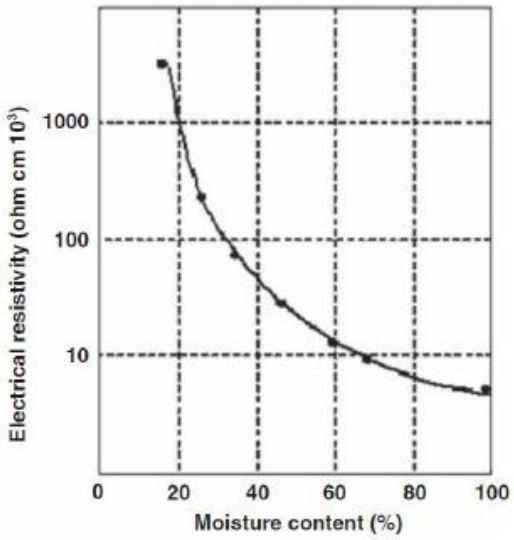

Figure 4.11: Influence of water content on concrete resistivity, Gjørv [99].

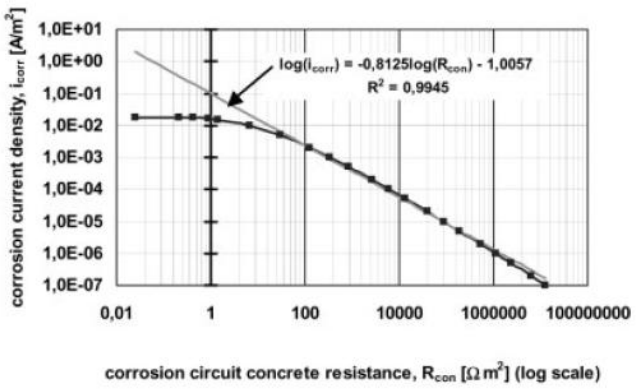

Figure 4.12: Example of linear relationship between concrete resistivity and corrosion velocity, Gulikers [107].

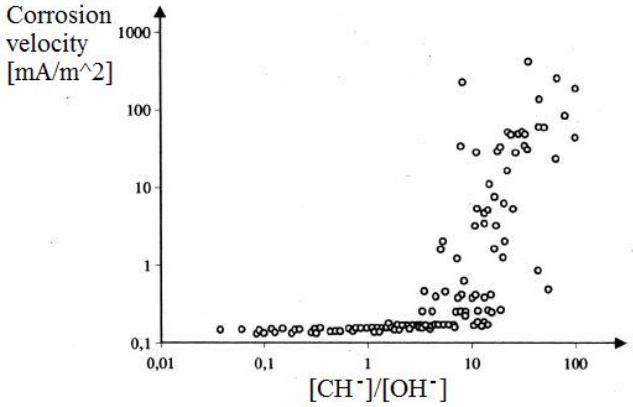

Figure 4.13: Relationship between corrosion velocity and concentration ratio CH^-/OH^-, Pedeferri and Bertolini [194].

Table 4.1: Qualitative description of corrosion rate, BRITE/EURAM [45].

Corrosion level	$i_{corr}[\mu A/cm^2]$
Negligible	< 0.1
Low	$0.1 - 0.5$
Moderate	$0.5 - 1$
High	> 1

In literature different empirical models are available, based on observed correlation between corrosion rate of steel in concrete and different parameters affecting it, Razaqpur and Isgor [206]; Liu and Weyers, see Chen and Mahadevan [54], developed an empirical model based on statistical analyses of experimental results carried out by accelerated corrosion testing programme on 44 uncracked bridge deck slabs. Corrosion rate i_{corr}, expressed in $\mu A/cm^2$, is defined as:

$$i_{corr} = 0.926 \exp\left[7.98 + 0.7771 \ln(1.69 C_t) - \frac{3.006}{T} - 0.000116 R_c + 2.24 t^{-0.215}\right] \tag{4.15}$$

where C_t is the chloride content at the steel level (kg/m^3), T is the temperature in Kelvin, R_c is the resistance (Ω) and t is the time, measured in years.

In the model developed by Vu and Stewart, Vu and Stewart [242], the O_2 availability at the steel surface is the governing parameter. For typical values of relative humidity and temperature ($RH = 75\%$ and T=20 °C), the corrosion rate up to 1 year can be related to the water to cement ratio (w/c) and thickness of concrete cover, Figure 4.14a:

$$i_{corr}(1) = \frac{37.8(1 - w/c)^{-1.64}}{x} \tag{4.16}$$

where w/c is the water to cement ratio and x is the cover thickness. Because the formation of rust products on the steel surface, the diffusion of the iron ions away from the steel surface tends to decrease, so the corrosion rate has consequently a reduction during time, Figure 4.14b:

$$i_{corr} = i_{corr(1)} 0.85 t_p^{-0.29} \tag{4.17}$$

where t_p is the propagation time. A comprehensive description of different models developed in past years can be found in Otieno et al. [184]. Finally, a qualitative description of corrosion rate can be found in Table 4.1, BRITE/EURAM [45] and Berto et al. [25].

In the following the effect of corrosion of steel reinforcement and concrete is analyzed; moreover, analytical models which describes the damage on these two materials are illustrated, in order to perform subsequently structural analyses during time, since it is important to

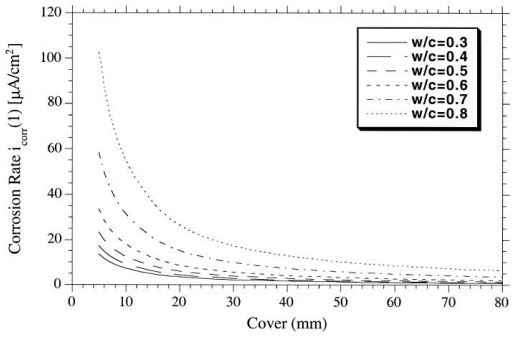

(a) Influence of cover depth and water to cement ratio.

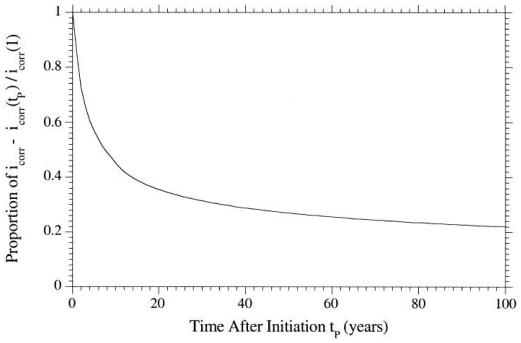

(b) Reduction of corrosion rate during time.

Figure 4.14: Corrosion rate prediction for Vu and Stewart model, Vu and Stewart [242].

have reliable tools for the assessment of lifetime performance of concrete structures, both for diffusion process and damage modeling.

4.4 Influence on reinforcements bars

The most significant effect of corrosion is the reduction of the cross-section of reinforcing steel bars. Depending on the source of corrosion, different models can be applied in order to simulate it, Figure 4.15. By denoting p the corrosion penetration depth, it is useful to introduce a dimensionless corrosion penetration index $\delta \in [0, 1]$ defined as:

$$\delta = \frac{p}{D_0} \tag{4.18}$$

where D_0 is the original diameter of the bar. Finally, the area of corroded steel can be represented by a function of corrosion penetration index, depending on type of corrosion.

$$A_s(\delta) = [1 - \delta_s(\delta)]A_{s0} \tag{4.19}$$

where $A_{s0} = \pi D_0^2/4$ is the area of the undamaged bar and $\delta_s = \delta_s(\delta)$ is the dimensionless damage index for reinforcing steel.

4.4.1 Uniform corrosion

In carbonated concrete, without a significant presence of chlorides, corrosion tends to develop in a uniform way around steel bars, Figure 4.15a. In this case the penetration depth $p = 2x$, and the damage function δ_s has the following expression:

$$\delta_s = \delta(2 - \delta) \tag{4.20}$$

Exploiting equation 4.19, the uniform reduction of area is:

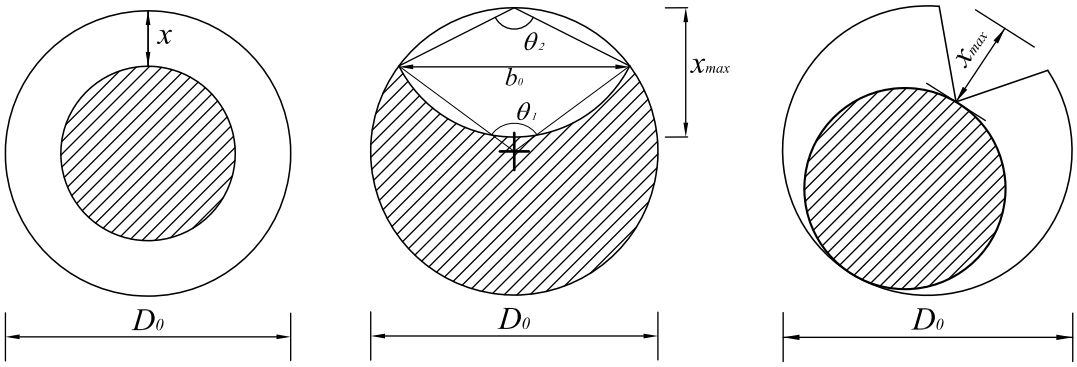

(a) Uniform corrosion. (b) Pitting corrosion. (c) Mix formulation.

Figure 4.15: Modeling of cross-section reduction of a steel bar, Biondini [28].

$$A_s(t) = \pi \left[\frac{D_0}{2} - x(t_p)\right]^2 \tag{4.21}$$

where t_p is the propagation time (the time related to the beginning of the corrosion). In Saetta et al. [216], it is possible to find a generalization of equation 4.21, which takes into account the possibility of a one-side or a two-side corrosion attack:

$$A_s(t) = \frac{\pi}{4}[D_0 - nx(t_p)]^2 \tag{4.22}$$

where coefficient n is equal to 1 or 2 in case of one-side or two-side attack, respectively.

4.4.2 Localized corrosion

If concrete is contaminated by chlorides, reduction of steel area is not uniform but tend to localize (pit); the model presented above is therefore not suitable. From measures of current intensity it is possible to obtain a mean value of penetration depth, $\overline{x}$; however, due to the localization of the damage, the maximum depth x_{max} in correspondence of the pit is significant higher. One solution is to define the pitting factor R, defined as:

$$R = \frac{x_{max}}{\overline{x}} \tag{4.23}$$

Usual values for pitting factor ranges from 4 to 8 in case of natural corrosion, and between 5 and 13 for accelerated tests, Gonzalez et al. [104]. Concerning spatial distribution, pits usually do not develop along concrete cracks but have a random distribution, depending on the presence of defects in the passive layer or at the interface, Zhang et al. [250]. Since pits have an irregular shape, simplified models are used; in particular, a hemispherical shape is assumed, Val and Melchers [231], where pitting surface is characterized by a circle with a radius equal to x_{max}, Figure 4.15b. The model is described by the following parameters, Biondini [28]:

$$\delta_s := \begin{cases} \delta_{s1} + \delta_{s2}, & \text{if} \quad 0 \leq \delta \leq 1/\sqrt{2} \\ 1 - \delta_{s1} + \delta_{s2}, & \text{if} \quad 1/\sqrt{2} < \delta \leq 1 \end{cases} \tag{4.24}$$

where:

$$\begin{aligned} \delta_{s1} &= \frac{1}{2\pi}(\vartheta_1 - 2\beta\left|1 - 2\delta^2\right|) \\ \delta_{s2} &= \frac{2\delta^2}{\pi}(\vartheta_2 - \beta) \end{aligned} \tag{4.25}$$

Finally, with reference to Figure 4.15b:

$$\begin{aligned} \beta &= \frac{b_0}{D_0} = 2\delta\sqrt{1-\delta^2} \\ \vartheta_1 &= 2\arcsin\beta \\ \vartheta_2 &= 2\arcsin\left(\frac{\beta}{2\delta}\right) \end{aligned} \tag{4.26}$$

It is possible also to include both types of corrosion in a single model, see Figure 4.15c; in this case the localized corrosion (with the formation of the pit) is coupled with a uniform one. The same damage function introduced before for uniform corrosion is applied (equation 4.20), using a penetration depth $p = x_{max}$; if a pitting factor R equal to 2 is considered, this model predicts the same steel area reduction of the uniform corrosion:

$$\Delta A_s = \frac{\pi}{4}(2p \cdot D_0 - p) \tag{4.27}$$

Such approach could be reliable to simulate results of accelerated corroded tests, but not appropriate for natural corrosion, where models depicted in Figures 4.15a and 4.15b are more appropriate, Zhang et al. [250].

4.4.3 Influence on ductility and strength

Another important consequence of a corrosion attack is the reduction of ductility of steel bars, which could lead to a brittle behavior, as it is shown in Figure 4.16, where the changing from a ductile to brittle occurs with a mass loss around 13%. In literature, ductility reduction is expressed as a function of section loss; based on such results, ultimate deformation can be related to the damage function for steel, Vergani [237]:

$$\varepsilon_{su} := \begin{cases} \varepsilon_{su0}, & \text{if} \quad 0 \leq \delta_s \leq 0.016 \\ 0.1521\delta_s^{-0.4583}\varepsilon_{su0}, & \text{if} \quad 0.016 < \delta_s \leq 1 \end{cases} \tag{4.28}$$

where ε_{su0} is the ultimate strain for uncorroded bars.

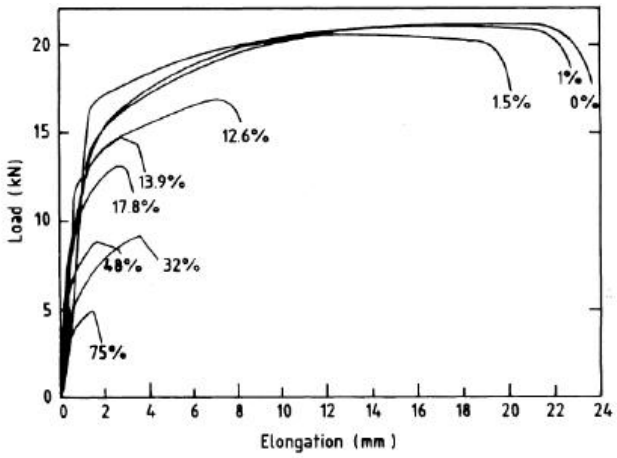

Figure 4.16: Load-elongation curves for bars, considering different corrosion levels, Almusallam [5].

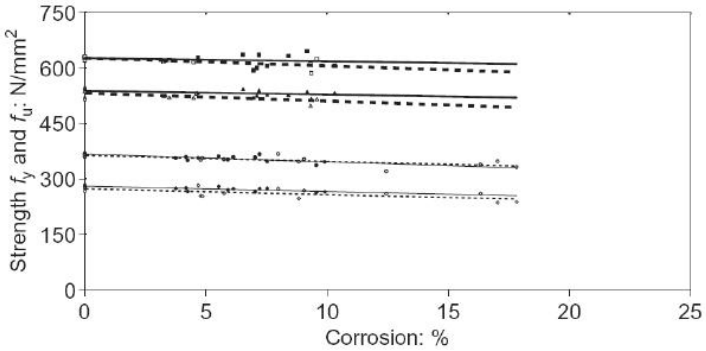

Figure 4.17: Reduction of yielding and ultimate strength for corroded bars, Cairns et al. [49].

About the evolution of yielding and ultimate strength, the reduction is negligible, as can be seen in Figure 4.17; in particular, a linear function can be extrapolated from the results of experimental tests on corroded bars, Cairns et al. [49]:

$$f = (1 - \beta \cdot Q) f_0 \tag{4.29}$$

where f_0 is the strength of the undamaged bars and Q is the corrosion level [%]. It is worth nothing to highlight that the strength reduction is related not to a uniform corrosion but to a localized one so, for the former case, a parameter $\beta = 0$ should be adopted. In any case, if someone wants to take into account the effect of corrosion on the strength, a value equal to 0.005 is suggested.

To conclude, the fundamental effect of corrosion on reinforcing bars is a reduction of cross-section area, with a simultaneous drop of ductility; the influence on mechanical properties is on the contrary not significant.

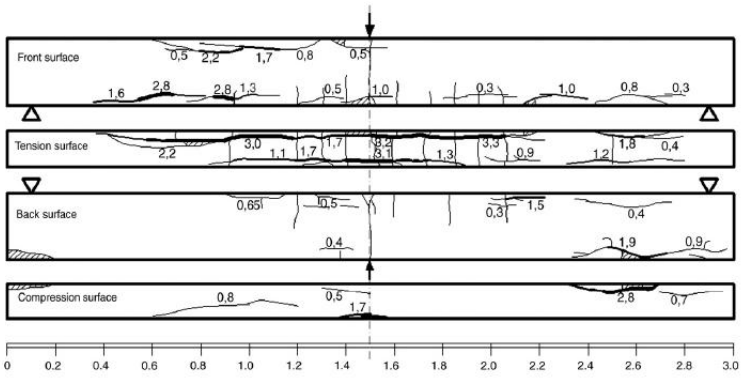

Figure 4.18: Development of cracks in a beam subjected to natural corrosion after 23 years of exposure, Zhang et al. [250].

4.5 Influence on concrete

The influence of corrosion of mechanical properties of RC members is not limited to reinforcing steel; in particular, in case of uniform corrosion with low penetration rate, the development of corrosion products leads to longitudinal cracks and cover spalling. This because rust and other oxidation products have a volume significant higher than 'virgin concrete'", see equation 4.5, therefore induce tension stress around steel bars. Clearly, once that longitudinal cracks appear, the diffusion of aggressive agents like chlorides within concrete sections is easier. Typically, cracks are longitudinal and parallel to the steel reinforcement, as can be seen in Figure 4.18; the arrangement of the bars governs the detachment mode of the concrete cover.

Two failure modes can be recognized, one with inclined fracture planes (scaling) and the other with horizontal planes parallel to longitudinal bars (delamination). Scaling occurs for wide spacing bars (Figure 4.19), in particular if:

$$S > 6D \tag{4.30}$$

where S is the space among reinforcing steel bars and D the diameter. On the contrary delamination, see Figure 4.20, is the predominant behavior if:

$$C > \frac{S - D}{2} \tag{4.31}$$

where C is the cover thickness. For corner bars, corrosion cracking induces local ruptures as those illustrated in Figure 4.21. The main parameters that influence cover cracking are the ratio c/D and the quality of the concrete; with a low ratio the corrosion products induce cracking in few time, while the presence of pores within the cementitious matrix allows an expansion of rust without the development of significant cracks.

Some authors have proposed models where the level of corrosion is predicted from measures of crack opening. In Vidal et al. [239], a linear relationship between crack opening and reduction of steel area is proposed:

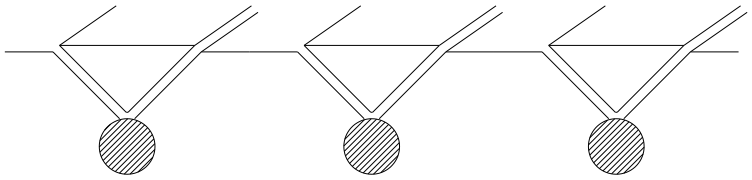

Figure 4.19: Concrete scaling due to corrosion cracking.

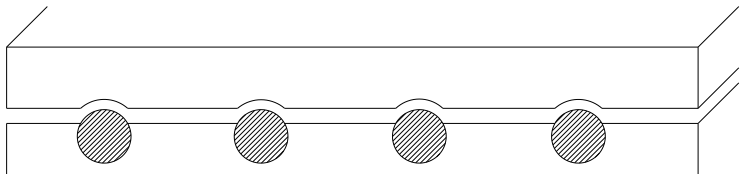

Figure 4.20: Delamination of concrete due to corrosion cracking.

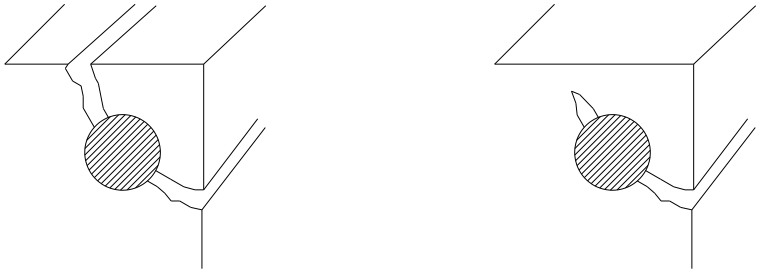

Figure 4.21: Corner effects due to corrosion cracking.

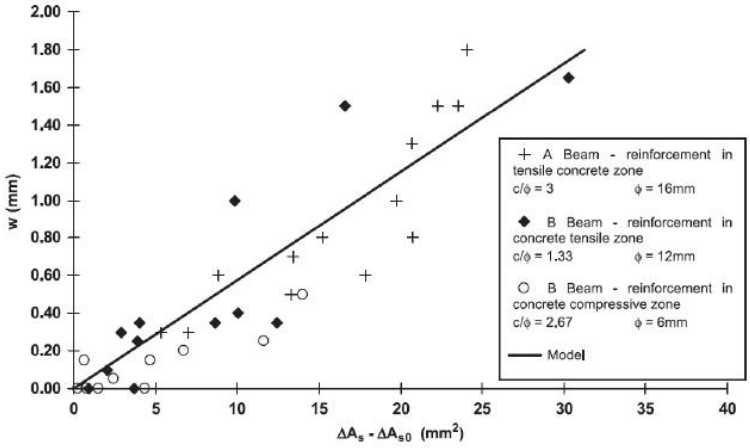

Figure 4.22: Relationship between crack opening and reduction of steel area, Vidal et al. [239]

$$w = K \cdot (\Delta A_s - \Delta A_{s0}) \tag{4.32}$$

where w is the crack opening [mm] and $K = 0.0575\,\text{mm}^{-1}$ (from Figure 4.22); ΔA_s is evaluated as indicated in equation 4.27, while ΔA_{s0} is the steel area necessary for cracking initiation, expressed in the following way:

$$\Delta A_{s0} = A_s \left[1 - \left(1 - \frac{R}{D_0}(7.53 - 9.32\frac{c}{D_0})10^{-3}\right)^2\right] \tag{4.33}$$

where R is the pitting factor, c the concrete cover and D_0 the initial diameter.

Other models proposed in literature try to estimate the time between corrosion initiation and the development of cracks in the concrete cover. In El Maaddawy and Soudki [75] an analytical model to estimate the time between corrosion initiation and cracking is developed; here there is the hypothesis that the corrosion products cover uniformly the steel bars, in order to develop a concentric circle around reinforcement. The different phases are depicted in Figure 4.23; once the corrosion products fill the porous layer around steel bar (free expansion), a radial pressure starts, and cracking appears when this pressure exceeds tension strength. In particular the authors propose a relationship among the steel mass loss and the internal radial pressure caused by the expansion of corrosion products, and from the knowledge of the corrosion rate, loss of mass steel and time to cracking can be evaluated. Other details can be found in El Maaddawy and Soudki [75] and Vergani [237].

To model the damage of concrete it is possible to follow the same approach as just seen for reinforcing steel; in this case a damage index δ_c is introduced, and the reduction of concrete area can be evaluated as:

$$A_c = [1 - \delta_c(\delta)]A_{c0} \tag{4.34}$$

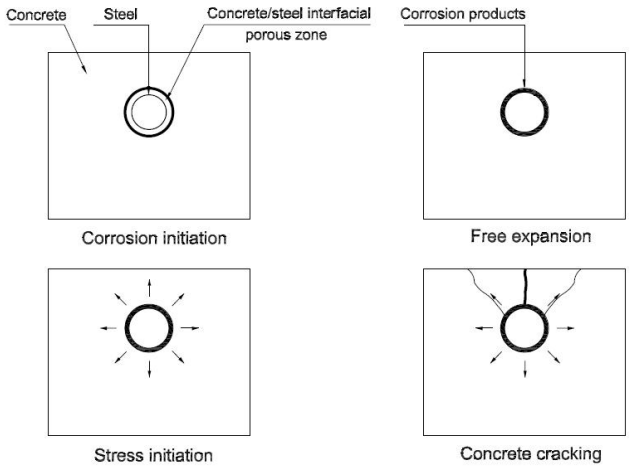

Figure 4.23: Cracking evolution in Maaddawy model, El Maaddawy and Soudki [75]

where A_{c0} is the area of the undamaged section. In this form it is not easy to find a relationship between damage index and corrosion penetration index, so the effect of corrosion can be related to a reduction of concrete strength, Vergani [237]:

$$f_c = [1 - \delta_c(\delta)] f_{c0} \tag{4.35}$$

where f_{c0} is the initial strength. One method to evaluate concrete strength reduction f_c due to cracking can be found in Coronelli and Gambarova [63]:

$$f_c = \frac{f_{c0}}{1 + \kappa \frac{\varepsilon_\perp}{\varepsilon_{c0}}} \tag{4.36}$$

where κ is a coefficient related to bar diameter and roughness (= 0.1 for medium diameter ribbed bars), ε_{c0} is the strain at peak stress in compression and $\varepsilon_\perp$ is an average value of the tensile strain in cracked concrete at right angles to the direction of the applied stress. The following relationship can be used:

$$\varepsilon_{perp} = \frac{b_f - b_i}{b_i} = \frac{\Delta b}{b_i} \tag{4.37}$$

where b_i is the width of the undamaged concrete cross-section and b_f is the width after cracking. The increase Δb of the member width is evaluated as:

$$\Delta b = n_{bar} w \tag{4.38}$$

where n_{bar} is the number of bars and w is the mean crack opening for each bar, equation 4.32. The reduction in concrete strength is usually applied to the entire concrete cover but, as stated before, the pattern of longitudinal cracks strongly depends on the arrangement of reinforcing steel.

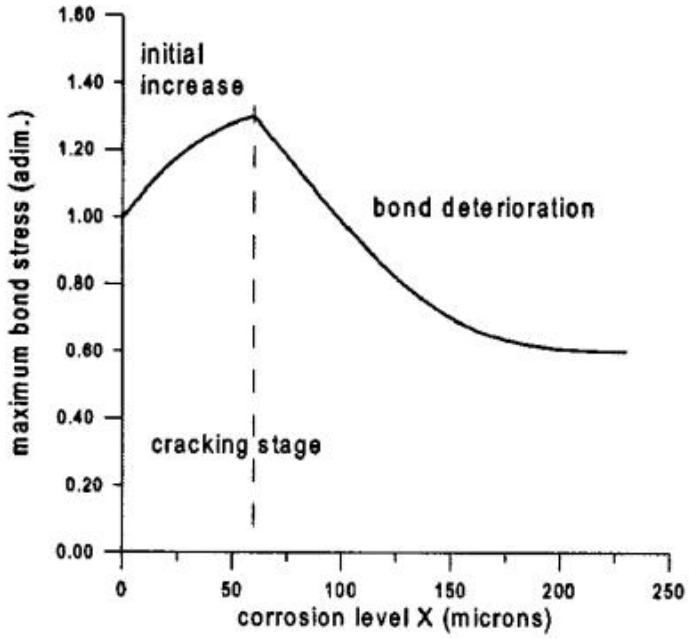

Figure 4.24: Variation of bond stress due to corrosion, Coronelli and Gambarova [63]

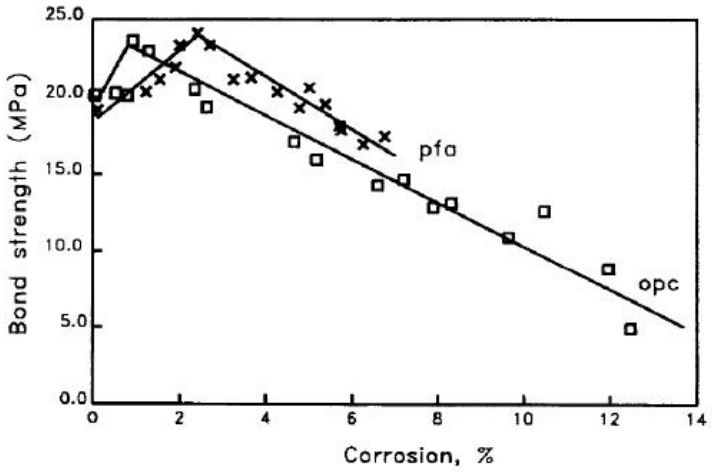

Figure 4.25: Relationship between corrosion and bond stress from pull-out tests, Cabrera [48]

It is worth nothing to underline that corrosion has an influence also on the bond between concrete and steel; in particular there is a reduction due to the development of longitudinal cracks and the formation of rust around steel bars. From result of experimental tests, maximum bond stress changes qualitatively as indicated in Figure 4.24; in an initial phase there is an increase in strength due to confinement induced by the expansion of corrosion products, and subsequently there is a significant reduction. Same trend can be seen also in Figure 4.25, where results coming from pull-out tests are illustrated, Cabrera [48]. A linear relationship is therefore proposed:

$$\tau_{bu} = 23.478 - 1.313 X_p \,[\text{MPa}] \tag{4.39}$$

where X_p is the corrosion level expressed in terms of mass loss [%]. Other relationships can be found in literature, but depend on the type of experimental (pull-out or bending) and the geometry of the specimens adopted.

4.6 Validation of damage model

In order to perform a reliable lifetime durability analysis on precast systems, it is important to validate damage models introduced in previous sections with reference to the influence of corrosion on steel bars and concrete. To this aim, numerical results of nonlinear analyses are compared with experimental tests described in Rodriguez et al. [210]. As an example, the simply supported beam shown in Figure 4.26 is considered for the validation procedure. The tested beams have been cast adding calcium chloride to the mixing water, subjected to an accelerated corrosion process with a current density of $100\,\mu\text{A/cm}^2$, and loaded up to failure. The beams type 11, with a lower reinforcement ratio, showed a flexural failure of the tensile bars. For beams type 31, with a higher reinforcement ratio, a crushing failure of concrete in compression occurred. For these members the mean and maximum values of corrosion penetration depth measured during the tests are listed in Table 4.4. The mechanical properties of concrete and steel are listed in Tables 4.2 and 4.3. For sake of brevity only beams type 11 will be considered.

It is worth nothing that maximum values of penetration are in some case three times the mean value; this is an important issue, because seems reasonable that the failure of the bars is related to the section with higher reduction. Moreover, the influence of corrosion is very significant on the stirrups, due to their small diameter.

Nonlinear analyses are performed by using OpenSees, Mazzoni et al. [163], where the beams are subdivided, due to symmetry, into 6 finite elements. Each element is modeled following a displacement-based approach, see Zienkiewicz and Taylor [251] for more details, even if in OpenSees also the force-based formulation is available, Spacone et al. [224] and Scott and Fenves [222]. A fiber discretization is used to describe RC cross-sections, in order to model

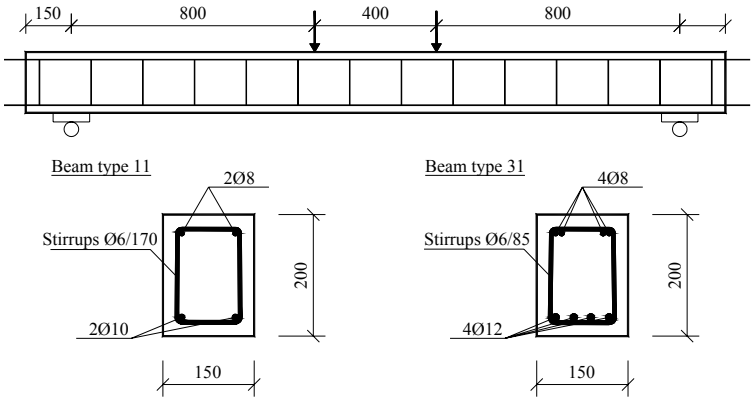

Figure 4.26: Geometrical dimension [mm], characteristics of the cross-sections and testig scheme, Biondini [28].

Table 4.2: Mechanical properties of concrete.

	Beam 111	**Beams 114-116**	**Beam 311**	**Beams 313-316**
$f_c\,[MPa]$	50	34	49	37
$f_{ct}\,[MPa]$	4.1	3.1	4.1	3.2
$E_c\,[GPa]$	37.3	33.8	37.1	34.5

Table 4.3: Mechanical properties of steel.

	Bars Ø8	**Bars Ø10**	**Bars Ø12**
$f_{sy}\,[MPa]$	615	575	585
$f_{su}\,[MPa]$	673	655	673
$E_s\,[GPa]$	210	210	210

Table 4.4: Measured corrosion penetration [mm]. Mean value (maximum value).

Beam	**Tensile bars**	**Compressive bars**	**Stirrups**
114	0.45(1.1)	0.52	0.39(1.1)
115	0.36(1.0)	0.26	0.37(3.0)
116	0.71(2.1)	0.48	0.66(5.0)
313	0.30(1.3)	0.20	0.35(2.8)
314	0.48(1.5)	0.26	0.50(4.0)
316	0.42(1.8)	0.37	0.54(4.3)

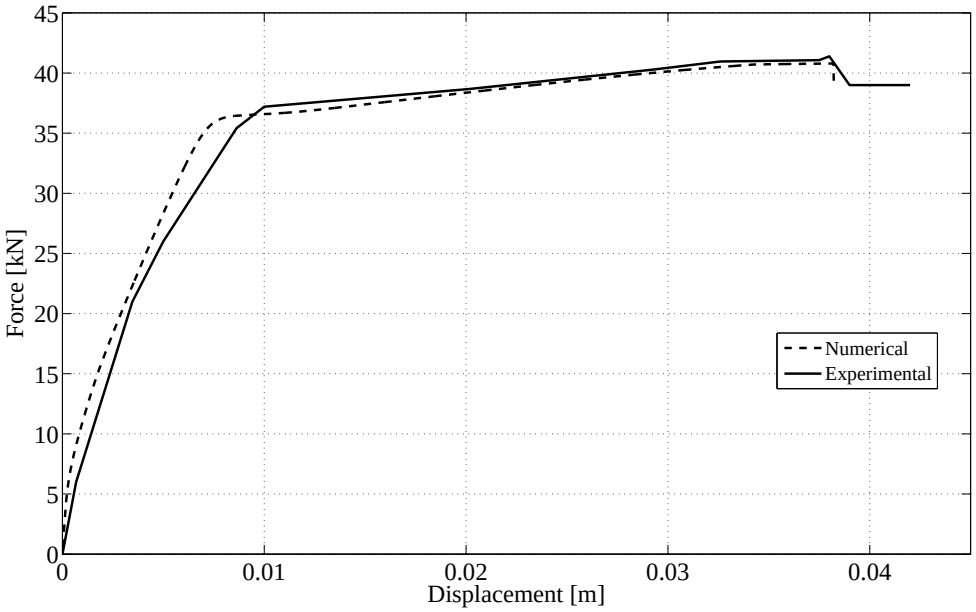

Figure 4.27: Force-displacement curve for beam 111 (no corrosion).

each longitudinal bars. For concrete, in compression the Mander model is adopted in order to take into account the confinement effect of stirrups, Mander et al. [158], while in tension a bilinear law is chosen. For steel, a simply bilinear model is used, with a hardening branch after yielding. All the analyses are performed considering a displacement control strategy, where each step Δx is set to 0.025 mm in order to have continuous curves. In all the experiments beams are pushed up to failure by using a 4 points bending test.

In Figure 4.27 is shown the comparison between experimental test and numerical simulation for beam 111 (undamaged), in terms of force-displacement curve; with reference to Figure 4.26, the displacement is referred to the middle section, while load is the sum of the concentrated loads P. As can be seen, yielding point and ultimate strength are very close to experimental data; about ultimate displacement, simulation predicts very well the failure point. Differences can be seen in the initial branch due to tensile strength of the concrete; however, the same behavior has been obtained also in other works, see e.g. Vergani [237].

In beam 115, subjected to accelerate corrosion for the shortest time, a mean penetration equal to 0.36 mm has been measured for tensile bars and 0.26 mm for compressive ones. At the beginning a uniform corrosion is assumed, considering only a reduction of steel bars area. The comparison between numerical and experimental result is illustrated in Figure 4.28; with respect to the undamaged situation there is a decrease in the ultimate strength and a corresponding increase in deformability. In any case the hypothesis of uniform corrosion is not appropriate, because simulation overestimates the strength and also the stiffness.

Due to the above considerations, the analysis is repeated with the hypothesis of a pitting

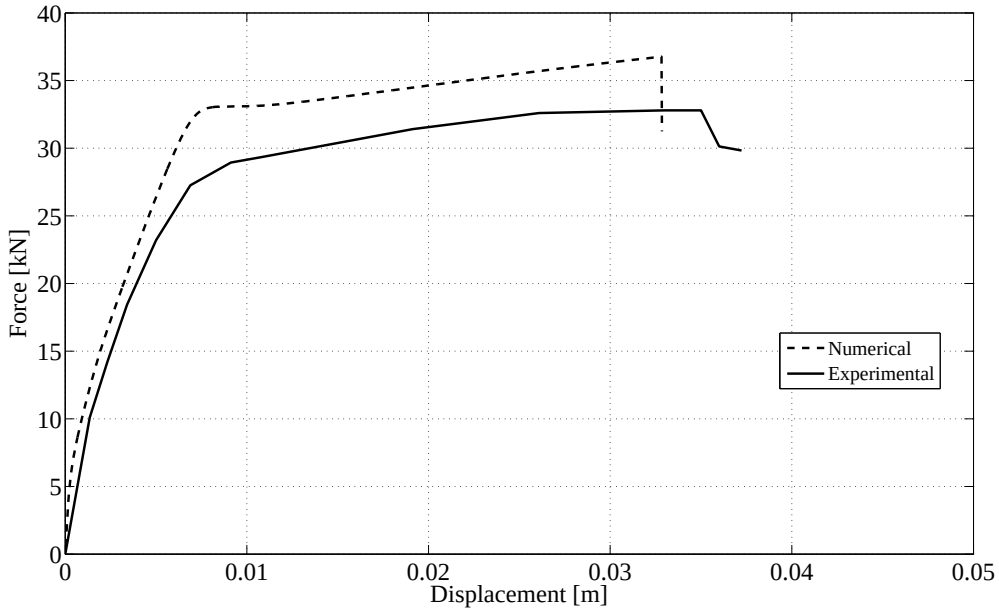

Figure 4.28: Force-displacement curve for beam 115 - Hypothesis of uniform corrosion.

corrosion, considering a maximum penetration depth equal to 1 mm, Table 4.4; Figure 4.29 shows the corresponding force-displacement diagram. In this case there is an improvement in the estimation of the ultimate strength, because after yielding the two curves are very close. In any case, as just seen for the case of uniform corrosion, numerical simulation underestimate a little bit the position of the failure point; in addition, initial stiffness is always bigger than actual value, and this can be related to the hypothesis of undamaged concrete.

To overcome this issue, in Figure 4.30 is shown the result of non-linear analysis considering also a damage of the concrete in terms of a reduction of compressive strength of the concrete cover as indicated in Table 4.2. Numerical simulation matches in a very good way the experimental result, both in the prediction of the failure point and estimation of the initial stiffness.

Finally, beam 114 is studied, which presents a higher value of corrosion (mean penetration equal to 0.45 mm and maximum penetration equal to 1.1 mm); in particular the corrosion penetration in compressive bars is double with respect to beam 115 (0.52 mm versus 0.26 mm). Force-displacement curve is presented in Figure 4.31; with respect to beam 111 and beam 115, from experimental data is evident a significant reduction of the displacement in the middle section, probably related to the loss of ductility of longitudinal bars. Even if the numerical model considers a pitting corrosion and a degradation of concrete cover, yielding point and ultimate strength are a little bit overestimated. Moreover, the failure point is underestimated.

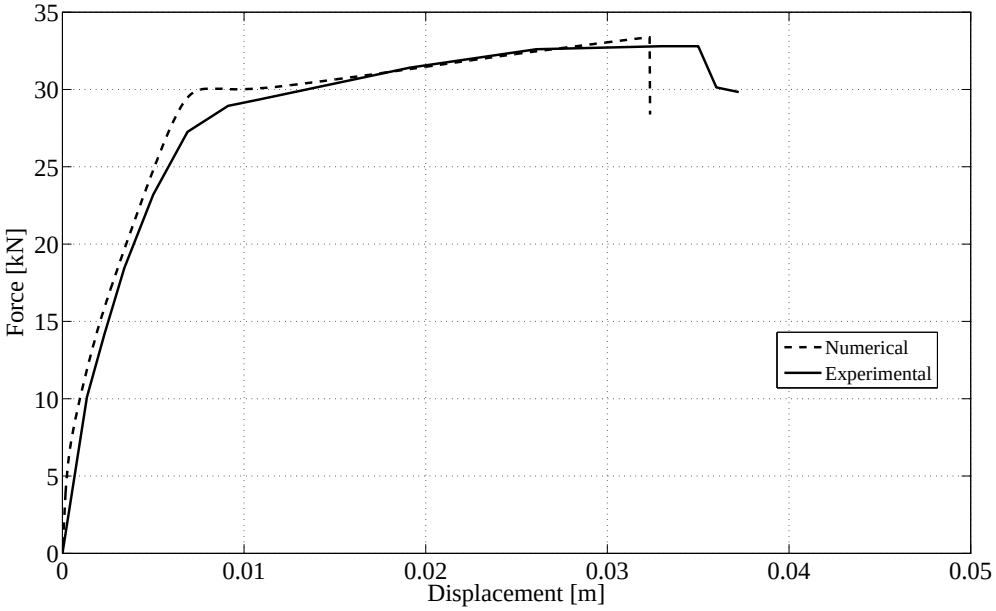

Figure 4.29: Force-displacement curve for beam 115 - Hypothesis of pitting corrosion.

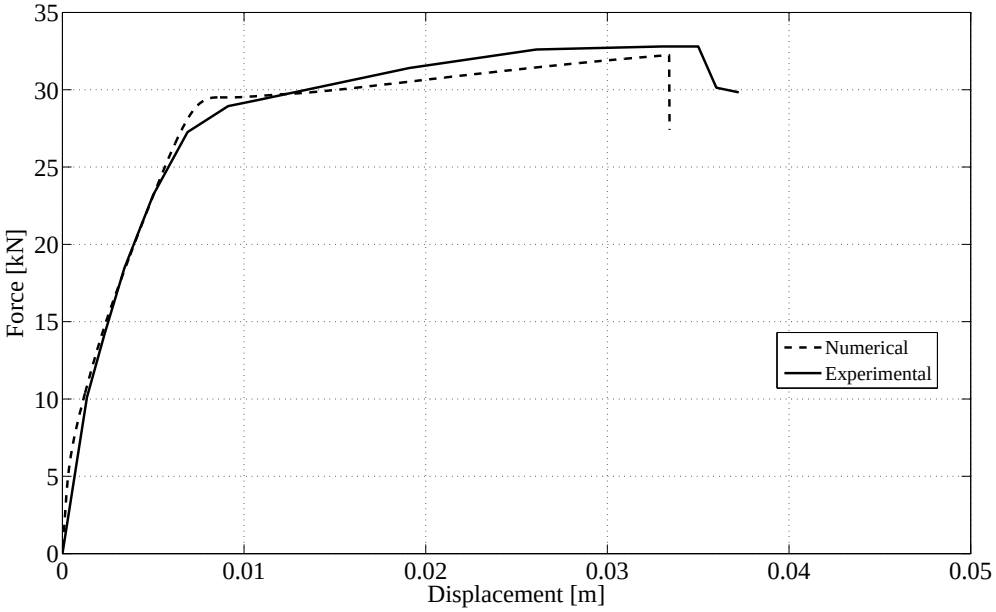

Figure 4.30: Force-displacement curve for beam 115 - Hypothesis of pitting corrosion and concrete cover damaged.

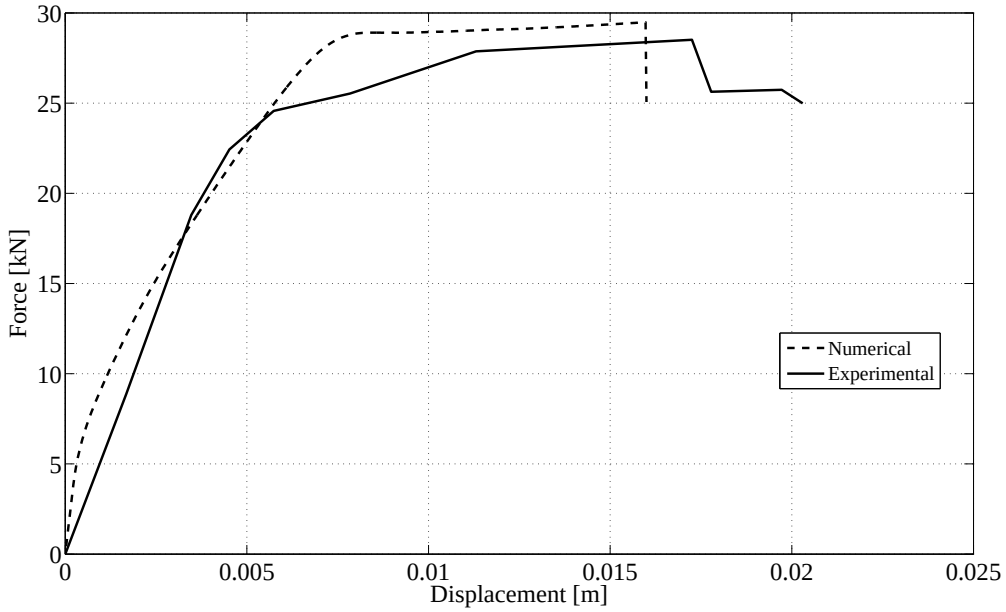

Figure 4.31: Force-displacement curve for beam 114 - Hypothesis of pitting corrosion and concrete cover damaged.

4.7 Influence on the global behavior

In the present investigation the aim is to study the lifetime seismic performance of multistory precast frames subjected to chloride induced corrosion, so it is important to highlight some results obtained in loading tests on structures subjected to corrosion, in order to understand the effect of this kind of environmental hazard on the overall behavior of structural systems.

In Castel et al. [51], beams subjected to natural corrosion and subsequently loaded have a reduction of ductility, stiffness and ultimate strength with respect to the undamaged situation; this depends on a reduction of ductility of reinforcing steel bars.

In Ballim and Reid [20] the effects of reinforcement corrosion on the serviceability deflections of reinforced concrete beams have been evaluated; beams under 4-point bending test have been subjected to 23% and 34% of the ultimate design load, measuring the central deflection and comparing it with the value related to undamaged beams. The result is a significant increase in the displacement, because with only a 6% of mass loss, beam deflections have been increased by $40 - 70\%$.

At the same time, an effort has been made in the last years to reproduce numerically the results indicated above, investigating the performance of different structural systems subjected to corrosion. As just an example, Figure 4.32 shows the result of a pushover analysis on a RC frame where both columns and beams are damaged by corrosion; a significant reduction of the total base shear strength, even thought gradual, is observed over the structural lifetime. Moreover, an abrupt reduction of the ultimate displacement and hence of the displacement

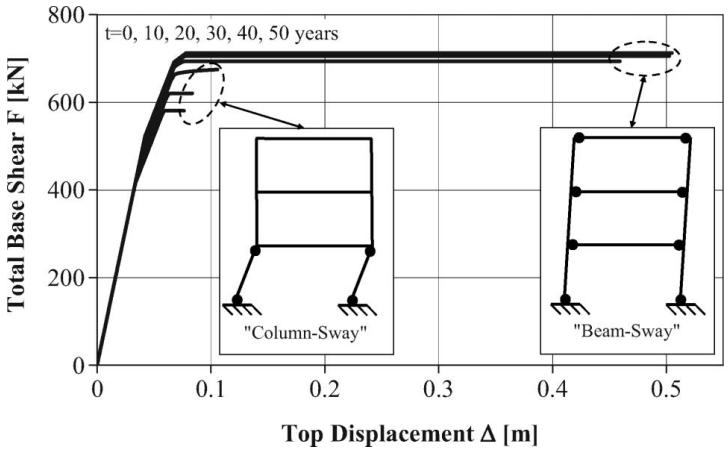

Figure 4.32: Total base shear F versus top displacement Δ for the low ductility frame, Biondini et al. [40]

ductility is obtained after about 20 to 30 years. In fact, as expected, due to the reduction of bending moment capacity of the columns, a change of collapse mechanism occurs moving from a typical "beam sway" to a "column sway" mechanism. As a consequence, since the overall dissipation capacity is totally lumped at the bottom of the columns, with all beams in the elastic range, a brittle failure occurs. Lifetime analysis can be applied not only to buildings but also on other structural systems such as bridges; remarkable examples can be found in Biondini et al. [34] and Biondini and Frangopol [30].

4.8 Conclusions

This chapter focuses on the damage process involving corrosion, because his leading importance in the lifetime assessment of performance of RC structural systems. In particular, different studies carried out in last two decades are presented, both considering the local effect of the materials and on the overall behavior. First, a brief review of theoretical aspects of corrosion is illustrated, starting from electrochemical issues regarding such phenomenon, and then considering the two typical sources of corrosion, namely carbonation and chloride propagation, because they are related to different mechanisms.

Subsequently, different phases involving corrosion process are illustrated, from initiation time to the onset of corrosion, with particular attention of chloride induced corrosion because the topic of the present investigation. It is explained how the diffusion model based on Fick's laws can be applied without loss of generality, introducing fundamental parameters such as initiation time and critical concentration. A section is devoted to the presentation of different models available in literature that predict the rate of corrosion, usually in terms of current intensity, subsequently transformed in a corrosion velocity µm/year exploiting Faraday's law. The influence of parameters such as resistivity of concrete and cover depth on corrosion rate is

shown, and also qualitative information are given.

After that, the local effects on the materials are studied. The fundamental aspect regarding reinforcing steel is the reduction of cross-section area, and different analytical models are presented, depending on type of corrosion (uniform, pitting or a mix formulation). Another important topic is the reduction of ductility of steel bars, and it is worth nothing that also with a not severe loss of mass the behavior of steel can change from ductile to brittle. About the influence on strength (yielding and ultimate), typically the effect is negligible.

Concerning concrete, damage can be induced by the formation of corrosion products like rust, which induce radial pressure in the cover, leading to cracks and spalling. Depending on the arrangement of reinforcing steel bars different mechanisms of cover detachment can occur, and models that predict rate of corrosion from crack opening and reduction of concrete strength are presented. Another effect is related to the change of bond stress; at the initial stage there is an improvement of bond strength due to the confinement induced by the expansion of corrosion products, and subsequently bond stress drops. Subsequently, the damage model here adopted is validated by simulating the experimental results coming from four-points bending tests on beams subjected to different rate of corrosion, underlining the effectiveness of the approach applied.

Last section is devoted to the illustration of the effects of corrosion on the overall behavior of RC structural members, considering the results of experimental tests performed in last years. Typically, corroded elements have a reduction of ultimate strength and ductility, and sometimes there is also a change in the failure mode, from ductile to brittle.

After this presentation, next chapter is dedicated to the analysis of the lifetime seismic performance of RC multistory precast frames introduced in Chapter 3, exploiting the analytical models here presented.

Chapter 5

Lifetime seismic performance of multistory precast buildings

5.1 Introduction

Due to the presence of aggressive agents in the environment like sulphates and chlorides, concrete structures are subjected to a progressive deterioration of their mechanical properties, which makes the structural systems less able to withstand the applied actions. A proper modeling of deterioration process is therefore essential to completely understand the phenomena illustrated in Chapter 4. In recent years, relevant advances have been accomplished in the fields of modeling, analysis, and design of deteriorating civil engineering systems, Biondini and Frangopol [29], and novel approaches to time-variant assessment and optimization of concrete structures have been proposed in deterministic and probabilistic terms, see e.g. Biondini et al. [34].

In this chapter the lifetime seismic performance of precast frames introduced previously is investigated. First, a special class of evolutionary algorithms, known as cellular automata, is presented, in order to simulate the diffusion process of chlorides within the concrete sections and subsequently the damage. The specific algorithm developed for the present study is validated by comparing the results coming from numerical analysis with the analytical solution of simple 1D and 2D problems. Both 1D and 2D approaches are considered, performing a parametric study to check the accuracy of the 1-D description of the problem with respect to the more accurate 2-D formulation, since the former method is proposed by some codes and recommendations (see e.g. fib 2006 [87]).

Subsequently, the tools implemented are used to simulate the progressive deterioration of RC structural members of precast systems, first at a local level, considering the time evolution of cross-section analysis, and then focusing on the overall behavior, in order to understand the influence of corrosion on the different limit states and to evaluate the corresponding seismic risk.

5.2 Simulation of diffusion processes

As indicated in Chapter 4, the diffusion of chemical components in solids can be described by relating the rate of mass diffusion to the concentration gradients responsible for the net mass transfer. The simplest model is represented by the Fick's first law, which assumes a linear relationship between the mass flow and the concentration gradient. The combination of the Fick's model with the mass conservation principle leads to the Fick's second law, which, in the case of a single component diffusion in isotropic media, is represented by equation 4.8, here repeated for convenience, Glicksman [101]:

$$\frac{\partial C}{\partial t} = D_e \nabla^2 C \tag{5.1}$$

where C is the concentration of the chemical species, D_e is the effective diffusion coefficient and the operator ∇ represents the derivative of a generic quantity with respect to the spatial variables; for example, in one-dimension problems, $\nabla u = u_x$ and, consequently, $\nabla^2 u = u_{xx}$.

As can be seen, equation 5.1 is a partial differential equation (PDE), in particular at the second order. Since many engineering problems can be described by using linear PDEs at the second order, it seems useful a briefly summary of their properties, before to introduce a possible numerical solution. Let assume for simplicity a 2D formulation, considering an open subset $\Omega \in \mathbb{R}^2$ and a *second order partial derivative differential operator* $A : C^2(\Omega) \rightarrow F(\Omega)$ which, $\forall u \in C^2(\Omega)$ and $(x, y) \in \Omega$, is defined as:

$$\begin{aligned} Au(x,y) = a(x,y)\frac{\partial^2 u}{\partial x^2} + 2b(x,y)\frac{\partial^2 u}{\partial x \partial y} + c(x,y)\frac{\partial^2 u}{\partial y^2} \\ + d(x,y)\frac{\partial u}{\partial x} + e(x,y)\frac{\partial u}{\partial y} + f(x,y)u \end{aligned} \tag{5.2}$$

where $a, b, c, d, e, f : \Omega \in \mathbb{R}$ are the *coefficients of the differential operator* A. A linear partial differential equation of the second order is therefore in the form:

$$Au(x,y) = g(x,y) \tag{5.3}$$

where $g : \Omega \in \mathbb{R}$ is a predefined function. Second order PDEs can be classified considering the value of the coefficients related to the second derivatives a, b and c in a generic point (x_0, y_0); denoting $a = a(x_0, y_0)$, $b = b(x_0, y_0)$ and $c = c(x_0, y_0)$, the operator A is:

- Elliptic if $b^2 - 4ac < 0$;
- Parabolic if $b^2 - 4ac = 0$;
- Hyperbolic if $b^2 - 4ac > 0$.

The same classification can be performed also in the light of the eigenvalues of the matrix M:

$$M(x_0, y_0) = \begin{bmatrix} a & b \\ b & c \end{bmatrix} \tag{5.4}$$

Operator A is:

- Elliptic if eigenvalues are both positive or negative;
- Parabolic if one of the eigenvalues is zero;
- Hyperbolic if eigenvalues have opposite sign.

It is possible to derive an archetype for each of these categories, namely:

Poisson equation

$$u_{xx} + u_{yy} + u_{zz} = f(x, y, z) \Leftrightarrow \nabla^2 u = f(x, y, z) \Leftrightarrow \Delta u = f(x, y, z) \tag{5.5}$$

The associated homogeneous equation $\Delta u = 0$ is the *Laplace equation*, prototype for elliptic PDEs.

Wave equation

$$u_{tt} = c^2(u_{xx} + u_{yy} + u_{zz}) \Leftrightarrow c^2(\nabla^2 u) \tag{5.6}$$

The wave equation is the prototype for hyperbolic PDEs.

Heat equation

$$u_t = \alpha(u_{xx} + u_{yy} + u_{zz}) \Leftrightarrow \alpha(\nabla^2 u) \tag{5.7}$$

The heat equation is the prototype for parabolic PDEs. As can be seen in equation 5.1, the second Fick's law is a particular application of the heat equation.

Since only for simple problems a partial differential equation can be solved in an analytical way, numerical procedures are essential. In literature different methods can be applied, Quarteroni et al. [204]; in the present investigation, the cellular automata approach is used, Schiff [219].

5.2.1 Basic concepts of cellular automata

Cellular automata were firstly introduced by von Neumann and Ulam in 1948-1950 (Burks and Von Neumann [47]) and subsequently developed by other researchers in many fields of science (see e.g. Wolfram [245]). Originally related to the study of self-replication problems on the Turing's machine, cellular automata left laboratories in the 1970s and became popular

in the academic circles with the now famous Game of Life invented by Conway (Conway [60], Gardner [94]). Basically, they represent simple mathematical idealizations of physical systems in which space and time are discrete, and physical quantities are taken from a finite set of discrete values. In fact, as already mentioned, any physical system satisfying differential equations may be approximated as a cellular automaton by introducing discrete coordinates and variables, as well as discrete time steps. Properly speaking, therefore, models based on cellular automata provide an alternative and more general approach to physical modeling rather than an approximation; they show a complex behavior analogous to that associated with complex differential equations, but in this case complexity emerges from the interaction of simple entities following simple rules.

In its basic form, a cellular automaton consists of a regular uniform grid of sites or cells, theoretically having infinite extension, with a discrete variable in each cell which can take only a finite number of states. The state of the cellular automaton is then completely specified by the values $s_i = s_i(t)$ of the variables at each cell i. During time, cellular automata evolve in discrete time steps according to a parallel state transition determined by a set of local rules: the variables $s_i^{k+1} = s_i(t_{k+1})$ at each site i at time t_{k+1} are updated synchronously based on the values of the variables s_n^k in their "neighborhood" n at the preceding time instant t_k. The neighborhood n of a cell i is typically taken to be the cell itself and a set of adjacent cells within a given radius r, or $i - r \leq n \leq i + r$. Thus, the dynamics of a cellular automaton can be formally represented as:

$$s_i^{k+1} = \Phi(s_i^k; s_n^k), \qquad i - r \leq n \leq i + r \tag{5.8}$$

where the function Φ is the evolutionary rule of the automaton. Clearly, a proper choice of the neighborhood plays a crucial role in determining the effectiveness of such a rule. Figure 5.1 shows an example of typical neighborhoods for two-dimensional cellular automata, but patterns of higher complexity can be also proposed. Since the actual extension of the automaton cannot be infinite as required by the theory, special attention has to be paid to neighborhoods along the sides of the finite grid, which may be defined in many different ways. The more frequent assumptions refer to the hypotheses of periodic boundaries, in which opposite cells are considered neighbors, or of absorbing boundaries, where the cells at the borders are assumed to have no neighbors beyond the limits of the grid. As an example of one-dimensional cellular automaton, consider a line of cells with the variable $s = s(t)$ at each cell i and time instant t_k which can take only the value $s_i^k = 0$ or $s_i^k = 1$. Concerning the evolutionary rule, defined on the base of a neighborhood with radius $r = 1$, it states that a cell remain alive or becomes alive if only one of its neighbors is also alive. If neither is alive, the cell dies from "isolation", or if both are alive it dies from "over-population".

Even with this very simple rule, complex behaviors can be nevertheless found. In fact, by assuming for example an initial state of the automaton consisting of a single cell with

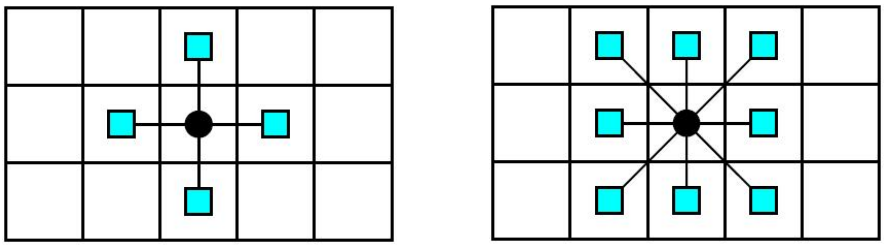

(a) von Neumann. (b) Moore.

Figure 5.1: Typical neighborhoods for two-dimensional cellular automata (radius $r = 1$), Biondini et al. [34].

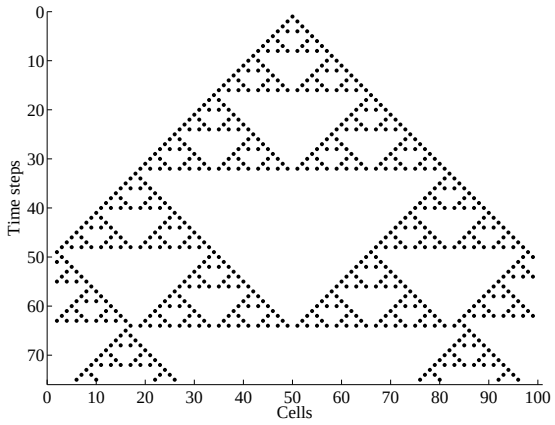

Figure 5.2: One-dimensional cellular automaton leading to geometrical pattern characterized by property of self-similarity and having fractal dimension.

value 1 and all other cells having value 0, after 75 time steps the pattern shown in Figure 5.2 appears, where the white cells denote the state $s_i^k = 0$ and the black ones the state $s_i^k = 1$. The geometry of such pattern is characterized by the property of self-similarity, since some of its regions, when magnified, are indistinguishable from the whole. In particular, it can be shown that such a self-similar pattern represents a fractal and can be characterized by a fractal dimension $\log_2 3 \approx 1.59$ (see also Wolfram [245]).

5.2.2 Simulation of transport process

Cellular automaton provides a very effective tools in the numerical solution of partial differential equations such as diffusion problems, see equation 5.1, or in multi-physics modeling (Vick [238]); in the present investigation the linear equation indicated below needs to be solved:

$$\frac{\partial C}{\partial t} = D_e \nabla^2 C \tag{5.9}$$

where the state variable C is the concentration of the chemical species in a diffusion process. A solution can be achieved through a proper selection of both the neighborhood n and the rule Φ. For example, the diffusion process described by Fick's laws in d dimensions ($d = 1, 2, 3$) can be effectively simulated by adopting a von Neumann neighborhood with radius $r = 1$ and the following rule of evolution (Biondini et al. [36] and Biondini et al. [37]):

$$C_i^{k+1} = \Phi_0 C_i^k + \sum_{j=1}^{d} (\Phi_j^- C_{i-1,j}^k + \Phi_j^+ C_{i+1,j}^k) \tag{5.10}$$

where the discrete variable $s_i^k = C_i^k = V(\boldsymbol{x_i}, t_k)$ represents the state variable in the cell i at time t_k. To satisfy the mass conservation law, the values of the evolutionary coefficients Φ_0, Φ_j^- and Φ_j^+ $(j = 1, \ldots, d)$ must obey to the following normality rule:

$$\Phi_0 + \sum_{j=1}^{d} (\Phi_j^- + \Phi_j^+) = 1 \tag{5.11}$$

In order to avoid directionality effects, for isotropic media the symmetry condition $\Phi_j^- = \Phi_j^+ = \Phi_1 (j = 1, \ldots, d)$ must be adopted. The equivalence between the evolutionary rule of the cellular automaton and the differential equations of mass diffusion can be proven by considering the problem in one-dimension for an homogeneous and isotropic solid medium. Therefore, specializing equation 5.10 and 5.11, where $d = 1$, it is possible to write:

$$C_i^{k+1} = \Phi_0 C_i^k + \frac{1 - \Phi_0}{2} (C_{i-1}^k + C_{i+1}^k) \tag{5.12}$$

The relationship can be arranged in an equivalent form:

$$C_(x, t + \Delta t) = \Phi_0 C_(x, t + \frac{1 - \Phi_0}{2} [C(x - \Delta x, t) + C(x + \Delta x, t)] \tag{5.13}$$

where $x_i = x$, $x_{i\pm1} = x \pm \Delta x$, $t_k = t$ and $t_{k+1} = t + \Delta t$. Subtracting $V(x, t)$ from both sides and dividing by Δt, the following expression is obtained:

$$\frac{C(x, t + \Delta t) - C(x, t)}{\Delta t} = \frac{1 - \Phi_0}{2} \frac{1}{\Delta t} [C(x - \Delta x, t) - 2C(x, t) + C(x + \Delta x, t)] \tag{5.14}$$

or, equally:

$$\frac{C(x, t + \Delta t) - C(x, t)}{\Delta t} = \frac{1 - \Phi_0}{2} \frac{\Delta x^2}{\Delta t} \frac{[C(x + \Delta x, t) - C(x, t)] - [C(x, t) - C(x - \Delta x, t)]}{\Delta x^2} \tag{5.15}$$

Assuming:

$$D = \frac{1 - \Phi_0}{2} \frac{\Delta x^2}{\Delta t} \tag{5.16}$$

and taking the limit $\Delta x \to 0$ and $\Delta t \to 0$ the equation here reported is derived:

$$\frac{\partial C(x,t)}{\partial t} = D\frac{\partial^2 C(x,t)}{\partial x^2} \tag{5.17}$$

The same procedure can be generalized in d dimensions; in particular equation 5.16 becomes:

$$D = \frac{1-\Phi_0}{2d}\frac{\Delta x^2}{\Delta t} = \Phi_1 \frac{\Delta x^2}{\Delta t} \tag{5.18}$$

Usually a deterministic value $\Phi_0 = 1/2$ is related to a good accuracy in the results; in any case an appropriate balance between grid dimension Δx and time step Δt must be achieved. With this aim, a suitable discretization in space and time may be chosen; since the diffusion coefficient is one of the input data of the problem, a consistent value of both grid dimension Δx and time step Δt is chosen to regulate the process according to equation 5.18. In the present investigation a deterministic definition of evolutionary coefficient is used; however, in order to consider stochastic effects in the diffusion process, a probabilistic formulation of the cellular automata can be applied, Biondini et al. [34].

5.2.3 1D and 2D formulation - Validation and comparison

In present study an algorithm for the resolution of the diffusion problem through cellular automata has been developed, both considering the 1D and 2D formulation. The validation is carried out by comparing the results coming from numerical simulation with the solution of simple problems where the analytical expression is available. Subsequently, by performing a parametric study, it is verified the accuracy of the 1D formulation with respect to the 2D approach, since the former method is proposed by some codes and recommendations (see e.g. fib 2006 [87]).

Case A: 1D problem

In this first example, the domain Ω is defined as $\Omega := [0, 0.5\,\mathrm{m}]$, and the only spatial variable is $x \in \Omega$. The chloride concentration on the surface C_0 is equal to $3\%\,[wt.\%c.]$, and two different values of the diffusion coefficient are considered, in order to explore the reliability of the numerical solution, namely $D_e = 10 \times 10^{-12}\,\mathrm{m^2/s}$ and $D_e = 25 \times 10^{-12}\,\mathrm{m^2/s}$, see fib 2006 [87], which correspond to CEM I 42.5 R with water to cement ratio equal respectively to 0.40 and 0.60. Other lower values of D_e are not considered since, as illustrated in next figures, numerical result matches practically in a perfect way the analytical solution, which is in the form:

$$C(x,t) = C_0[1 - \mathrm{erf}\left(\frac{x}{2\sqrt{D_e t}}\right)] \tag{5.19}$$

Chloride profiles evaluated by using equation 5.19 for different times ($t = 10, 20, 30, 40, 50$ years) can be seen in Figures 5.3a and 5.4a; concerning numerical solution, the evolutionary

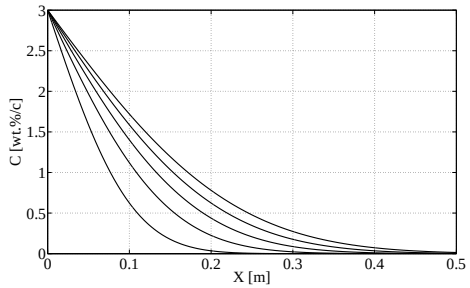

(a) Analytical solution for different times.

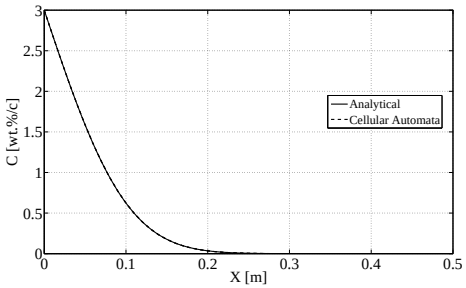

(b) $t = 10$ years.

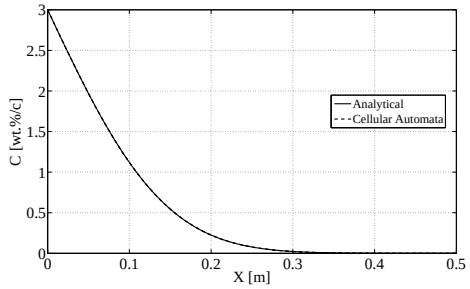

(c) $t = 20$ years.

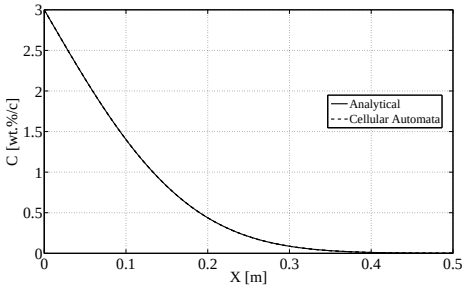

(d) $t = 30$ years.

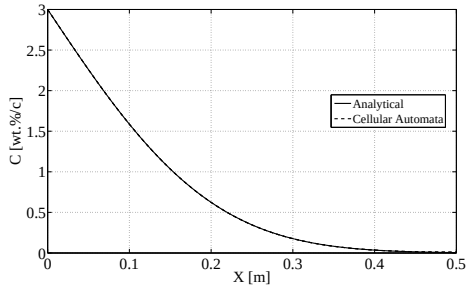

(e) $t = 40$ years.

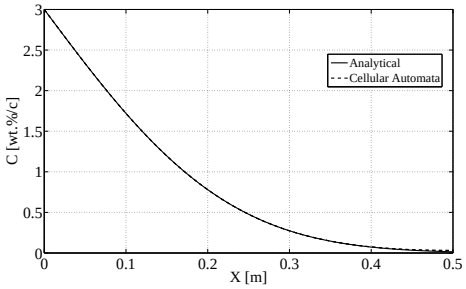

(f) $t = 50$ years.

Figure 5.3: Comparison between analytical and numerical solution for 1D problem, $D_e = 10 \cdot 10^{-12}\, m^2/s$.

coefficient Φ_0 is set to 1/2, and a grid step $\Delta x = 0.01$ m is chosen; time step Δt is therefore evaluated in order to satisfy equation 5.16. The accuracy of the adopted approach can be seen in Figures 5.3 and 5.4, where the comparison between analytical expression and numerical simulation is shown for different times and for the two different values of diffusion coefficient. There is a very good agreement between different profiles, and only for the higher diffusion coefficient the curves tend to have a gap beyond 30 years; in any case numerical solution is on the safety side because it estimates higher values of the chlorides concentration along the domain Ω.

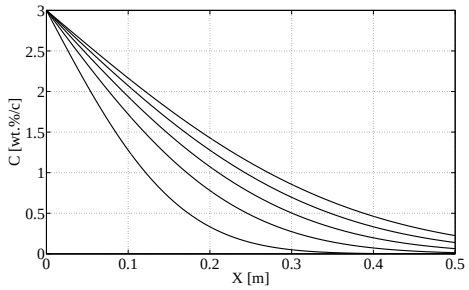

(a) Analytical solution for different times.

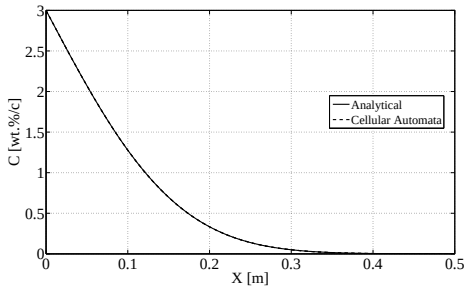

(b) $t = 10$ years.

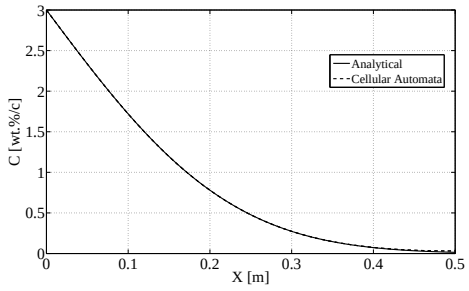

(c) $t = 20$ years.

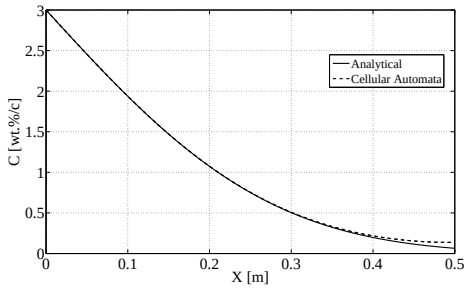

(d) $t = 30$ years.

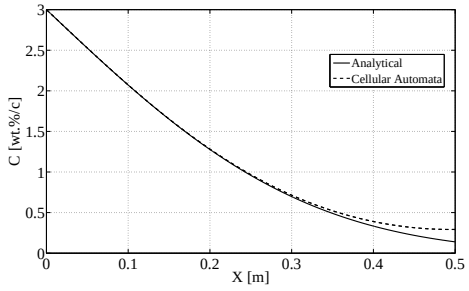

(e) $t = 40$ years.

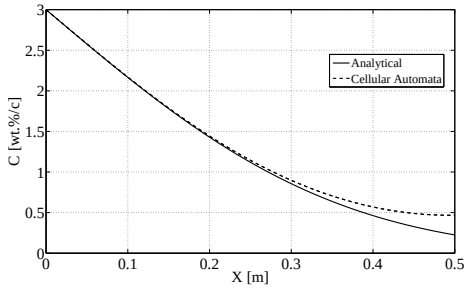

(f) $t = 50$ years.

Figure 5.4: Comparison between analytical and numerical solution for 1D problem, $D_e = 25 \cdot 10^{-12}\, m^2/s$.

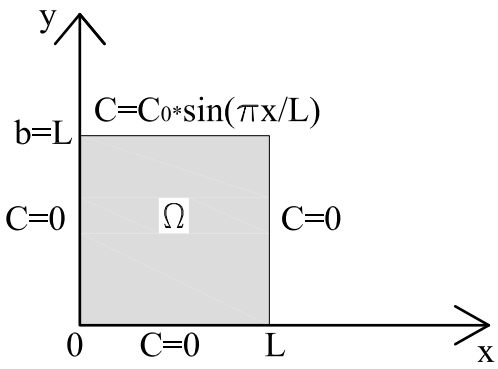

Figure 5.5: 2D domain to check asymptotic behavior of numerical solution.

Case B: 2D problem - Asymptotic behavior

In this second example the asymptotic behavior of the solution predicted by cellular automata is studied, considering the 2D domain depicted in Figure 5.5. Each side of the domain Ω has a length equal to $L = 0.45\,\mathrm{m}$, and boundary conditions are defined as:

$$C(x,y) := \begin{cases} 0, & \text{on } x = 0, L \quad \forall y \\ 0, & \text{on } y = 0 \quad \forall x \\ C_0 \sin(\pi x/L), & \text{on } y = L \quad \forall x \end{cases} \tag{5.20}$$

where $C_0 = 3\%\,[wt.\%c.]$ is the concentration on the surface, keeping constant for all the analysis. Because the focus is on the asymptotic behavior, the *Laplace equation* $\nabla^2 C(x,y) = 0$ needs to be solved. In this case, exploiting the separation of variables and applying boundary conditions, analytical solution is:

$$C(x,y) = \frac{C_0}{\sinh(\pi b/L)} \sin\left(\frac{\pi x}{L}\right) \sin\left(\frac{\pi y}{L}\right) \tag{5.21}$$

Regarding numerical analysis, a grid step $\Delta x = 0.01\,\mathrm{m}$ is used and two different values of diffusion coefficient, $D_e = 10 \times 10^{-12}\,\mathrm{m^2/s}$ and $D_e = 25 \times 10^{-12}\,\mathrm{m^2/s}$, are considered. Asymptotic behavior is simulated considering different times; theoretically, for $t \to \infty$, cellular automata should tend to the analytical result. Figures 5.6a and 5.7a show the distribution of concentration, normalized with respect to the surface value C_0, coming from equation 5.21, for the two different values of diffusion coefficient; clearly the pictures are identical because Laplace equation is not influenced by D_e. The comparison between analytical and numerical solution is on the contrary depicted in Figures 5.6b and 5.7b, considering a section in the middle of the domain Ω, namely $y = b/2$, $\forall x$ and different times, $t = 10, 20, 30, 50, 100, 200$ years. Correctly, when time increases, theoretically to infinite, solution predicted by cellular automata is very close to the analytical one; this is the proof that the algorithm satisfies the asymptotic behavior. To complete the validation of the developed numerical code, next

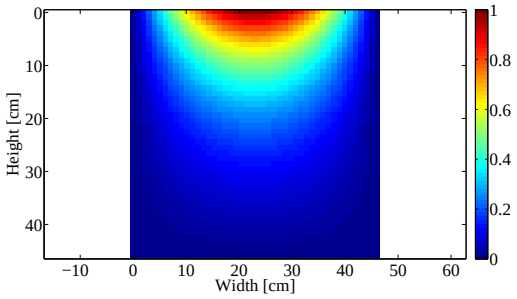

(a) Analytical solution.

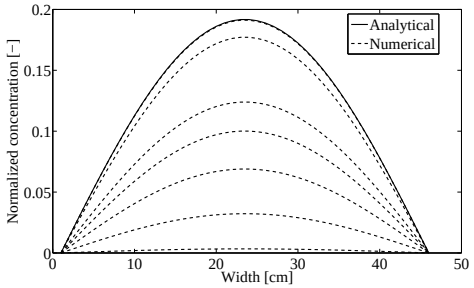

(b) Asymptotic behavior of numerical solution for different time steps.

Figure 5.6: Validation of asymptotic behavior, $D_e = 10 \cdot 10^{-12} m^2/s$.

example compares the solution of diffusion equation for different time steps.

Case C: 2D problem - Complete solution

In the last example the complete numerical solution of equation 5.1 for a simple 2D problem is compared with the analytical expression, in order to fully validate the proposal cellular automata algorithm. The problem is depicted in Figure 5.8, where domain Ω is defined as $\Omega := [0, 2\pi] \times [0, 2\pi]$. To solve the equation, both boundary conditions and initial ones are required; in particular:

$$\begin{cases} u_t - \Delta u = 0 & \text{on } \Omega \times [0, \tau] \\ u(x, y, t = 0) = \sin(nx)\sin(my), & \text{on } \Omega \\ u(x, y, t) = 0, & \text{on } \partial\Omega \end{cases} \tag{5.22}$$

where D_e is set to 1 and $n = m = 2$. The solution is on the form, Altieri and Stefanoni [6]:

$$u(x, y, t) = e^{-(n^2+m^2)t} \sin(nx)\sin(my) \tag{5.23}$$

Each side of the domain is divided into 50 spatial intervals, and time is increased up to 1 second, namely $\tau = [0, 1]$. Figure 5.9 presents the difference in terms of concentration between

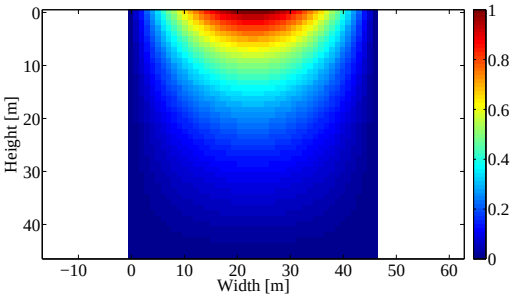

(a) Analytical solution.

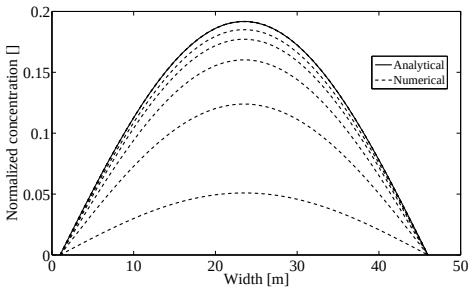

(b) Asymptotic behavior of numerical solution for different time steps.

Figure 5.7: Validation of asymptotic behavior, $D_e = 25 \cdot 10^{-12} m^2/s$.

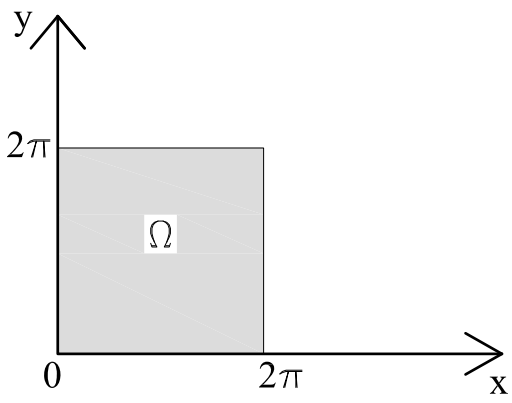

Figure 5.8: 2D domain to check the accuracy of numerical solution.

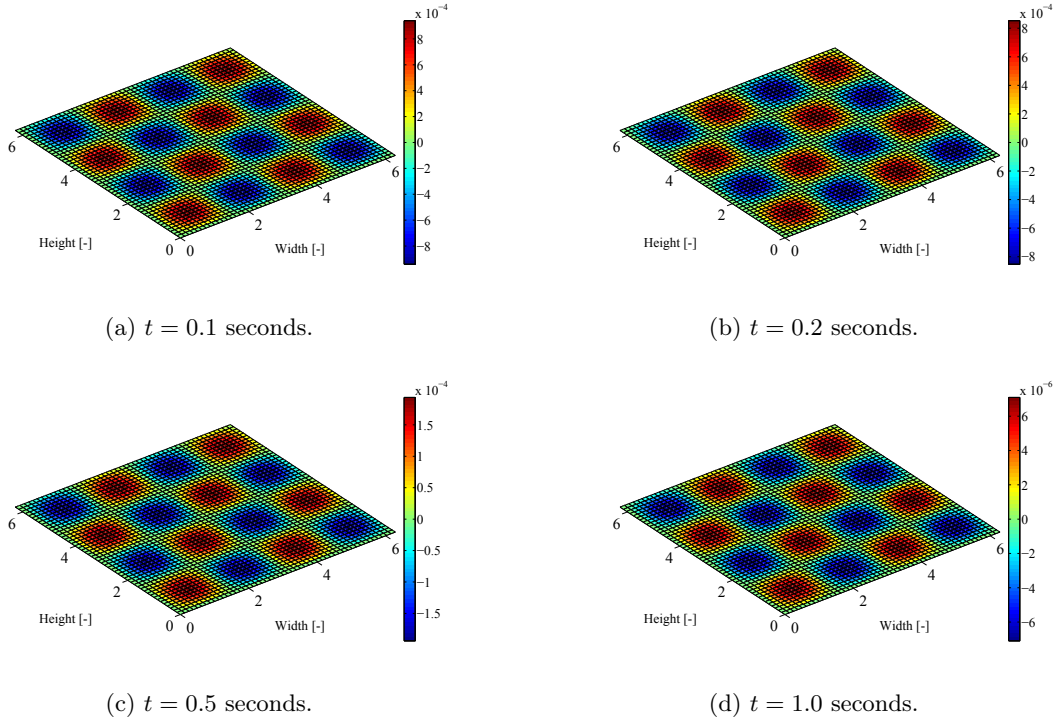

(a) $t = 0.1$ seconds.

(b) $t = 0.2$ seconds.

(c) $t = 0.5$ seconds.

(d) $t = 1.0$ seconds.

Figure 5.9: Difference in terms of concentration between analytical and numerical analysis.

analytical and numerical analysis for different time steps; as can be seen the prediction coming from cellular automata is always very good, because in each point the gap is always lower than 10^{-3}. Same information can be visualized also in an equivalent form, Figures 5.10 and 5.11; here the comparison is carried with reference to two different values of normalized coordinate $\eta = y/(2\pi)$, $\forall x$, one close to the boundary and one in the middle of the domain, namely $\eta = 0.05$ and $\eta = 0.5$. As can be seen dot points (related to numerical simulation) match very well the sinusoidal behavior of the analytical solution.

Once that the algorithm for simulation of diffusion process is validated, it is worth nothing to compare the results coming from numerical simulation using both 1D and 2D formulation, in order to check the accuracy of the former method with respect to the more reliable bi-dimensional description of the problem. Such comparison is done because usually the evaluation of chlorides concentration within RC cross-section of structural is carried considering the one-dimensional Fick's law, see e.g. Vu and Stewart [242] and Glass and Buenfeld [100], so it is important to understand if and in which situations the prediction carried out from 1D formulation is appropriate. To this aim, a parametric analysis is performed; in particular the diffusion process is studied by using the tools developed with reference to different rectangular RC cross-sections, where the shape factor $\beta = B/H$ ranges from 0.25 up to 5, Figure 5.12.

It is assumed that on the top of the section there is a surface concentration C_0, kept constant for all the duration of the analysis; on the other sides it is imposed a null flow, so

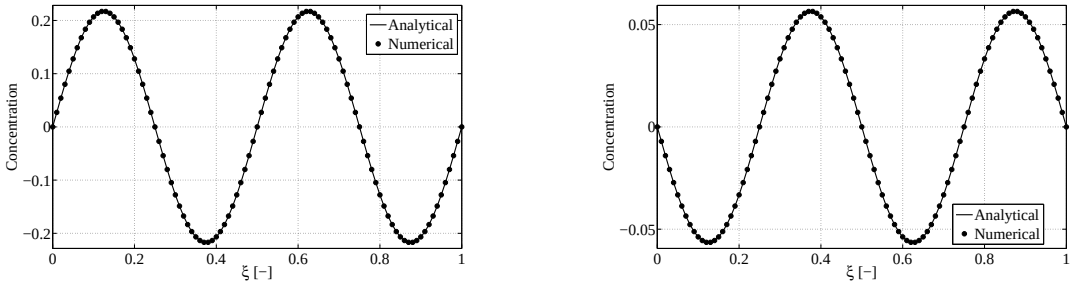

(a) $\eta = 0.05$. (b) $\eta = 0.5$ seconds.

Figure 5.10: Sinusoidal behavior of analytical solution (continuos line) and numerical result (dots) for $t = 0.1$ seconds.

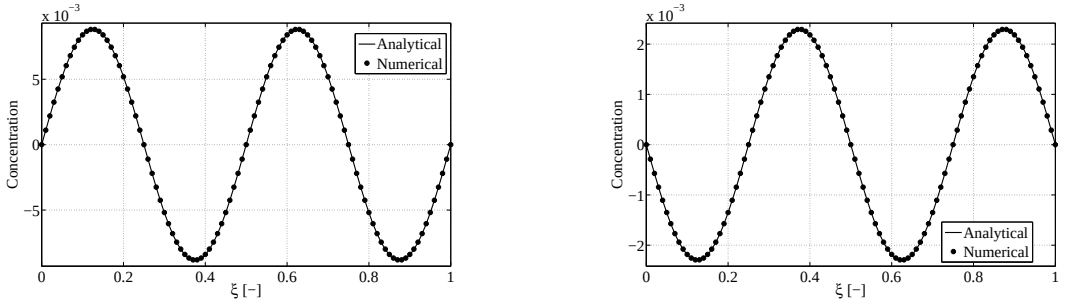

(a) $\eta = 0.05$. (b) $\eta = 0.5$.

Figure 5.11: Sinusoidal behavior of analytical solution (continuos line) and numerical result (dots) for $t = 0.5$ seconds.

Figure 5.12: Example of RC cross-sections studied in the parametric analysis.

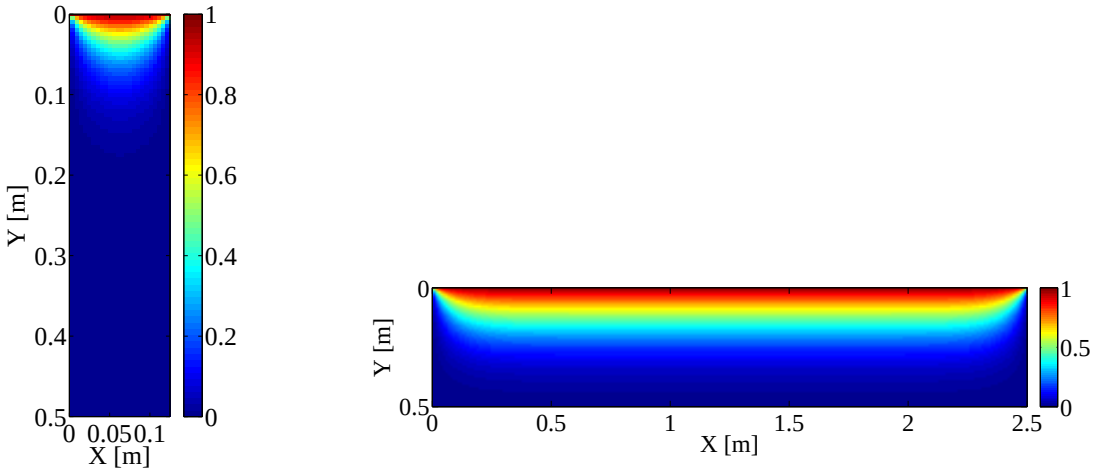

(a) $\beta = 0.25$.

(b) $\beta = 5$.

Figure 5.13: Map of chlorides concentration after $t = 50$ years (normalized with respect to the surface concentration C_0).

the corresponding concentration is zero at the beginning of the simulation, and subsequently increases due to the chlorides diffusion from inner cells. In this configuration, it is expected that a satisfactory comparison among the two different approaches is achieved when shape factor $\beta = B/H$ increases; in particular if $\beta \to \infty$ the results should be the same. The explanation can be found by a visual inspection of the curves of "equal concentration"; in a 1D approach the concentration front is uniform along the entire width of the section, while in the bi-dimensional formulation the curves has the shape indicated in Figure 5.13. Clearly, if $B >> H$, at least in the middle of the section the profiles tend to be uniform, because the effect of boundaries is limited to a region close to the external sides; on the contrary, if $B << H$, the influence of the boundaries is reflected along the entire section, so the hypothesis of uniform front concentration is not appropriate.

For the presentation of the results carried out from parametric analysis it is convenient to introduce dimensionless quantities; in particular, the geometric coordinates $\xi = x/B$ and $\eta = y/H$ and time coordinate $\tau = t/T_{max}$ are used, where T_{max} is set to 50 years. The effect of shape factor on the response coming from 1D and 2D formulation can be seen in Figures 5.14 and 5.15; it is shown, with respect to time τ and for different sections ξ, the ratio C/C^{1D}, where C is the concentration coming from one the two approaches and C^{1D} is the concentration evaluated in the one-dimensional case. If the shape factor is small, Figure 5.14, the approximated formulation predicts for almost the entire duration of the analysis

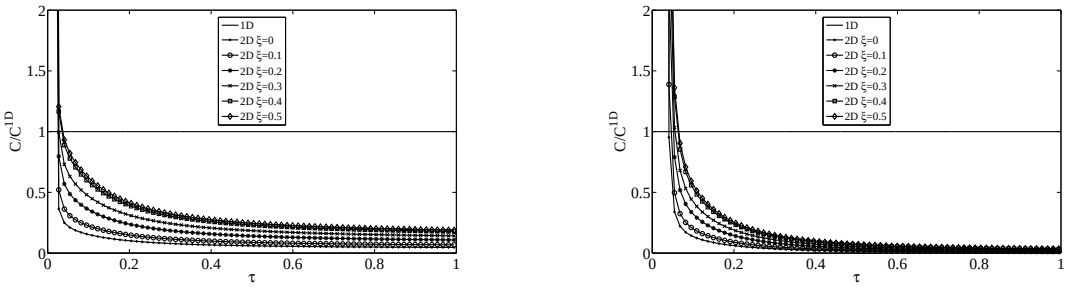

(a) $\eta = 0.2$.

(b) $\eta = 0.4$.

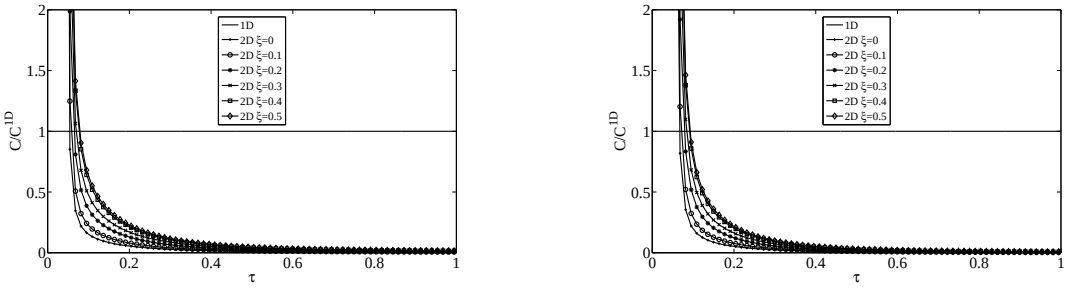

(c) $\eta = 0.5$.

(d) $\eta = 0.6$.

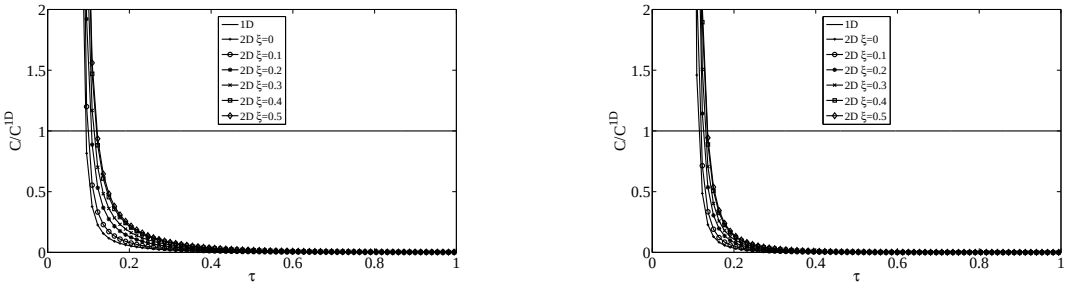

(e) $\eta = 0.8$.

(f) $\eta = 1$.

Figure 5.14: Comparison between 1D and 2D formulation in terms of concentration estimation for a shape factor $\beta = 0.25$.

higher values with respect to the bi-dimensional approach due to the strong influence of the boundaries. On the contrary, it is possible to see in Figure 5.15 that, if β is higher enough, the two approaches give more or less the same results, at least in a region sufficiently far from the external sides.

The influence of the shape factor can be clearly visualized looking at Figure 5.16, where the same ratio C/C^{1D} introduced before is illustrated for different time steps and values of β, considering the middle section $\xi = 0.5$. Again, if the width of the base where chlorides can spread is big enough, the results predicted by the two formulations are close one to each other, at least sufficiently far from the external side with zero flow ($\eta = 1$).

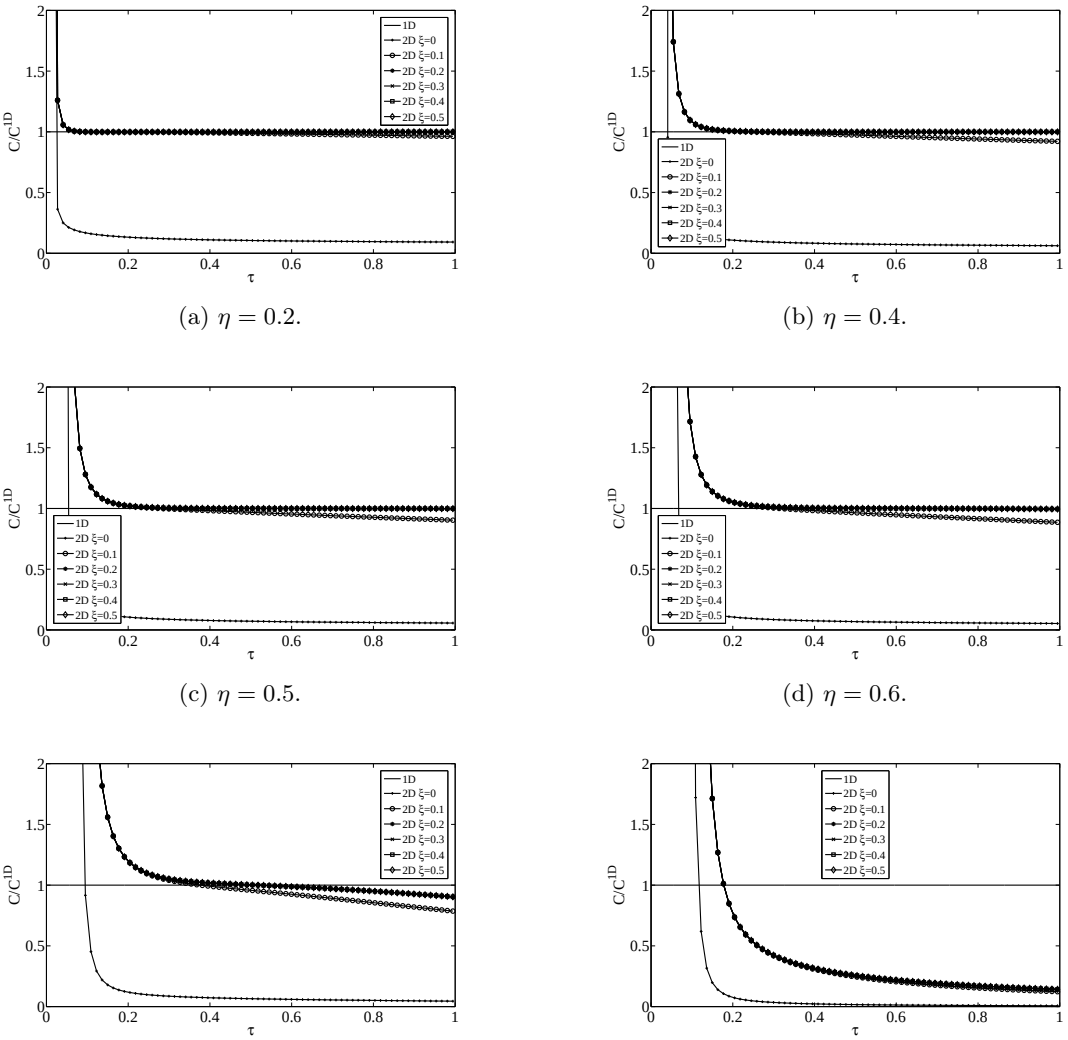

(a) $\eta = 0.2$.

(b) $\eta = 0.4$.

(c) $\eta = 0.5$.

(d) $\eta = 0.6$.

(e) $\eta = 0.8$.

(f) $\eta = 1$.

Figure 5.15: Comparison between 1D and 2D formulation in terms of concentration estimation for a shape factor $\beta = 5.0$.

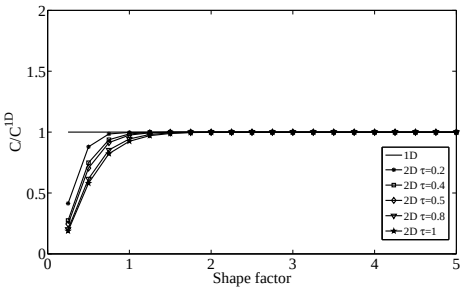

(a) $\eta = 0.2$.

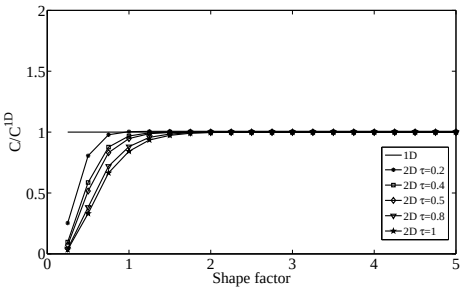

(b) $\eta = 0.4$.

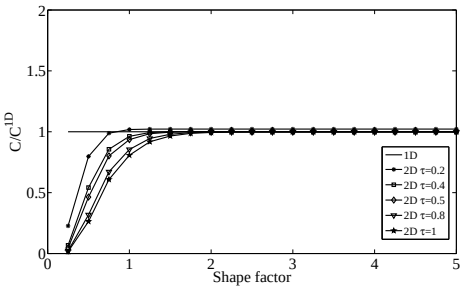

(c) $\eta = 0.5$.

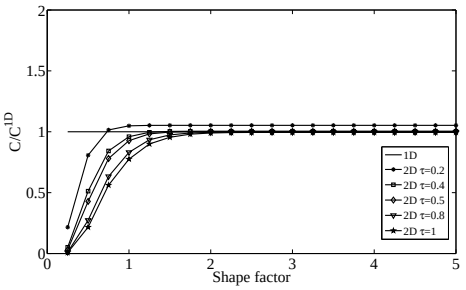

(d) $\eta = 0.6$.

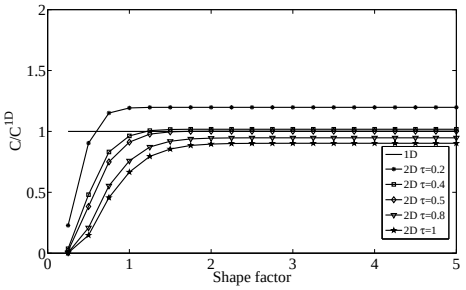

(e) $\eta = 0.8$.

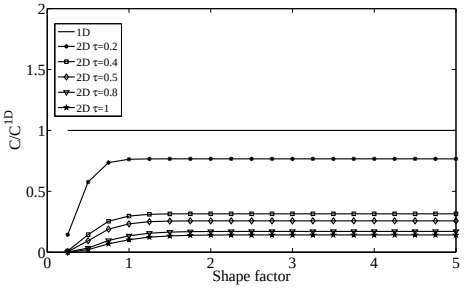

(f) $\eta = 1$.

Figure 5.16: Comparison between 1D and 2D formulation in terms of concentration estimation for the middle section $\xi = 0.5$.

5.3 Diffusion process and damage evolution

In a durability analysis, the time evolution of damage induced by corrosion is not independent, but it is strictly related to the corresponding evolution of the diffusion process. When aggressive agents like sulphates or chlorides propagate within a concrete section, the corrosion rate depends, among different parameters, on the level of concentration of the chemical substance. Clearly the entire process is complex and many uncertainties are involved; in any case, it is possible to adopt simple but reliable models for the lifetime assessment of concrete structures. Among different methods proposed in literature, the approach presented in Biondini et al. [34] seems promising; here, the damage functions for concrete and steel are related to the concentration of the aggressive agent in the following way:

$$\begin{aligned} \frac{\partial \delta_c(\boldsymbol{x},t)}{\partial t} &= \frac{C(\boldsymbol{x},t)}{C_c \Delta t_c} = q_c C(t) \\ \frac{\partial \delta_s(\boldsymbol{x},t)}{\partial t} &= \frac{C(\boldsymbol{x},t)}{C_s \Delta t_s} = q_s C(t) \end{aligned} \tag{5.24}$$

where C_c and C_s represent the values of constant concentration $C(\boldsymbol{x},t)$ which lead to a complete damage of the materials after the time periods Δt_c and Δt_s, respectively. To solve the problem, initial conditions are necessary; in particular, denoting as C_{cr} the critical threshold of concentration, damage functions δ_c and δ_s are zero until the initiation time is not reached. Finally, q_c and q_s depend on actual rate of damaging process. Details can be found in Biondini et al. [34] and Biondini et al. [40].

5.4 Evaluation of seismic performance during lifetime

The corrosion process has influence both at local and global level. In particular, in the present investigation, with respect to the corrosion models illustrated in previous sections, some hypotheses are made in order to simplify the problem, but at the same time to provide an effective tool for the estimation of seismic risk of multistory RC frames, namely:

- Only a reduction of the steel bars (longitudinal and transversal) is considered, see e.g. Celarec et al. [53]. Concrete damage is not included here, even if in recent works a reduction of cover compressive strength is introduced, Berto et al. [25] and Biondini et al. [40];
- A linear relationship between rate of damage index δ_s and concentration is assumed.

With respect to last point, the following expression is applied, see e.g. Biondini et al. [34], Biondini et al. [40] and Biondini [28]:

$$\frac{\partial \delta_s(\boldsymbol{x},t)}{\partial t} = r C(\boldsymbol{x},t) \tag{5.25}$$

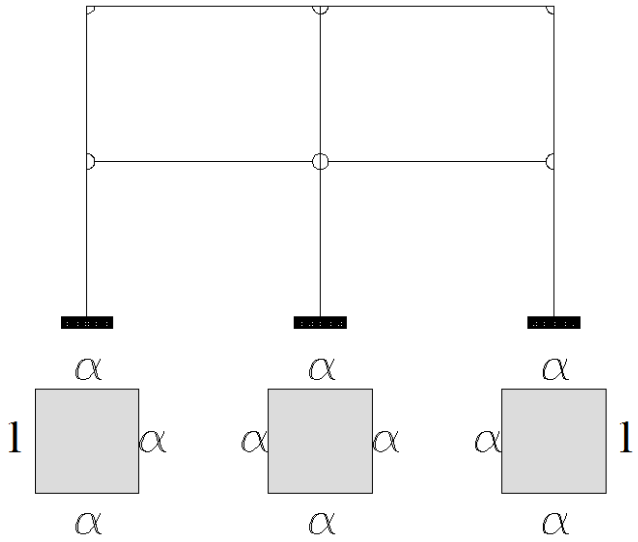

Figure 5.17: Scheme for the distribution of chlorides concentration of the surface of the columns. Example on 2 story building.

where r is a damage coefficient, here taken equal to $0.02/C_0$, where C_0 is the chloride concentration on the surface ($= 3\%[wt.\%c]$, fib 2006 [87]). Such value is adopted so to reproduce a deterioration process with severe damage of materials, as may occur for heavily chloride-contaminated concrete and high relative humidity, Bertolini et al. [26]. Clearly, the damage index is set to zero until the chloride concentration reaches the critical value C_{cr} in correspondence of the bars; in particular, following the recommendations of Model Code, fib 2006 [87], $C_{cr} = 0.6\%[wt.\%c]$. To conclude, diffusion coefficient D is set to $10.58 \times 10^{-12}\,\mathrm{m/s^2}$, Sahmaran et al. [217], in order to subsequently perform a comparison with the composite material adopted for the enhancing of lifetime seismic performance.

5.4.1 Lifetime cross-section analysis

In order to clear understand the role of corrosion on the performance of structural members, the scheme depicted in Figure 5.17 is adopted. In particular, a parametric analysis is carried out introducing the dimensionless factor α which ranges from 0 to 1, namely $\alpha = 0, 0.25, 0.5, 0.75, 1$. In this way the chloride concentration on the surface changes, so for each external side $\overline{C}_0 = \alpha C_0$; only the sides of external columns exposed directly to the atmosphere have always a surface concentration equal to C_0.

An example of such simulations is represented in Figures 5.18 and 5.19, which illustrate the concentration map, normalized with respect to the surface value, within cross-section 45×45, for different times, assuming respectively $\alpha = 0$ and $\alpha = 1$. As it can be seen, cellular automaton represents an effective tool to investigate the diffusion process of a generic chemical species in bi-dimensional domains. Clearly, the same procedure is carried out for all the other cross-sections, changing the value of α. After that, equation 5.25 is exploited to evaluate

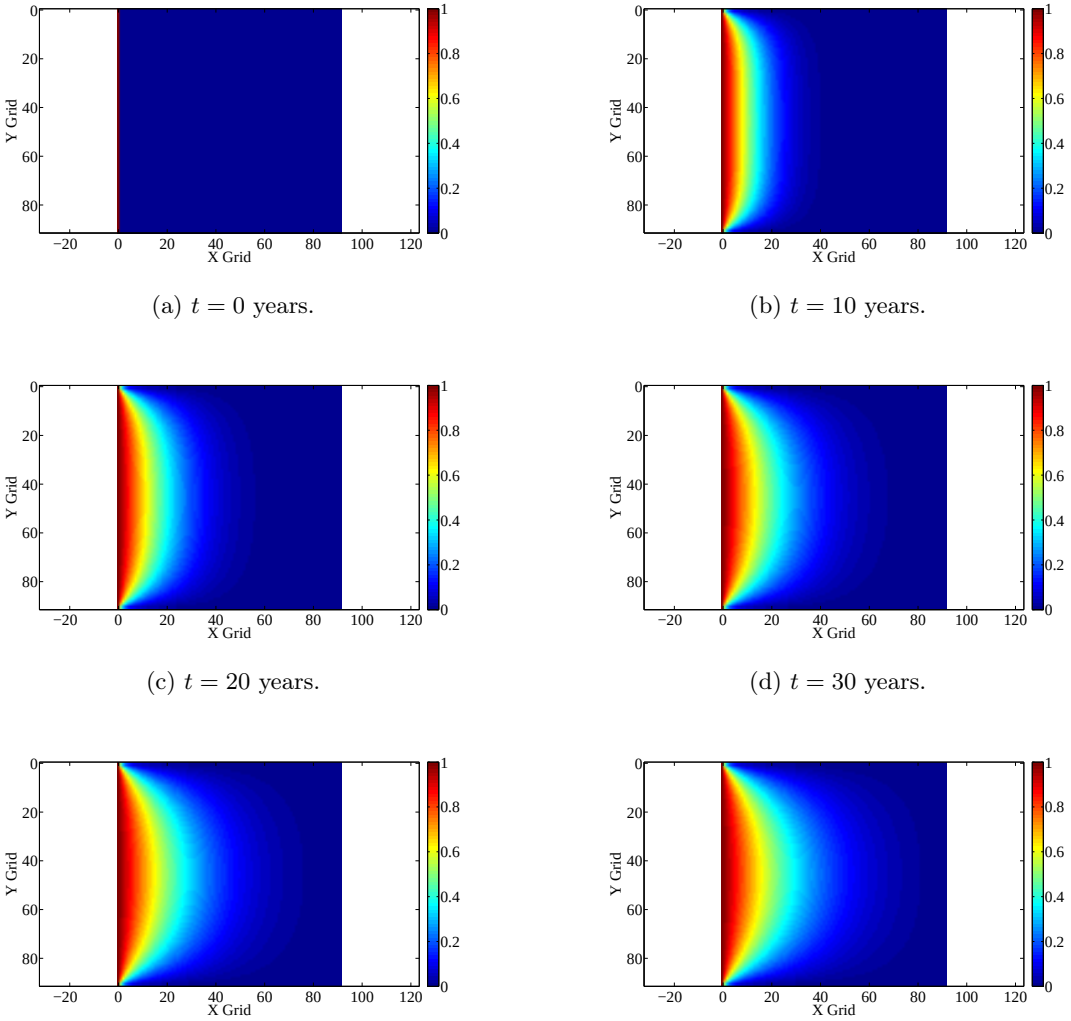

(a) $t = 0$ years.

(b) $t = 10$ years.

(c) $t = 20$ years.

(d) $t = 30$ years.

(e) $t = 40$ years.

(f) $t = 50$ years.

Figure 5.18: Normalized concentration maps for cross-section 45×45, $\alpha = 0$.

damage index δ_s at a level of longitudinal and transversal bars, with the final purpose to estimate the reduction of steel area by using equation 4.19. For the stirrups, since corrosion can propagate in unsymmetric modes depending on the value of α and due to boundary effects, it assumed that the section with the higher reduction determines the total transversal area A_{sh}, that it is used subsequently as one of the parameter for the Ibarra model.

The propagation of chlorides leads therefore to a reduction of mechanical properties of structural members during their lifetime; this is evident by looking at Figure 5.20, which shows the envelope of the Ibarra model for the external column at the base of the 2 story building with cross-section 45×45, assuming two different values of α. In particular moment-rotation diagrams are depicted at the beginning of lifetime ($t = 0$, no corrosion) and after 50 years. Some important considerations can be done: first, considering Figure 5.20a, there is a different

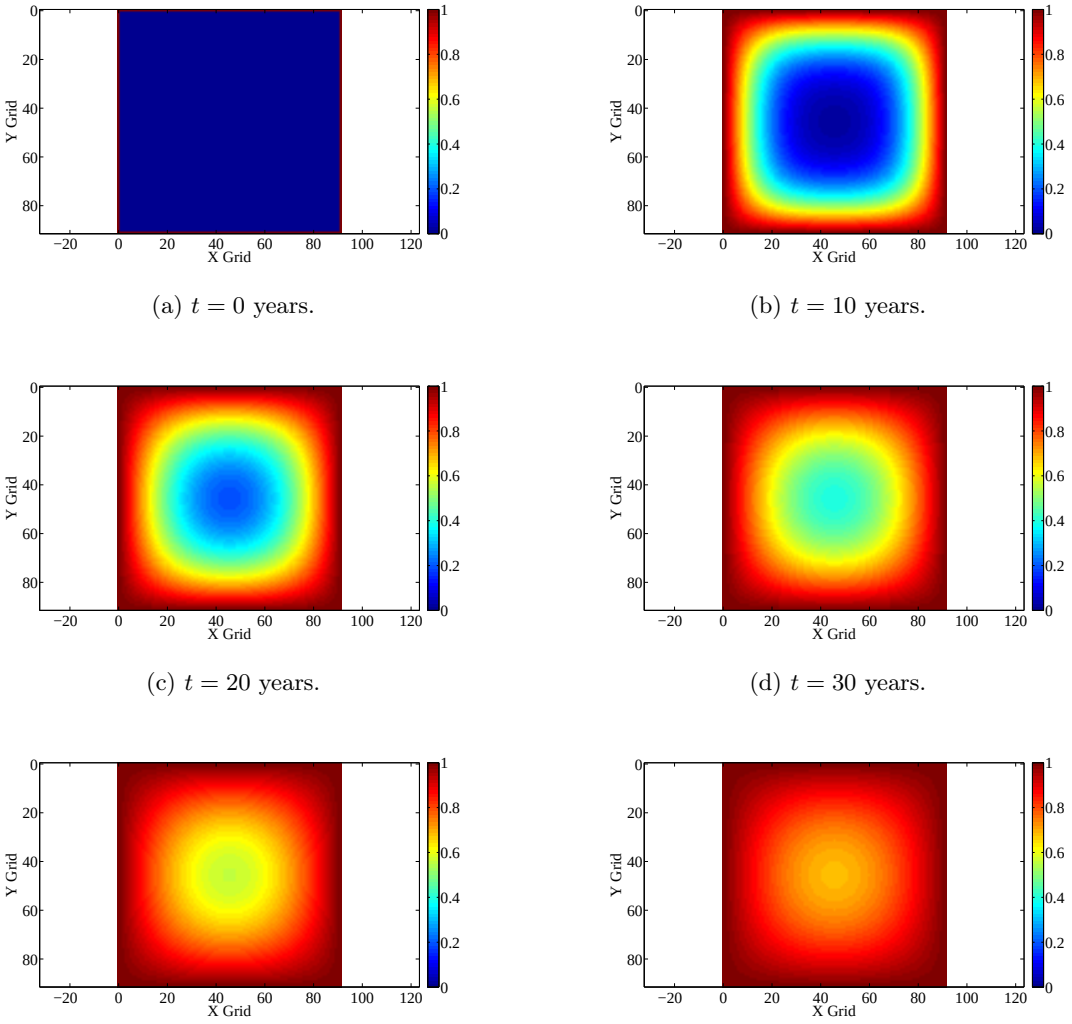

(a) $t = 0$ years.

(b) $t = 10$ years.

(c) $t = 20$ years.

(d) $t = 30$ years.

(e) $t = 40$ years.

(f) $t = 50$ years.

Figure 5.19: Normalized concentration maps for cross-section 45×45, $\alpha = 1$.

behavior for $M < 0$ and $M > 0$, because the exposure conditions are not symmetric. A significant reduction in the strength is achieved especially for the positive direction, since the bars in tension are located in the most exposed part of the cross-section, Biondini et al. [40]. On the contrary, when corrosion can propagates along each side, the corresponding moment-rotation curve is symmetric, as expected, Figure 5.20b. In both cases there is a remarkable drop in ductility due to the transversal steel area reduction, which is translated in a decrease of the parameter ρ_{sh} in the Ibarra model, see Haselton [112].

5.4.2 Time evolution of structural capacity

The deterioration of mechanical properties of structural members are then reflected on the capacity of the multistory frames. As an example, Figure 5.21 represents the time evolution of median base shear coming from the probabilistic approach for the 2 story building with cross-section 45×45 and 80×80, respectively. As expected, for each limit state, there is a significant drop of structural capacity with respect to the initial value due to the severe damage coefficient adopted. Moreover, the most important issue emerging is the significant effect of the exposure conditions (different values of α). A similar information is given also in Figure 5.22, but in this case the variation of median base shear refers to Near Collapse limit state for all the systems investigated. Increasing the environmental hazard, $\alpha \to 1$, structural capacity can have a decrease around 55%. As just explained, corrosion affects in a decisive way the transverse reinforcement, because the small diameter; for this reason, during time shear capacity, defined as indicated in equation 3.11, tends to decrease, and a brittle failure can appear in ordinary reinforced concrete structures.

In the present investigation, however, frames studied are not subjected to a brittle collapse, as can be seen from Figure 5.23, where the story shear demand/capacity ratios evaluated during time for two different configurations are always lower than 1. Anyway, as suggested by Celarec (Celarec et al. [53]), a potential brittle limit state can be defined, assuming for DCR a threshold equal to 0.5; such condition can represent in a reliable way a probable shear failure. An increase in the exposure conditions ($\alpha \to 1$) leads to higher DCR values, so the influence of corrosion on shear behavior is well caught.

To conclude, by using the N2 method, Fajfar and Gašperšič [82], the capacity of the structural systems can be translated into PGA capacity, defined for different limit states. For sake of brevity, only the results for the 2 story building with cross-sections 45 and 80×80 are presented, even if all the multistory frames are studied. Median values are indicated in Tables 5.1 and 5.2, assuming $\alpha = 0$ and $\alpha = 1$. When the environmental exposure is not so severe ($\alpha = 0$), the reduction during the entire lifetime is not so significant, even if the effect of corrosion has a higher influence increasing the limit state. The explanation can be found in the definition used; in particular, Near Collapse refers to the softening behavior, and usually numerical simulations are more sensitive to changes in this branch.

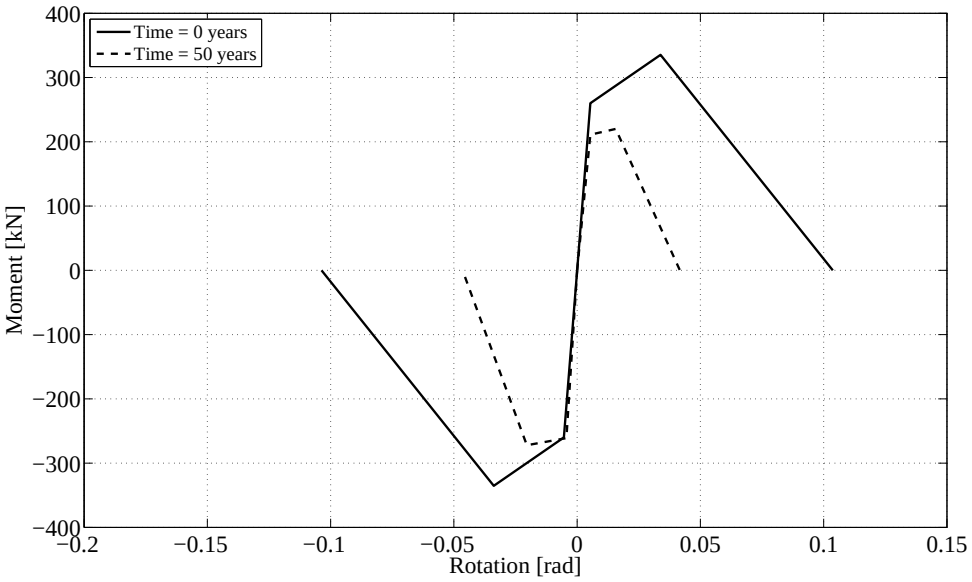

(a) $\alpha = 0$.

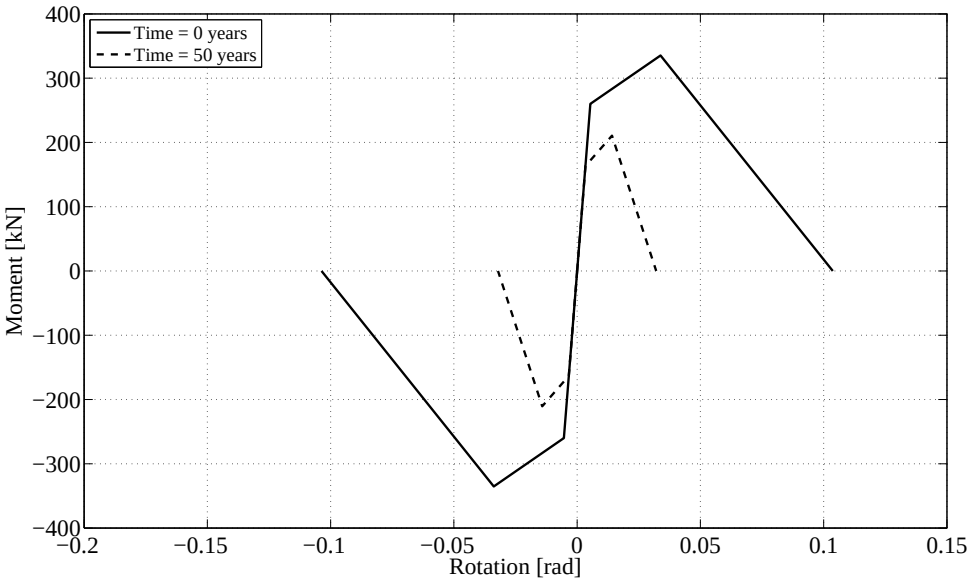

(b) $\alpha = 1$.

Figure 5.20: Influence of corrosion on the moment-rotation envelope for a base column of the 2 story building with cross-section 45×45.

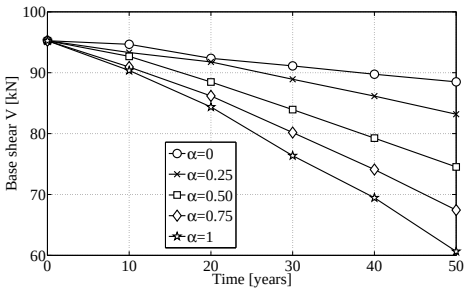

(a) DL, cross-section 45 × 45.

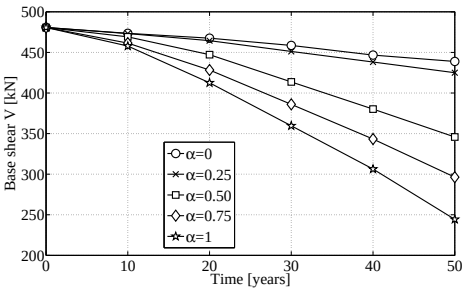

(b) DL, cross-section 80 × 80.

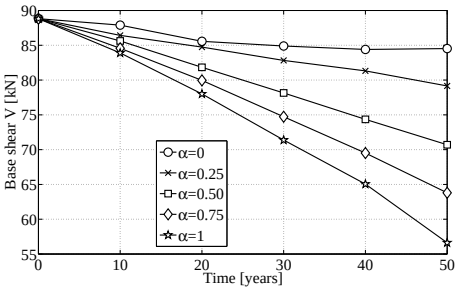

(c) LS, cross-section 45 × 45.

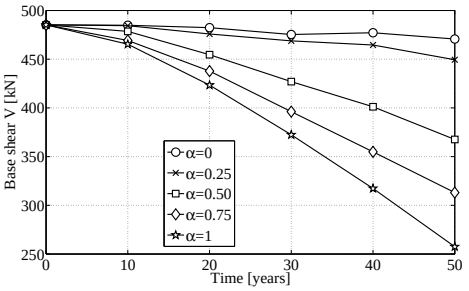

(d) LS, cross-section 80 × 80.

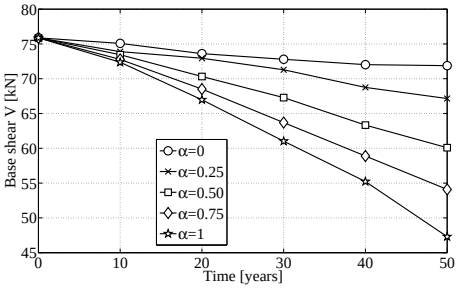

(e) NC, cross-section 45 × 45.

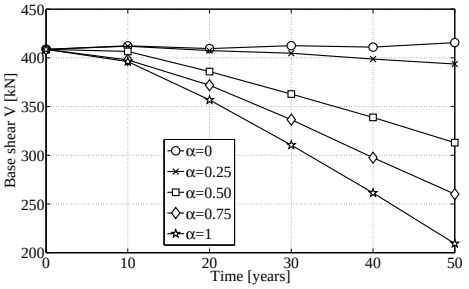

(f) NC, cross-section 80 × 80.

Figure 5.21: Time evolution of base shear for different limit states, 2 story building.

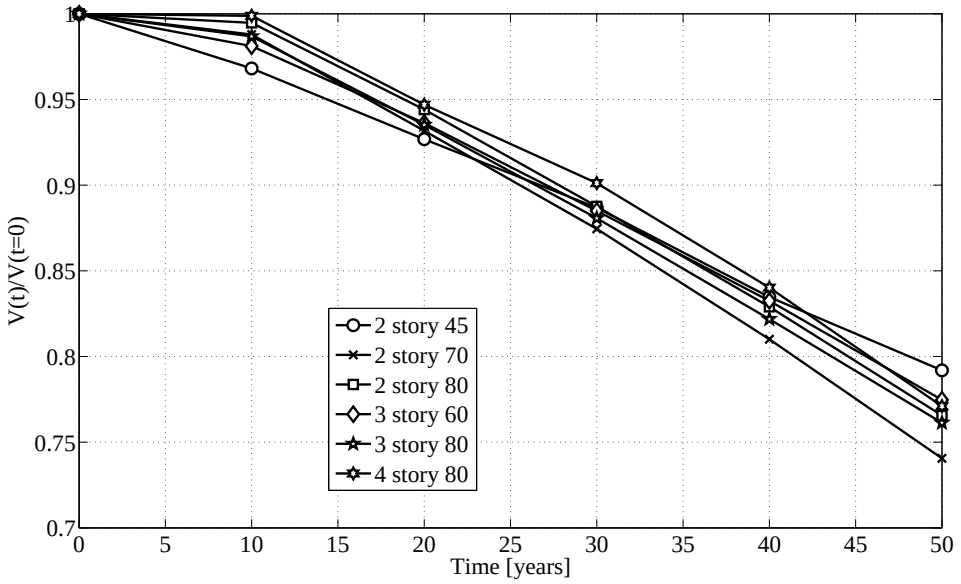

(a) $\alpha = 0.50$.

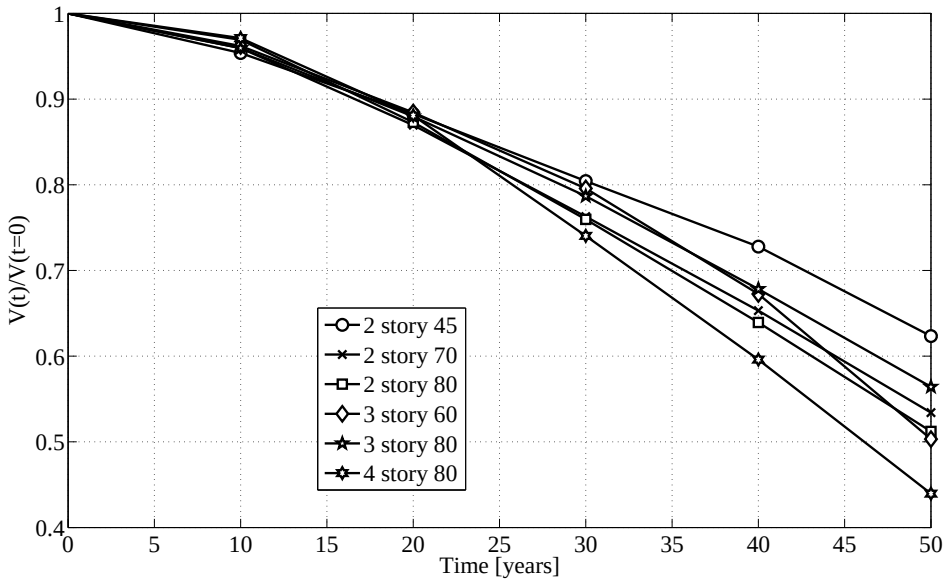

(b) $\alpha = 1$.

Figure 5.22: Decrease of base shear for NC limit state during time.

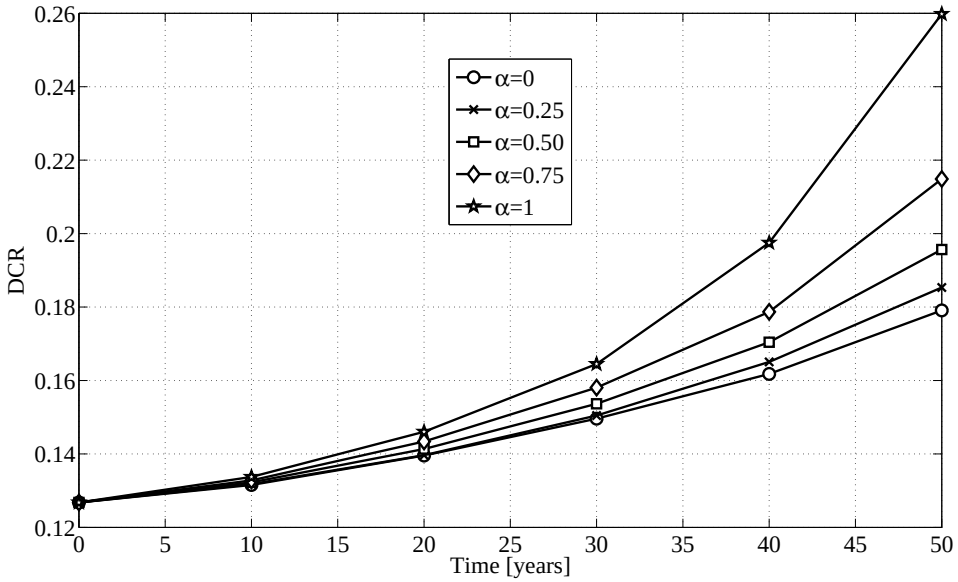

(a) Cross-section 45×45.

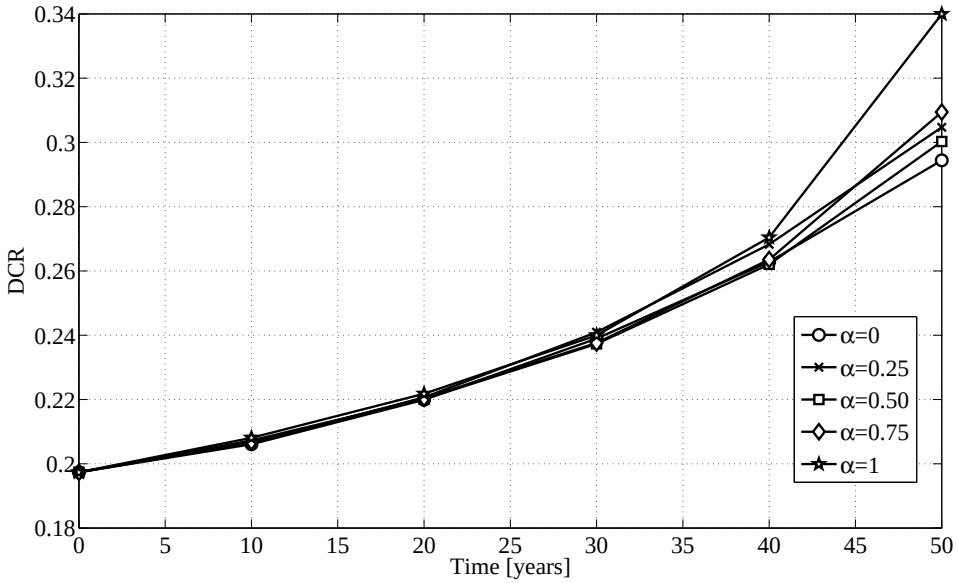

(b) Cross-section 80×80.

Figure 5.23: Time evolution of the first story shear demand over capacity ratio (DCR) for the 2 story building.

Table 5.1: Structural capacity as peak ground acceleration ([g]) for different limit states, 2 story 45×45.

(a) $\alpha = 0$.

Time [years]	***DL***	***LS***	***NC***
0	0.107	0.147	0.196
10	0.107	0.147	0.196
20	0.106	0.144	0.193
30	0.106	0.142	0.189
40	0.106	0.138	0.185
50	0.105	0.135	0.182

(b) $\alpha = 1$.

Time [years]	***DL***	***LS***	***NC***
0	0.107	0.147	0.196
10	0.103	0.142	0.191
20	0.098	0.134	0.181
30	0.090	0.125	0.168
40	0.083	0.114	0.153
50	0.075	0.104	0.137

Table 5.2: Structural capacity as peak ground acceleration ([g]) for different limit states, 2 story 80×80.

(a) $\alpha = 0$.

Time [years]	***DL***	***LS***	***NC***
0	0.173	0.987	1.320
10	0.173	0.982	1.315
20	0.173	0.963	1.284
30	0.173	0.933	1.249
40	0.172	0.916	1.220
50	0.170	0.893	1.197

(b) $\alpha = 1$.

Time [years]	***DL***	***LS***	***NC***
0	0.173	0.987	1.320
10	0.169	0.826	1.101
20	0.151	0.756	1.003
30	0.135	0.679	0.898
40	0.114	0.590	0.777
50	0.096	0.479	0.613

5.4.3 Influence on seismic risk

By using PEER methodology, chlorides induced damage can be seen also in the light of a seismic risk analysis. As indicated in section 3.8.3, risk study is based on two parameters: PGA capacity and probability of exceedance a particular limit state in 50 years, see Kramar et al. [136]. The former is computed with reference to the 5^{th} percentile of PGA capacity resulting from the probabilistic approach here adopted and compared with the design value prescribed by national code for the specific site, NTC 2008 [181], while the second is compared with the recommended values always reported in NTC 2008 [181] (63%, 10% and 5% for DL, LS and NC limit state, respectively). Two sites, namely Gemona and S.Benedetto, and two different configurations of the 2 story building are selected for the presentation of results; when capacity design criteria is not appropriate (columns cross-section 45×45) probability of exceedance a predefined limit state is alway higher than the threshold value, see Figure 7.2. At the same time, PGA capacity is lower than the design value recommend by the code for the particular sites selected, Figure 5.25.

For the stiffer configuration (cross-section 80×80), there is a lower probability to exceed limit states, because for such configuration capacity design criteria gives reliable results and seismic behavior is good, see Biondini et al. [39]. Anyway, during time, the influence of exposure conditions plays a fundamental role, resulting in a final capacity that in some cases is lower than the design value, Figure 7.2. Looking at this results, the most important issue emerging is that same structures, placing at sites with the same seismic hazard, can lead to a different seismic risk depending on the environmental conditions.

5.5 Conclusions

This chapter is devoted to the prediction of lifetime seismic performance of multistory precast frames subjected to a corrosion process. First of all the problem of the numerical simulation of diffusion phenomena of chemical species in concrete sections is addressed by using a special class of evolutionary algorithms, known as cellular automata. Because the propagation of aggressive agents can be represented as a diffusion process, cellular automata method is used to solve Fick's law, and the algorithm is successfully validated both in one-dimensional and bi-dimensional formulation by comparing the numerical results with the analytical solution of simple problems. Subsequently, a parametric study is carried out considering different concrete cross-sections, in order to understand the reliability of the 1D approach with respect to the more accurate 2D formulation, since the former method is proposed by some codes and recommendations (see e.g. fib 2006 [87]). The comparison in terms of evaluation of concentration shows that the geometric ratio between the dimensions of the sections (here indicated as shape factor) and the position for which the differential equation is solved are the most important parameters. In particular, 1D approach usually predicts higher values, and

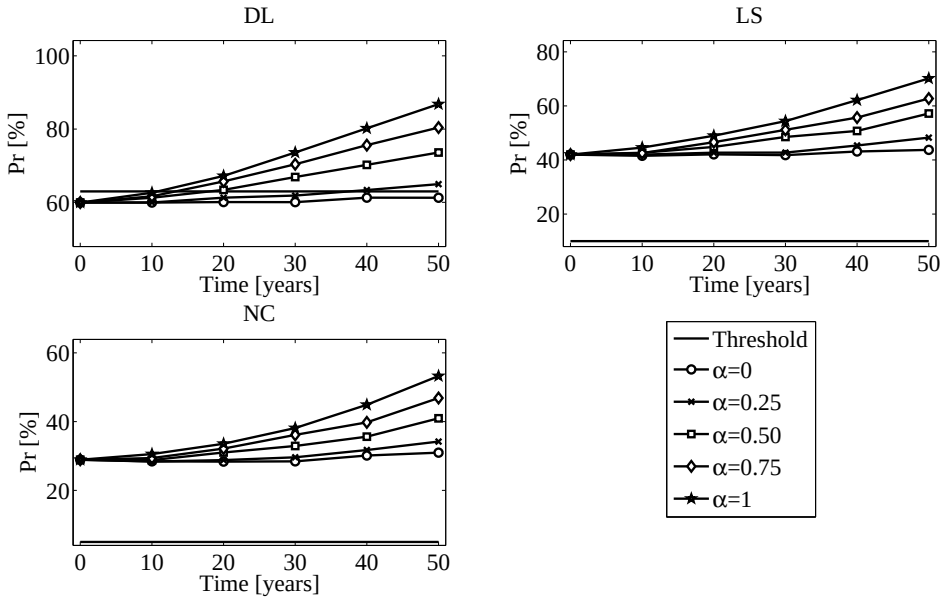

(a) Gemona.

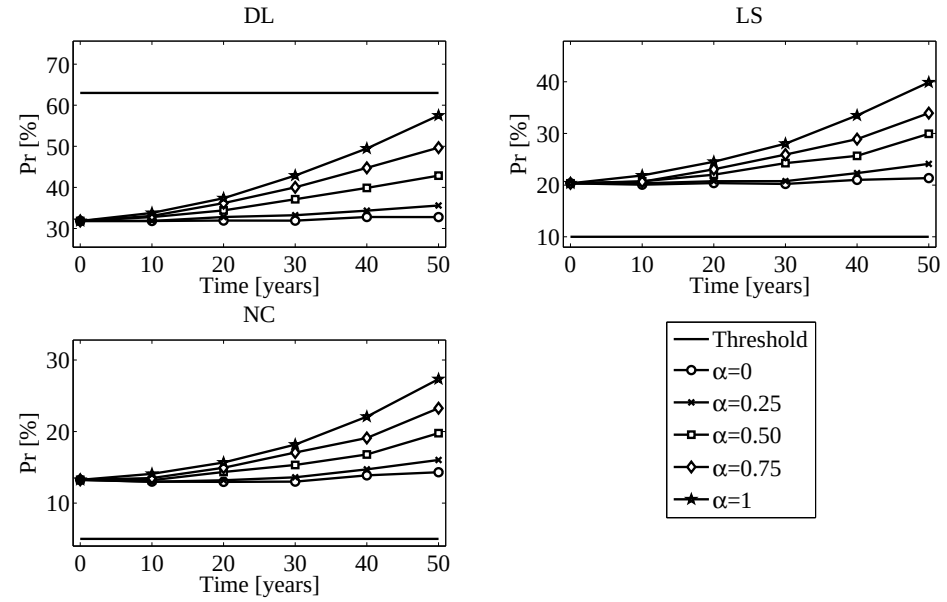

(b) San Benedetto.

Figure 5.24: Time evolution of probability of exceedance and comparison with design value for 2 story building with cross-section 45×45.

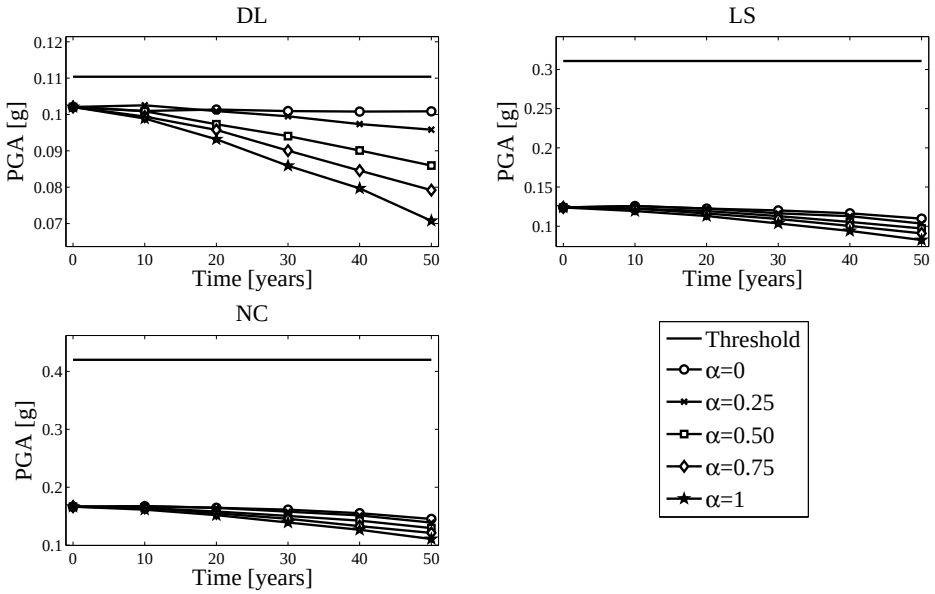

(a) Gemona.

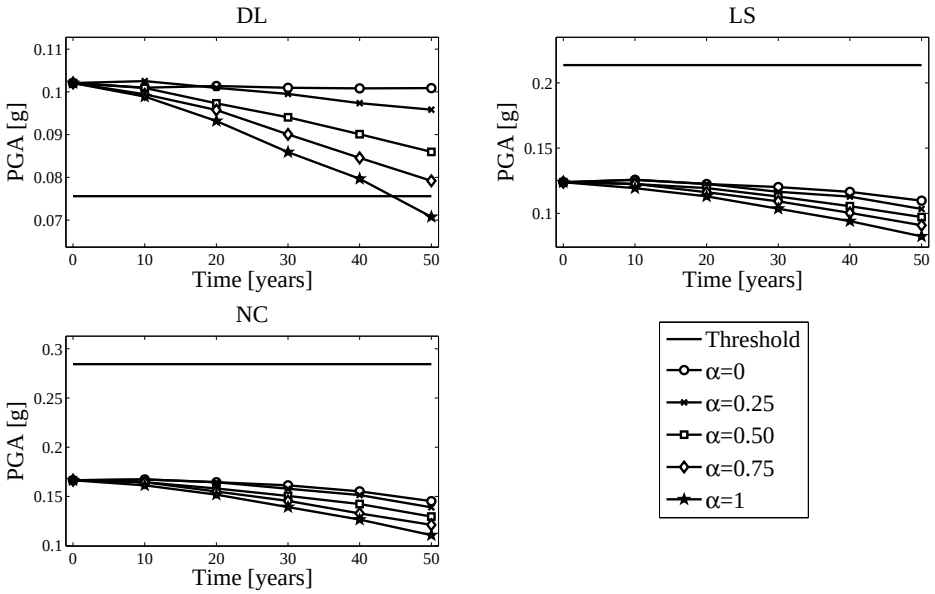

(b) San Benedetto.

Figure 5.25: Time evolution of PGA at 5^{th} percentile and comparison with design value for 2 story building with cross-section 45×45.

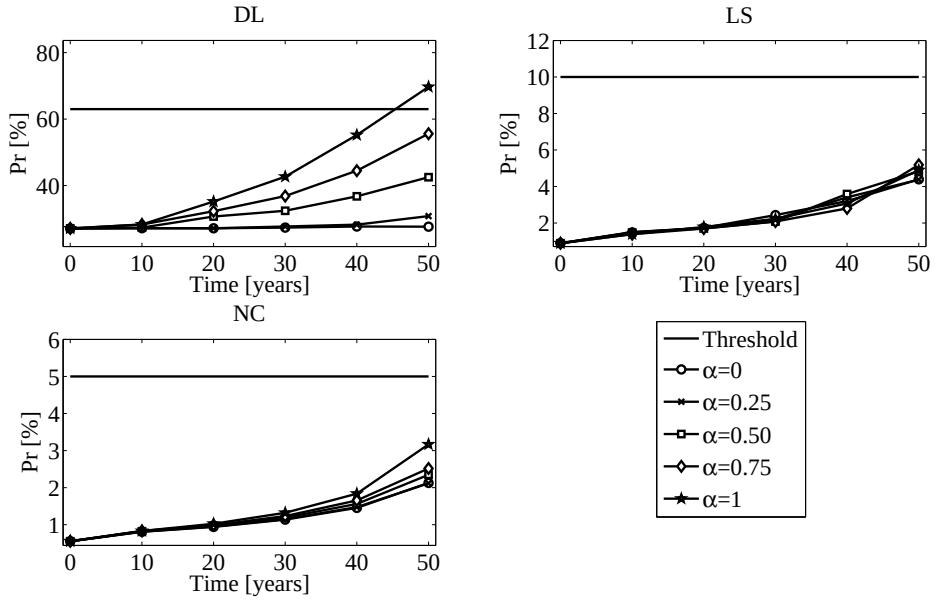

(a) Gemona.

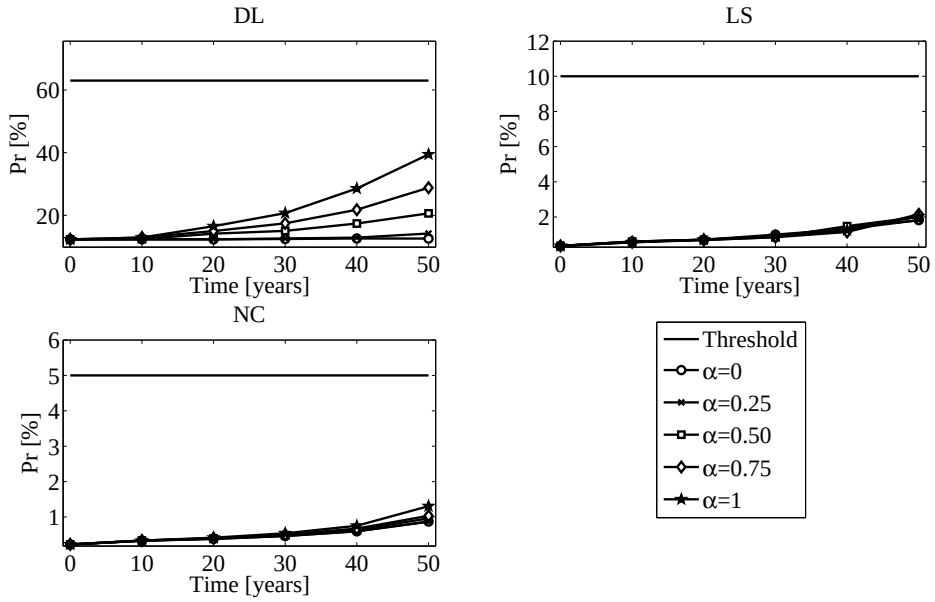

(b) San Benedetto.

Figure 5.26: Time evolution of probability of exceedance and comparison with design value for 2 story building with cross-section 80×80.

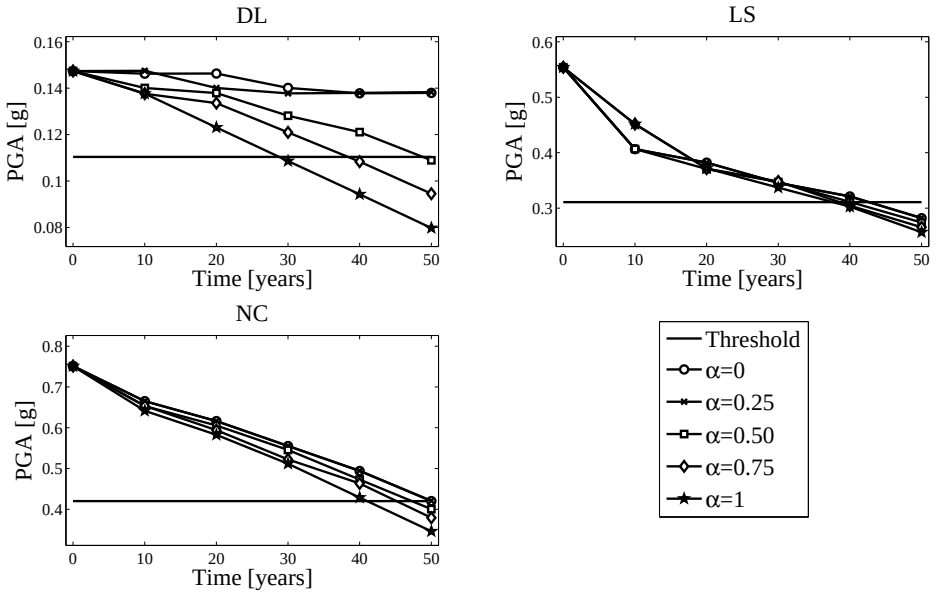

(a) Gemona.

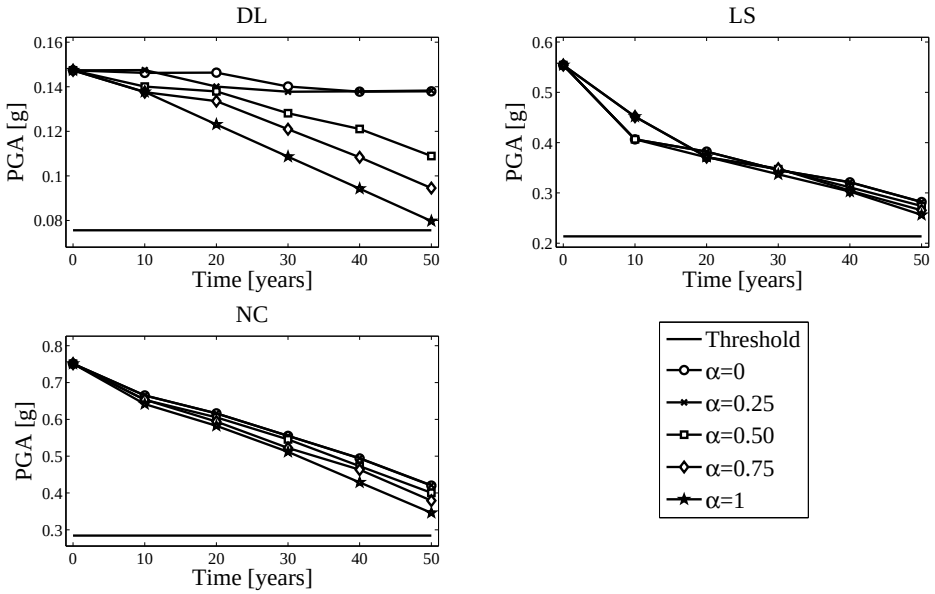

(b) San Benedetto.

Figure 5.27: Time evolution of PGA at 5^{th} percentile and comparison with design value for 2 story building with cross-section 80×80.

only when shape factor increases the results of the two methods are close one to each other.

The tools developed are therefore used to predict the deterioration of structural members of the precast frames studied in the present investigation, changing the exposure conditions and assuming a severe damage coefficient in order to understand their influence. Chlorides induce damage results in a decrease of the mechanical properties of plastic hinges, with a consequent drops of structural capacity for each limit state. Finally, applying PEER methodology, a risk study is performed for each configuration; typically, even if the probability of exceedance a limit state is lower than the recommended value at the beginning of the lifetime, this can not be true at the end, proving the important role plays by environmental hazard. It is however worth nothing to remember that in this study severe exposure conditions have been used in order to clearly highlight the influence of corrosion during time; for structures exposed to ordinary environmental hazard, it is expected a lower deterioration of seismic performance.

Since the role of environmental hazard emerged in a decisive way, in order to extend the lifetime seismic performance of multistory precast frames, a mitigation strategy based on a material level is presented in Chapter 6.

Chapter 6

Enhancing the lifetime seismic performance by using ECC

6.1 Introduction

As illustrated in previous chapters, the effect of environmental hazard such as the diffusion of chlorides in RC cross-sections coupled with seismic hazard leads to a significant decrease of structural capacity of multistory precast buildings. In particular, it is shown that structures for which their capacity at time 0 is higher than the demand, at the end of the lifetime can not match the requirements given by structural codes. It is therefore important to find possible mitigation strategies of seismic risk, in order to improve the overall behavior. In literature and in practice applications several methodologies can be found, operating on different levels. For example, the introduction of a base-isolation system allows a reduction of the forces acting on the structure working at a global level (Chopra [55]); on a local level FRP strengthening of structural members such as columns and joints revealed an effective method for the retrofitting of under-designed RC frames, see e.g. Balsamo et al. [21] and Di Ludovico et al. [67]. Finally, it is also possible to work on a material level by replacing ordinary concrete with advanced cementitious composites; this is just the methodology investigated in the present study.

The research focuses on a particular class of high-performance fiber reinforced cementious composites, known as *Engineered Cementitious Composites* (ECC), Li [147], or strain-hardening cementitious composites. In particular, after a brief review of historical developments of such material, the chapter presents a summary on his main characteristics, from micromechanics to mechanical properties, underlining the practical advantages regarding seismic applications. Because the purpose is to illustrate how such strategy can improve the lifetime performance, durability properties of ECC are also summarized. Finally, the analytical model presented in section 3.3 is modified according to the peculiarity shown by this material, in order to perform structural analyses and seismic risk studies. The same buildings previously investigated are therefore analyzed replacing in the possible locations of the plastic hinges the ordinary concrete

with ECC, and a comparison between results obtained is done.

6.2 Brief history of the material

First studies on the use of fibers within concrete matrix started in the 1960's with the work of Romualdi (e.g. Romualdi and Mandel [212]), which demonstrated the effectiveness of short steel fibers to reduce the brittleness of concrete. However, the first detailed study on tensile characteristics of fiber reinforced composites (FRC) has been carried out by Naaman (Naaman [177]); tests were performed by using straight smooth steel fibers of aspect ratio less than 100, and all the composites showed a strain-softening response after first cracking. During last decades developments have been carried on using a variety of fibers such as glass, carbon, synthetics and, recently, hybrid ones that combine different fiber types or fiber lengths. Due to the availability of these advanced materials, also standard codes have been updated, in order to give to the practitioners new tools for the design of concrete structures, see e.g. di Prisco et al. [68].

From the 1980's, the interest started to move through fiber composites with tensile ductility. In ordinary FRC material toughness can be increased, but no change in ductility is obtained with respect to standard concrete. Within this field a new class of cementitious material has been developed, namely SIFCON (slurry infiltrated fiber concrete, Lankard [141]), where a relative high fibers content is used (usually $5-20\%$ in volume). This material have excellent mechanical properties, including improvement in strength toughness and sometimes a strain-hardening behavior. Because the peculiarity of such composite with respect to normal FRC, Naaman and Reinhardt proposed to classify it with the nomenclature *High Performance Fiber Reinforced Cementitious Composites, HPFRCC*, see e.g. Naaman and Reinhardt [179]. The main characteristic is a ductile behavior in tension, as indicated in Figure 6.1, where a schematic representation of tensile behavior for different cementitious from uniaxial tension test is shown.

Despite to significant advantages, main drawback is the high cost and weight associated with the high fiber volume fraction. In order to maintain flexible processing, reducing cost and weight, in recent years other classes of HPFRCC have been developed. Among them, the present study focus on the so called Engineered Cementitious Composites, originally developed in the University of Michigan under the supervision of prof. Li and co-workers, Li [147]. In particular the strain-hardening behavior in tension is achieved with a moderate fiber content (around 2% in volume), through an optimization process involving micromechanics; more detail are addressed in Section 6.3. In this way multiple cracks can develop after first cracking, with a crack width usually limited to 100 µm; this behavior can be clearly recognized in Figure 6.2, where are shown the differences in terms of cracks width and their distribution for RC and R/ECC sections. Recently, a number of full-scale structural applications is appeared around

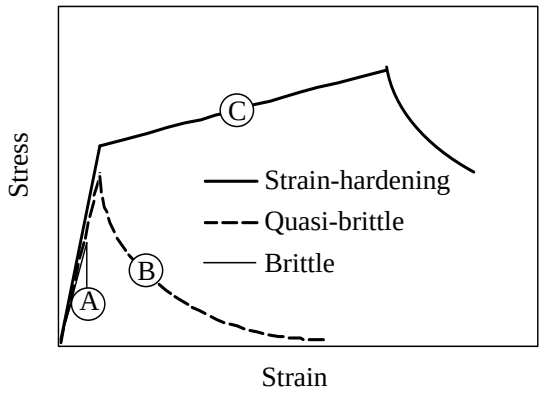

Figure 6.1: Tensile behavior for different classes of cementitious composites, Li [145].

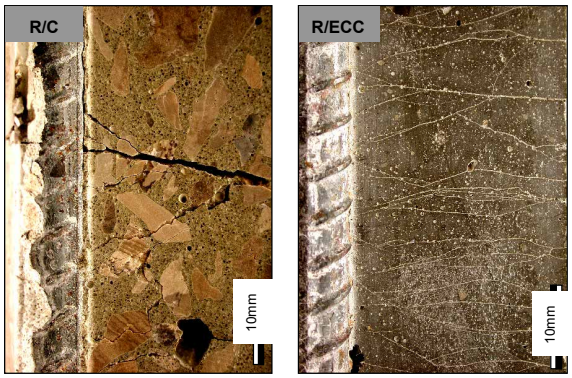

Figure 6.2: Cracks width and their distribution for concrete and ECC, Li [147].

the world, and a brief summary can be found in Li [148]; in particular, due to characteristics indicated above, this material seems very promising when the structure is subjected to severe mechanical and environmental loading such as seismic and corrosion.

Readers interested in historical developments can find other details in Naaman [178] and Li [149].

6.3 Micromechanics tailoring for strain-hardening behavior

In order to achieve a strain-hardening behavior, it is fundamental to understand the micromechanics of the material, which leads to material design and optimization of different components. Because models currently used are based on the theory of fracture mechanics, it seems appropriate a brief overview of the fundamental issues; here only the ingredients strictly necessary for the comprehension will be recalled, see e.g. http://en.wikipedia.org/wiki/Fracture_mechanics#cite_note-0. All the details can be found in Anderson [9].

6.3.1 Elements of fracture mechanics

Fracture mechanics regards the study of the propagation of cracks in materials. It was developed during World War I by Griffith, to explain the failure of brittle materials, Griffith [106]. On the basis of his work there was a contradictory behavior:

- The stress needed to fracture bulk glass is around 100 MPa;
- The theoretical stress needed for breaking atomic bonds is approximately 10×10^3 MPa.

Experiments on glass fibers were also performed by Griffith himself, and he found that fracture stress increases as the fiber diameter decreases. In order to explain the low fracture strength observed in experiments, he guessed the presence of microscopic flaws in the bulk material. To verify such hypothesis, Griffith introduced an artificial flaw in his experimental specimens, much larger than other flaws in a specimen. The experiments showed that the product of the square root of the flaw length (a) and the stress at fracture (σ_f) was nearly constant, which is expressed by the equation:

$$\sigma_f \sqrt{a} \approx C \tag{6.1}$$

In the linear elastic theory it is difficult to explain the relation expressed in equation 6.1, because theoretically the stress (and hence the strain) at the tip of a sharp flaw in a linear elastic material is infinite. To solve such problem, Griffith developed a thermodynamic approach. The growth of a crack requires the creation of two new surfaces and hence an increase in the surface energy. Griffith found an expression for the constant C in terms of the surface energy of the crack by solving the elasticity problem of a finite crack in an elastic plate. In summary, he found that:

$$C = \sqrt{\frac{2E\gamma}{\pi}} \tag{6.2}$$

where E is the Young's modulus of the material and γ is the surface energy density of the material. Assuming $E = 62$ GPa and $\gamma = 1\,\mathrm{J/m^2}$ gives excellent agreement of Griffith's predicted fracture stress with experimental results for glass. Despite to the significant importance of Griffith's work, his studies were not considered by engineering community until the 1950's.

The limitation is that Griffith's theory provides excellent agreement with experimental data for brittle materials such as glass, but for ductile materials, though the relation 6.1 still holds, the surface energy γ predicted by Griffith's theory is usually unrealistically high. An improvement was done by a group working under G. R. Irwin at the U.S. Naval Research Laboratory (NRL) during World War II, because they recognized that plasticity must play a significant role in the fracture of ductile materials. For this kind of materials a plastic zone develops at the tip of the crack. As the applied load increases, the plastic zone increases in size until the crack grows and the material behind the crack tip unloads. The plastic loading

and unloading cycle near the crack tip leads to the dissipation of energy as heat. Hence, a dissipative term has to be added to the energy balance relation devised by Griffith for brittle materials. In physical terms, additional energy is needed for crack growth in ductile materials when compared to brittle materials.

To this aim total energy was subdivided into two parts: the stored elastic strain energy which is released as a crack grows and the dissipated energy which includes plastic dissipation and the surface energy. Then the total energy dissipated is $G = 2\gamma + G_p$, where γ is the surface energy and G_p is the plastic dissipation per unit area of crack growth. The modified version of Griffith's energy criterion can then be written as:

$$\sigma_f \sqrt{a} = \sqrt{\frac{EG}{\pi}} \tag{6.3}$$

For brittle materials such as glass, the surface energy term dominates and $G \approx 2\gamma = 2\,\mathrm{J/m^2}$. For ductile materials such as steel, the plastic dissipation term dominates and $G \approx G_p = 1000\,\mathrm{J/m^2}$.

Another significant achievement of Irwin and his colleagues was to find a method to evaluate the stress state near the tip of a crack induced by a remote load or residual stresses. Usually it is applied to a homogeneous, linear elastic material and is useful for providing a failure criterion for brittle materials. The stress field close to the crack tip in polar coordinates (r, θ) with origin at the crack tip can be expressed as:

$$\sigma_{i,j} \approx (\frac{K}{\sqrt{2\pi r}}) f_{i,j}(\theta) \tag{6.4}$$

where σ_{ij} is the Cauchy stress, r is the distance from the crack tip, θ is the angle with respect to the plane of the crack, and f_{ij} is a dimensionless quantity that are independent of the crack geometry and loading conditions. Irwin called the quantity K the stress intensity factor, which can be expressed in units of $\mathrm{MPa}\sqrt{\mathrm{m}}$. Because in fracture mechanics three linearly independent cracking modes are used, it is possible to define for each of them the corresponding stress intensity factor. These load types are categorized as Mode I, II, or III as shown in Figure 6.3. Mode I is an opening (tensile) mode where the crack surfaces move directly apart. Mode II is a sliding (in-plane shear) mode where the crack surfaces slide over one another in a direction perpendicular to the leading edge of the crack. Mode III is a tearing (antiplane shear) mode where the crack surfaces move relative to one another and parallel to the leading edge of the crack. Different subscripts are used to designate the stress intensity factor for the three different modes. The stress intensity factor for mode I is designated K_I and applied to the crack opening mode. The mode II stress intensity factor, K_{II}, applies to the crack sliding mode and the mode III stress intensity factor, K_{III}, applies to the tearing mode. These factors are formally defined as:

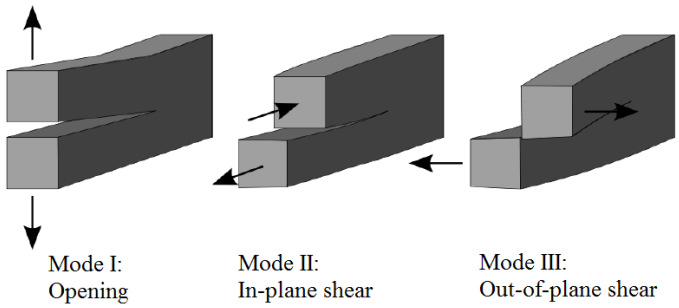

Figure 6.3: Fracture modes.

$$\begin{aligned} K_I &= \lim_{r\to 0} \sqrt{2\pi r}\sigma_{yy}(r,0) \\ K_{II} &= \lim_{r\to 0} \sqrt{2\pi r}\sigma_{yx}(r,0) \\ K_{III} &= \lim_{r\to 0} \sqrt{2\pi r}\sigma_{yz}(r,0) \end{aligned} \tag{6.5}$$

Even if the model introduced by Irwin improved Griffith's work, limitations still held. In particular different materials are not perfectly elastic but undergo significant plastic deformation close to the crack tip, and the hypothesis that the size of the plastic zone is small compared to the crack length is not true. In order to overcome such limitations, starting from the 1960's the elasto-plastic fracture mechanics theory emerged; within this field in 1968 Rice developed the concept of *J-integral*, Rice [207], a way to measure in a material the energy per unit fracture surface area. Such tool was introduced due to the difficulties in the evaluation of the stress close to a crack when the behavior is nonlinear, and the main advantage is that the integral is not influenced by the chosen path around a crack. Moreover the J-integral is equal to the strain energy release rate for a crack in a body subjected to monotonic loading, at least if the material experiences small-scale yielding at the crack tip.

With reference to Figure 6.4, J-integral in a bi-dimensional domain is defined as:

$$J := \int_\Gamma (W dx_2 - \boldsymbol{t} \cdot \frac{\partial \boldsymbol{u}}{\partial x_1} ds) \tag{6.6}$$

where $W(x_1, x_2)$ is the strain energy density, x_1 and x_2 are the coordinate directions, $\boldsymbol{t} = \boldsymbol{n} \cdot \boldsymbol{\sigma}$ is the surface traction vector, $\boldsymbol{n}$ is the normal to the curve Γ, σ is the Cauchy stress tensor, and $\boldsymbol{u}$ is the displacement vector. The strain energy density is given by:

$$W = \int_0^{\varepsilon} \boldsymbol{\sigma} : d\boldsymbol{\varepsilon}; \qquad \boldsymbol{\varepsilon} = \frac{1}{2}[\nabla u + (\nabla u)^T] \tag{6.7}$$

6.3.2 Strength and energy criterion

In order to achieve high tensile ductility and due to the formation of multiple cracking, ECC is optimized by using micromechanics, which is a branch of mechanics that links material

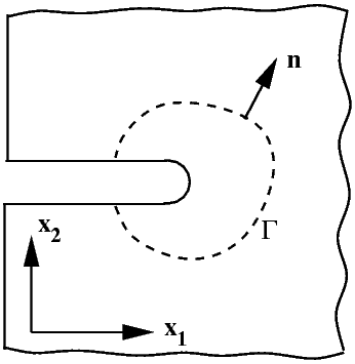

Figure 6.4: Line J-integral around a notch in a bi-dimensional problem.

constituents such as fiber, matrix and interface with macro-scale properties like strain-hardening behavior through fiber-bridging curve, which is well recognized as the most important property of fiber reinforced composites, Li [147]. In particular, within certain hypothesis, it is possible to develop closed-form solutions in order to determine the optimal content of different constituents, such as the minimum fiber volume to attain a tensile strain-hardening behavior. Fiber-bridging curve, in the following indicated also as $\sigma - \delta$ curve, represents the average tensile stress transmitted across a crack with a uniform crack opening δ; in practice, it can be seen as the constitutive law of a nonlinear spring (where the spring is the fiber), able to transfer a load when a crack opens.

Two criteria can be defined in order to achieve a strain-hardening behavior, namely a *strength criterion* and an *energy criterion*; let start to consider the first one. With reference to Figure 6.5, such criterion states that the matrix cracking strength σ_{ss} must not exceed the maximum bridging stress σ_0, so:

$$\sigma_{ss} \leq \sigma_0 \tag{6.8}$$

Because failure of the fiber means a rupture of the fiber itself or a slippage/pull-out phenomenon, equation 6.8 requires that the maximum fiber-bridging capacities is higher than the matrix cracking strength, in order to develop a sequence of small cracks instead of a big one, as usually happens for standard concrete. Within certain hypothesis, it is therefore possible to derive analytical expressions for fiber bridging curve; assuming for example randomly oriented fibers in which pull-out (rather than rupture) can occur, Li developed the equation here reported, Leung and Li [143] and Li [145]:

$$\sigma(\delta) = \begin{cases} \sigma_0[2(\delta/\delta_0)^{1/2} - (\delta/\delta_0)], & \text{for } \delta \leq \delta_0 \\ \sigma_0 \left(1 - 2\delta/L_f\right)^2, & \text{for } \delta_0 \leq \delta \leq L_f/2 \\ 0, & \text{for } L_f/2 \leq \delta \end{cases} \tag{6.9}$$

where δ_0 is the crack opening corresponding to the maximum bridging stress and L_f is the

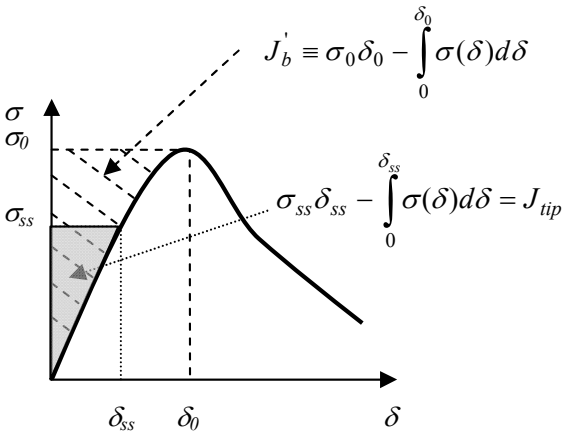

Figure 6.5: Fiber-bridging law which satisfies the condition for strain-hardening behavior, Yang et al. [248].

length of the fiber. Finally, based on J-integral analysis of a steady-state cracking, Marshall and Cox, Marshall and Cox [160], showed that:

$$J_{tip} = \sigma_{ss}\delta_{ss} - \int_0^{\delta_{ss}} \sigma(\delta)d\delta \tag{6.10}$$

where J_{tip} is the crack tip toughness, that can be approximated to the cementitious matrix toughness for composites with less than 5% fiber volume fraction, Li [145]. Using equations 6.9 and 6.10 within equation 6.8, it is possible to define the critical fiber volume fraction:

$$V_f^{\text{crit}} = \frac{12J_{tip}}{g\tau(L_f/d_f)\delta_0} \tag{6.11}$$

where τ is the fiber/frictional bond strength, d_f is the diameter of the fibers and g is the snubbing factor. Details can be found in Li [145]. Using the same procedure also Naaman (Naaman [178]) found an analogous expression for the optimal fiber volume.

Second criterion in an energy criterion and it is related to the crack propagation mode. In particular a strain-hardening behavior is related to the formation of a "steady state" cracking, defines as "... a steady state crack can be made to extend indefinitely in the matrix without fibers rupturing in the wake", Marshall and Cox [160]. With reference to equation 6.10, right-hand side can be seen as the difference between external work and the energy consumed by the bridging elements which open from 0 to δ_{ss}, and the physical meaning is the complementary energy of the fiber bridging curve (shaded area in Figure 6.5). If the fiber/matrix interface is too weak, a pull-out of the fibers occur, so the fiber bridging curve has a low peak σ_0; on the contrary, if the interface is too strong, fibers tend to break, resulting in a small value of the opening δ_0. For both situations the complementary energy is small with respect to the crack tip toughness, so cracks propagate in a Griffith mode; in particular, starting from the middle of the crack, fibers tend to unload and the opening δ_m exceeds δ_0. This leads to a softening

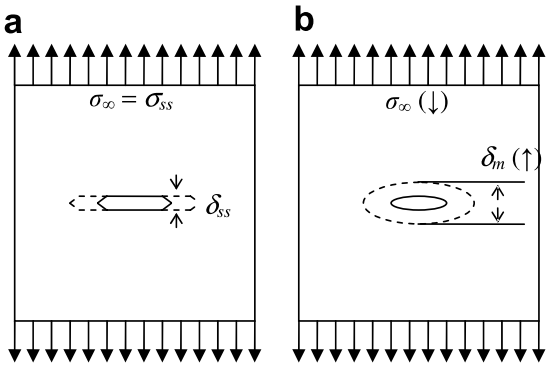

Figure 6.6: Differences in crack opening for ECC and standard concrete. (a): Steady-state cracking (flat crack). (b): Griffith crack, Yang and Li [247].

behavior, and the crack continues to open, Figure 6.6(b).

If the complementary energy is large (always with respect to J_{tip}), crack remains flat as it propagates, so a steady-state cracking mode starts ($\delta_{ss} < \delta_0$), Figure 6.6(b); in this way there is an unloading of the fibers and load can be transmitted from the fibers themselves and the surrounding matrix, where an other cracks will appear. Repetition of process allows to develop a multiple cracking. To conclude, energy criterion can be expressed as:

$$J_b^{'} = \sigma_0\delta_0 - \int_0^{\delta_0} \sigma(\delta)d\delta \geq J_{tip} \tag{6.12}$$

where $J_b^{'}$ is the maximum complementary energy (hatched area in Figure 6.5.

6.3.3 Tailoring of different components and mixture proportioning

By using the criteria above illustrated it is possible to optimize the dosage of different components; clearly, because fibers have a higher cost with respect to cement and in order to make easier the industrial processing, it is fundamental to achieve a strain-hardening behavior with the minimum amount of fibers. These can be obtained in different ways (see e.g. equation 6.11):

- Reducing matrix toughness: if matrix toughness J_{tip} is small, multiple cracking is activated with a lower percentage of fibers. A too low value is however not advisable because it should related to a low first cracking strength, not recommended for ordinary service loads;
- Modifying interfacial bond: improving the frictional bond strenth τ, without leading to a rupture, allows to reduce the volume of fibers necessary to the transition from quasi-brittle behavior to strain-hardening one. Such result can be visualized in Figure 6.7, where it shown the relationship between critical volume and bond strength for different values of matrix toughness J_c;

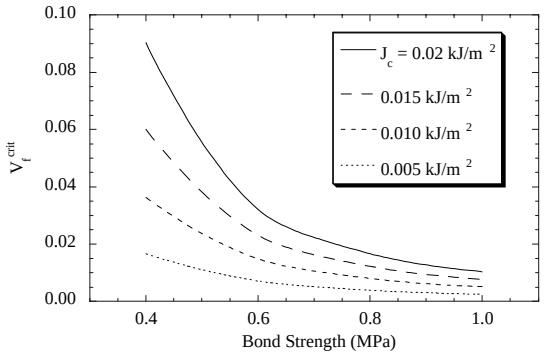

Figure 6.7: Relationship between critical fiber volume and bond strength for different values of matrix toughness, Li [145].

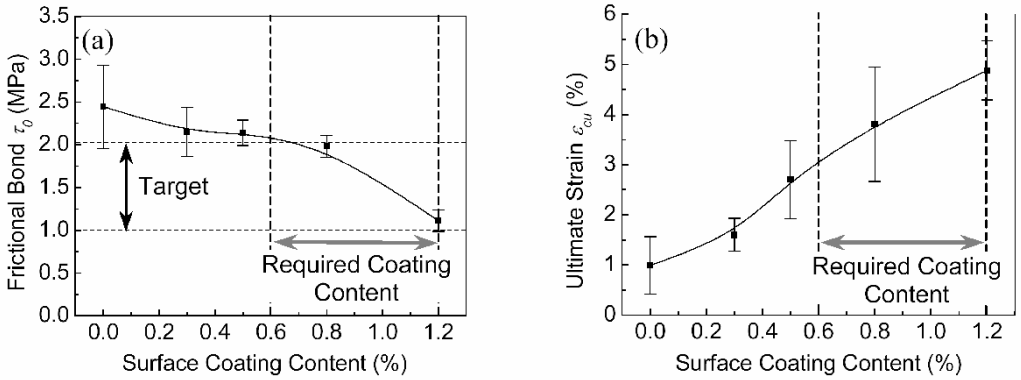

Figure 6.8: Optimal range for frictional bond using PVA fiber. (Left): result of a pull-put test showing the target range. (Right): Relationship between tensile strain and surface coating content from uniaxial test, Li [147].

- Tailoring aspect ratio: increasing aspect ratio L_f/d_f allow a reduction of critical volume. However, too long fibers are not recommended due to difficulties in material processing.

Frictional bond can be also reduced when fibers with high chemical and frictional strength are adopted, e.g. PVA. In this case the bond properties are adjusted via control on the surface coating of the fibers. For example, a surface coating content between 0.8 and 1.2% by weight of fibers tend to lower the interface strength in order to reach a critical volume close to 2%. Figure 6.8 shows the significant influence of tailoring bond strength on tensile strain capacity. Engineered cementitious composite can be realized using different types of fiber, such as polymeric, carbon or steel. The matrices used are mostly cement and mortar; typically only fine aggregates are used. Depending on the mixture proportioning the material has particular properties; however, main characteristics can be summarized in Table 6.1. In Table 6.2 it is shown the typical mix of ECC with self-consolidating casting properties (ECC-M45), which has currently the largest experimental database. It uses poly-vinyl-alcohl (PVA) as fibers, even if also poly-ethylene (PE) is common for this kind of cementitious composite. All the

Table 6.1: Principal charachteristcs of ECC, Li [149].

Compressive strength [MPa]	First crack strength [MPa]	Ultimate tensile strength [MPa]	Ultimate tensile strain [%]	Young's modulus [GPa]
20 – 95	3 – 7	4 – 12	1 – 8	18 – 34

Table 6.2: Mix design of ECC-M45, Li [149].

Cement	Fly ash	Sand	Water	HRWR	Fiber [Vol. %]
1.0	1.2	0.8	0.56	0.012	2

details regarding mix design of this particular class of ECC can be found e.g. in Sahmaran et al. [217] and Sahmaran et al. [218]; concerning the characteristics of the fibers, Table 6.3 shows the main properties of PVA and PE.

Despite of general properties indicated above, for particular application different ECC classes have been developed. For example, Wang and Li (Wang and Li [243]) carried out an experimental program using high-early strength engineered cementitious composites, with a compressive strength of 21 MPa within four hours after replacement. In Wang and Li, Wang and Li [244], it is a reported a study on ECC with high volume fly-ash, using two different types of fiber (PVA and PE). It is shown how an increase of fly ash leads to higher complementary energy in the fiber-bridging curve and to a decrease in matrix toughness, in order to improve strain-hardening behavior.

6.4 Mechanical properties of ECC

This section summarizes the mechanical properties of ECC in terms of monotonic behavior (tensile and compressive) as well as the cyclic one. Fundamental characteristics are addressed, and a review of numerical modeling proposed in literature is briefly illustrated. For simplicity, in the following both the terms ECC and DFRCC (ductile fiber renforced cementitious composite) are used in order to indicate cementious composites with a tensile strain-hardening behavior.

Table 6.3: Main characteristics of polymeric fibers used within ECC.

Type	Diamer [µm]	Length [mm]	Elastic modulus [MPa]	Strength [MPa]
PVA	39	8	42.8	1620
PE	38	12.7	120	2700

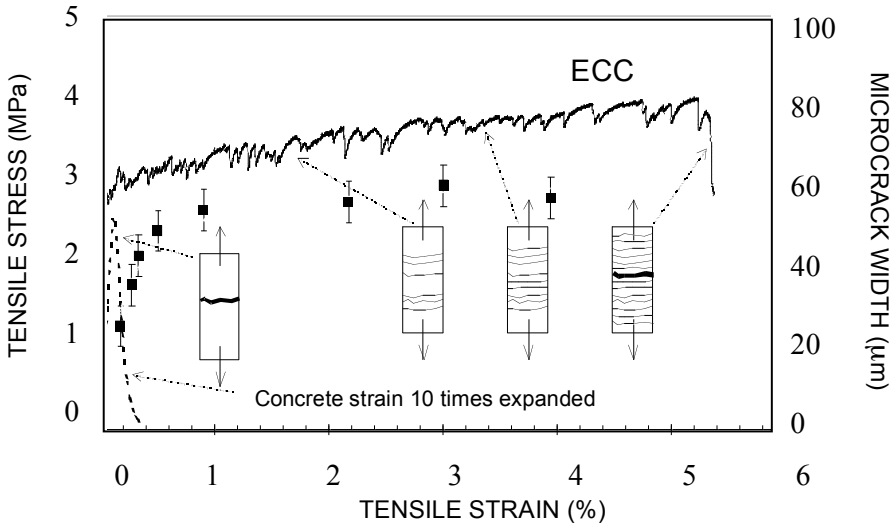

Figure 6.9: Tensile behavior of ECC compared with stress-strain of standard concrete, including also the crack width propagation, Li [149].

6.4.1 Monotonic behavior

Tensile behavior

The significant difference in the mechanical properties between standard concrete and ECC is related to their behavior under tensile loads. Figure 6.9 illustrates in a clear way such difference: considering standard concrete, when the tensile strength is reached there is a sudden drop in the capacity. The corresponding behavior can be defined brittle. On the contrary, ECC has a ductile behavior due to the formation of multiple cracking. In particular, after the first crack opening, the material is able to sustain an increasing load because fibers crossing the crack have a strength higher than the matrix. In this way the stresses can be transferred to an adjacent zone, and a subsequent crack will develop when the corresponding strength is reached. Again, load can be yet sustain due to the activation of the fibers across the crack, and a strain-hardening behavior appears. Finally, when the fiber bridging capacity is exhausted and the strain begins to localize at one crack, the peak tensile stress is reached and failure occurs. In any case, a peak deformation in order of $3-5\%$ is achieved, hundreds of times higher than the maximum strain obtained with standard concrete.

During the last decade the mechanical properties of such material have been tested by different research groups. For example, in Kesner et al. [133], cylindrical and dogbone specimens have been studied under uniaxial and cyclic tests in order to develop a suitable constitutive law. Different mixture proportions have been used, adopting as fibers both polyethylene with and without aggregate (PE-A and PE) and polyvinyl alcohol (PVA) with and without a presoaked process. Results of tensile test are shown in Figure 6.10. Cylindrical specimens have a lower peak tensile strength and strain capacities than the dogbone specimens, because

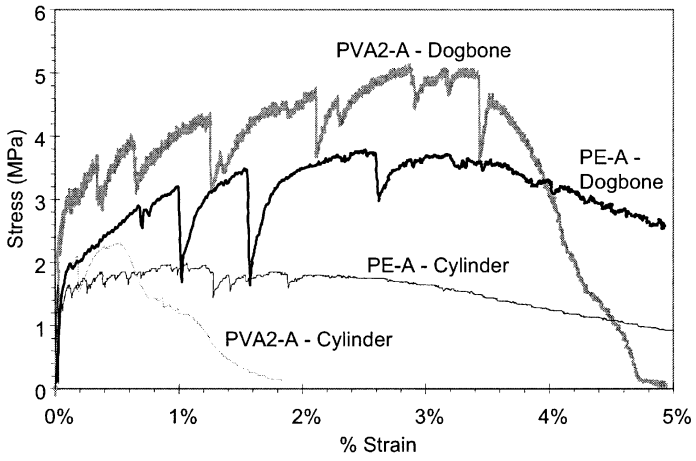

Figure 6.10: Stress-strain curves for DFRCC specimens with different geometry and mixture proportions, Kesner et al. [133].

different reasons. One it is related to the presence of initial flaws, and casting of the thinner dogbone specimens allows for better material consolidation. Another explanation concerns the alignment of the fibers; again, casting of dogbone specimens makes easier a better alignment, resulting in a better reinforcement.

In the study of Parra-Montesinos, Parra-Montesinos [191], the performance of ECC with different types of fiber (steel and polyethylene) are compared and different applications for earthquake-resistant structures are illustrated. Steel fibers have a length equal to $30\,mm$, a diameter of $50\mu m$ and a volume ranges from 1.5 to 2%. The tensile stress-strain response is shown in Figure 6.11; the most significant aspect is that PE fibers have a larger strain capacity before failure occurs. In any case, the post-peak behavior is similar to that of ECC with twisted steel fibers.

Studies have been also carried on in Europe; recently Mechtcherine (Jun and Mechtcherine [130]) presented the results of an experimental program to a better understanding of mechanical properties of this composite material; in particular dogbone specimens have been tested under monotonic and cyclic tensile loading. Moreover, also the properties of the single fibers have been studied by using tension and pull-out tests. In the investigated DFRCC a combination of Portland cement 42.5R HS and fly ash has been utilized as binder. Furthermore, polyvinyl alcohol fibers, with a 2.25% of the total mix by volume, 12 mm in length, diameter of 40 µm have been used. A superplasticiser and a viscosity agent have been added to the mix in order to adjust its rheological properties. Specimens tested had a cross-section of 24×40 mm; all the details can be found in Jun and Mechtcherine [130]. Tensile and cyclic tests have been performed in displacement-control, with a deformation rate equal to 0.01 mm/s, Figure 6.12 shows the results of tensile tests compared with those coming from cyclic ones. As can be seen, after first cracking a hardening branch starts due to the development of multiple cracking,

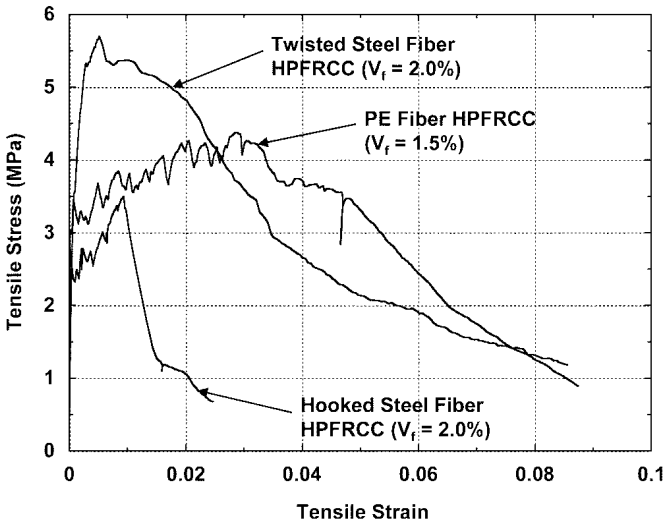

Figure 6.11: Tensile response for ECC material with steel and polymeric fibers, Parra-Montesinos [191].

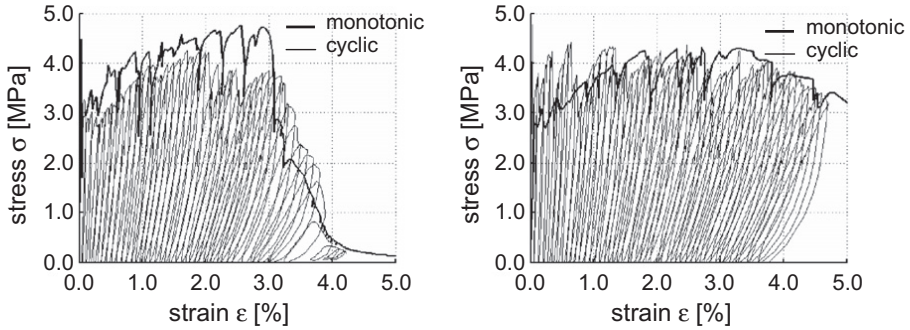

Figure 6.12: Uniaxial and cyclic tensile response of ECC specimens, Jun and Mechtcherine [130].

until peak stress is reached. Also in this case ultimate tensile strain is around 3%, much higher than standard concrete.

Compressive behavior

Also in compression ECC presents differences with respect to ordinary concrete; in particular the most relevant property is a lower initial stiffness due to the lack of coarse aggregates. This is clearly shown in Figure 6.13, where the compressive behavior of ECC is compared with that of concrete in terms of stress-strain curves. As indicated, fiber composite has a higher strain capacity, even if the strength is equal. After peak is achieved, a softening-branch begins, but capacity decreases in a smooth way, with a behavior similar to that of a well-confined concrete. This property makes such material very attractive for seismic applications, because a reduction in terms of shear reinforcement requirement seems possible, Li [147].

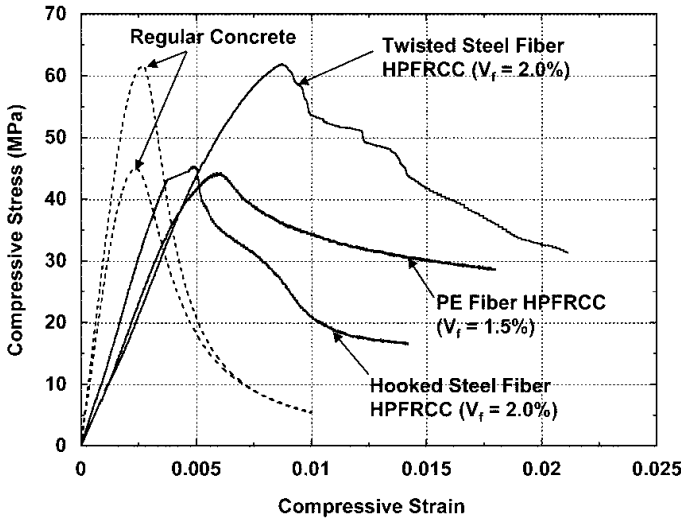

Figure 6.13: Compressive stress-strain curves for concrete and ECC, Parra-Montesinos [191].

Results of compressive tests can be found also in Kesner et al. [133], where it is indicated that the compressive strength of such composite is similar to traditional cementitious materials using similar water to cement ratio. Figure 6.14 illustrates the stress-strain curves using two types of fibers (PE and PVA) with and without fine aggregate. The behavior is practically linear-elastic up to the peak for PE, while there is a deviation in case of PE-A and PVA2-A, attributed to the propagation of bond cracks between the aggregate and cement paste during loading, Kesner et al. [133]. Softening branch is on the contrary similar regardless the type of composite.

6.4.2 Cyclic behavior

Having in mind earthquake-resistant applications, it is fundamental a proper understanding of the cyclic behavior of the engineered cementitious composites; in this field a comprehensive document is the work carried out by Kesner, Billington and Douglas, Kesner et al. [133]. Here only the key points are underlined. In particular different loading protocols have been considered, in one case using only cyclic compression, in the other including reversals in load from tension to compression. Results of the first test are reported in Figure 6.15; regardless mixture proportions unloading and reloading paths are similar. When softening branch is reached and unloading occurs, initial portion is linear elastic, followed by a parabolic behavior. Reloading of the specimen is then parabolic until reaching the strain where unloading occurred. Regarding second type of test, one of main issue was to examine how compressive softening of ECC affected his tensile response; so, specimens have been alternately loaded in compression, followed by tension, to progressively increasing strain levels. Such influence emerges looking at Figure 6.16, where it is indicated the tensile strain cycle reached immediately after softening occured in compression. At this point, the tensile capacity of the material drops as it continued

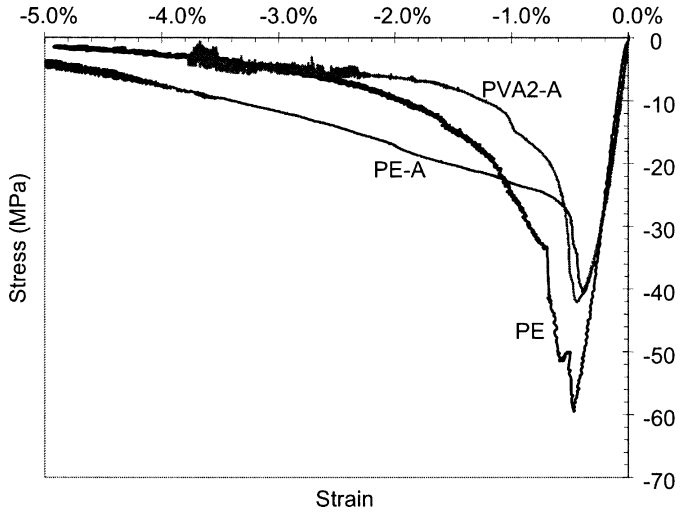

Figure 6.14: Compressive stress-strain curves with different polymeric fibers, Kesner et al. [133].

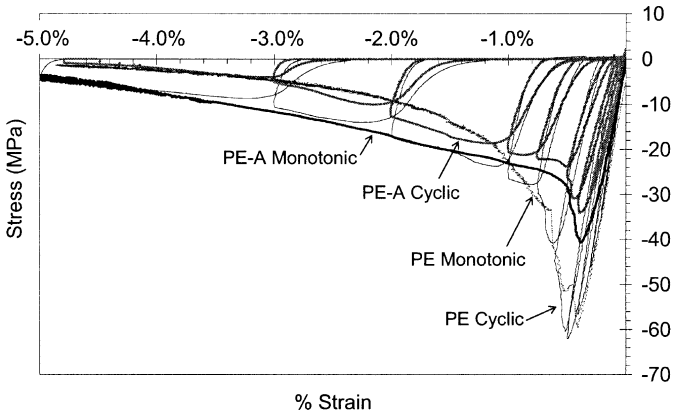

Figure 6.15: Cyclic compression stress-strain curves for DFRCC materials with and without aggregate, Kesner et al. [133].

to strain in tension, and a localization of the cracks begins.

Such behavior not appear in Figure 6.12, where a comparison of the monotonic curves with those obtained from the tests using the cyclic loading regime shows that practically tensile capacity is not affected by cyclic loading, because only a small decrease in stresses occurs. This is probably due to the different testing protocol used; in fact, in the work of Mechtcherine (Jun and Mechtcherine [130]) only tensile loading has been considered in the cyclic tests.

6.4.3 Survey of analytical models available in literature

In order to simulate in a reliable way the characteristics of engineered cementitious composited illustrated above, in last years an attempt has been done to develop appropriate constitutive laws. To give an example, recently Mechtcherine (Jun and Mechtcherine [131]) derived

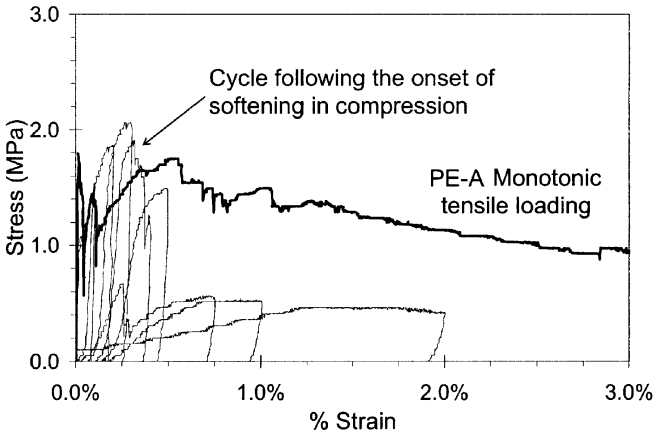

Figure 6.16: Tensile behavior considering monotonic and cyclic loading, Kesner et al. [133].

constitutive relationships on the basis of a multi-scale modeling approach, following the experimental results described in Jun and Mechtcherine [131]. First step is the reproduction of the fiber-pullout behavior under monotonic as well as under cyclic loading by a multi-linear approximation. The responses obtained have been therefore superimposed in order to describe the stress-crack opening behavior of each individual crack while being loaded, unloaded, or reloaded. Finally, the overall stress-strain relationships for material under tensile loading have been derived by considering an increasing number of serial cracks and the contribution of the uncracked matrix. For a review of different models proposed in literature readers can refer to Gencturk [96].

Here the attention is focused on analytical models able to predict the response at the structural level, with particular reference to the analytical formulation proposed by Han, Han et al. [110], because it is the model used in the following for the cross-sectional analysis of the structures investigated in the present study. The constitutive relationship is based on the cyclic behavior observed in the experimental program on ECC described in detail in Kesner et al. [133]; the uniaxial model follows the total strain rotating crack model. The model is relatively simple, and all the parameters introduced can be derived through cyclic loading experiments.

In tension, the material presents three different regions: in the initial portion the behavior is linear elastic until the first cracking strain ε_{t0} is reached. Subsequently, multiple cracking starts to develop and the stiffness reduces; in any case the load can be sustained due to the strain-hardening behavior. When the ultimate strength σ_{tp} is achieved, capacity sudden drops due to the localization of the cracks. Once the ultimate strain ε_{tu} is exceeded, the material is no more able to carry any tensile stress. The multi-linear curve is indicated in the following expression and depicted in Figure 6.17(a):

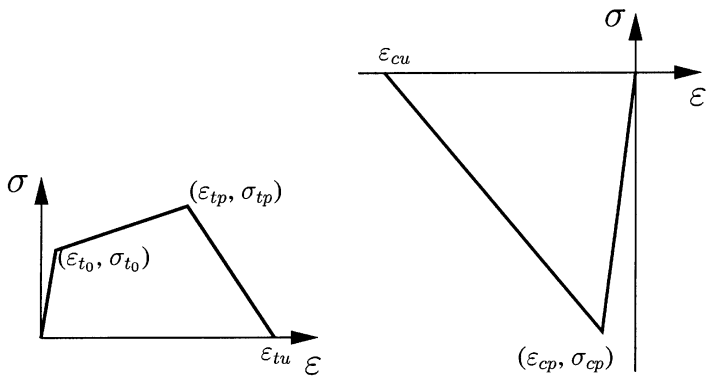

(a) Tension (b) Compression

Figure 6.17: Analytical modeling of ECC stress-strain envelope, Han et al. [110].

$$\sigma_t = \begin{cases} E\varepsilon, & 0 \leq \varepsilon < \varepsilon_{t0} \\ \sigma_{t0} + (\sigma_{tp} - \sigma_{t0}) \left(\dfrac{\varepsilon - \varepsilon_{t0}}{\varepsilon_{tp} - \varepsilon_{t0}} \right), & \varepsilon_{t0} \leq \varepsilon < \varepsilon_{tp} \\ \sigma_{tp} \left(1 - \dfrac{\varepsilon - \varepsilon_{tp}}{\varepsilon_{tu} - \varepsilon_{tp}} \right), & \varepsilon_{tp} \leq \varepsilon < \varepsilon_{tu} \\ 0, & \varepsilon_{tu} \leq \varepsilon \end{cases} \tag{6.13}$$

where E is the Young's modulus. Regarding compressive envelope, experimental showed that the pre-peak response can be approximated by a linear-elastic branch, while post-peak behavior is similar to ordinary concrete. In the original model, a multi-linear relationship was however introduced, Figure 6.17(b):

$$\sigma_c = \begin{cases} E\varepsilon, & 0 \leq \varepsilon_{cp} < 0 \\ \sigma_{cp} \left(1 - \dfrac{\varepsilon - \varepsilon_{cp}}{\varepsilon_{cu} - \varepsilon_{cp}} \right), & \varepsilon_{cu} \leq \varepsilon < \varepsilon_{cp} \\ 0, & \varepsilon \leq \varepsilon_{cu} \end{cases} \tag{6.14}$$

Figure 6.18 shows the unloading and reloading scheme adopted, based on the experimental observations found in Kesner et al. [133]. Concerning tensile region ($\varepsilon \geq 0$ and $\varepsilon < \varepsilon_{t,max}$), where $\varepsilon_{t,max}$ is the experienced maximum tensile strain, it is possible to write:

$$\sigma_t = \begin{cases} E\varepsilon, & 0 \le \varepsilon_{t,max} < \varepsilon_{t0} \\ \max\left[0, \sigma^*_{t,max}\left(\dfrac{\varepsilon - \varepsilon_{t,ul}}{\varepsilon^*_{t,max} - \varepsilon_{t,ul}}\right)^{\alpha_t}\right], & \varepsilon_{t0} \le \varepsilon_{t,max} < \varepsilon_{tp} \quad \dot{\varepsilon} < 0 \\ \max\left[0, \sigma^*_{t,ul} + (\sigma_{t,max} - \sigma^*_{t,ul})\left(\dfrac{\varepsilon - \varepsilon^*_{t,ul}}{\varepsilon^*_{t,max} - \varepsilon^*_{t,ul}}\right)\right], & \varepsilon_{t0} \le \varepsilon_{t,max} < \varepsilon_{tp} \quad \dot{\varepsilon} \ge 0 \\ \max\left[0, \sigma_{t,max}\left(\dfrac{\varepsilon - \varepsilon_{t,ul}}{\varepsilon_{t,max} - \varepsilon_{t,ul}}\right)\right], & \varepsilon_{tp} \le \varepsilon_{t,max} < \varepsilon_{tu} \\ 0, & \varepsilon_{tu} \le \varepsilon_{t,max} \end{cases} \tag{6.15}$$

where $\alpha_t \ge 1$ is a constant parameter calibrated according to experimental tests (related to unloading behavior in tension). The value $\varepsilon^*_{t,max}$ in equation 6.15 is defined as:

$$\varepsilon^*_{t,max} = \begin{cases} \varepsilon_{t,max}, & \text{for initial loading} \\ \varepsilon_{t,prl}, & \text{for unloading followed by partial reloading} \end{cases} \tag{6.16}$$

where $\varepsilon_{t,prl}$ is the maximum tensile strain during partial reloading and $\sigma^*_{t,max}$ is the stress related to $\varepsilon^*_{t,max}$. Parameter $\varepsilon^*_{t,ul}$ is instead defined as:

$$\varepsilon^*_{t,ul} = \begin{cases} \varepsilon_{t,ul}, & \text{for initial loading} \\ \varepsilon_{t,pul}, & \text{for unloading followed by partial reloading} \end{cases} \tag{6.17}$$

where $\varepsilon_{t,ul} = b_t \cdot \varepsilon_{t,max}$ (b_t is a constant calibrated on the basis of experimental tests, corresponding to residual strain in tension). $\varepsilon_{t,pul}$ is the minimum strain during partial reloading and $\sigma^*_{t,ul}$ is the stress corresponding to $\varepsilon^*_{t,ul}$. Unloading and reloading behavior can be visualized in Figures 6.18(a) and (b), during strain-hardening or softening, respectively. Compressive behavior in compression follows the same approach ($\varepsilon < 0$ and $\varepsilon > \varepsilon_{c,min}$, where $\varepsilon_{c,min}$ is the experienced minimum compressive strain):

$$\sigma_c = \begin{cases} E\varepsilon, & \varepsilon_{cp} \le \varepsilon_{c,min} < 0 \\ \min\left[0, \sigma^*_{c,min}\left(\dfrac{\varepsilon - \varepsilon_{c,ul}}{\varepsilon^*_{c,min} - \varepsilon_{c,ul}}\right)^{\alpha_c}\right], & \varepsilon_{cu} \le \varepsilon_{c,min} < \varepsilon_{cp} \quad \dot{\varepsilon} > 0 \\ \min\left[0, \sigma^*_{c,u} + (\sigma_{c,min} - \sigma^*_{c,min})\left(\dfrac{\varepsilon - \varepsilon^*_{c,ul}}{\varepsilon^*_{c,min} - \varepsilon^*_{c,ul}}\right)\right], & \varepsilon_{cu} \le \varepsilon_{c,min} < \varepsilon_{cp} \quad \dot{\varepsilon} \ge 0 \\ 0, & \varepsilon_{c,min} \le \varepsilon_{cu} \end{cases} \tag{6.18}$$

where $\alpha_c \ge 1$ is a constant parameter calibrated according to experimental tests (related to unloading behavior in compression after peak strength). The value $\varepsilon^*_{c,min}$ in equation 6.18 is defined as:

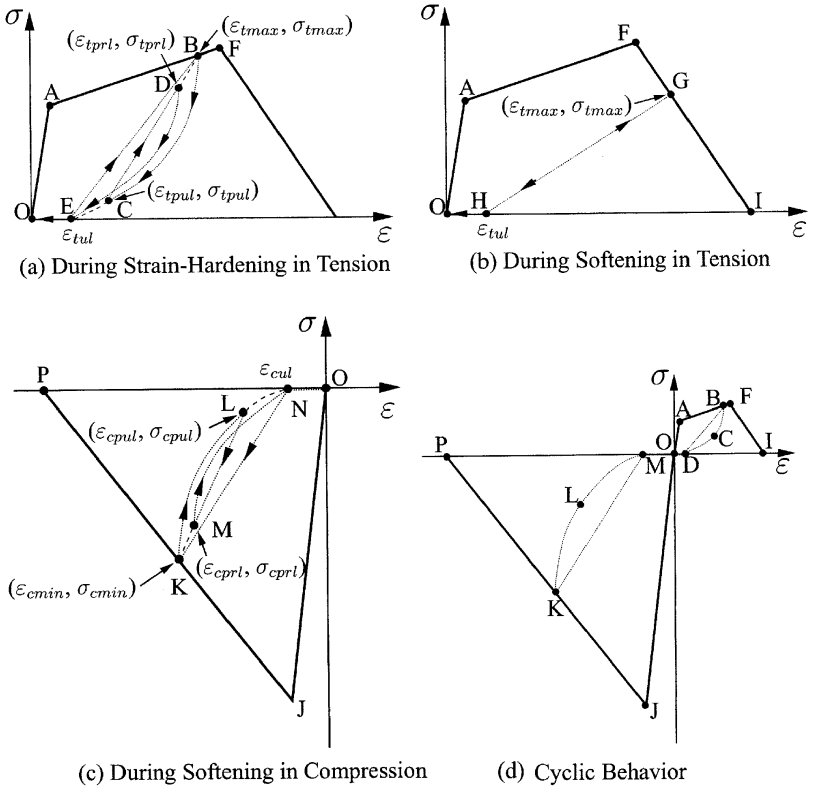

Figure 6.18: Scheme of ECC cyclic modeling, Han et al. [110].

$$\varepsilon^*_{c,min} = \begin{cases} \varepsilon_{c,min}, & \text{for initial loading} \\ \varepsilon_{c,prl}, & \text{for unloading followed by partial reloading} \end{cases} \tag{6.19}$$

where $\varepsilon_{c,prl}$ is the minimum compressive strain during partial reloading and $\sigma^*_{c,min}$ is the stress related to $\varepsilon^*_{c,min}$. Parameter $\varepsilon^*_{c,ul}$ is instead defined as:

$$\varepsilon^*_{c,ul} = \begin{cases} \varepsilon_{c,ul}, & \text{for initial loading} \\ \varepsilon_{c,pul}, & \text{for unloading followed by partial reloading} \end{cases} \tag{6.20}$$

where $\varepsilon_{c,ul} = b_c \cdot \varepsilon_{c,min}$ (b_c is a constant calibrated on the basis of experimental tests, corresponding to residual strain in compression). $\varepsilon_{c,pul}$ is the minimum strain during partial reloading. Unloading and reloading behavior can be visualized in Figure 6.18(c). As indicated in Han et al. [110] such model requires 10 parameters that can be determined through cyclic tests.

In the original formulation above illustrated the unloading and reloading schemes for the strain-hardening range in tension and the softening range in compression have been assumed to be governed by power laws, while the unloading in the tensile softening range has been considered linear. With respect to such model, subsequent improvements have been done. In particular, the softening branch in compression is no more limited to a linear function, but

can be described by a power law; moreover, also the unloading branch during softening in tension is now described by a power law. Clearly the relationship described in this section can be derived using an exponent equal to 1. Such improved formulation is therefore used in the present investigation.

A similar constitutive law has been recently proposed by Genturk working in the University of Illinois at Urbana-Champaign, Gencturk [96]. With respect to the original model of Han, Han et al. [110], this model presents some improvements, including higher order reloading relationships in tension and compression, plastic strain model based on regression analysis, and transition curves from tension to compression and vice versa. All the details can be found in Gencturk [96].

6.4.4 Advantages and target applications

In the previous sections the mechanical properties of engineered cementitious composites have been highlighted; the peculiar feature is the significant ductility, and this implies a reduced probability of brittle failure of structural members. The increase in toughness allows a higher strength of the elements, even if the nominal strength of the composite is lower than standard concrete. This is evident in the experimental studies carried out by Kesner and Billington, Kesner and Billington [132], where precast infill panels for seismic retrofitting of buildings have been studied, using both ordinary concrete and ECC. Although the compressive strength of concrete was higher (58 MPa vs 41 MPa), cyclic shear load tests revealed a lower structural strength 38 kN vs 56 kN. This because if tensile failure occurs, high strength material does not mean necessary high structural strength, Li [147].

One of the most important advantages is related to the potential reduction of shear reinforcement, which is particular significant for seismic applications; because tensile behavior is ductile, also shear response is ductile. Load capacity is therefore higher than standard concrete, and this is clear looking at Figure 6.19, where it is shown the comparison between cyclic tests on a cantilever column using both RC (with shear reinforcement) and R/ECC (without shear reinforcement). No significant damage occurred in the second case, while ordinary concrete presents cover splitting.

Due to the improvement in ductility, cementitious matrix and reinforcement have compatible deformations within a significant range, even if bars yield. In this way the hypothesis of perfect bond between the two materials is not so critic as for ordinary concrete, resulting in a more uniform strain deformation, Figure 6.20. Such result clearly emerges in the study carried on by Fischer and Li, Fischer and Li [89], where uniaxial tension tests have been performed on RC and R/ECC specimens. Because multiple cracking behavior, the width of the cracks is not so dramatic. Typically the value depends on type of fibers included in the matrix; by using PVA fibers the width is generally less than 100 µm. If external load increases within strain-hardening behavior, more cracks appear but the width not exceed a predefined

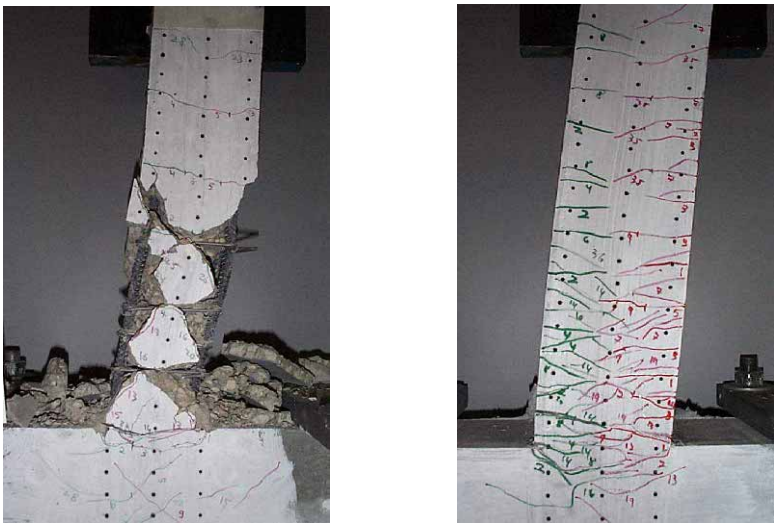

Figure 6.19: Damage experienced by a RC (left) and R/ECC (right) cantilever column after cyclic test, Li [147].

threshold.

As stated before, certainly on the main application for this kind of material is the use for seismic-resistant structures. For example, in Fischer and Li [91] the response of moment-resisting frame system with ECC combined with fiber reinforced polymers (FRP) has been ivestigated. With this configuration column elements have a relatively high flexural strength and sufficient elastic deflection capacity to permit frame sway and prevent the formation of a collapse mechanism due to lateral loading. In Parra-Montesinos [191] the author reviews a list of potential applications, in particular for use in members with shear-dominated behavior or in flexural members under high shear stresses. These include beam-column connections, low-rise walls and coupling beams.

Second fundamental class of applications regards structures requiring durability even if subjected to severe environmental conditions. Due to the small crack opening, transport rate of aggressive agents such as chlorides and sulphates is lower than ordinary concrete, so ECC delays steel corrosion, extending the lifetime of the structures. A review of the behavior of this composite under freeze-thaw cycles, hot-cold temperature cycles, carbonation exposure, fatigue loading and long term mechanical performance can be found in Lepech and Li [142]. It is worth nothing that field inspections have been performed in addition to laboratory tests, in order to check durability of ECC in actual service conditions. In particular, with the cooperation of Michigan Department of Transportation, one section of a damaged bridge deck has been repaired with such composite, while the remaining part retrofitted with standard concrete. After four years, maximum crack width experienced by ECC patch is around 50 µm, while concrete patches have been already been replaced. A detailed description can be found in Li and Lepech [150]. Readers interested in a review of different applications using ECC for

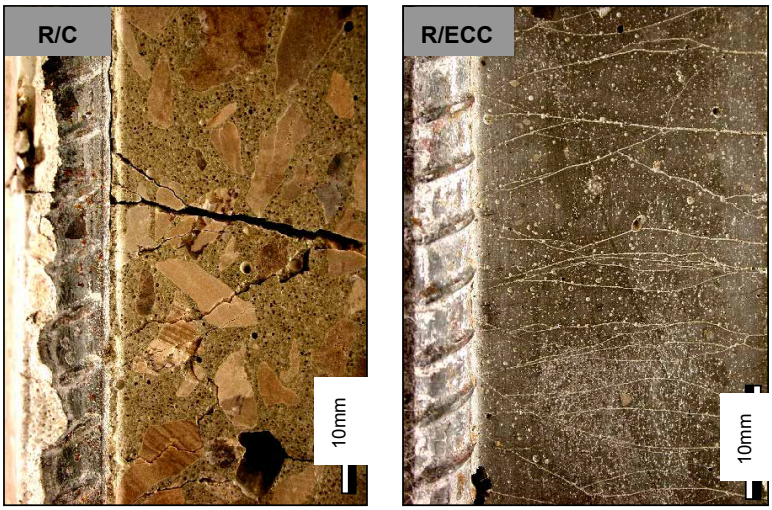

Figure 6.20: Cracking distribution for RC and R/ECC specimen. Compatible deformations between steel and cementitious matrix for ECC result in a multiple cracking behavior, Li [147].

durability improvement can refer to Li [149].

The concepts expressed above seems very attractive within the present study, because the goal is to study the lifetime seismic performance of multistory precast frames, with the final intent to propose a potential mitigation strategy for damage induced by seismic and environmental hazard. To this purpose, next section is devoted to the description of durability properties of engineered cementitious composite related to chloride diffusion.

6.5 Durability properties of ECC

Since in last years the concept of durability and sustainability has become one of the key point in the design of structures, new materials need to fulfill this requirement. As indicated in previous sections, the mainly advantage of ECC is his capability to sustain increasing loads due to the very high ductility, so it should retain serviceable conditions even if a multiple cracking developing, Li [149]. To this purpose, durability tests on such composite should be carried out in the deformed state in order to check the influence of cracks; however, due to their simplicity, experimental tests are usually performed in the unloaded condition. In the following it is illustrated a brief review of durability studies presented in last years; more details can be found in Li [149] and Ahmed and Mihashi [2].

Time evolution of tensile properties has been studied by Lepech and Li, Li and Lepech [150]; Figure 6.21 shows the result of uniaxial tensile tests performed during time on such composite. Because hydration processes, matrix toughness tends to increase, leading to a reduction of ductility. Nevertheless, a strain deformation around 3% is maintained also in long-terms tests. In the field of transportation constructions, durability of material regarding

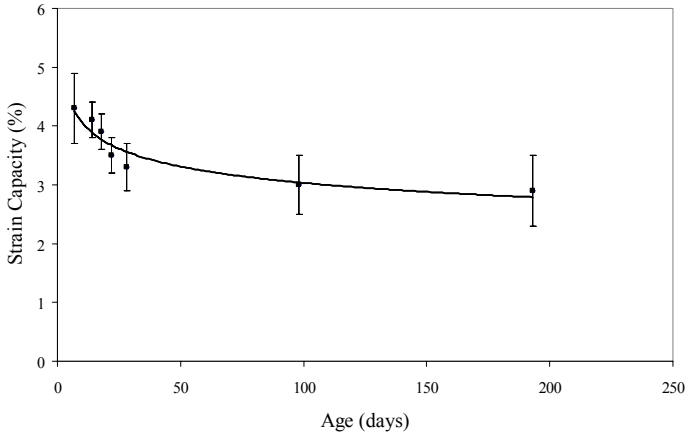

Figure 6.21: Long-term strain capacity of ECC, resulting from uniaxial tests (Li and Lepech [150]).

freeze-thaw cycles plays a fundamental role. To this purpose, in Li et al. [151] is described the development of durable link slabs for jointless bridge decks based on strain-hardening cementitious composites. Concrete and ECC specimens have been subjected to freeze-thawing cycles according to ASTM C 666; after 110 cycles concrete revealed serious damages, while ECC was able to sustain the entire cycle process (around 300 cycles) without significant damage, as can be seen in Figure 6.22, which illustrates the evolution of dynamic modulus for concrete and engineered cementitious composite.

Opposite to freeze-thaw tests, durability of ECC with PVA fibers has been tested also in tropical climate exposure, Li et al. [152]; in particular authors used hot water immersion test simulating a long-term hot and humid environment. Specimens have been treated for 28 days at room temperature prior to immersion in hot water at 60 °C for 26 weeks. Even if there was a decrease in strain capacity (from 4.5% to 2.7%), final value was however hundreds of times higher that of normal concrete. To conclude, tests on chloride immersion were also performed, in order to simulate the exposure in a marine environment or the effect of de-icing salts used for bridge decks. ECC specimens have been loaded under uniaxial tension to achieve different strain levels prior to immersion to a 3% NaCl solution at room temperature for 1, 2 and 3 months, and subsequently reloaded up to failure, Li et al. [144]. In all cases the strain-hardening behavior was maintained, with a tensile capacity around 3%, even if the average width of the cracks increased from 40 µm to 100 µm and the tensile strength had a 10% of drop.

In a common view, a dense cementitious matrix stands for a better durability of the material due to the reduced permeability, so aggressive agents have difficulties to reach steel bars. It is however important to remember that the development of cracks under serviceable loads is unavoidable for reinforced concrete structural members, leading to an increase in the transport rate of chemical species like sulphates and chlorides. Have in mind the considerations

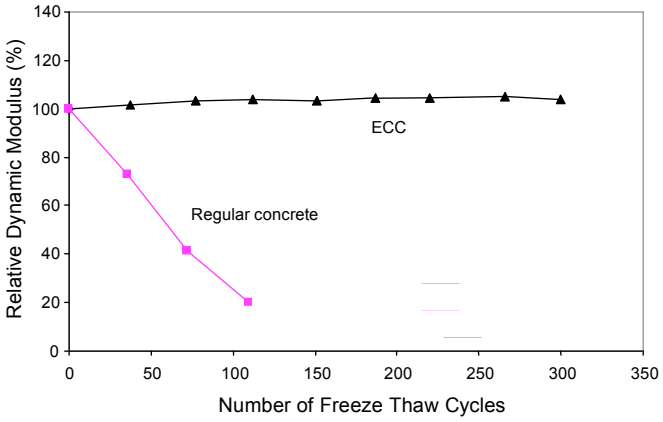

Figure 6.22: Evolution of dynamic modulus considering freeze-thawing cycles, Li et al. [151].

above explained, the replacement of standard concrete with ECC has a double effect:

- Change of transport properties, extending the life of reinforcement;
- Change in the nature of corrosion, potentially avoiding pitting and slowing the rate of corrosion.

With reference to chloride-induced damage, the mentioned advantages are presented in the following.

6.5.1 Diffusion mechanism of chlorides

Regarding diffusion mechanism of chlorides, in Sahmaran et al. [217] it is presented an investigation on transport properties of engineered cementitious composite under combined mechanical and environmental loads. Both ECC with PVA fibers and mortar beams have been ponded in solution with 3% NaCl according to AASHTO recommendations for different times (30, 60 and 90 days), in order to evaluate chloride profiles and corresponding diffusion coefficients D, adopting the solution of Fick's law, see equation 4.8. Regarding uncracked specimens, mortar experienced a diffusion coefficient equal to $6.75 \times 10^{-12}\,\mathrm{m}^2/\mathrm{s}$, while mortar $10.58 \times 10^{-12}\,\mathrm{m}^2/\mathrm{s}$. Same procedure has been repeated after a four-point bending tests on the specimens in order to induce a pre-damage state and to understand the role of cracking on transport properties.

Under high imposing bending deformation, ECC beams experienced in any case a maximum crack width not exceeding 50 µm, while in mortar cracks achieved a maximum value around 400 µm; the fundamental issue emerged was the different influence of cracks o diffusion coefficient. Concerning engineered cementitious composite, coefficient of diffusion changes linearly with respect to the number of cracks, while for mortar there is a parabolic relationship among D and crack width, Figure 6.23. Due to strain-hardening behavior, an increase in load

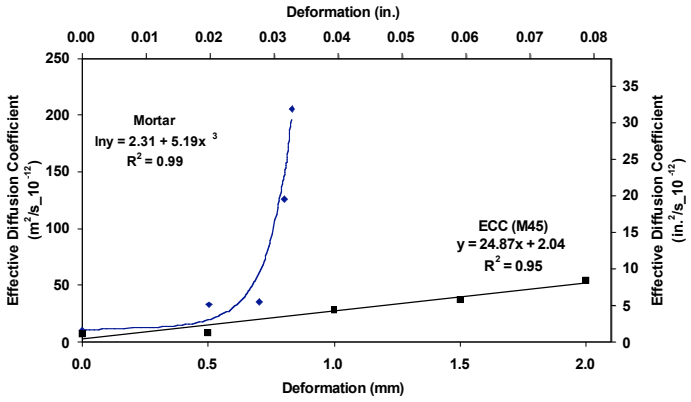

Figure 6.23: Evolution of diffusion coefficient under pre-loading state, Sahmaran et al. [217].

is not reflected in wider cracks but only in an increase of their number. Chloride diffusion process has been also investigated by Oh and Shin, Oh and Shin [182]; specimens have been subjected to 100,000 cycles of flexural bending, checking the variation of diffusion coefficient. Authors found that no significant increase occured, due to the development of narrow multiple cracking.

6.5.2 Nature and rate of corrosion

An important study on the nature of corrosion when cementitious matrix is based on ECC has been carried out by Miyazato and Hiraishi, Miyazato and Hiraishi [168]. Pre-loaded RC and R/ECC beams with special divided steel bars (in order to evaluate micro cell current density) have been subjected to chloride accelerated environment for 28 days with wet and dry cycles. At the end of the procedure they measured a penetration depth for ECC ranged from 0 mm to 20 mm, while for standard concrete from 80 mm to 100 mm. Subsequently, by evaluating current density, they found a corrosion rate less than 0.0004 mm/year for engineered cementitious composite, while 0.008 mm/year for mortar, Figure 6.24. It is important to underline the alteration in the nature of corrosion; for concrete, corrosion practically occurs in the pre-damaged section, leading to a localized attack (pitting). In this case the corrosion cell formation pattern is macro cell. In case of ECC, due to multiple cracking, corrosion occurs in a more uniform way (micro cell), leading to a reduction of damage rate.

In the study performed by Sahmaran, Sahmaran et al. [218], the goal was to understand the potential ability of ECC to extend the lifetime of structural members even if subjected to corrosion, due to the significant tensile ductility. In particular mortar and engineered cementitious composite specimens with the same compressive strength have been subjected to an accelerated corrosion test to induce different degrees of corrosion into the reinforcing bar embedded within. Looking at concrete specimen, higher corrosion levels led to large crack width (around 2 mm after 75 hours of test), while ECC specimens experienced multiple narrow cracks less than 0.1 mm after 150 hours testing. This implies a significant resistance against

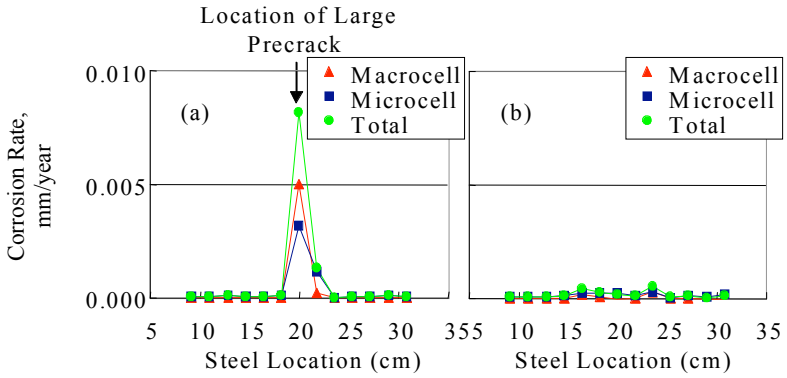

Figure 6.24: Corrosion rate along steel bar for pre-loaded RC and R/ECC beams, Miyazato and Hiraishi [168].

cover spalling in R/ECC members in the presence of significant steel bar corrosion, Figure 6.25. Concerning load capacity, concrete beams had a drop around 34% in terms of flexural strength after 25 hours of test, while ECC sustained approximately total capacity up to 50 hours, and after 300 hours the residual capacity was over 45%. Corrosion influenced also failure mode, Figure 6.26; before corrosion has been induced, four-points bending test revealed a bending failure in case of ECC due to his significant ductility, while concrete beam failed in shear. After corrosion test, no changes in collapse mode appeared for engineered cementitious composite, while in mortar a bond splitting failure occurred, due to the propagation of corrosion along bar. To conclude, Figure 6.27 illustrates the evolution of loss of steel mass for the two types of specimen. Corrosion test on concrete has been exhausted after 75 hours because severe damage appeared. We can see that around 5 hours, steel embedded in mortar lost 5% of mass, while reinforcement in ECC was practically undamaged. The picture highlights in a clear way that corrosion rate experienced by engineered cementitious composite is significantly lower than that resulting in ordinary concrete.

Due to significant advantages experienced by such composite, both for seismic and durability application, the use of engineered cementitious composite seems very attractive in the present investigation. To this aim, in the following sections the results of seismic risk study on the different multistory structures previously introduced are presented, in order to underline the significant advantages with respect to the use of standard concrete.

6.6 Concentrated plasticity model for ECC

In this section the seismic performance (at time 0) of multistory precast frames introduced previously is investigated by replacing in the location of potential plastic hinges standard concrete with ECC; in particular the model of nonlinear spring adopted for collapse analyses ("Ibarra model", see Ibarra et al. [121]) is modified in order to take into account the main

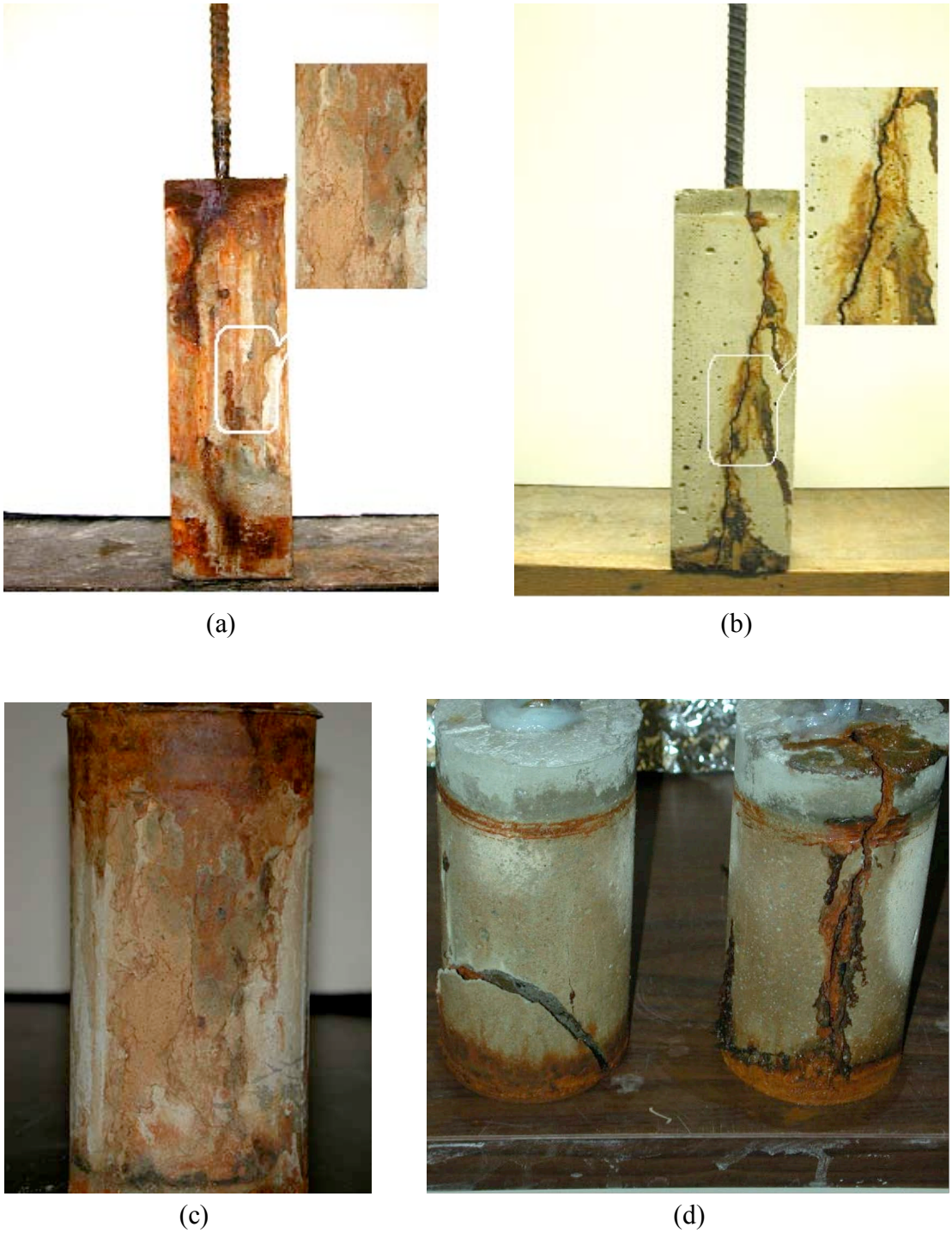

Figure 6.25: ECC and mortar specimens after accelerated corrosion test: (a) ECC prismatic specimen after 300 hours, (b) Mortar prismatic specimen after 75 hours, (c) ECC cylindrical specimen after 350 hours, (d) Mortar cylindrical specimen after 95 hours, Sahmaran et al. [218].

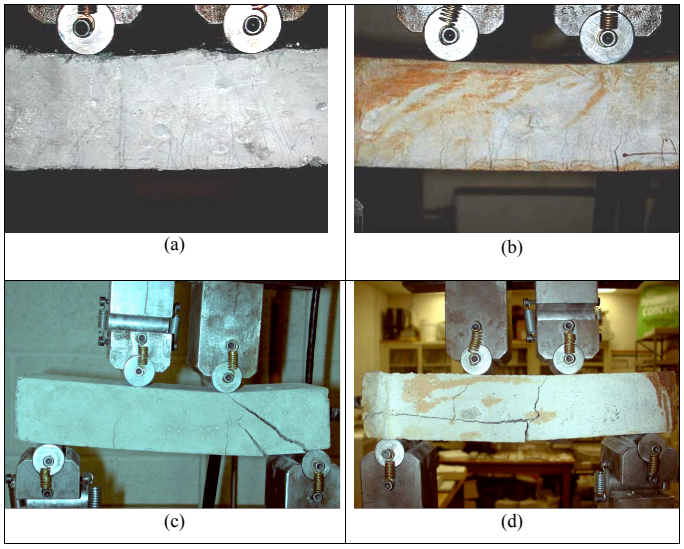

Figure 6.26: Failure modes of reinforced mortar and ECC beams under four point bending test: (a) ECC before accelerated corrosion, (b) ECC after 150 hours accelerated corrosion, (c) Mortar before accelerated corrosion, and (d) Mortar after 50 hours accelerated corrosion, Sahmaran et al. [218].

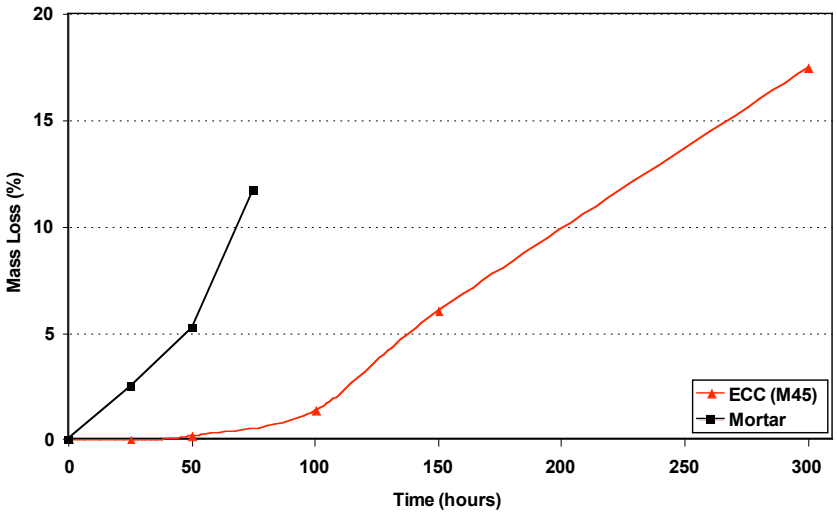

Figure 6.27: Evolution of steel mass loss for ECC and mortar corrosion specimens, Sahmaran et al. [218].

characteristics of such composite above mentioned. The model proposed is therefore calibrated and validated on the basis of cyclic tests reported in literature, with the final goal to evaluate the seismic risk for R/ECC frames, compared with that coming by using standard concrete, in order to highlight potential advantages.

6.6.1 Proposal of a nonlinear spring model for the PBEE approach

As indicated in Chapter 3, the application of the PEER methodology requires a suitable choice of the hysteretic model to simulate the nonlinear behavior of structural members. Because the study of seismic performance of the structures investigated covers the entire range of the behavior, from elastic up to collapse, a good compromise between computational cost and analytical formulation is given by the use of concentrated plasticity models, able to include also a softening branch required to simulate collapse. For standard concrete, hysteretic model calibrated by Haselton on the basis of experimental tests on hundreds of cantilever beam-column elements, Haselton [112], is revealed an effective approach during last years. In the present investigation the idea is therefore to adapt such model, Figure 3.5, for engineered cementitious composites, on the basis of available experimental tests.

The calibration has been carried out on the basis of the peculiarity of this material illustrated in previous sections and looking at the results of experimental tests performed by Fischer and Li, Fischer and Li [88]. In particular cantilever columns, Figure 6.28 have been subjected to reversed cyclic loading conditions, comparing the flexural response among RC and R/ECC members, with or without transversal steel, changing also the axial load applied. ECC matrix used is characterized by 1% volume polyethylene fibers, a first cracking strength equal to 4.5 MPa and ultimate strength of 6.0 MPa at 3.8% strain. Compressive strength is 80 MPa. Longitudinal steel reinforcement (with diameter 10 mm) in all configurations has a yield strength equal to 410 MPa at 0.2% strain, ultimate strength of 620 MPa at 14% strain. Transversal steel bars (diameter mm) has a yield strength set to 315 MPa. Small cantilever beams have been used, with 500 mm height and square cross-sectional dimensions of 100 mm, Figure 6.28; about different configurations investigated, S-1 ad S-2 refer to RC and R/ECC members with transverse reinforcement and no axial load, S-3 and S-4 refer to R/ECC members without transverse reinforcement, with no axial load (S-3) and $N = 80$ kN (S-4). All the details of the cyclic tests can be found in Fischer and Li [88].

Regarding the modification of the calibration equation proposed by Haselton, the following considerations are done:

- The flexural contribution of the yield drift θ_y is amplified by the 40% because the Young's modulus of ECC is lower (around 40%) than that of normal concrete due to the lack of coarse aggregates (see e.g. Fischer and Li [90]);
- Denoting ν as the axial load ratio and performing moment-curvature analyses on the

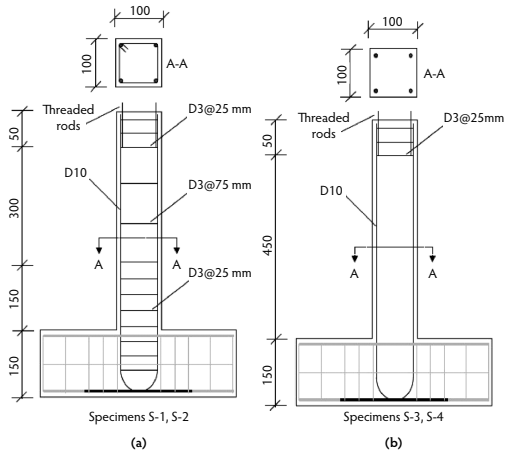

Figure 6.28: Specimens configuration adopted in the experimental program, Fischer and Li [88].

cross-section above described, the parameter M_c/M_y is amplified by the term $1.1 \cdot (1-\nu)$;

- The capping rotation is amplified by the terms $(1.2) \cdot (1-3\nu)(1-\nu)$, considering the good agreement with the experimental test;
- For the post-capping rotation the limit of 0.1 introduced in Haselton [112] is removed, due to the significan ductility of such material. A new value is therefore proposed, equal to $1-\nu$;
- Because the development of multiple cracking, ECC is able to sustain higher loads with respect to standard concrete. Moreover, there is a compatibility in terms of strain between cementitious matrix and steel for a wider range, resulting in more stable hysteresis loops. To cite Li, Li [147], *"Despite the considerable tensile strength and strain capacity of ECC, its direct contribution to flexural strength and energy dissipation is negligible. The synergistic interaction between steel reinforcement and the ECC matrix, however, leads to improved performance of flexural member as compared with conventional RC"*. So the strain compatibility between steel and ECC matrix allows to extend the use of steel reinforcement both in the sense of a longer segment of reinforcement undergoing plastic yielding in tension and compression and in the sense of more stable hysteresis loops. This is the most fundamental characteristic in the cyclic behavior of R/ECC members and in this way the cyclic degradation is lower. To this aim, cyclic parameter λ is amplified by the factor $n_s \cdot (2-\nu)$, where n_s is the ratio between steel and ECC Young's modulus.

When Haselton proposed his calibration equation for Ibarra model he said that, among different parameters, axial load ratio ν and transversal steel ratio ρ_{sh} played the key role. Looking at the modification factors above proposed, only axial load ratio appears. The explanation is that for ECC transversal steel reinforcement is not so important because shear

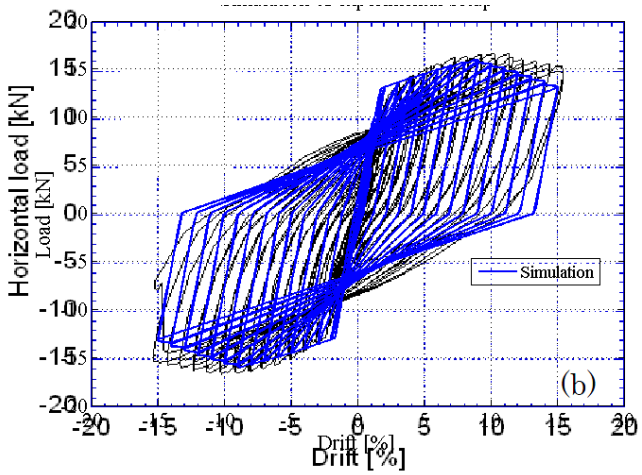

(a) No axial load.

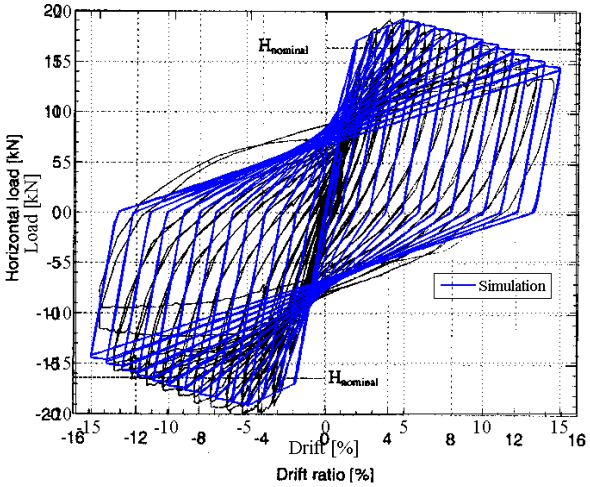

(b) Axial load $N = 80\,\mathrm{kN}$.

Figure 6.29: Comparison between numerical and experimental results of cyclic tests for cantilever beams illustrated in Figure 6.28.)

behavior is typically ductile due to significant ductility of the material. So, R/ECC members without shear reinforcement performs better than corresponding RC members with transversal bars, see e.g. Li [147], and hysteresis loops resulting from cyclic tests on R/ECC cantilever beams with and without shear reinforcement looks very similar, Fischer and Li [88]. Cyclic tests on cantilever beams illustrated in Figure 6.28 are therefore simulated with the proposed modification, including a concentrated plastic spring at the base of the element; the comparison between experimental and numerical results can be appreciated in Figure 6.29 (I apologize for the poor quality, but it was not possible to obtain digital data from experimental tests, so the picture coming from numerical simulation is simply overlapped to the figure reported in the corresponding paper). As can be seen the agreement between numerical simulation and experimental result is good in both cases, even if there is a slight difference in the prediction of initial stiffness. However peak strength is caught properly also when axial load is applied; regarding cyclic degradation, in Figure 6.29a ultimate capacity is underestimated, in Figure 6.29b is a bit overestimated. Anyway, discrepancy is not significant.

6.6.2 Validation of the model

In order to enforce the robustness of the model proposed, same equations are used to simulate the results of cyclic tests described in Fischer et al. [92]. Flexural response of RC and R/ECC cantilever beams subjected to cyclic tests has been compared considering two types of reinforcement (steel and FRP); here the attention is focus only to the first one. In this case the ECC matrix used includes 2% volume of polyvinyl alcohol (PVA) fibers. Material properties in uniaxial tension reveales a first cracking strength of 1.5 MPa at 0.01% strain and ultimate tensile strength equal to 2.0 MPa at approximately 1% strain. In compression, the particular version of ECC used in this experimental investigation has a significantly lower modulus of elasticity compared to concrete due to the lack of large; compressive strength is evaluated around 40 MPa, significantly lower than the value experiences by the concrete (63 MPa). Steel rebars has a diameter equal to 13 mm with a yield strength of 380 MPa at 0.203% strain and ultimate strength of 480 MPa as well as bars of 6 mm diameter for longitudinal and transverse reinforcement with a yield strength of 290 MPa at 0.15% strain and ultimate strength of 500 MPa. Both types of reinforcing bars has an elastic modulus of approximately 190 GPa.

Regarding geometric properties, specimens has square cross-sections with a dimension of 240 mm and column height equal to 1400 mm. Concerning steel reinforced specimens, configuration S-1 is longitudinally reinforced with eight bars (diameter 13 mm) and four bars (6 mm), symmetrically arranged in four layers within the cross-section, Figure 6.30. Transverse steel reinforcement (diameter 6 mm) is placed at 50 mm spacing at the column base, at 100 mm spacing between 400 mm and 1100 mm column height, and at 50 mm spacing above 1100 mm to prevent possible damage at the top of the specimen due to the application of axial and horizontal loading, Fischer et al. [92]. Specimen S-3 (ECC matrix) has the same reinforcement

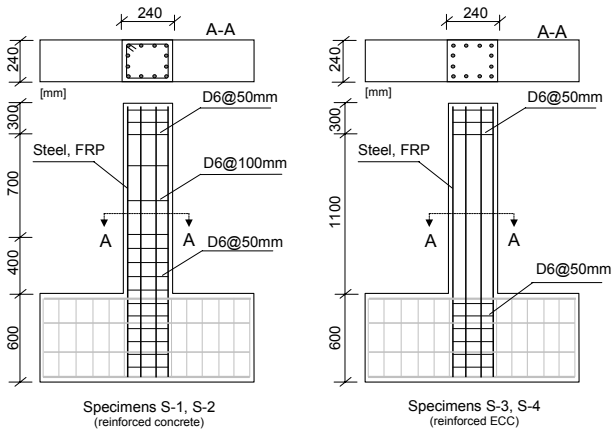

Figure 6.30: Specimens configuration adopted in the experimental program, Fischer et al. [92].

layout of specimen S-1 but transversal reinforcement is not provided between the column base and 1100 mm height, 6.30. Finally, axial load applied is equal to 330 kN.

The comparison between experimental and numerical result regarding cyclic tests on configuration S-3 (steel/ECC matrix) can be seen in Figure 6.31 and reveales the feasibility of the model proposed, even if in this case there is a slightly difference in terms of initial stiffness. Because the configuration of the specimen is symmetric, numerical simulation predicts the same behavior in both directions, while in the experimental test capacity in the negative direction is a bit lower than in the positive one. Anyway, ultimate strength is well caught, as well as the hysteresis loops. Last cycle (up to 10% of drift) is not simulated, in order to set the last displacement of the cyclic test equal to zero.

To conclude, since the changes on the Ibarra model proved their capability to simulate the peculiar characteristics of engineered cementitious composite, it is now possible to apply the PEER methodology on the multistory precast frames introduced previously in order to evaluate their seismic performance with this advanced cementitious material during the entire lifetime, comparing the results with those obtained using ordinary concrete. In particular, material properties refers to the data reported in Han et al. [110] (e.g. ultimate tensile strain equal to 6%), but using the same compressive strength of standard concrete ($f_{ck} = 40$ MPa).

6.7 Seismic performance of R/ECC frame structures

PEER methodology previously applied on RC multistory buildings introduced in now carried out by replacing in the potential plastic hinges of structural members standard concrete with engineered cementitious composite, in order to evaluate the corresponding capacity for different limit states and to highlight the advantages in the use of such material during the entire lifetime.

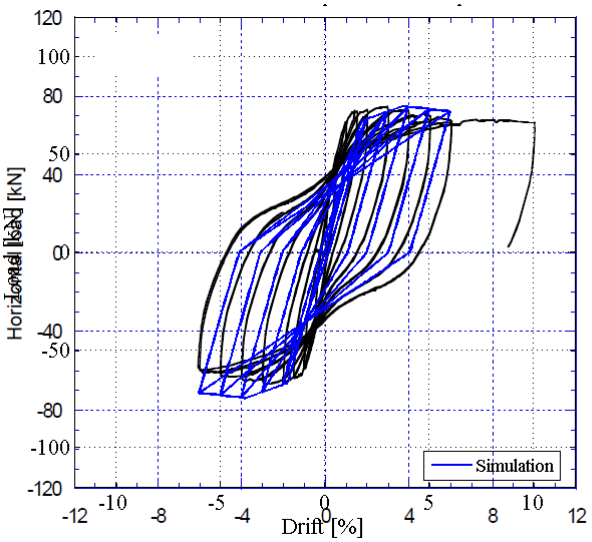

Figure 6.31: Comparison between numerical and experimental results of cyclic tests for cantilever beam (S-3) illustrated in Figure 6.30.

6.7.1 Results of pushover analysis on multistory frames

Within the probabilistic approach, pushover analyses are performed on different configurations, and the results expressed in terms of capacity curves are illustrated in Figure 6.32. Considering the seismic response obtained by RC buildings (see Figure 3.30), there is a significant improvement of the overall behavior, both in strength and particularly in ductility, due to the peculiar characteristics of this kind of cementitious composite. A hardening behavior appears also in some cases for more flexible structures (2 story 45×45, 3 story 60×60 and 4 story 80×80), and in all the configurations the capacity increases. Due to the improvement in tensile properties, R/ECC frames can sustain increasing loads for a wider range, and the different limit states are achieved later, which can be clearly seen looking at the corresponding top displacements.

In order to summarize the results of the probabilistic approach, Table 6.4 shows the median values of base shear corresponding to different limit states for the set of R/ECC structures analyzed; by replacing ordinary concrete with ECC leads to an increase in strength ranges from $20-25\%$, but for the stiffer configuration (2 story 80×80) the gain is around 35%. Same conclusions can be done looking at Table 6.5, which presents the median top displacements for different limit states; also in this case there is a significant improvement in terms of ductility, which proofs the effectiveness of using this material. As just pointed out previously, one important issue is the influence of the cross-section size with respect to the displacement reached. For example, taking constant the number of stories, an increase in the size of columns tends to decrease the displacement corresponding to the DL limit state, but at the same time tends to increase the displacements related to LS and NC limit state. Because DL limit state

Table 6.4: Median base shear from pushover analysis at different limit states for all the structures investigated (R/ECC frames)

Frame	**DL [kN]**	**LS [kN]**	**NC [kN]**
2 Story 45x45	114.80	107.44	93.13
2 Story 70x70	450.38	445.60	382.35
2 Story 80x80	640.09	658.46	581.43
3 Story 60x60	194.84	180.80	157.016
3 Story 80x80	459.74	446.34	379.53
4 Story 80x80	333.17	307.99	272.83

corresponds in practice to the last point of the elastic branch, an increase in stiffness, due to the increase of cross-section size, reduces the range of elastic behavior but at the same, because a simultaneous increase in ductility, the plastic resources (related to LS and NC limit state) are enhanced. With respect to RC frames, the difference between LS and DL top displacements increases due to a better exploitation of steel plastic resources, depending on compatible deformation between reinforcement and and fiber matrix.

Because the goal is to perform a seismic risk analysis, following the IM approach, it required to represent the capacity of the structures investigated in terms of a proper intensity measure, here defined in terms of peak ground acceleration. To this purpose, Table 6.6 gives the median PGA capacity for each limit state. In particular, an increase in cross-section size taking constant the number of stories, improves the capacity, due to the increase in strength and ductility. At the same time, considering the same cross-section, structural capacity in terms of DL limit state is also improved increasing the number of stories, while LS and NC limit states are related to a lower intensity, due to a wider spreading of plastic resources within the frame. The most significant feature is the different influence of ECC on PGA capacity with respect to the configuration studied. More precisely, for structures where capacity design was found not acceptable, namely 2 story 45×45, 3 story 60×60, and 4 story 80×80 (see Biondini et al. [39]), the improvement is not so determinant. On the contrary, for configuration where capacity design criteria is acceptable, the replacement in the plastic hinges of concrete with such composite is revealed an effective method.

The above considerations can be well summarized looking at Figure 6.33, which illustrates the comparison between RC and R/ECC frames in terms of PGA at 5% fractile, which is used in the following for the seismic risk analysis. For each limit state R/ECC frames, as expected, have a higher capacity, and the gap between values typically increases if we move from limited damage up to collapse. One possible explanation is related to the characteristics of ECC,

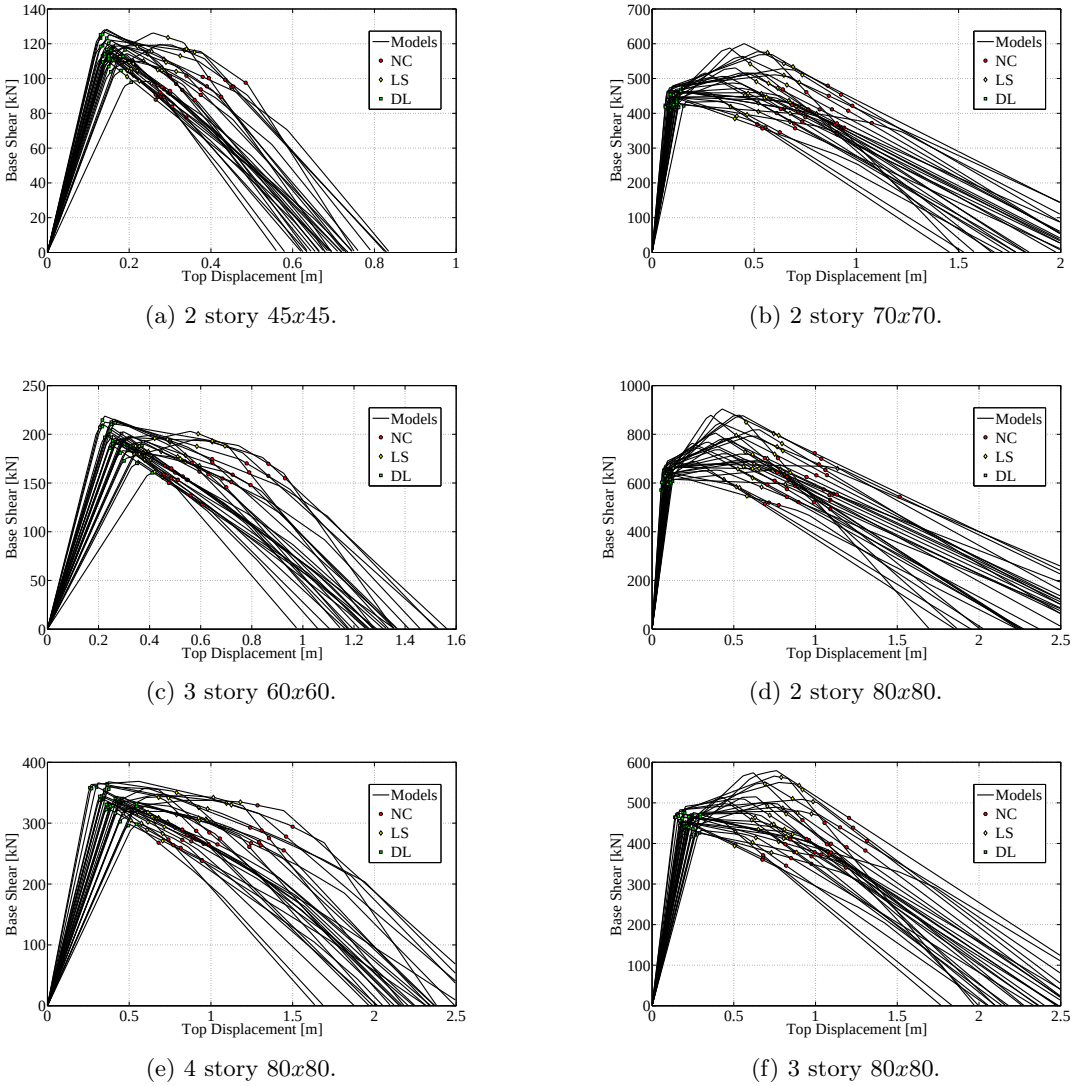

(a) 2 story $45x45$.

(b) 2 story $70x70$.

(c) 3 story $60x60$.

(d) 2 story $80x80$.

(e) 4 story $80x80$.

(f) 3 story $80x80$.

Figure 6.32: Capacity curves for R/ECC buildings studied at time $t = 0$.

Table 6.5: Median top displacement from pushover analysis at different limit states for all the structures investigated (R/ECC frames)

Frame	**DL** [m]	**LS** [m]	**NC** [m]
2 Story $45x45$	0.150	0.229	0.305
2 Story $70x70$	0.100	0.591	0.788
2 Story $80x80$	0.093	0.686	0.915
3 Story $60x60$	0.273	0.431	0.575
3 Story $80x80$	0.213	0.780	1.040
4 Story $80x80$	0.395	0.737	0.983

Table 6.6: Median capacity in terms of PGA from pushover analysis at different limit states for all the structures investigated (R/ECC frames)

Frame	DL [g]	LS [g]	NC [g]
2 Story 45x45	0.125	0.189	0.254
2 Story 70x70	0.201	1.118	1.490
2 Story 80x80	0.227	1.613	2.155
3 Story 60x60	0.177	0.266	0.354
3 Story 80x80	0.237	0.815	1.090
4 Story 80x80	0.237	0.454	0.605

which allows a better exploitation of plastic resources due to the significant ductility. Same information can be derived looking at Figure 6.34, which shows the comparison between the two materials in terms of fragility functions for all the configurations investigated, considering NC limit state. It is evident the shift of the curves toward higher capacity, namely higher PGA, using the advanced cementitious composite.

To explain how the use of ECC can be suitable for design, Figure 6.35 depicts the ratio in terms of PGA between capacity and demand, considering the two materials, for near collapse limit state. Capacity is defined as the 5% fractile coming from structural analysis, while demand is evaluated according to the National code (NTC 2008 [181]), see equation 3.18. As just mentioned before, the influence of the advanced material is different with respect to the structural system considered. For flexible systems, the improvement is not so significant, since also in this configuration demand is higher than the capacity; the effectiveness emerges clearly for frames where capacity design criteria can be used. This is an important issue coming from the present investigation: regardless the material adopted, a proper design of structural members is always mandatory to achieve a good seismic performance; once this requirement is matched, the use of advanced cementitious material has the capability to improve the overall behavior and to mitigate seismic risk.

6.7.2 Lifetime improvement of seismic behavior

As illustrated in previous sections, engineered cementitious composite is capable to delay the diffusion of aggressive agents within concrete sections due to development of multiple narrow cracks. Such behavior becomes of consequence very attractive when a lifetime analysis is performed. To this purpose, the seismic performance of precast frames is investigated during the entire lifetime, considering the influence of corrosion on the properties of structural elements. Final goal is to compare the results obtained by replacing in the plastic hinges

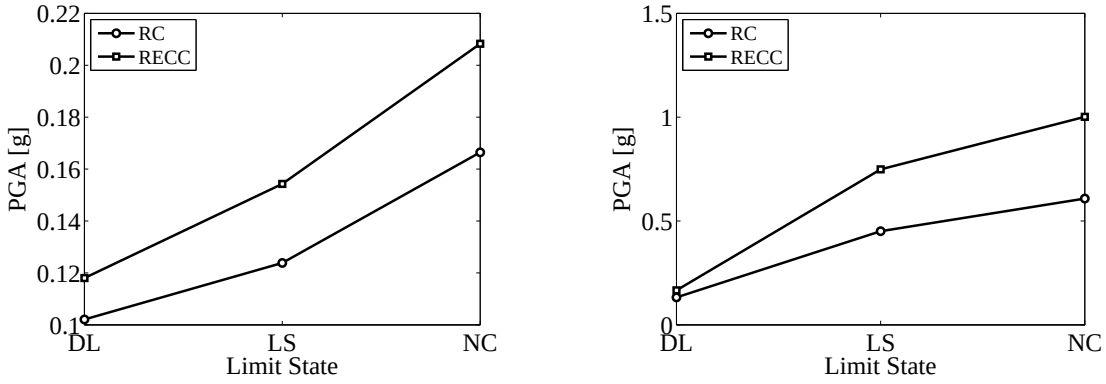

(a) 2 story 45 × 45.

(b) 2 story 70 × 70.

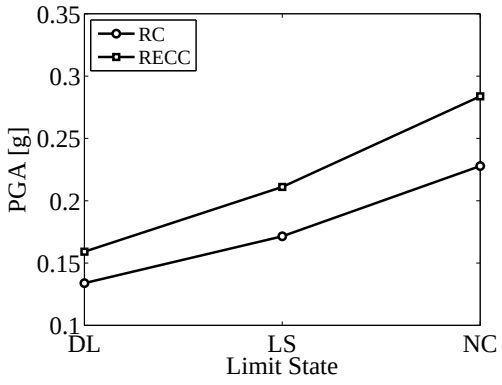

(c) 3 story 60 × 60.

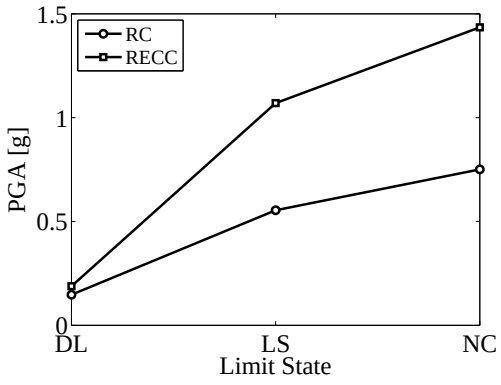

(d) 2 story 80 × 80.

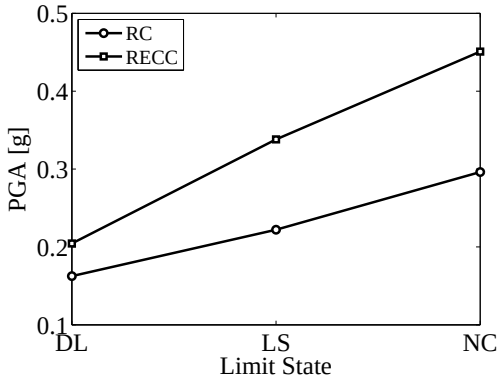

(e) 4 story 80 × 80.

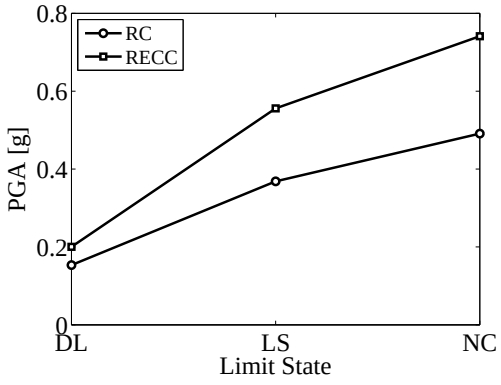

(f) 3 story 80 × 80.

Figure 6.33: Comparison between capacity in terms of PGA for buildings studied at time $t = 0$.

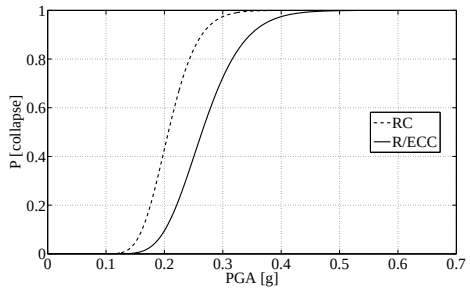

(a) 2 story $45x45$.

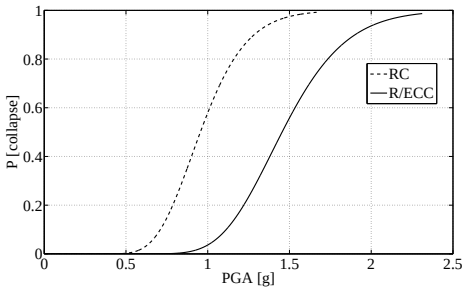

(b) 2 story $70x70$.

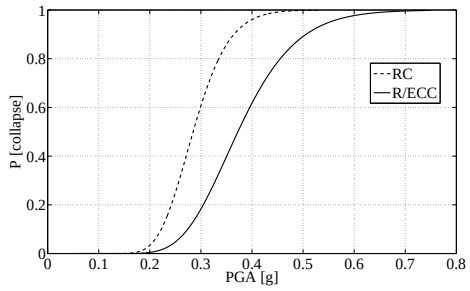

(c) 3 story $60x60$.

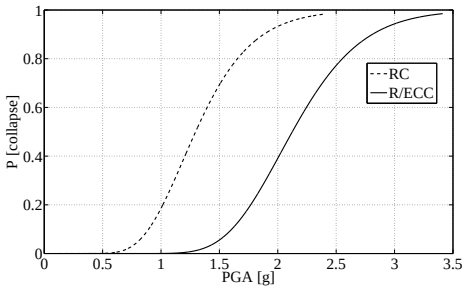

(d) 2 story $80x80$.

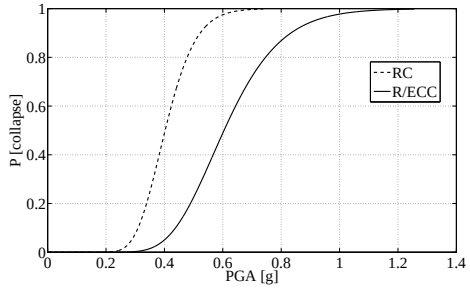

(e) 4 story $80x80$.

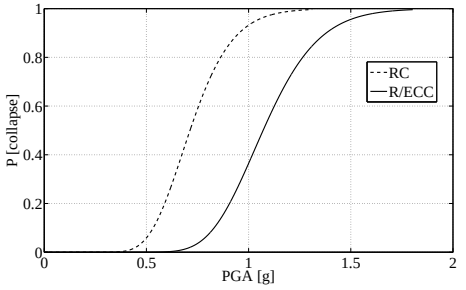

(f) 3 story $80x80$.

Figure 6.34: Comparison between fragility curves at near collapse limit state for buildings studied at time $t = 0$.

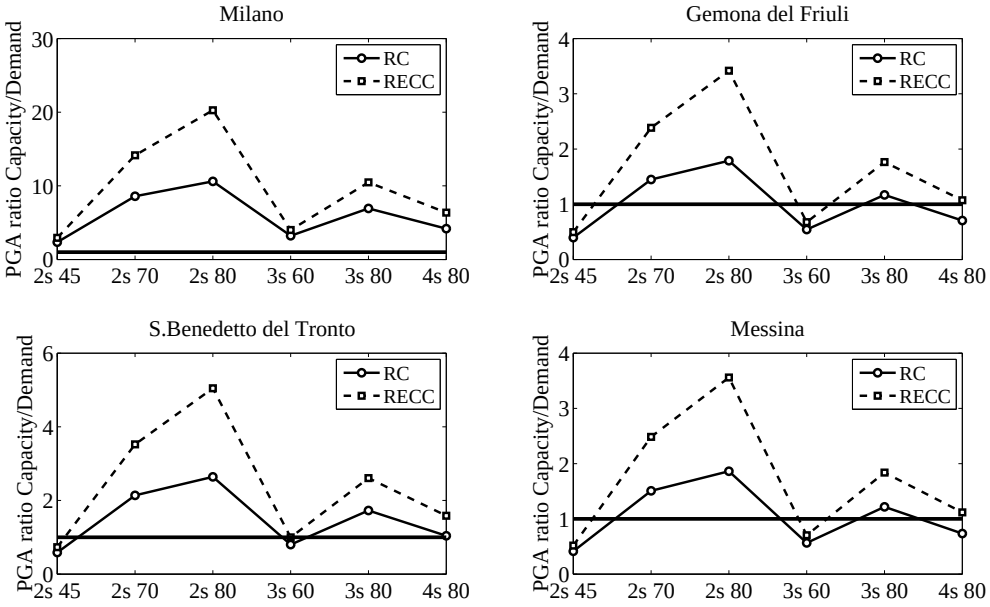

Figure 6.35: Ratio between capacity and demand PGA for NC limit state.

ordinary concrete with ECC, in order to highlight the potential benefits. In particular two different values of the coefficient of diffusion are adopted; in the first set of analyses it is assumed that the same corrosion process, so the same corrosion velocity, affects the two materials, while in the second case a more correct value is used. The above hypothesis has a double motivation: from one side the aim is to prove the advantages using the advanced composite considering the same exposure conditions, from the other the goal is to combine the better mechanical performance with the better durability properties in order to obtain reliable results in terms of seismic risk analysis. With reference to the work of Sahmaran (Sahmaran et al. [217]), the coefficient of diffusion is assumed respectively equal to $10.58 \times 10^{-12}\,\mathrm{m}^2/\mathrm{s}$ and $6.75 \times 10^{-12}\,\mathrm{m}^2/\mathrm{s}$.

One interesting issue concerns the time evolution of base shear corresponding to a predefined limit state, because such parameter can be used as a measure of the capacity of the structure. To this aim, Figures 6.36 and 6.37 show the ratio between median base shear evaluated at different times and median base shear at time zero for different exposure conditions ($\alpha = 0.5$ and $\alpha = 1$, see Figure 5.17), different structural configurations (2 story 45×45 and 2 story 80×80) and assuming Near Collapse limit state, even if the same trend is obtained for all the frames studied. As expected, corrosion has a negative influence on the capacity of the structural systems, resulting in a decrease of median base shear; however the behavior is slightly different considering the two frames, because in the first case, see Figure 6.36, the slope of the curves is always negative, while in the second at the beginning of the lifetime capacity is practically unchanged, with a small improvement in one circumstance (ECC with lower

diffusion coefficient). This can be explained considering that a structure partially damaged, due to a reduction in stiffness, is subjected to lower seismic forces, resulting in some case more able to sustain external loads. Looking at these results, clearly emerges the ability of ECC to reduce the influence of corrosion on structural performance; assuming the same corrosion velocity (RC and R/ECC), at the end of lifetime capacity has a lower drop with respect to the initial value, and a further improvement is achieved when a more correct diffusion coefficient is used (R/ECC corrosion red).

One the main advantages in the use of ECC is the improvement of shear behavior due to the tensile strain-hardening behavior, Li [147]. Because corrosion strongly affects transverse reinforcement, during time shear capacity, see equation 3.11, tends to decrease, and a brittle failure can appear in ordinary reinforced concrete structures. As just explained, frames investigated are not subjected to a brittle collapse, as can be seen from Figure 5.23 where the story shear demand/capacity ratios evaluated during time for two different configurations are always lower than 1. Anyway, as suggested by Celarec (Celarec et al. [53]), a potential brittle limit state can be defined, assuming for DCR a threshold equal to 0.5; such condition can represent in a reliable way a probable shear failure. When the performance of RECC frames is studied, it is expected an increase in the DCR values because the system can sustain higher seismic loading, so the corresponding shear demand grows, even if capacity is a little bit higher due to minor damage of the stirrups. An example of the results obtained is depicted in Figure 6.38, which shows the evolution in time of first story shear demand/capacity ratio.

Increasing the exposure conditions ($\alpha \to 1$) leads to higher DCR values, so the influence of corrosion on shear behavior is well caught; for the stiffer configuration, Figure 6.38b, the threshold value related to potential brittle failure (0.5) is exceeded at the end of the life. Anyway, as just mentioned above, this condition is completely different when the advanced cementitious material is adopted; in this case, such limit state is no more associated to possible brittle failure because, due to the tensile strain-hardening behavior, also in shear a ductile behavior is activated.

One the main outcome of the PEER methodology is the evaluation of the MAF values (mean annual frequency of exceedance) corresponding to different limit states; exploiting equation 3.16, such values are computed for all the structures investigated, considering different exposure conditions in order to check the influence of corrosion. As example, the results related to 2 story building with cross-sections 45×45 and 80×80 are presented, with reference to the site of Gemona, checking Damage Limitation (DL) and Near Collapse (NC) limit states; also in this case the superior performance of ECC clearly emerges. In particular, Figures 6.39 and 6.40 compare the results considering the more flexible configuration (2 story 45×45); increasing the environmental hazard ($\alpha \to 1$) the corresponding MAF values increases as expected due to the damage suffered by the structure during time. Anyway, R/ECC frame is associated to lower values, and also the rate of growth is a little bit slower; this proves once again the

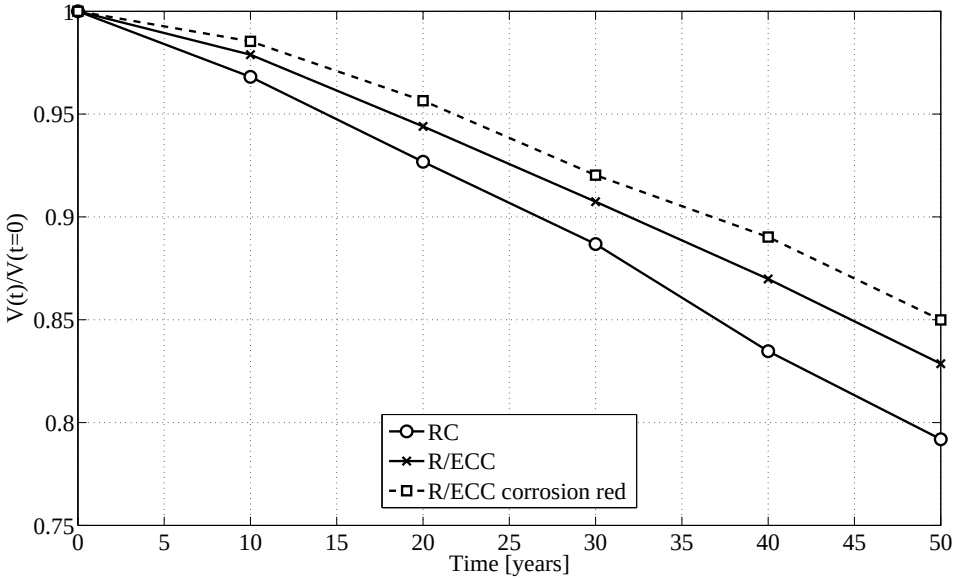

(a) $\alpha = 0.5$.

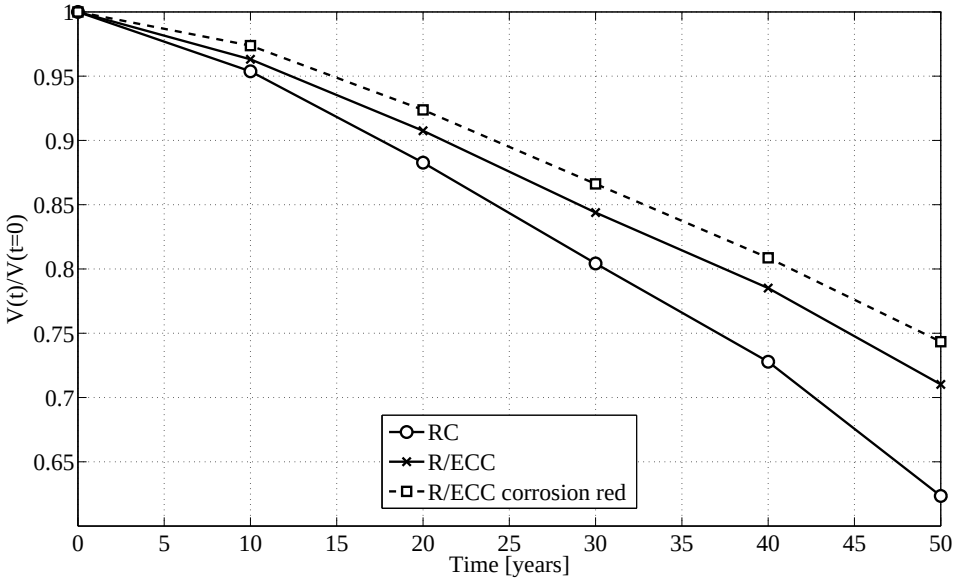

(b) $\alpha = 1$.

Figure 6.36: Decrease of base shear for NC limit state during time using different materials (2 story 45×45).

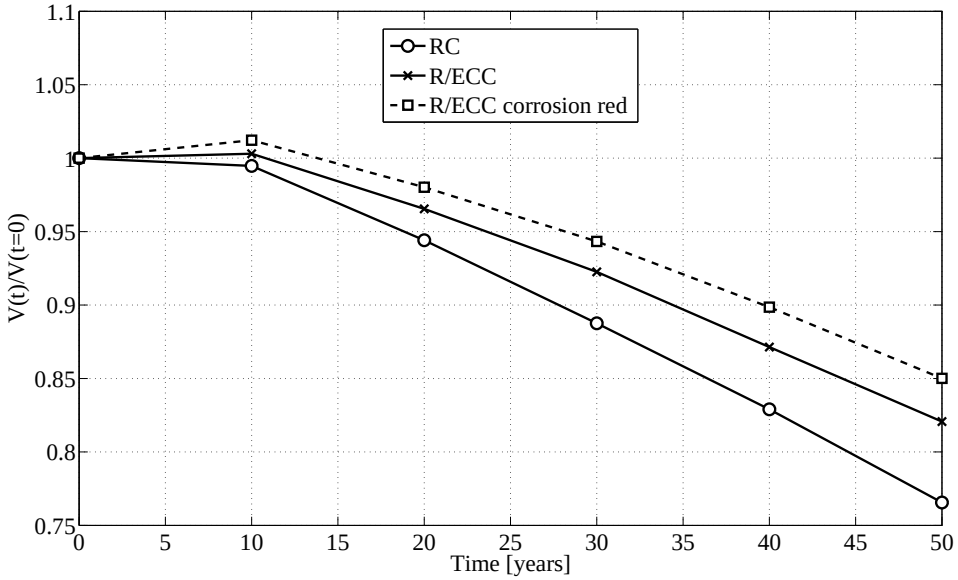

(a) $\alpha = 0.5$.

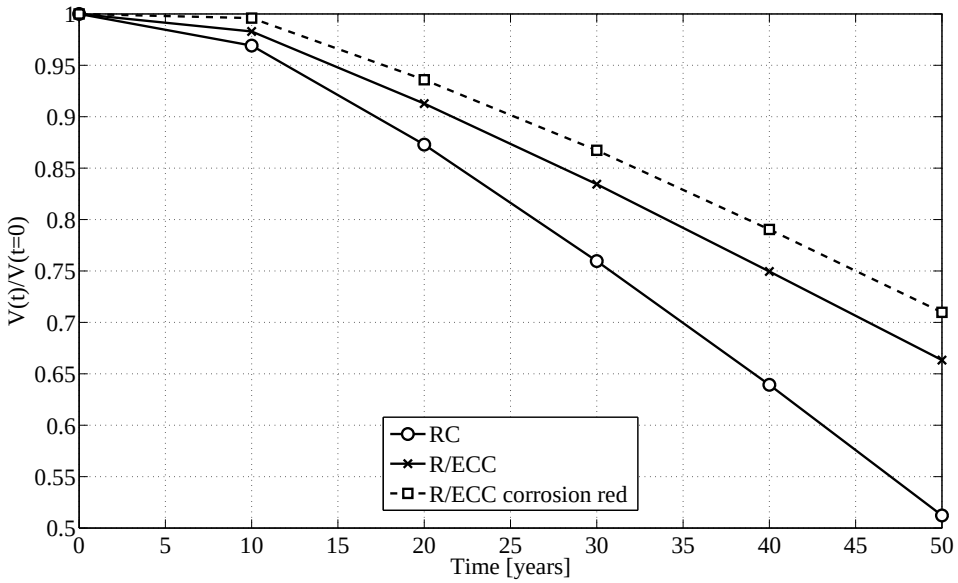

(b) $\alpha = 1$.

Figure 6.37: Decrease of base shear for NC limit state during time using different materials (2 story 80×80).

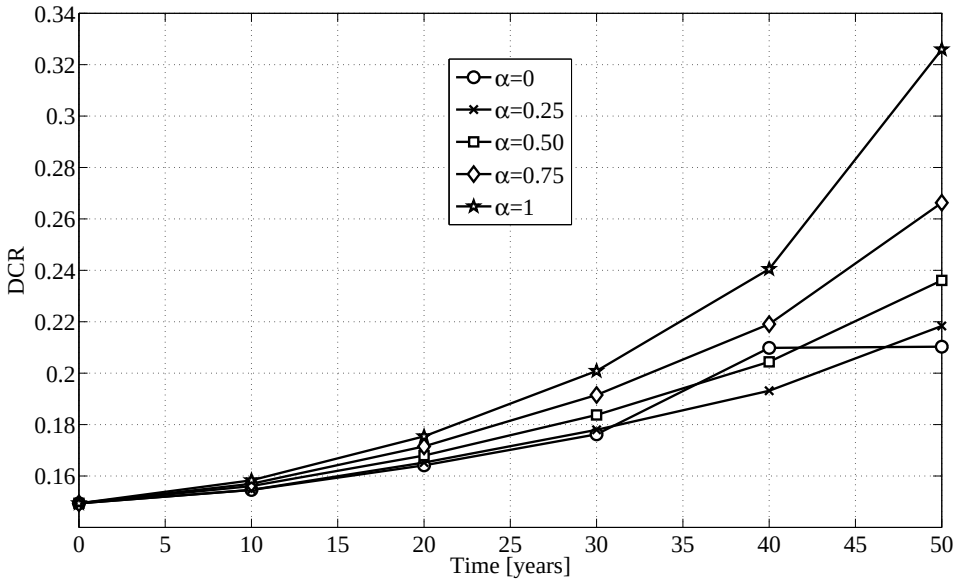

(a) 2 story 45×45.

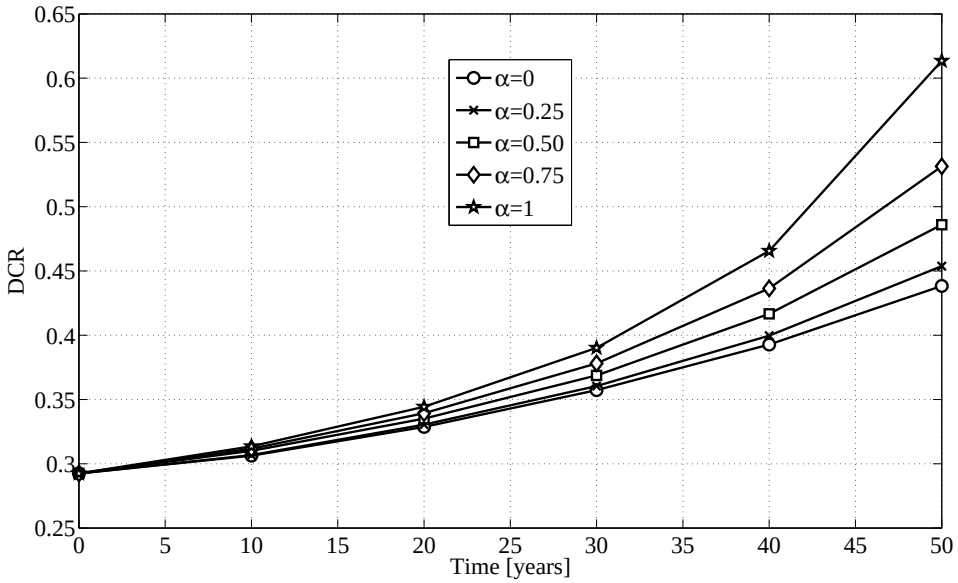

(b) 2 story 80×80.

Figure 6.38: Time evolution of the first story shear demand over capacity ratio (DCR) for the 2 story building.

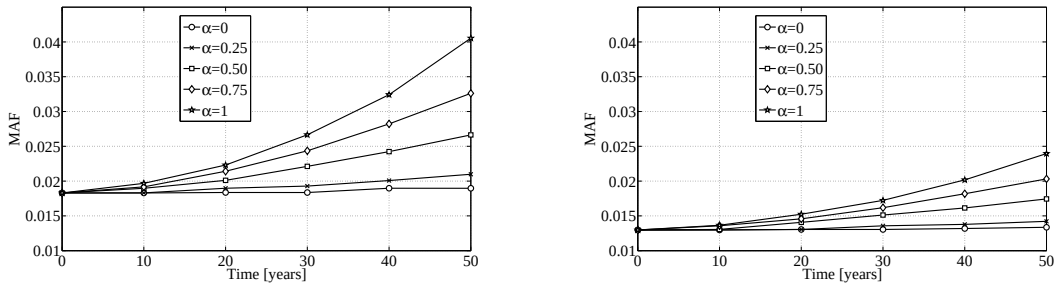

(a) RC. (b) RECC.

Figure 6.39: Time evolution of MAF values for 2 story frame with cross-section 45 × 45, assuming Damage Limitation limit state.

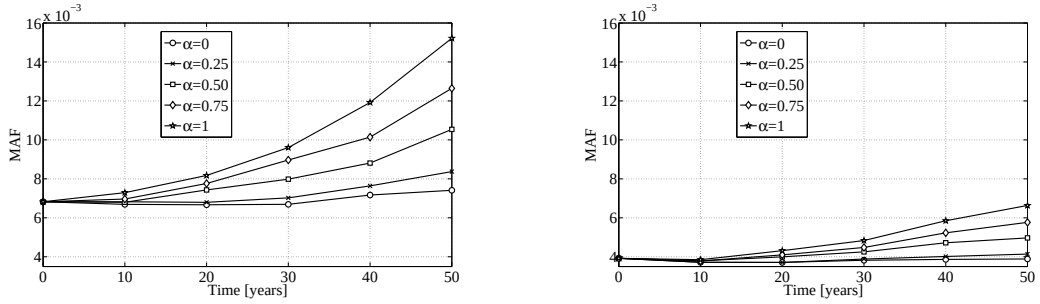

(a) RC. (b) RECC.

Figure 6.40: Time evolution of MAF values for 2 story frame with cross-section 45 × 45, assuming Near Collapse limit state.

advantages given by such cementious composite in the mitigation of seismic risk, due to a significant improvement in mechanical and durability properties. It is worth to emphasize however that this structural configuration leads to high value, regardless the material adopted because, as indicated in previous chapter, capacity design criteria proposed in Biondini et al. [39] is not appropriated. On the contrary, Figures 6.41 and 6.42 depict MAF values for 2 story frame with columns cross-section 80 × 80. Here there is a significant improvement in the performance for both limit states investigated when engineered cementitious composite is adopted; as just appeared in Figure 6.35, the use of this advanced material reveals his effectiveness for frames where capacity design criteria can be used.

To conclude, Figures from 6.43 to 6.46 illustrate the outcomes of the seismic risk for the same structural systems above mentioned (2 story 45 × 45 and 2 story 80 × 80), even if all the frames are investigated. As just indicated for RC frames, risk study is based on two parameters: PGA capacity and probability of exceedance a particular limit state in 50 years, see Kramar et al. [136]. The former is computed with reference to the 5^{th} percentile of PGA capacity resulting from the probabilistic approach here adopted and compared with the design

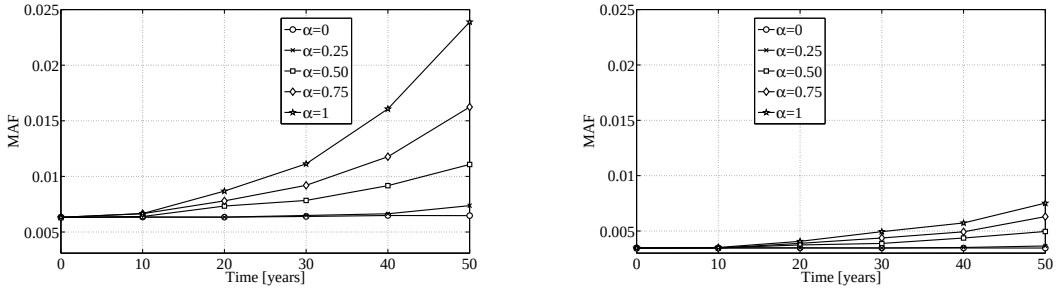

(a) RC. (b) RECC.

Figure 6.41: Time evolution of MAF values for 2 story frame with cross-section 80 × 80, assuming Damage Limitation limit state.

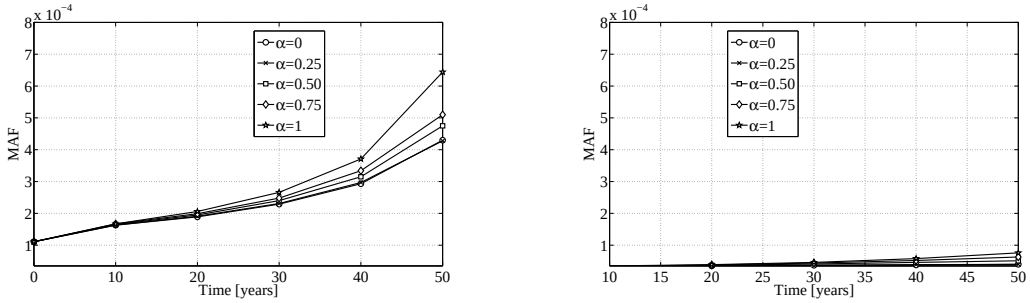

(a) RC. (b) RECC.

Figure 6.42: Time evolution of MAF values for 2 story frame with cross-section 80 × 80, assuming Near Collapse limit state.

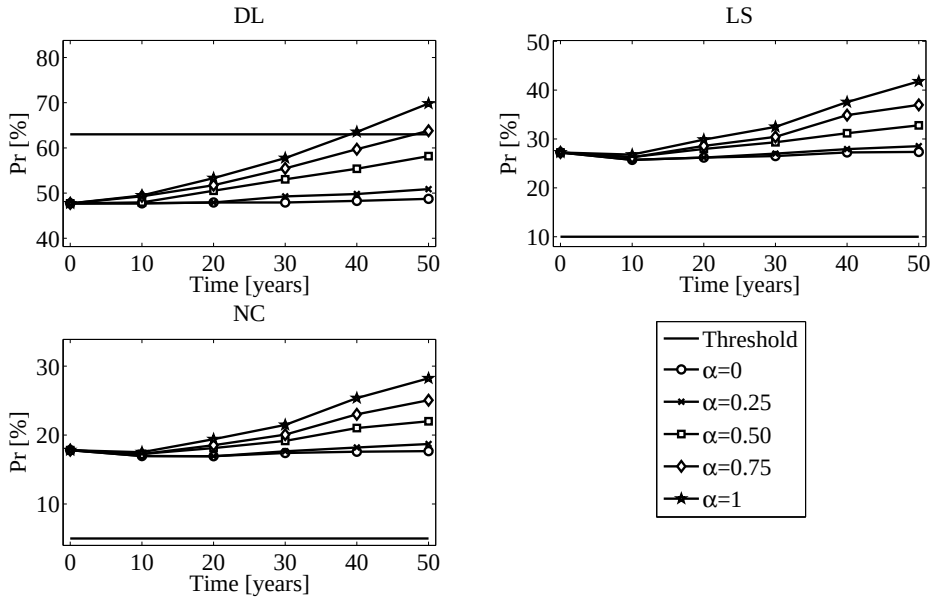

(a) Gemona.

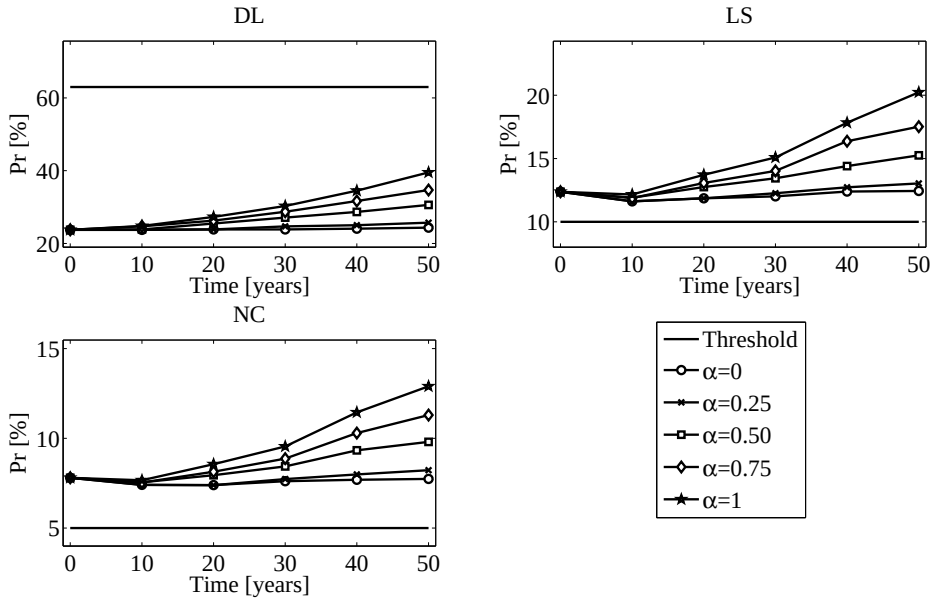

(b) San Benedetto.

Figure 6.43: Time evolution of probability of exceedence and comparison with design value for 2 story building with cross-section 45×45.

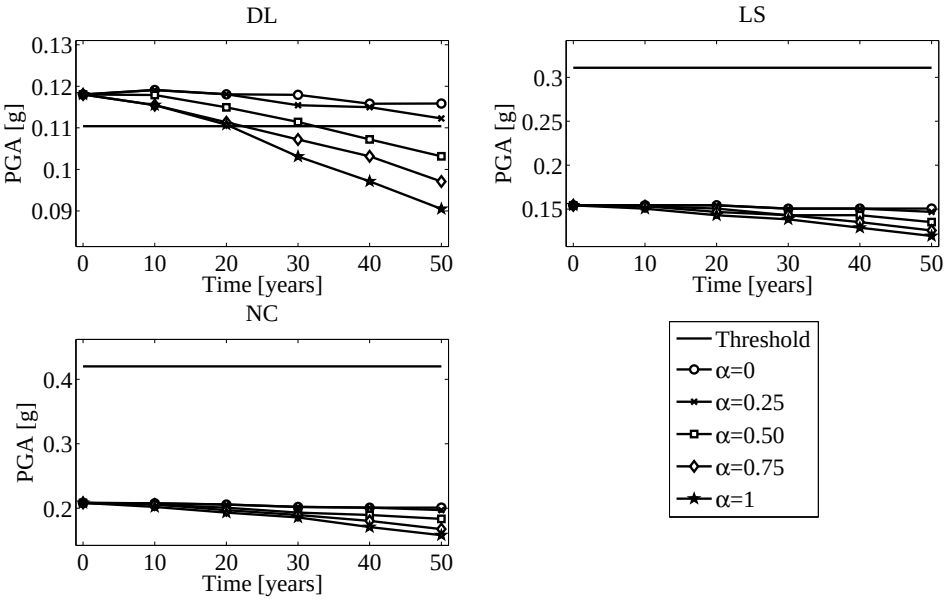

(a) Gemona.

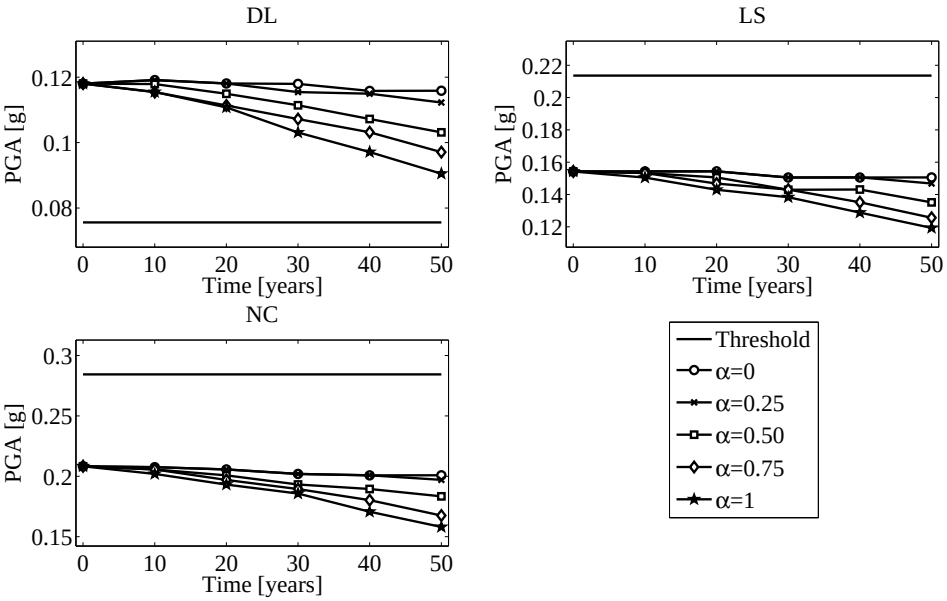

(b) San Benedetto.

Figure 6.44: Time evolution of PGA at 5% percentile and comparison with design value for 2 story building with cross-section 45×45.

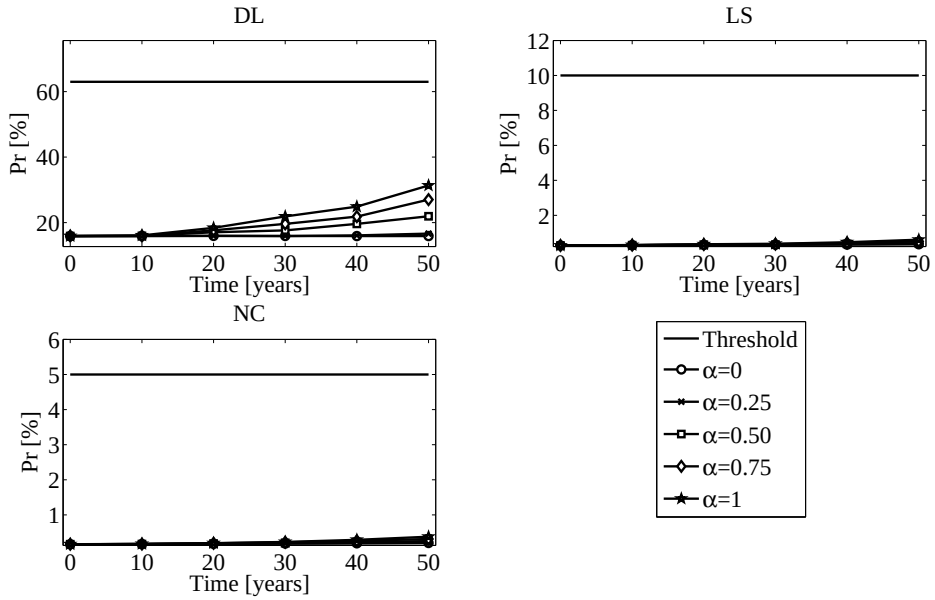

(a) Gemona.

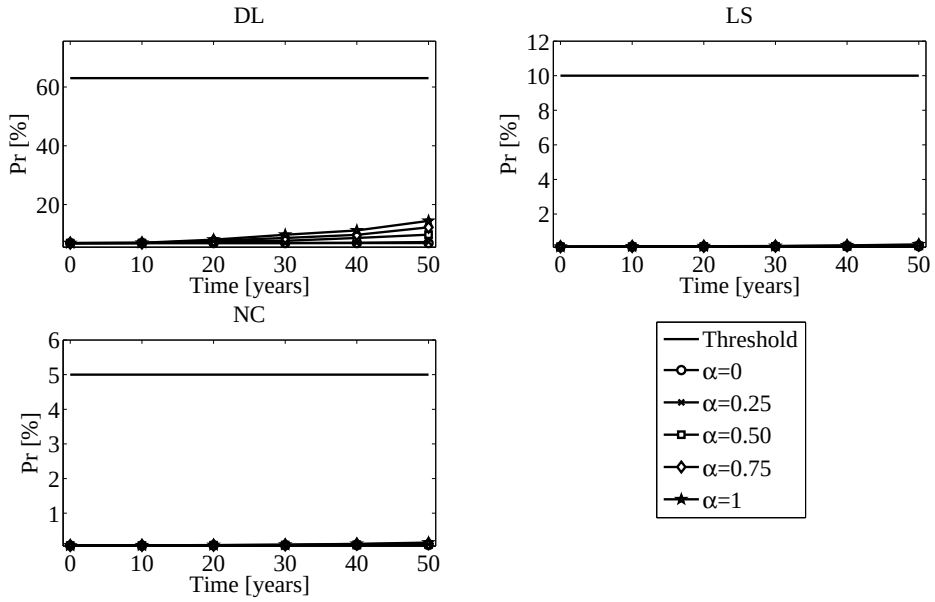

(b) San Benedetto.

Figure 6.45: Time evolution of probability of exceedence and comparison with design value for 2 story building with cross-section 80×80.

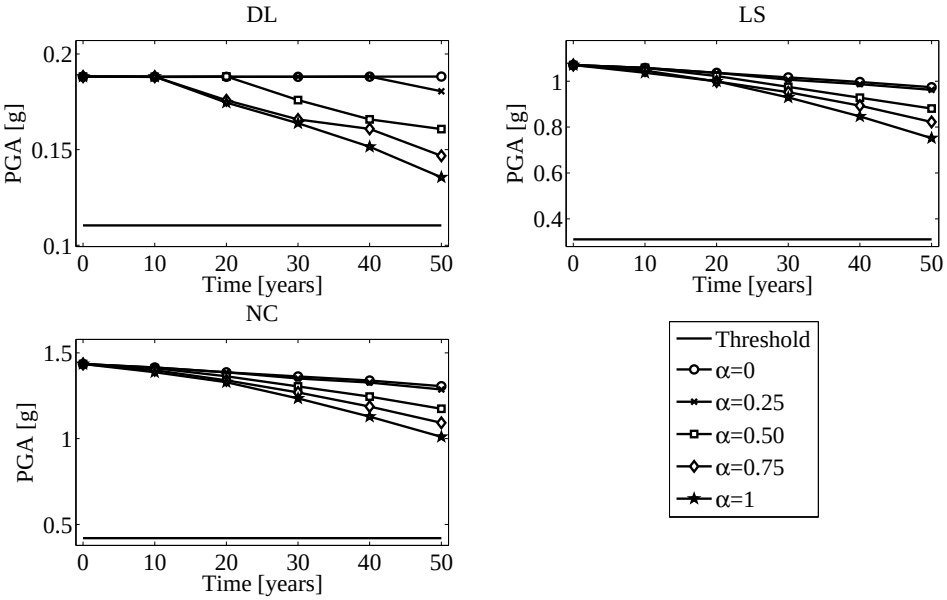

(a) Gemona.

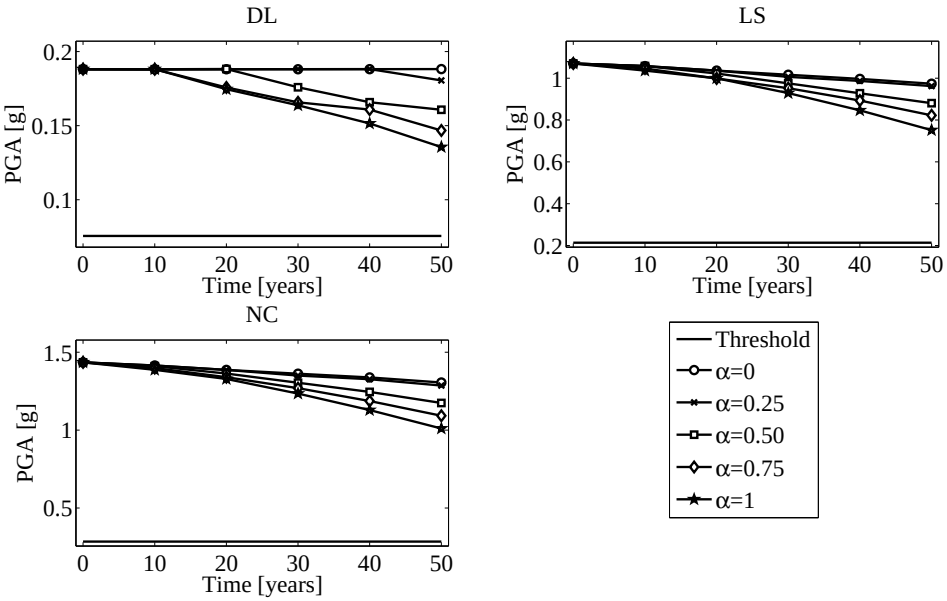

(b) San Benedetto.

Figure 6.46: Time evolution of PGA at 5% percentile and comparison with design value for 2 story building with cross-section 80×80.

value prescribed by national code for the specific site, NTC 2008 [181], while the second is compared with the recommended values always reported in NTC 2008 [181] (63%, 10% and 5% for DL, LS and NC limit state, respectively). Concerning the corrosion process included in the analyses, the results are based on the assumption of the lower diffusion coefficient for ECC, namely $D_e = 6.75 \times 10^{-12}\,\mathrm{m}^2/\mathrm{s}$. As expected, no significant advantages are obtained when the seismic risk is computed for systems where capacity design is not reliable, Figures 6.43 and 6.44; typically the probability of failure exceeds the recommended values and PGA capacity is lower than design threshold. On the contrary, seismic risk is mitigated for the stiffer system, Figures 6.45 and 6.46, where design criteria is suitable; in particular, comparing PGA capacity with that resulting by using ordinary concrete (Figure 7.2), it is evident how the advanced cementious material is capable to drive the overall seismic behavior on the safety side during all the lifetime.

6.8 Conclusions

This chapter is devoted to the study of a possible mitigation strategy to reduce seismic risk for precast frames subjected to chloride induced damage during their lifetime. In particular the investigation is focused on a material level, replacing ordinary concrete in the zones where plastic hinges can occur with an advanced cementitious composite, in literature denoted as ECC (engineered cementitious composite) or DFRCC (ductile fiber reinforced cementitious composite). After a brief review of historical developments of such material, his main characteristics are presented, focusing in particular on micromechanics tailoring, which results in a tensile strain-hardening behavior and a consequent significant ductility, specially suitable for seismic applications. Because the goal of the investigation is to illustrate the potential improvement of lifetime performance, durability properties of ECC are also summarized, with particular reference to corrosion process; as explained in previous sections, the development of multiple cracking leads to delay the corrosion initiation and to change the nature of the mechanism, from macro to micro-cell.

Starting from these considerations, the plastic hinge model introduced to perform risk analyses on RC precast frames is revised in order to include in a simple way the mechanical properties noticed in such material. The proposal formulation is therefore calibrated and validated on the basis of experimental cyclic tests available in literature; finally, pushover method is applied to perform structural analyses and seismic risk studies. The same buildings previously investigated are therefore analyzed replacing in the possible locations of the plastic hinges the ordinary concrete with ECC, and a comparison between results obtained is done. Regardless the material adopted, it is found that a proper capacity design criteria is in any case mandatory to have an appropriate seismic behavior, because if the above requirement is not matched the improvement by using the advanced composite is not significant. On

the contrary, when capacity design can be applied in a reliable way, seismic performance is remarkably enhanced during all the life of the structures investigated.

Chapter 7

Concluding remarks

... E quindi uscimmo a riveder le stelle.

Dante
Divina Commedia, Canto XXXIV

7.1 Summary of the research proposed

The investigation moved from the general assumption that current seismic codes and capacity design criteria are time-invariant and do not take into account the interaction with environmental hazards. It is however important to predict the lifetime performance of a generic structures because undesired mechanisms, not considered at design stage, can arise and modify in a decisive way the structural behavior. To this aim, the primary goal of this study was to understand the seismic behavior of multistory RC precast structures during their lifetime, in particular when the diffusive attack induced by chlorides is considered, in order to quantify in a reliable way the structural safety for this kind of buildings. The present research places oneself in a wider investigation on the seismic performance of precast frames carried out in US (see e.g. the PRESS Programme, Priestley [202]) and in Europe (see Biondini and Toniolo [32]) during last decades.

Regarding second case, different important outcomes emerged in last years. For example, the performance of precast structures under earthquake, assuming a suitable capacity design of connections, can be compared to that of cast-in-place structures in terms of global strength and ductility, as proved in the "ECOLEADER" project, Biondini and Toniolo [32]. Numerical studies have been performed on one story industrial frames, within a probabilistic approach, in order to highlight how precast structures can have the same seismic capacity of the corresponding cast-in-situ structures; subsequent pseudodynamic tests on full scale prototypes carried out at ELSA (European Laboratory for Seismic Assessment) Laboratory confirmed such results. The effectiveness of the hypothesis of a rigid diaphragm, even if roof elements are

not connected one to each other, has been underlined in the "GROWTH" project, Biondini and Toniolo [32], both performing numerical analyses and experimental tests.

Anyway, the results achieved showed the good seismic performance of precast structures under condition that the connections were properly over-dimensioned ("strong connections"). To complete the investigation, actual behaviour of connections under seismic excitation had to be addressed. To this aim, the European research program Safecast has been developed to investigate the seismic performance of connections in precast systems, Biondini et al. [41], involving a campaign of experimental static tests carried out on single specimens, as well as pseudo-dynamic tests on the three-story full-scale prototype. Changing the type of connection, four different structural schemes can be studied on the same prototype, from shear wall frame to emulative one. The results soon available will give a fundamental contribution for a more comprehensive understanding of the overall behavior of precast buildings. Despite of different research programs, few studies focused on the lifetime behavior of precast structures subjected to environmental hazards. In such conditions, the diffusive attack of aggressive agents like sulphates and chlorides can lead to a deterioration of mechanical properties of structural members, decreasing subsequently the overall response. As a consequence, capacity design criteria should be properly calibrated to consider the severity of environmental exposure and the required structural lifetime. In the present investigation the corrosion of reinforcement due to chloride attack has been considered, assuming a contamination by chlorides the most significant source of environmental hazard for reinforced concrete structure, Stewart and Rosowsky [229] and Vu and Stewart [242].

Because the above considerations, how to extend the lifetime of reinforced concrete structures or to reduce the potential damage due to a strong ground motion become an important issue, and in recent years different mitigation strategies emerged. The enhancement of the global behavior can be reached acting on different levels, from structure to material. Concerning last point, new advanced materials have been proposed in order to improve the seismic performance and durability properties of structures. Among them, the use of the so called Engineered Cementitious Composite (ECC), see e.g. Li [146] and Li [147], in place of normal concrete allows, by an appropriate mix design and adding a minimum quantity of polimeric fibers (about 2%), the formation of multiple narrow cracking in structural elements. This leads to localize damage and a more uniform distribution of energy dissipation. Neverthless, the reduction of the crack width leads to a decrease in the diffusion process of aggressive agents such as chlorides, with significant benefits in terms of durability. With a proper tailoring of the micromechanics, this kind of composite material suggests different classes of target applications like collapse resistance under severe mechanical loading and structures requiring durability even when subjected to environmental hazards, Li [147]. In this study such material has been adopted, comparing the results with those coming from the analysis of ordinary RC structures, in order to highlight the potential advantages.

Finally, all the phenomena involved in this investigation has an inherent variability, and the rational approach to take into account their randomness is based on a probabilistic assessment. Since the nature of the problem is highly non linear, numerical simulations provides the only practical and effective approach. In particular, if random variables are included, numerical process with repeated simulations can be based on Monte Carlo sampling technique, which is particular effective in treatment of aleatory and epistemic uncertainties. For specialized problem there are also approximated numerical methods for finding solution for a probabilistic application, such as FOSM (Wong [246]). However, Monte Carlo simulation is the principal numerical tool to solve engineering problems involving probability, Ang and Tang [11] and Schueller and Pradlwarter [220]. Anyway, in order to reduce the computational cost involved in the simulation analysis based on plain Monte Carlo method, advanced tools are needed to have reliable results. Among them, a stratified sampling called Latin Hypercube sampling is implemented, Iman and Conover [126], Stein [226] and Helton and Davis [113]. This technique requires relatively small number of simulations to have reliable information on the performance of structural systems.

7.2 Objectives achieved

The present study highlighted how the diffusion of aggressive agents into reinforced concrete cross-sections of structural members can lead to a significant reduction of seismic capacity during lifetime of multistory precast frames. This is an important outcome because current seismic codes do not consider the evolution of the performance during lifetime, but coupling between seismic and environmental hazard has a significant influence on the overall behavior. Due to the uncertainties involved in the problem, it is considered that only a probabilistic approach could give reliable results; among different methods available in literature, the attention focused on Monte Carlo simulations, able to take into account directly different sources of randomness. Anyway, due to the computational cost of the standard approach, an effort has been done to search advanced procedures, less demanding, finally considering the Latin Hypercube Sampling technique, recently adopted in seismic analysis (see Dolšek [69]). The effectiveness of the algorithm developed has been proved through the resolution of simple probabilistic schemes, where the analytical solution is available, comparing the results in terms of sampling size with those coming from a random sampling technique. Since a significant improvement has been proved (at least two orders of magnitude), such probabilistic approach has been successfully implemented within PEER methodology in order to perform nonlinear analyses on different structural systems. Such approach allowed to understand the role of different random variables on the overall seismic response looking at the Spearman rank correlation coefficients. As expected, damping, ultimate rotation and energy dissipation has a strong positive influence on the capacity of structural systems; on the other hand, mass

and initial stiffness have a negative correlation with seismic performance.

Both dynamic and static nonlinear analyses have been performed at the beginning of lifetime of multistory precast frames, comparing the results in terms of structural capacity, in order to underline in which conditions pushover method can give appropriate accuracy, avoiding to carried out more complex simulations. Moreover, because two different definitions of limit states have been implemented, such comparison allowed to have important information on the reliability of threshold values in terms on maximum interstory drift recommended by codes (e.g. FEMA 356 [84]), usually associated to cast-in-situ frames. In particular, it has been found that the suggested values for DL and LS limit states (respectively equal to 1% and 2%) are generally too conservative for precast buildings; on the opposite, a maximum interstory drift equal to 4%, related to the NC limit state, is appropriate. Such difference can be explained considering the intrinsic flexibility of such structural schemes, higher than emulative frames, which gives the opportunity to sustain higher displacements before achieving a particular limit state, especially considering DL and LS, where the stiffness plays an important role. Uncertainties in modeling affect also the dispersion of collapse fragility, and for the precast structures studied in the present investigation the mean estimate approach seems appropriate. Since artificial ground motions are used, the record-to-record variability is typically small (e.g. $\sigma = 0.09$ for 2 story building with cross section 80×80, using the IM formulation). Adding modeling uncertainties ($\sigma = 0.24$), the resulting total dispersion is 0.25, very close to the theoretical value. This demonstrates the fundamental importance to include in structural analyses also the uncertainties related to modeling, involving a probabilistic approach, in order to obtain reliable information on the performance of systems investigated. Since different structural configurations have been studied, some comments can be done by looking at MAF values; considering for example NC limit state and the site of Messina (but the same conclusion can be made also for other sites), an increase in the size of columns, taking constant the number of stories, leads to a significant reduction of the probability of collapse, up to 10 times ($\lambda = 1.19 \times 10^{-3}$) for 2 story building with cross section 45×45 and $\lambda = 1.3 \times 10^{-4}$ when cross section is 80×80). At the same time, increasing the height of the frame, assuming the same dimension for the columns, leads to an increase in the probability of failure due to the higher deformability ($\lambda = 1.3 \times 10^{-4}$ for 2 story building with cross section 80×80 and $\lambda = 4.8 \times 10^{-4}$ considering four stories).

Subsequently, in order to consider in a proper way the evolution of chlorides and the subsequent damage on the materials within reinforced concrete cross-sections, the differential problem which describes the diffusion process of aggressive agents such as chlorides has been studied using the cellular automata method, that provides an alternative and more general approach to physical modeling rather than an approximation; the algorithm has been validated through simple problems where the analytical solution is known, both in one and two-dimensional domains, proving his effectiveness. A parametric study has been carried

out considering different concrete cross-sections, in order to understand the reliability of the 1D approach with respect to the more accurate 2D formulation, since the former method is proposed by some codes and recommendations (see e.g. fib 2006 [87]). The comparison in terms of evaluation of concentration showed that the geometric ratio between the dimensions of the sections (here indicated as shape factor) and the position for which the differential equation is solved are the most important parameters. In particular, 1D approach usually predicts higher values, and only when shape factor increases the results of the two methods are close one to each other. Afterwards, by introducing a proper degradation law for steel reinforcement, the time evolution of damage in RC sections has been studied, performing again nonlinear static analyses on structural systems to check the reduction of capacity for each limit state. It has been proved that environmental hazard affects in a decisive way the overall performance; the time evolution of different parameters have been checked, and a significant reduction of seismic capacity has been found, especially assuming the more severe exposure conditions (α near 1). Depending on the structural scheme considered, the capacity in terms of base shear or PGA has a drop up to 50%; moreover, due to the significant deterioration of transversal steel bars, shear demand increases (e.g. in terms of DCR), potentially leading to a brittle collapse mechanism. Finally, the most significant outcome achieved is that same structures, placing at sites with the same seismic hazard, can lead to a different seismic risk depending on the environmental conditions, as can be seen in a quantitative way looking at Figures from to .

To conclude, an attempt has been done to find a possible mitigation strategy of seismic risk, acting on a material level. An advanced fiber-reinforced composite, named ECC (engineered cementitious composite) has been proposed, due to his significant ductility and durability, particularly convenient for seismic applications. Considering his peculiar characteristics, an analytical model in the form of a plastic hinge spring has been developed, modifying the formulation used for standard concrete; such model has been validated through the comparison of cyclic test results available in literature and subsequently applied to different multistory frames, performing during time the same nonlinear analyses. The results obtained have been compared with those coming from the performance of ordinary concrete structures, underlining the benefits in the use of such material. In particular, it has been shown a significant improvement in the overall behavior and a consequent reduction of seismic risk for those buildings where capacity design criteria adopted are effectively appropriate. In these cases, such systems can sustain the seismic demand over the entire lifetime, with a corresponding smoother decrease of structural capacity.

7.3 Future challenges

In the present investigation some outcomes emerged, but still others remain to be explored. First of all, as just mentioned before, the role of connections is an open issue; looking at first results coming from SAFECAST project, connections have a fundamental importance in the overall behavior of multistory precast frames. In this study the hypothesis of "strong" connections has been adopted, so it is strongly recommended for future researches to perform nonlinear analyses including in the analytical models also the appropriate hysteretic behavior of connections.

Moreover, it could be advisable to compare the seismic performance between multistory cast-in-situ and precast buildings. Past European research programs (e.g. "ECOLEADER") showed that an equivalent behavior can be achieved if proper capacity design criteria are used; anyway, such comparison has been limited to one-story structures. Within the framework here developed, it should be worth nothing to extend such analyses on multistory frames during time because, in case of cast-in-situ buildings, plastic hinges could appear also at the ends of beams, and the subsequent damage of all structural members could lead to undesired collapse mechanisms.

Concerning the type of analysis, this study is devoted mostly to nonlinear static analyses, even if preliminary incremental dynamic simulations have been also performed. The choice has been motivated to the need to perform repeated highly nonlinear simulations for different times within a probabilistic approach, leading to a huge number. Clearly, due to the improvements in computer simulations, in the future will be easy to carried out more accurate incremental dynamic analyses because, as just illustrated, the use of pushover method cannot be reliable for some classes of structural systems. Moreover, here only 2D investigations have been performed; in next years, 3D simulations should become the principal tool.

Another issue regards the importance of a proper calibration of diffusive and damage models; for example, the description of corrosion process strongly depends on the evaluation of diffusion coefficient, because also little changes in his value can lead to significant differences in the structural performance. Clearly such condition can be achieved only with the availability of a comprehensive database of experimental tests, in order to carried out reliable durability analyses, with the goal to develop recommendations for a future implementation in design codes. Moreover, it should be advisable to integrate seismic risk with the environmental one, developing appropriate hazard curves related to specific chlorides exposure.

Finally, a deeper study of the advanced cementitious material here adopted is suggested, because it seems very promising for seismic applications where durability properties play a fundamental role. In particular, it is required to carried out several experimental tests, both monotonic and cyclic, in order to have a comprehensive database for a consequent better calibration of the analytical model here proposed. In this way more reliable results can be

obtained when seismic risk analyses are performed, using them as an effective tool to propose this kind of material also for ordinary design.

Appendix A

Ground motion indices

"It is inherently" impossible to describe a complex phenomenon by a single number, Housner and Jennings [118]. None of the intensity indexes give a completely reliable response over the entire range of frequencies, but for each spectral region (short, intermediate and long period) some indices are more suitable than others. First, basic indices related to the ground motion history are presented

Acceleration

1. Peak ground acceleration: $PGA = \max|a(t)|$.

   Pro: Simple to use.
   Contra: It refers only to a value of the acceleration spectrum, but not appropriate to cover all the range of periods.

2. Mean square value: $P_a = \frac{1}{t_2-t_1}\int_{t_1}^{t_2} a^2(t)\,dt$.

   Pro: It considers a range of the signal.
   Contra: Two ground motions with the same mean square value can lead to a different response due to the different ground duration.

3. Square value: $a_{sq} = \int_{t_1}^{t_2} a^2(t)\,dt$.

   Pro: It is related to the duration.
   Contra: Cannot be applied in the overall range of frequencies.

4. Root square value: $a_{rs} = \sqrt{a_{sq}}$.

Velocity

1. Peak ground velocity: $PGV = \max|v(t)|$.
2. Mean square value: $P_v = \frac{1}{t_2-t_1}\int_{t_1}^{t_2} v^2(t)\,dt$.
3. Square value: $v_{sq} = \int_{t_1}^{t_2} v^2(t)\,dt$.

4. Root square value: $v_{rs} = \sqrt{v_{sq}}$.

Displacement

1. Peak ground displacement: $PGD = \max|d(t)|$.
2. Mean square value: $P_d = \frac{1}{t_2-t_1}\int_{t_1}^{t_2} d^2(t)\,dt$.
3. Square value: $d_{sq} = \int_{t_1}^{t_2} d^2(t)\,dt$.
4. Root square value: $d_{rs} = \sqrt{d_{sq}}$.

In the following, a review of different indices proposed during the past decades is illustrated.

1. Housner Spectral Intensity, 1952 (Housner [114]):

$$SI_H = \int_{0.1}^{2.5} S_v(T,\xi)\,dT.$$

Pro: It is based on a energetic equivalence between seismic energy imparted by the scaled earthquake and that implied in the design spectrum. The limits of the integral cover a range of typical periods of vibration. It is very good for the intermediate spectral region.

Contra: It is *a posteriori* index (response index). It ignores the characteristics of the inelastic response, i.e. period elongation.

2. Housner and Jennings, 1964 (Housner and Jennings [117]):

$$a_{rms} = \sqrt{P_a}.$$

Pro: It considers a range of the signal.

Contra: Two ground motions with the same mean square value can lead to a different response due to the different ground duration.

3. Housner, 1970 (Housner [115]):

$$a_{rs} = \sqrt{a_{sq}}.$$

Pro: It considers the duration of the earthquake.

Contra: It is good for the acceleration-spectra region.

4. Arias, 1970 (Arias [14]):

$$I_A(\xi) = \frac{\arccos\xi}{g\sqrt{1-\xi^2}}\int_0^{t_f} a^2\,dt.$$

Pro: It considers the duration of the signal. It can be interpreted as the sum of the energies dissipated, per unit of mass, by a population of damped oscillators of all natural frequencies.

Contra: It is good for the acceleration-spectra region.

5. Housner, 1975 (Housner [116]), "Earthquake power index":

$$P_a = \frac{1}{t_2 - t_1} \int_{t_1}^{t_2} a^2(t)\, dt.$$

Pro: The limits of the integrals refer to the duration of an earthquake as defined by Trifunac and Brady.

Contra: It is good for the acceleration-spectra region.

6. Araya and Saragoni, 1980 (Araya and Saragoni [13]), "Potential destructiveness of an earthquake":

$$P_D = \frac{I_A}{\nu_0^2}.$$

Pro: It considers the frequency content, so it allows the shift between acceleration region to velocity region.

Contra: It does not give a good correlation also in the velocity region.

7. Nau and Hall, 1984 (Nau and Hall [180]):

$$SI_a = \int_{0.03}^{0.19} S_v(T, \xi)\, dT, SI_v = \int_{0.29}^{2.0} S_v(T, \xi)\, dT, SI_d = \int_{4.17}^{12.50} S_v(T, \xi)\, dT.$$

Pro: Use of different limits to cover the three regions.

Contra: Number of records considered limited (12), variation of ratio PGA/PGV limited and calibration based primarily on the elastic case.

8. Park and Ang, 1985 (Park et al. [189]), "Characteristic intensity":

$$I_C = a_{rms}^{1.5} t_d^{0.5}.$$

Pro: Good correlation with the corresponding damage index and influence of the significant duration.

Contra: It is good for the acceleration-spectra region.

9. Fajfar, 1990 (fajfar1990measure):

$$I_F = v_{max} t_d^{0.25}.$$

Pro: It considers the significant duration. Very good correlation in the acceleration and velocity spectra.

Contra: Cannot be applied in the displacement region (flexible systems).

10. Matsumura Spectral Intensities, 1992 (Matsumura [162]):

$$SI_M = \frac{1}{T_y} \int_{T_y}^{2T_y} S_v(T, 0.05)\, dT, V_e = \sqrt{\frac{2E_i}{m}}.$$

Pro: Very good measure in a wide range of frequencies.

Contra: Number of records considered limited (12), interval found with a ductility value equal to 2, post-yield stiffness ratio equal to 0.5.

11. Martinez-Rueda, 1998 (Martínez-Rueda [161]):

$$SI_M = \frac{1}{T_h - T_y} \int_{T_y}^{T_h} S_v(T, 0.05)\, dT.$$

Pro: Extensive numerical campaign.

Contra: Lower correlation with respect to the Matsumura indices.

12. Cordova, 2000 (Cordova et al. [61]):

$$S_aC = S_a(T_1) \left[\frac{S_a(cT_1)}{S_a(T_1)} \right]^{\alpha}.$$

Pro: Take into account the elongation of the period due to the inelastic behavior.

Contra: The two parameters calibrated considering the response of systems with long periods.

13. Riddell and Garcia, 2001 (Riddell and Garcia [209]):

$$I_a = a_{max} t_d^{1/3}, I_v = v_{max}^{2/3} t_d^{1/3}, I_d = d_{max} t_d^{1/3}.$$

Pro: Each of the above index give good results in the corresponding region.

Contra: Moderate ductility level considered.

14. Manfredi, 2001 (Manfredi [159]):

$$I_D = \frac{I_E}{PGA \cdot PGV}.$$

Pro: Combine single value parameters with an integral value, taking into account the significant duration of an earthquake.

Contra: Not suitable for the displacement region.

15. Hutchinson, 2002 (Hutchinson et al. [120]):

$$\Delta_{mean} = \frac{1}{T_{sec} - T_1} \int_{T_1}^{T_{sec}} S_d(T, \xi)\, dT.$$

Pro: Suitable for the DBD (T_{sec}) is the period corresponding to the secant stiffness at the maximum displacement.

Contra: Not suitable for the acceleration and velocity region.

References

[1] N.A. Abrahamson and J.J. Bommer. Probability and uncertainty in seismic hazard analysis. *Earthquake Spectra*, 21:603, 2005.

[2] S.F.U. Ahmed and H. Mihashi. A review on durability properties of strain hardening fibre reinforced cementitious composites (SHFRCC). *Cement and Concrete Composites*, 29(5):365–376, 2007. ISSN 0958-9465.

[3] M. Akiyama, D.M. Frangopol, and M. Suzuki. Integration of the effects of airborne chlorides into reliability-based durability design of reinforced concrete structures in a marine environment. *Structure and Infrastructure Engineering*, 2009.

[4] M. Akiyama, D.M. Frangopol, and I. Yoshida. Time-dependent reliability analysis of existing rc structures in a marine environment using hazard associated with airborne chlorides. *Engineering Structures*, 2010.

[5] A.A. Almusallam. Effect of degree of corrosion on the properties of reinforcing steel bars. *Construction and Building Materials*, 15(8):361–368, 2001.

[6] M.S. Altieri and A. Stefanoni. Metodi sem-ni per la risoluzione di problemi parabolici bidimensionali. Technical report, Politecnico di Milano, 2009.

[7] A. Altoontash. *Simulation and damage models for performance assessment of reinforced concrete beam-column joints.* PhD thesis, Stanford University, 2004.

[8] N. Ambraseys, P. Smit, J. Douglas, B. Margaris, R. Sigbjörnsson, S. Olafsson, P. Suhadolc, and G. Costa. Internet site for european strong-motion data. *Bollettino di Geofisica Teorica ed Applicata*, 45(3):113–129, 2004.

[9] T.L. Anderson. *Fracture mechanics: fundamentals and applications.* CRC, 2005.

[10] C. Andrade and C. Alonso. On-site measurements of corrosion rate of reinforcements. *Construction and building materials*, 15(2-3):141–145, 2001.

[11] A.H.S. Ang and W.H. Tang. *Probability concepts in engineering: Emphasis on applications to civil and environmental engineering*, volume 1. John Wiley & Sons, Inc., second edition, 2007.

[12] S. Antoniou and R. Pinho. Advantages and limitations of adaptive and non-adaptive force-based pushover procedures. *Journal of Earthquake Engineering*, 8(4):497–522, 2004.

[13] R. Araya and GR Saragoni. Capacity of the strong ground-motion to cause structural damage. In *Proceedings of the Seventh World Conference on Earthquake Engineering*, pages 483–490, 1980.

[14] A. Arias. A measure of earthquake intensity. *Seismic design for nuclear power plants*, pages 438–483, 1970.

[15] S.K. Au and J.L. Beck. Estimation of small failure probabilities in high dimensions by subset simulation. *Probabilistic Engineering Mechanics*, 16(4):263–277, 2001. ISSN 0266-8920.

[16] SK Au and JL Beck. Subset simulation and its application to seismic risk based on dynamic analysis. *Journal of Engineering Mechanics*, 129:901, 2003.

[17] SK Au, J. Ching, and JL Beck. Application of subset simulation methods to reliability benchmark problems. *Structural Safety*, 29(3):183–193, 2007. ISSN 0167-4730.

[18] J.W. Baker and C.A. Cornell. A vector-valued ground motion intensity measure consisting of spectral acceleration and epsilon. *Earthquake Engineering & Structural Dynamics*, 34 (10):1193–1217, 2005. ISSN 1096-9845.

[19] J.W. Baker and C.A. Cornell. Spectral shape, epsilon and record selection. *Earthquake engineering & structural dynamics*, 35(9):1077–1095, 2006.

[20] Y. Ballim and JC Reid. Reinforcement corrosion and the deflection of rc beams—-an experimental critique of current test methods. *Cement and concrete composites*, 25(6): 625–632, 2003.

[21] A. Balsamo, A. Colombo, G. Manfredi, P. Negro, and A. Prota. Seismic behavior of a full-scale rc frame repaired using cfrp laminates. *Engineering structures*, 27(5):769–780, 2005.

[22] P. Bazzurro and C.A. Cornell. Disaggregation of seismic hazard. *Bulletin of the Seismological Society of America*, 89(2):501–520, 1999.

[23] J.S. Bendat and A.G. Piersol. *Engineering applications of correlation and spectral analysis*. Wiley-Interscience, 1980.

[24] M. Berry, M. Parrish, and M. Eberhard. PEER Structural Performance Database User's Manual (Version 1.0). Technical report, Pacific Earthquake Engineering Research Center, 2004.

[25] L. Berto, R. Vitaliani, A. Saetta, and P. Simioni. Seismic assessment of existing RC structures affected by degradation phenomena. *Structural Safety*, 31(4):284–297, 2009. ISSN 0167-4730.

[26] L. Bertolini, B. Elsener, P. Pedeferri, and R.B. Polder. *Corrosion of steel in concrete: prevention, diagnosis, repair*. Vch Verlagsgesellschaft Mbh, 2004.

[27] F. Biondini. A Three-dimensional Finite Beam Element for Multiscale Damage Measure and Seismic Analysis of Concrete Structures. In *13th World Conference on Earthquake Engineering*, pages 1–6, 2004.

[28] F. Biondini. Cellular automata simulation of damage processes in concrete structures. *Soft Computing Methods for Civil and Structural Engineering*, 29:229–264, 2011.

[29] F. Biondini and D.M. Frangopol. *Life-cycle Civil Engineering: Proceedings of the First International Symposium on Life-Cycle Civil Engineering, Varenna, Lake Como, Italy, June 10-14, 2008*. Taylor & Francis, 2008.

[30] F. Biondini and D.M. Frangopol. Probabilistic limit analysis and lifetime prediction of concrete structures. *Structure and Infrastructure Engineering*, 4(5):399–412, 2008.

[31] F. Biondini and G. Toniolo. Validation of seismic design criteria for concrete frames based on monte carlo simulation and full-scale pseudo-dynamic tests. In *Proceedings of the 13th World Conference on Earthquake Engineering*, 2004.

[32] F. Biondini and G. Toniolo. Probabilistic Calibration and Experimental Validation of the Seismic Design Criteria for One-Story Concrete Frames. *Journal of Earthquake Engineering*, 13(4):426–462, 2009. ISSN 1363-2469.

[33] F. Biondini and G. Toniolo. Pseudodynamic tests on full-scale prototype of a multi-storey precast structure. In *XIV Convegno Anidis, Bari*, 2011.

[34] F. Biondini, F. Bontempi, D.M. Frangopol, and P.G. Malerba. Cellular automata approach to durability analysis of concrete structures in aggressive environments. *Journal of Structural Engineering*, 130:1724, 2004.

[35] F. Biondini, L. Ferrara, G. Toniolo, and P. Negro. Results of pseudodynamic test on a prototype of precast rc frame. In *International Conference on Advances in Concrete and Structures*, pages 1534–1548. RILEM Publications SARL, 2004.

[36] F. Biondini, F. Bontempi, D.M. Frangopol, P.G. Malerba, et al. Probabilistic service life assessment and maintenance planning of concrete structures. *Journal of structural engineering*, 132:810, 2006.

[37] F. Biondini, D.M. Frangopol, and P.G. Malerba. Uncertainty effects on lifetime structural performance of cable-stayed bridges. *Probabilistic Engineering Mechanics*, 23(4):509–522, 2008.

[38] F. Biondini, G. Toniolo, and G. Tsionis. Seismic design criteria for multi-storey precast structures. In *14th World Conference on Earthquake Engineering*, pages 12–17, 2008.

[39] F. Biondini, G. Toniolo, and G. Tsionis. Capacity design and seismic performance of multi-storey precast structures. *European Journal of Environmental and Civil Engineering.*, 14(1), 2010.

[40] F. Biondini, A. Palermo, and G. Toniolo. Seismic performance of concrete structures exposed to corrosion: case studies of low-rise precast buildings. *Structure and Infrastructure Engineering*, 7(1):109–119, 2011. ISSN 1573-2479.

[41] F. Biondini, A. Titi, and G. Toniolo. On the accuracy of the response spectrum analysis in the seismic design of concrete structures. In *Structural Engineering World Congress*, pages 4–6, 2011.

[42] F. Biondini, E. Camnasio, and A. Palermo. Life-cycle performance of concrete bridges exposed to corrosion and seismic hazard. In *Structures Congress 2012 (ASCE2012)*, 2012.

[43] J.J. Bommer. Deterministic vs. probabilistic seismic hazard assessment: an exaggerated and obstructive dichotomy. *Journal of Earthquake Engineering*, 6(S1):43–73, 2002.

[44] J.M. Bracci, S.K. Kunnath, and A.M. Reinhorn. Seismic performance and retrofit evaluation of reinforced concrete structures. *Journal of Structural Engineering-American Society of Civil Engineers*, 123(1):3–10, 1997.

[45] BRITE/EURAM. The residual service life of reinforced concrete structures. Technical Report BRUE-CT92-0591, European Union, 1995.

[46] N. Buratti. *Assessment of Seismic Safety: Response Surface Approach and Accelerogram Selection Issues*. PhD thesis, Ph. D. Dissertation, DISTART-Structural engineering, University of Bologna, Bologna, Italy, 2009.

[47] A.W. Burks and J. Von Neumann. *Theory of self-reproducing automata*. University of Illinois Press, 1966.

[48] JG Cabrera. Deterioration of concrete due to reinforcement steel corrosion. *Cement and concrete composites*, 18(1):47–59, 1996.

[49] J. Cairns, G.A. Plizzari, Y. Du, D.W. Law, and C. Franzoni. Mechanical properties of corrosion-damaged reinforcement. *ACI materials journal*, 102(4), 2005.

[50] K.W. Campbell and Y. Bozorgnia. Next generation attenuation (nga) empirical ground motion models: can they be used in europe. In *Proceedings, First European Conference on Earthquake Engineering and Seismology*, 2006.

[51] A. Castel, R. François, and G. Arliguie. Mechanical behaviour of corroded reinforced concrete beams. Part 1: experimental study of corroded beams. *Materials and Structures*, 33(9):539–544, 2000.

[52] C. Cauzzi and E. Faccioli. Broadband (0.05 to 20 s) prediction of displacement response spectra based on worldwide digital records. *Journal of seismology*, 12(4):453–475, 2008.

[53] D. Celarec, D. Vamvatsikos, and M. Dolšek. Simplified estimation of seismic risk for reinforced concrete buildings with consideration of corrosion over time. *Bulletin of Earthquake Engineering*, pages 1–19, 2010.

[54] D. Chen and S. Mahadevan. Chloride-induced reinforcement corrosion and concrete cracking simulation. *Cement and Concrete Composites*, 30(3):227–238, 2008.

[55] A.K. Chopra. *Dynamics of structures: theory and applications to earthquake engineering*. Prentice Hall Englewood Cliffs, New Jersey, third edition, 2007.

[56] A.K. Chopra and R.K. Goel. A modal pushover analysis procedure for estimating seismic demands for buildings. *Earthquake Engineering & Structural Dynamics*, 31(3):561–582, 2002.

[57] A.K. Chopra and R.K. Goel. A modal pushover analysis procedure to estimate seismic demands for unsymmetric-plan buildings. *Earthquake Engineering & Structural Dynamics*, 33(8):903–927, 2004. ISSN 1096-9845.

[58] R.W. Clough and J. Penzien. *Dynamics of structures*. Computer & Structures, Inc., third edition, 2003.

[59] W.J. Conover. *Practical nonparametric statistics*. John Wiley & Sons, Inc., third edition, 1999. ISBN 0471160687.

[60] J. Conway. The game of life. *Scientific American*, 223(4):4, 1970.

[61] P.P. Cordova, G.G. Deierlein, S.S.F. Mehanny, and C.A. Cornell. Development of a two-parameter seismic intensity measure and probabilistic assessment procedure. In *Proceedings of the 2nd US-Japan Workshop on Performance-Based Earthquake Engineering Methodology for Reinforced Concrete Building Structures*, pages 187–206, 2000.

[62] C.A. Cornell. Engineering seismic risk analysis. *Bulletin of the Seismological Society of America*, 58(5):1583, 1968. ISSN 0037-1106.

[63] D. Coronelli and P. Gambarova. Structural assessment of corroded reinforced concrete beams: modeling guidelines. *Journal of structural engineering*, 130:1214, 2004.

[64] T.K. Datta. *Seismic analysis of structures*. John Wiley & Sons, Inc., 2010. ISBN 0470824610.

[65] A. Der Kiureghian. Structural reliability methods for seismic safety assessment: a review. *Engineering Structures*, 18(6):412–424, 1996.

[66] A. Der Kiureghian and O. Ditlevsen. Aleatory or epistemic? does it matter? *Structural Safety*, 31(2):105–112, 2009.

[67] M. Di Ludovico, A. Prota, G. Manfredi, and E. Cosenza. Seismic strengthening of an under-designed rc structure with frp. *Earthquake Engineering & Structural Dynamics*, 37(1):141–162, 2008.

[68] M. di Prisco, G. Plizzari, and L. Vandewalle. Fibre reinforced concrete: new design perspectives. *Materials and Structures*, 42(9):1261–1281, 2009.

[69] M. Dolšek. Incremental dynamic analysis with consideration of modeling uncertainties. *Earthquake Engineering & Structural Dynamics*, 38(6):805–825, 2009. ISSN 1096-9845.

[70] M. Dolšek. Simplified method for seismic risk assessment of buildings with consideration of aleatory and epistemic uncertainty. *Structure and Infrastructure Engineering*, 4(1): 1–15, 2011.

[71] M. Dolšek and P. Fajfar. Simplified probabilistic seismic performance assessment of plan-asymmetric buildings. *Earthquake Engineering & Structural Dynamics*, 36(13): 2021–2041, 2007.

[72] J.E. Ebel and A.L. Kafka. A Monte Carlo approach to seismic hazard analysis. *Bulletin of the Seismological Society of America*, 89(4):854, 1999. ISSN 0037-1106.

[73] EC2. Eurocode 2: Design of concrete structures-Part 1: General rules and rules for buildings. *CEN, Brussels, Belgium*, 2002.

[74] EC8. Eurocode 8: Design of Structures for Earthquake Resistance. Part 1: General Rules, Seismic Actions and Rules for Buildings. *CEN, Brussels, Belgium*, 1:2005, 2004.

[75] T. El Maaddawy and K. Soudki. A model for prediction of time from corrosion initiation to corrosion cracking. *Cement and Concrete Composites*, 29(3):168–175, 2007.

[76] B. Ellingwood. *Development of a probability based load criterion for American National Standard A58: Building code requirements for minimum design loads in buildings and other structures*. Number 577. US Dept. of Commerce, National Bureau of Standards: for sale by the Supt. of Docs., US Govt. Print. Off., 1980.

[77] A.S. Elnashai, L. Di Sarno, and Ebooks Corporation. *Fundamentals of earthquake engineering*. Wiley Online Library, 2008. ISBN 0470024844.

[78] M.P. Enright and D.M. Frangopol. Probabilistic analysis of resistance degradation of reinforced concrete bridge beams under corrosion. *Engineering Structures*, 20(11): 960–971, 1998. ISSN 0141-0296.

[79] E. Faccioli and M. Villani. Seismic hazard mapping for italy in terms of broadband displacement response spectra. *Earthquake Spectra*, 25:515, 2009.

[80] P. Fajfar. Capacity spectrum method based on inelastic demand spectra. *Earthquake Engineering & Structural Dynamics*, 28(9):979–993, 1999. ISSN 1096-9845.

[81] P. Fajfar. A nonlinear analysis method for performance-based seismic design. *Earthquake Spectra*, 16(3):573–592, 2000. ISSN 8755-2930.

[82] P. Fajfar and P. Gašperšič. The n2 method for the seismic damage analysis of rc buildings. *Earthquake engineering & structural dynamics*, 25(1):31–46, 1996.

[83] M.N. Fardis and D.E. Biskinis. Deformation capacity of rc members, as controlled by flexure or shear. In *Otani Symposium*, pages 511–530, 2003.

[84] FEMA 356. Prestandard and commentary for the seismic rehabilitation of buildings. Technical report, Federal Emergency Management Agency Washington, DC, 2000.

[85] FEMA 440. Improvement of Nonlinear Static Seismic Analysis Procedures. Technical report, Federal Emergency Management Agency Washington, DC, 2005.

[86] FEMA P695. Quantification of building seismic performance factors. Technical report, Federal Emergency Management Agency Washington, DC, 2009.

[87] fib 2006. *Model code for service life design*, volume 34. FIB-Féd. Int. du Béton, 2006.

[88] G. Fischer and V.C. Li. Effect of matrix ductility on deformation behavior of steel-reinforced ecc flexural members under reversed cyclic loading conditions. *ACI Structural Journal*, 99(6):781–790, 2002.

[89] G. Fischer and V.C. Li. Influence of matrix ductility on tension-stiffening behavior of steel reinforced engineered cementitious composites (ecc). *ACI Structural journal*, 99(1): 104–111, 2002.

[90] G. Fischer and V.C. Li. Deformation behavior of fiber-reinforced polymer reinforced engineered cementitious composite (ECC) flexural members under reversed cyclic loading conditions. *ACI Structural Journal*, 100(1):25–35, 2003. ISSN 0889-3241.

[91] G. Fischer and V.C. Li. Intrinsic response control of moment-resisting frames utilizing advanced composite materials and structural elements. *ACI Structural journal*, 100(2): 166–176, 2003.

[92] G. Fischer, H. Fukuyama, and V.C. Li. Effect of matrix ductility on the performance of reinforced ecc column members under reversed cyclic loading conditions. In *JCI International Workshop on Ductile Fiber Reinforced Cementitious Composites (DFRCC)*, pages 269–278, 2002.

[93] M. Fischinger, M. Kramar, and T. Isaković. Cyclic response of slender RC columns typical of precast industrial buildings. *Bulletin of Earthquake Engineering*, 6(3):519–534, 2008. ISSN 1570-761X.

[94] M. Gardner. Mathematical games: The fantastic combinations of john conway's new solitaire game "life". *Scientific American*, 223(4):120–123, 1970.

[95] D. Gasparini and EH Vanmarcke. Simqke: A program for artificial motion generation. *Department of Civil Engineering, Massachusetts Institute of Technology, Cambridge, MA*, 1976.

[96] B.E. Gencturk. *Multi-objective optimal seismic design of buildings using advanced engineering materials*. PhD thesis, University of Illinois at Urbana-Champaign, 2011.

[97] A. Ghobarah. Performance-based design in earthquake engineering: state of development. *Engineering Structures*, 23(8):878–884, 2001. ISSN 0141-0296.

[98] P. Giovenale, C.A. Cornell, and L. Esteva. Comparing the adequacy of alternative ground motion intensity measures for the estimation of structural responses. *Earthquake Engineering & Structural Dynamics*, 33(8):951–979, 2004. ISSN 0098-8847.

[99] O.E. Gjørv. *Durability design of concrete structures in severe environments*. Taylor & Francis Group, 2009.

[100] GK Glass and NR Buenfeld. Chloride-induced corrosion of steel in concrete. *Progress in Structural Engineering and Materials*, 2(4):448–458, 2000.

[101] M.E. Glicksman. *Diffusion in solids: field theory, solid-state principles, and applications*. Number v. 1. John Wiley & Sons, Inc., 2000. ISBN 0471239720.

[102] P.W. Glynn and D.L. Iglehart. Importance sampling for stochastic simulations. *Management Science*, pages 1367–1392, 1989.

[103] R.K. Goel and A.K. Chopra. Extension of modal pushover analysis to compute member forces. *Earthquake Spectra*, 21:125, 2005.

[104] JA Gonzalez, C. Andrade, C. Alonso, and S. Feliu. Comparison of rates of general corrosion and maximum pitting penetration on concrete embedded steel reinforcement. *Cement and Concrete Research*, 25(2):257–264, 1995.

[105] C.A. Goulet, C.B. Haselton, J. Mitrani-Reiser, J.L. Beck, G.G. Deierlein, K.A. Porter, and J.P. Stewart. Evaluation of the seismic performance of a code-conforming reinforced-concrete frame building-from seismic hazard to collapse safety and economic losses. *Earthquake Engineering and Structural Dynamics*, 36(13):1973–1998, 2007.

[106] A.A. Griffith. The phenomena of rupture and flow in solids. *Philosophical transactions of the royal society of london. Series A, containing papers of a mathematical or physical character*, 221:163–198, 1921.

[107] J. Gulikers. Theoretical considerations on the supposed linear relationship between concrete resistivity and corrosion rate of steel reinforcement. *Materials and Corrosion*, 56(6):393–403, 2005.

[108] K. Gurley and A. Kareem. Applications of wavelet transforms in earthquake, wind and ocean engineering. *Engineering Structures*, 21(2):149–167, 1999.

[109] B. Gutenberg and C.F. Richter. Seismicity of the earth. *Geological Society of America Bulletin*, 56(6):603, 1945.

[110] T.S. Han, P.H. Feenstra, and S.L. Billington. Simulation of highly ductile fiber-reinforced cement-based composite components under cyclic loading. *ACI Structural Journal*, 100 (6):749–757, 2003. ISSN 0889-3241.

[111] J. Hancock, J. Watson-Lamprey, A.A. NORMAN, J.B. JULIAN, A. Markatis, E. McCOYH, and R. Mendis. An improved method of matching response spectra of recorded earthquake ground motion using wavelets. *Journal of Earthquake Engineering*, 10(S1): 67–89, 2006.

[112] C.B. Haselton. *Assessing seismic collapse safety of modern reinforced concrete moment frame buildings*. PhD thesis, Stanford University, 2006.

[113] J.C. Helton and F.J. Davis. Latin hypercube sampling and the propagation of uncertainty in analyses of complex systems. *Reliability Engineering & System Safety*, 81(1):23–69, 2003. ISSN 0951-8320.

[114] GW Housner. Spectrum intensities of strong motion earthquakes. In *Proceedings of the Symposium on Earthquake and Blast Effects on Structures*, pages 20–36, 1952.

[115] G.W. Housner. Strong ground motion. *Earthquake Engineering*, pages 75–91, 1970.

[116] GW Housner. Measures of severity of earthquake ground shaking. In *Proceedings, US National Conference on Earthquake Engineering*, pages 25–33, 1975.

[117] GW Housner and P.C. Jennings. Generation of artificial earthquakes. In *Selected Earthquake Engineering Papers of George W. Housner*, pages 438–475. ASCE, 1964.

[118] G.W. Housner and P.C. Jennings. *Earthquake design criteria*. Earthquake Engineering Research Institute, 1982.

[119] D.E. Huntington and C.S. Lyrintzis. Improvements to and limitations of latin hypercube sampling. *Probabilistic Engineering Mechanics*, 13(4):245–253, 1998.

[120] T.C. Hutchinson, R.W. Boulanger, Y.H. Chai, and I.M Idriss. Inelastic seismic response of extended pile shaft supported bridge structures. Technical report, PEER-Pacific Earthquake Engineering Center, 2002.

[121] L.F. Ibarra, R.A. Medina, and H. Krawinkler. Hysteretic models that incorporate strength and stiffness deterioration. *Earthquake engineering & structural dynamics*, 34 (12):1489–1511, 2005. ISSN 1096-9845.

[122] I. Iervolino and C.A. Cornell. Record selection for nonlinear seismic analysis of structures. *Earthquake Spectra*, 21:685, 2005.

[123] I. Iervolino, G. Maddaloni, and E. Cosenza. Eurocode 8 compliant real record sets for seismic analysis of structures. *Journal of Earthquake Engineering*, 12(1):54–90, 2008.

[124] I. Iervolino, F. De Luca, and E. Cosenza. Spectral shape-based assessment of SDOF nonlinear response to real, adjusted and artificial accelerograms. *Engineering Structures*, 32(9):2776–2792, 2010.

[125] I. Iervolino, C. Galasso, and E. Cosenza. REXEL: computer aided record selection for code-based seismic structural analysis. *Bulletin of Earthquake Engineering*, 8:339–362, 2010.

[126] R.L. Iman and WJ Conover. Small sample sensitivity analysis techniques for computer models, with an application to risk assessment. *COMMUN. STAT. THEORY METH.*, A9(17):1749–1842, 1980.

[127] R.L. Iman and WJ Conover. Distribution-Free Approach to Inducing Rank Correlation Among Input Variables. *COMMUN. STAT. SIMUL. COMPUT.*, 11(3):311–334, 1982.

[128] T. Isaković, L. Bevc, and M. Fischinger. Modeling the cyclic flexural and shear response of the rc hollow box columns of an existing viaduct. *Journal of Earthquake Engineering*, 12(7):1120–1138, 2008.

[129] F. Jalayer. Probabilistic basis for 2000 SAC Federal Emergency Management Agency steel moment frame guidelines. *Journal of Structural Engineering*, 128:526, 2002.

[130] P. Jun and V. Mechtcherine. Behaviour of Strain-hardening Cement-based Composites (SHCC) under monotonic and cyclic tensile loading:: Part 1-Experimental investigations. *Cement and Concrete Composites*, 32(10):801–809, 2010.

[131] P. Jun and V. Mechtcherine. Behaviour of Strain-hardening Cement-based Composites (SHCC) under monotonic and cyclic tensile loading:: Part 2-Modelling. *Cement and Concrete Composites*, 32(10):810–818, 2010.

[132] K. Kesner and S.L. Billington. Experimental response of precast infill panels made with dfrcc. In *Proceedings, DFRCC Inter'l Workshop*, pages 289–298, 2002.

[133] K.E. Kesner, S.L. Billington, and K.S. Douglas. Cyclic response of highly ductile fiber-reinforced cement-based composites. *ACI Materials Journal*, 100(5):381–390, 2003. ISSN 0889-325X.

[134] S. Kirkpatrick, C.D. Gelatt, and M.P. Vecchi. Optimization by simulated annealing. *science*, 220(4598):671, 1983.

[135] M. Kramar. *Potresna ranljivost montažnih armiranobetonskih hal (in Slovenian)*. PhD thesis, University of Ljubljana, FGG, 2008.

[136] M. Kramar, T. Isaković, and M. Fischinger. Seismic collapse risk of precast industrial buildings with strong connections. *Earthquake Engineering & Structural Dynamics*, 39 (8):847–868, 2010. ISSN 1096-9845.

[137] S.L. Kramer. *Geotechnical earthquake engineering*. Number Prentice-Hall International Series in Civil Engineering and Engineering Mechanics. Prentice Hall, 1996.

[138] H. Krawinkler and D.G. Lignos. How to Predict the Probability of Collapse of Non-Ductile Building Structures. *Seismic Risk Assessment and Retrofitting*, pages 343–365, 2009.

[139] H. Krawinkler and G. Seneviratna. Pros and cons of a pushover analysis of seismic performance evaluation. *Engineering Structures*, 20(4-6):452–464, 1998. ISSN 0141-0296.

[140] E.L. Krinitzsky. Deterministic versus probabilistic seismic hazard analysis for critical structures. *Engineering geology*, 40(1-2):1–7, 1995.

[141] D.R. Lankard. Slurry infiltrated fiber concrete (sifcon): properties and applications. In *MRS Proceedings*, volume 42. Cambridge Univ Press, 1984.

[142] MD Lepech and VC Li. Long term durability performance of engineered cementitious composites. *Restoration of Buildings and Monuments*, 12(2):119–132, 2006. ISSN 0947-4498.

[143] C.K.Y. Leung and V.C. Li. Steady-state and multiple cracking of short random fiber composites. *Journal of Engineering Mechanics*, 118(11):2246–2263, 1992.

[144] M. Li, M. Sahmaran, and V.C. Li. Effect of cracking and healing on durability of engineered cementitious composites under marine environment. *HPFRCC 5-High Performance Fiber Reinforced Cement Composites*, pages 10–13, 2007.

[145] V. Li. Engineered Cementitious Composites - Tailored composites through micromechanical modeling. In N. Banthia, A. Bentur, and A.A. Mufti, editors, *Fiber cementious composites: present and future*, pages 64–97. Canadian Society for Civil Engineering, 1998.

[146] V.C. Li. Reflections on the research and development of Engineered Cementitious Composites (ECC). In *Proceedings of the JCI International Workshop on Ductile Fiber Reinforced Cementitious Composites (DFRCC): application and evaluation (DFRCC-2002): Takayama, Japan, 21-22 October 2002*, page 1. Citeseer, 2002. ISBN 4931451454.

[147] V.C. Li. On engineered cementitious composites (ECC). *Journal of advanced concrete technology*, 1(3):215–230, 2003. ISSN 1346-8014.

[148] V.C. Li. Bendable composites: Ductile concrete for structures. *Structure*, pages 45–48, 2006.

[149] V.C. Li. Engineered Cementitious Composites (ECC)–Material, Structural, and Durability Performance. *Concrete construction engineering handbook, CRC Press, Boca Raton*, 2007.

[150] V.C. Li and M. Lepech. Crack resistant concrete material for transportation construction. In *Proc., Transportation Research Board Conf.* Citeseer, 2004.

[151] V.C. Li, G. Fischer, Y. Kim, M.D. Lepech, S. Qian, M. Weimann, and S. Wang. Durable link slabs for jointless bridge decks based on strain-hardening cementitious composites. Technical report, Michigan Department of Transportation, 2003.

[152] V.C. Li, T. Horikoshi, A. Ogawa, S. Torigoe, and T. Saito. Micromechanics-based durability study of polyvinyl alcohol-engineered cementitious composite. *ACI Materials Journal*, 101(3):242–248, 2004.

[153] A.B. Liel. *Assessing the collapse risk of California's existing reinforced concrete frame structures: Metrics for seismic safety decisions.* PhD thesis, Stanford University, 2008.

[154] A.B. Liel, C.B. Haselton, and G.G. Deierlein. Simulating structural collpse due to earthquakes: model idealization, model calibration and numerical solution algorithms. In *COMPDYN 2009, 2nd Internacional Conference on Computational Methods in Structural Dynamics and Earthquake Engineering, Greece*, 2009.

[155] A.B. Liel, C.B. Haselton, G.G. Deierlein, and J.W. Baker. Incorporating modeling uncertainties in the assessment of seismic collapse risk of buildings. *Structural Safety*, 31 (2):197–211, 2009. ISSN 0167-4730.

[156] D. Lignos. *Sidesway collapse of deteriorating structural systems under seismic excitations.* PhD thesis, Stanford University, 2008.

[157] G. Lupoi, P. Franchin, A. Lupoi, and P.E. Pinto. Seismic fragility analysis of structural systems. *Journal of Engineering Mechanics*, 132:385, 2006.

[158] J.B. Mander, MJN Priestley, and R. Park. Theoretical Stress-Strain Model for Confined Concrete. *Journal of Structural Engineering*, 114:1804, 1988.

[159] G. Manfredi. Evaluation of seismic energy demand. *Earthquake engineering & structural dynamics*, 30(4):485–499, 2001.

[160] DB Marshall and BN Cox. A j-integral method for calculating steady-state matrix cracking stresses in composites. *Mechanics of materials*, 7(2):127–133, 1988.

[161] J.E. Martínez-Rueda. Scaling procedure for natural accelerograms based on a system of spectrum intensity scales. *Earthquake spectra*, 14:135, 1998.

[162] K. Matsumura. On the intensity measure of strong motions related to structural failures. In *Proceedings of the 10th World Conference on Earthquake Engineering*, volume 1, pages 375–380, 1992.

[163] S. Mazzoni, F. McKenna, and G.L. Fenves. OpenSees command language manual. *Pacific Earthquake Engineering Research (PEER) Center*, 2005.

[164] RE Melchers. Importance sampling in structural systems. *Structural safety*, 6(1):3–10, 1989.

[165] R.E. Melchers. Structural reliability analysis and prediction. 1999.

[166] C. Meletti and V. Montaldo. Stime di pericolosità sismica per diverse probabilità di superamento in 50 anni: valori di ag. *Progetto DPC-INGV S1, Deliverable D*, 2007.

[167] N. Metropolis, A.W. Rosenbluth, M.N. Rosenbluth, A.H. Teller, E. Teller, et al. Equation of state calculations by fast computing machines. *The journal of chemical physics*, 21(6): 1087, 1953.

[168] S. Miyazato and Y. Hiraishi. Transport properties and steel corrosion in ductile fiber reinforced cement composites. In *Proceedings of the Eleventh International Conference on Fracture*, pages 20–25, 2005.

[169] J. Moehle and G.G. Deierlein. A framework methodology for performance-based earthquake engineering. In *Proceedings, 13th World Conference on Earthquake Engineering, Vancouver, Canada*, pages 1–6, 2004.

[170] V. Montaldo, E. Faccioli, G. Zonno, A. Akinci, and L. Malagnini. Treatment of ground-motion predictive relationships for the reference seismic hazard map of italy. *Journal of seismology*, 9(3):295–316, 2005.

[171] G. Monti and C. Nuti. Nonlinear cyclic behavior of reinforcing bars including buckling. *Journal of Structural Engineering*, 118:3268, 1992.

[172] W. Morris, A. Vico, and M. Vazquez. Chloride induced corrosion of reinforcing steel evaluated by concrete resistivity measurements. *Electrochimica acta*, 49(25):4447–4453, 2004.

[173] M. Mucciarelli, A. Spinelli, and F. Pacor. Un programma per la generazione di accelerogrammi sintetici "fisici" adeguati alla nuova normativa. *XI Convegno ANIDIS,"L'Ingegneria Sismica in Italia"*, pages 25–29, 2004.

[174] S. Mukherjee and V.K. Gupta. Wavelet-based generation of spectrum-compatible time-histories. *Soil Dynamics and Earthquake Engineering*, 22(9-12):799–804, 2002.

[175] RMW Musson et al. The use of Monte Carlo simulations for seismic hazard assessment in the UK. *Annals of Geophysics*, 43(1), 2000.

[176] AM Mwafy and AS Elnashai. Static pushover versus dynamic collapse analysis of RC buildings. *Engineering Structures*, 23(5):407–424, 2001. ISSN 0141-0296.

[177] A.E. Naaman. *A statistical theory of strength for fiber reinforced concrete*. PhD thesis, Massachusetts Institute of Technology, 1972.

[178] A.E. Naaman. Tensile strain-hardening frc composites: Historical evolution since the 1960. *Advances in Construction Materials 2007*, pages 181–202, 2007.

[179] AE Naaman and HW Reinhardt. Proposed classification of hpfrc composites based on their tensile response. *Materials and structures*, 39(5):547–555, 2006.

[180] J.M. Nau and W.J. Hall. Scaling methods for earthquake response spectra. *Journal of Structural Engineering*, 110(7):1533–1548, 1984.

[181] NTC 2008. Dm 14/01/2008. *GU n. 29 del 04.02. 2008, Suppl. Ordinario n*, 30, 2008.

[182] B.H. Oh and K.J Shin. Cracking, ductility and durability characteristics of hpfrcc with various mixture proportions and fibers. In *International RILEM Workshop on High Performance Fiber Reinforced Cementitious Composites in Structural Applications*, pages 213–222. RILEM Publications SARL, 2006.

[183] S. Otani. Nonlinear dynamic analysis of reinforced concrete building structures. *Canadian Journal of Civil Engineering*, 7(2):333–344, 1980. ISSN 1208-6029.

[184] M. Otieno, H. Beushausen, and M. Alexander. Prediction of corrosion rate in rc structures-a critical review. *Modelling of Corroding Concrete Structures*, pages 15–37, 2011.

[185] S. Pampanin. Emerging solutions for high seismic performance of precast/prestressed concrete buildings. *Journal of Advanced Concrete Technology*, 3(2):207–223, 2005.

[186] S. Pampanin, M.J.N. Priestley, and S. Sritharan. Analytical modelling of the seismic behaviour of precast concrete frames designed with ductile connections. *Journal of Earthquake Engineering*, 5(3):329–367, 2001.

[187] T.B. Panagiotakos and M.N. Fardis. Deformations of reinforced concrete members at yielding and ultimate. *ACI Structural Journal*, 98(2), 2001.

[188] TS Paraskeva, AJ Kappos, and AG Sextos. Extension of modal pushover analysis to seismic assessment of bridges. *Earthquake engineering & structural dynamics*, 35(10): 1269–1293, 2006.

[189] Y. Park, AH Ang, and Y.K. Wen. Seismic damage analysis of reinforced concrete buildings. *Journal of Structural Engineering*, 111(4):740–757, 1985.

[190] Y.J. Park and A.H.S. Ang. Mechanistic seismic damage model for reinforced concrete. *Journal of Structural Engineering*, 111:722–739, 1985.

[191] G.J. Parra-Montesinos. High-performance fiber-reinforced cement composites: An alternative for seismic design of structures. *ACI structural journal*, 102(5):668–675, 2005. ISSN 0889-3241.

[192] T. Paulay and M.J.N. Priestley. *Seismic design of reinforced concrete and masonry buildings*. Wiley Online Library, 1992.

[193] P. Pedeferri. La corrosione delle armature nel calcestruzzo, 1992.

[194] P. Pedeferri and L. Bertolini. *La corrosione nel calcestruzzo e negli ambienti naturali*. McGraw-Hill, 1996.

[195] P.E. Pinto. Reliability methods in earthquake engineering. *Progress in Structural Engineering and Materials*, 3(1):76–85, 2001. ISSN 1528-2716.

[196] PE Pinto. Probabilistic methods for seismic assessment of existing structures. *LessLoss Report*, 2007.

[197] K. Porter, R. Kennedy, and R. Bachman. Creating fragility functions for performance-based earthquake engineering. *Earthquake Spectra*, 23:471, 2007.

[198] K.A. Porter. An overview of PEER's performance-based earthquake engineering methodology. In *Proceedings of Ninth International Conference on Applications of Statistics and Probability in Civil Engineering*, 2003.

[199] K.A. Porter, J.L. Beck, and R.V. Shaikhutdinov. Sensitivity of building loss estimates to major uncertain variables. *Earthquake Spectra*, 18:719, 2002.

[200] G. Pousse, L.F. Bonilla, F. Cotton, and L. Margerin. Nonstationary stochastic simulation of strong ground motion time histories including natural variability: Application to the k-net japanese database. *Bulletin of the Seismological Society of America*, 96(6):2103, 2006.

[201] M. Power, B. Chiou, N. Abrahamson, and C. Roblee. The next generation of ground motion attenuation models (nga) project: an overview. In *Proceedings, Eighth National Conference on Earthquake Engineering*, 2006.

[202] M.J.N. Priestley. Overview of presss research program. *Pci Journal*, 36(4):50–57, 1991.

[203] MJN Priestley, G.M. Calvi, and M.J Kowalsky. *Displacement-Based seismic design of structures*. IUSS PRESS, 2007.

[204] A. Quarteroni, R. Sacco, and F. Saleri. *Numerical mathematics*, volume 37. Springer Verlag, 2007.

[205] Al-Saadoun S.S. Rasheeduzzafar and A.S. Al-Gahtani. Corrosion cracking in relation to bar diameter, cover, and concrete quality. *Journal of Materials in Civil Engineering*, 4: 327–332, 1992.

[206] AG Razaqpur and OB Isgor. Prediction of reinforcement corrosion in concrete structures. *Frontier Technologies for Infrastructures Engineering: Structures and Infrastructures Book Series*, 4:45, 2009.

[207] JR Rice. A path independent integral and the approximate analysis of strain concentration by notches and cracks. *Journal of Applied Mechanics*, 35:379, 1968.

[208] R. Riddell. On ground motion intensity indices. *Earthquake Spectra*, 23:147, 2007.

[209] R. Riddell and J.E. Garcia. Hysteretic energy spectrum and damage control. *Earthquake engineering & structural dynamics*, 30(12):1791–1816, 2001.

[210] J. Rodriguez, LM Ortega, and J. Casal. Load carrying capacity of concrete structures with corroded reinforcement. *Construction and Building Materials*, 11(4):239–248, 1997.

[211] R. Romeo and A. Prestininzi. Probabilistic versus deterministic seismic hazard analysis: an integrated approach for siting problems. *Soil Dynamics and Earthquake Engineering*, 20(1-4):75–84, 2000.

[212] J.P. Romualdi and J.A. Mandel. Tensile strength of concrete affected by uniformly distributed and closely spaced short lengths of wire reinforcement. In *ACI Journal Proceedings*, volume 61. ACI, 1964.

[213] S.M. Ross. *Simulation*. Academic Press, fourth edition, 2006. ISBN 0125980630.

[214] R.Y Rubinstein and D.P. Kroese. *Simulation and the Monte Carlo method*. John Wiley & Sons, Inc., second edition, 2008.

[215] F. Sabetta and A. Pugliese. Estimation of response spectra and simulation of nonstationary earthquake ground motions. *Bulletin of the Seismological Society of America*, 86 (2):337, 1996. ISSN 0037-1106.

[216] A. Saetta, R. Scotta, and R. Vitaliani. Coupled environmental-mechanical damage model of rc structures. *Journal of engineering mechanics*, 125:930, 1999.

[217] M. Sahmaran, M. Li, and V.C. Li. Transport properties of engineered cementitious composites under chloride exposure. *ACI Materials Journal*, 104(6):604–611, 2007. ISSN 0889-325X.

[218] M. Sahmaran, V.C. Li, and C. Andrade. Corrosion resistance performance of steel-reinforced engineered cementitious composite beams. *ACI Materials Journal*, 105(3):243, 2008.

[219] J.L. Schiff. *Cellular automata: a discrete view of the world*. Wiley-Interscience, 2008. ISBN 0470168790.

[220] G.I. Schueller and H.J. Pradlwarter. Uncertainty analysis of complex structural systems. *International Journal for Numerical Methods in Engineering*, 80(6-7):881–913, 2009.

[221] D.P. Schwartz and KJ Coppersmith. Seismic hazards: new trends in analysis using geologic data. *Active Tectonics*, pages 215–230, 1986.

[222] M.H. Scott and G.L. Fenves. Plastic hinge integration methods for force-based beam–column elements. *Journal of structural engineering*, 132:244, 2006.

[223] T.K. Sen. *Fundamentals of seismic loading on structures*. Wiley Online Library, 2009. ISBN 0470017554.

[224] E. Spacone, F.C. Filippou, and F.F. Taucer. Fibre beam-column model for non-linear analysis of r/c frames: Part i. formulation. *Earthquake Engineering and Structural Dynamics*, 25(7):711–726, 1996.

[225] E. Spacone, F.C. Filippou, and F.F. Taucer. Fibre beam-column model for non-linear analysis of r/c frames: part ii. applications. *Earthquake Engineering and Structural Dynamics*, 25(7):727–742, 1996.

[226] M. Stein. Large sample properties of simulations using Latin hypercube sampling. *Technometrics*, 29(2):143–151, 1987. ISSN 0040-1706.

[227] J.C. Stepp, I. Wong, J. Whitney, R. Quittmeyer, N. Abrahamson, G. Toro, R. Youngs, K. Coppersmith, J. Savy, T. Sullivan, et al. Probabilistic seismic hazard analyses for ground motions and fault displacement at yucca mountain, nevada. *Earthquake spectra*, 17:113, 2001.

[228] J.P. Stewart, S.J. Chiou, J.D. Bray, R.W. Graves, P.G. Somerville, and N.A. Abrahamson. Ground motion evaluation procedures for performance-based design. *Soil dynamics and earthquake engineering*, 22(9-12):765–772, 2002. ISSN 0267-7261.

[229] M.G. Stewart and D.V. Rosowsky. Time-dependent reliability of deteriorating reinforced concrete bridge decks. *Structural Safety*, 20(1):91–109, 1998.

[230] K. Tuutti. Service life of structures with regard to corrosion of embedded steel. *Performance of concrete in marine environment*, pages 223–236, 1980.

[231] D.V. Val and R.E. Melchers. Reliability of deteriorating rc slab bridges. *Journal of structural engineering*, 123:1638, 1997.

[232] D. Vamvatsikos. *Seismic performance, capacity and reliability of structures as seen through incremental dynamic analysis*. PhD thesis, Stanford University, 2002.

[233] D. Vamvatsikos. Performing incremental dynamic analysis in parallel. *Computers & Structures*, 2010.

[234] D. Vamvatsikos and C.A. Cornell. Incremental dynamic analysis. *Earthquake Engineering & Structural Dynamics*, 31(3):491–514, 2002. ISSN 1096-9845.

[235] D. Vamvatsikos and C.A. Cornell. The incremental dynamic analysis and its application to performance-based earthquake engineering. In *Proceedings of the 12th European Conference on Earthquake Engineering*, 2002.

[236] D. Vamvatsikos and C.A. Cornell. Applied incremental dynamic analysis. *Earthquake Spectra*, 20:523, 2004.

[237] M. Vergani. Modellazione del degrado di strutture in calcestruzzo armato soggette a corrosione. Master's thesis, Politecnico di Milano, 2009.

[238] B. Vick. Multi-physics modeling using cellular automata. *COMPLEX SYSTEMS-CHAMPAIGN-*, 17(1/2):65, 2007.

[239] T. Vidal, A. Castel, and R. Francois. Analyzing crack width to predict corrosion in reinforced concrete. *Cement and Concrete Research*, 34(1):165–174, 2004.

[240] M. Vorechovskı and D. Novák. Correlation control in small-sample monte carlo type simulations i: A simulated annealing approach. *Probabilistic Engineering Mechanics*, 24 (3):452–462, 2009.

[241] M. Vořechovskỳ and D. Novák. Statistical correlation in stratified sampling. In *Proc. of 9th Int. Conf. on Applications of Statistics and Probability in Civil Engineering–ICASP*, volume 9, pages 119–124, 2003.

[242] K.A.T. Vu and M.G. Stewart. Structural reliability of concrete bridges including improved chloride-induced corrosion models. *Structural safety*, 22(4):313–333, 2000.

[243] S. Wang and V.C. Li. High-early-strength engineered cementitious composites. *ACI materials journal*, 103(2):97, 2006.

[244] S. Wang and V.C. Li. Engineered cementitious composites with high-volume fly ash. *ACI Materials Journal*, 104(3):233–241, 2007. ISSN 0889-325X.

[245] S. Wolfram. Statistical mechanics of cellular automata. *Reviews of Modern Physics*, 55 (3):601, 1983.

[246] F.S. Wong. First-order, second-moment methods. *Computers & Structures*, 20(4): 779–791, 1985. ISSN 0045-7949.

[247] E. Yang and V.C. Li. Numerical study on steady-state cracking of composites. *Composites science and technology*, 67(2):151–156, 2007.

[248] E.H. Yang, S. Wang, Y. Yang, and V.C. Li. Fiber-bridging constitutive law of engineered cementitious composites. *Journal of Advanced Concrete Technology*, 6(1):181–193, 2008. ISSN 1346-8014.

[249] F. Zareian and H. Krawinkler. Assessment of probability of collapse and design for collapse safety. *Earthquake Engineering & Structural Dynamics*, 36(13):1901–1914, 2007. ISSN 1096-9845.

[250] R. Zhang, A. Castel, and R. François. Concrete cover cracking with reinforcement corrosion of rc beam during chloride-induced corrosion process. *Cement and Concrete Research*, 40(3):415–425, 2010.

[251] O.C. Zienkiewicz and R.L. Taylor. *The finite element method*, volume 1: The basis. Butterworth-Heinemann, 2000.